A study of the effect of process conditions on the fluidization behaviour of cohesive industrial powders linked with rheological studies

Roberto Chirone

Department of Chemical Engineering

University College London

A thesis submitted for the degree of Doctor of Philosophy of University College London

March 2018

I, Roberto Chirone, confirm that the work presented in this thesis is my own. Where information has been derived from other sources, I confirm that this has been indicated in the thesis.

A Marco…
Non aver paura delle diversita'
Non aver paura di ascoltare
Non aver paura di sbagliare
Non aver paura di scegliere
Di' sempre la tua e fallo a testa alta

Abstract

The role that fluidized bed reactors and other unit operations play for a wide range of industries is well recognized. Although fluidized bed systems offer several advantages such as high heat transfer rate, rapid solids mixing, large surface contact, high heat and mass transfer rates between gas and particles, a complete understanding of the phenomena occurring in these reactors is still a challenge, with reference to the role of the process conditions, such as pressure, temperature and humidity. Generally, the temperature affects both the properties of the material and the fluid, such as density and fluidizing gas viscosity. These changes can influence significantly the design and efficiency of the reactor. For these reasons, the effect of the temperature on fluidization became the center of a significant academic effort aimed at providing a theoretical framework to underpin the major physical phenomena involved and, in particular, to develop correlations for the scale-up of fluidized bed reactors.

Several works have demonstrated that process conditions can influence the role of the interparticle forces (IPFs) in the fluidization behaviour of powders. Given the complexity of the phenomena involved, a direct quantification of the particle-particle interactions in fluidized beds and of their changes at process conditions is very difficult. Within this framework, powder rheology represents an appealing tool to evaluate indirectly the effects of the interparticles forces on fluidization.

The main objective of the present work is to provide a basis for understanding the factor responsible for changes in fluidization behaviour of industrial particles under realistic process conditions. In order to address the problem of assessing the fluidization behavior of powders at high temperature, a multidisciplinary approach linking micro and macro properties of the particulate system is adopted in this project. On the one hand, the investigation of the fluidization behavior at process conditions is carried out by means of standard fluidization tests; on the other hand, the characterization of the flow properties of the same powders is performed by means of powder rheology tests. To this end, the

experimental campaign was performed using a 140x1000 mm heated gas fluidized bed and a modified Schulze annular shear cell. Both experimental apparatuses allowed a safe operation of the system up to 600 °C. Five cuts of the same mother particles covering Group B, A and C of Geldart's classification were investigated over a range of temperatures from ambient to 500 °C. Furthermore, two reacted samples of the same mother particles but, containing different levels of impurities were tested.

Shear test experiments show changes of the flow properties at high temperatures. The powder cohesion is the parameter which appears to be mostly affected by temperature while the angle of internal friction shows a weaker dependence on temperature and consolidation level. A model combining the continuum approach and the particle–particle interaction description was used to correlate the powder tensile strength with the interparticle forces. In the presence of only van der Waals forces, the model with the assumption of plastic deformation at contact points and a reasonable value of the mean curvature radius is able to predict the correct order of magnitude of the tensile strength. Furthermore, the significant increase of the cohesion of the reacted material with increasing temperature can be only justified by considering an active role of capillary bridges between the particle asperities. These findings, together with the nature of the impurities characterized by means of EDX analysis applied to SEM imaging, strongly suggest that the observed changes for the reacted material are due to the occurrence of capillary bridges between particles, even if thermal analyses are not able to detect any significant phase changes.

This work assessed also the validity of some classical concepts and equations commonly used for describing the fluidization behaviour at low and high temperature. The minimum fluidization conditions were well predicted by the Ergun equation when accounting for the experimental values of the bed voidage. The bed collapse test was used to quantify changes in the aeratability of the powders between low and high temperature and to identify the minimum bubbling conditions. For systems dominated by IPFs the analysis of the voidage of the dense phase and the overall bed expansion as a function of the flow rate allowed reconstructing the sequence of phenomena through which a stable flow of bubbles across the solid mass were achieved.

The role of hydrodynamic forces and of interparticle forces on the fluidization behaviour of the particulate systems studied was investigated by looking at the applicability of the Foscolo and Gibilaro stability criterion [*Chem Eng Sci. 1984, 39 (12): 1667-1675*]. In particular the analysis followed the approach indicated by Valverde et al. [*Europhys Lett. 2007, 54: 329-334.*], which makes use of the initial settling velocity of cohesive particles and of the Bond number derived from rheometry results. The results of the analysis show the capability of predicting the final structure of the bed with temperature when considering an aggregative fluidization behaviour caused by interparticle adhesive forces.

These results also suggest the potential use of the powder rheometry carried out at high temperature as a sensitive method to detect phase changes in particulate systems that are limited to the particle surface that can significantly affect the working conditions of fluidized bed reactors. More in general, the results indicate that shear testing results at ambient and high temperatures allow to correctly estimate the intensity of interparticle forces in particulate systems.

Impact of the research

A recent report of the Chemical Industry Association states that almost 90% of all chemical products in production involve the use of relatively fine particles at a certain stage in the manufacturing process. Research in particle technology is an essential platform to tackle most of the contemporary challenges and make significant progress in different fields, such as in advanced manufacturing, global health, water purification, food preservation and an increasingly efficient use of renewable sources for sustainable energy production.

Fluidization technology is a suitable operation for processing of powders and it is employed in a wide range of industrial applications. Furthermore, fluidization is recognized to be one of the most promising technologies to optimize the exploitation of the available potential of renewable energy sources. Even if a certain fundamental understanding of the mechanisms governing the fluidized bed behaviour is already achieved at ambient conditions, the full control of several phenomena of fluidized bed at process conditions still represents a scientific and engineering challenge. This is true, in particular, when an improvement of the operability of commercial fluidized bed processes is desired or, even more, in cases in which the design of new industrial processes that use fine materials is required.

High temperature is one of the most significant factors that introduces significant changes between the behaviour of model fluidized beds at ambient conditions and the industrial application of powder fluidization. Consequently, the scale-up from laboratory to commercial scale of fluidized bed reactors can be very risky indeed and, even today, represents a key challenge in the development of innovations in fluidized bed processes. A reason of this lack of predictively is the fact that available fluidized-bed models and scaling up relationships do not properly account for the effects that operating conditions such as temperature, pressure and velocity may have on particles fluidization behaviour.

The proposed research provides bases for understanding the main factors that are responsible of introducing significant changes in multiphase and particulate processes that can distort the model predictions of the flow behaviour of dense multiphase reactive industrial powders. The knowledge produced by this research has the potential to drive

the commercial application of fluidization by improving the possibility of a correct optimization of the processes and by providing industry with the sustaining scientific knowledge from which to develop innovative future technologies of process engineering, in particular applied to the manufacturing and the energy sector.

Acknowledgments

First of all, I would like to express my immense gratitude to Prof. Paola Lettieri for her support and constant encouragement throughout this project. I am grateful for her guidance to think freely and for introducing me to the fascinating world of University College London. She is a unique supervisor, a great mentor and an amazing woman.

I am deeply grateful to Prof. Massimo Poletto. This work would not have been possible without his constant dedication, guidance and advice. He has provided me with invaluable source of inspiration, encouragement and critical analysis. A special thank you is also reserved to Dr. Diego Barletta for his inestimable help during the practical work

My sincere thanks go to Michael Molnar and Jing Huang for the many fruitful discussions and for supporting me throughout the project.

Many thanks are also due to the researchers and technicians at Istituto di Ricerche sulla Combustione, Massimo, Paola, Federica and Luciano, which help me with their skills and expertise.

Thank you to all my friends: Andrea, Domenico, Max, Luca, Fabio, Giancarlo, Giovanni, Daniele, Simona and Martina who made this PhD journey much more enjoyable.

I owe a great debt to my family who have been a constant source of inestimable encouragement and support with their love over the years. I wish also to thank my second family to take care of me along these years.

I want to say thanks to my oldest friend Bengy and Riki because they are what they are... my best friends.

Finally, un grazie speciale va a te, Rita. Tu che ti prendi cura di me sempre in ogni istante con un sorriso, una carezza, una “cazziata”... Tu che riesci a farmi ridere nei momenti piu difficili, tu che mi sopporti quando non mi sopporterei neanche io. A te dico GRAZIE Amore Mio...

I acknowledge financial support for this project from Dow Corning Corporation.

Table of Contents

List of Figures

List of Tables

1 Introduction

Fluidization is one of the most common unit operation involving granular materials at high temperature. First industrial fluidized beds date back to 1942. During the Second World War a group of companies, including Standard Oil Indiana, M.W. Kellogg's, Shell and Standard Oil Development Company developed the first fluidized solid system process for Catalytic Cracking. This process was used to convert the high-molecular weight hydrocarbon fractions of petroleum oils to gasoline. Since that, it has been employed in industry for many other processes including processes of roasting and calcination of minerals, combustion and gasification of fossil fuels, incineration of waste or in heat transfer processes, such as drying of mineral and synthetic products like fertilizers, drugs or polymeric compounds. Consequently, fluidization also became the center of great deal of academic studies.

1.1 Motivation

Fluidization is the most powerful method to handle a variety of solid particulate materials in industry. Generally, this process is used to achieve an intimate contact between a solid phase (granular material) and fluid phase (liquid or gas) [1].

A bed of solid particles is transformed into a fluid-like state through suspension in a gas or liquid. The fluid is uniformly supplied through a distribution plate placed at the bottom of the bed of solid particles. It will move upwards through the bed via the void spaces among the particles. At low values of the fluid velocity, the solid particles form a fixed bed through which the fluid percolates. Increasing the fluid velocity, there comes a point where the bed is supported by the fluidizing gas. In such condition, the drag force on the particles becomes equal to the buoyant weight of the bed and the pressure drop across the bed is equal to the weight of the bed per unit cross sectional area.

This phenomenon is known as fluidization and the bed is referred to as an incipient fluidized bed or a bed at minimum fluidization condition. The velocity of the fluid and the voidage of the bed at minimum fluidization condition are called u_{mf} and ε_{mf} respectively.

In this condition the behavior of the fluid-solid system is analogous to that of a liquid with an average density ρ_b:

$$\rho_b = (\rho_p - \rho_f)(1 - \epsilon) \quad \text{Eq. 1}$$

Where ρ_p is the solid particle density, ρ_f is the fluid density and ε is the bed voidage. It may be observed that the surface of the bed maintains a horizontal level when the bed is tilted; when two beds are connected their levels equalize; objects with density lower than ρ_b will float on the bed surface while objects with density higher than it will sink to the bottom of the bed.

The fluid-like properties of fluidized beds make them attractive for industrial processes where a solid (often the catalyst for a reaction) and a gas are to be put in contact. Moreover, another very interesting point is the rapid mixing and circulation of solids in bubbling beds which allows for a uniform temperature in the system. Therefore, high temperature operations in fluidized beds can be simply and reliably controlled. In particular, the main features of that process are high heat transfer rate, rapid solids mixing, large surface contact, high heat and mass transfer rates between gas and particles compared with other techniques. For these reasons this technique is widely applied for both process and energy industries. In most cases the operating conditions (temperature and pressure) of fluidized bed reactors are far from ambient condition [1]. Some examples of industrial applications are presented in Table 1. Generally, the temperature affects both the properties of the material and the fluid, such as density and fluidizing gas viscosity. These changes can influence significantly the design and efficiency of the reactor. For these reasons, the effect of the temperature on fluidization became the center of a significant academic effort aimed at providing a theoretical framework to underpin the major physical phenomena involved and, in particular, to develop correlations for the scale-up of fluidized bed reactors.

Table 1 - Some industrial applications of fluidized beds [1]

Process	Example	Process conditions		
		T, °C	P, atm	Fines, %
Cracking of Hydrocarbons	FCC	480-550	1-3	10-30
	Ethylene and Propylene	750	~1	10-30
Chemicals Synthesis	Acrylonitrile	400-500	1.5 - 3	20-40
	Melamine	400	>1	-
	Maleic Anhydride (Mitsubishi Chem. Ind.)	410-420	1-5	25-55
	Maleic Anhydride (DuPont)	360-420	<5	-
	Ethylene dichloride	220-245	2.5 - 6	30
	Phthalic Anhydride	345-385	2.7	28
	Polyethylene	75-105	20 - 25	-
Metallurgical industry	Iron	850	3.5	-
	AlF_3 synthesis	530	1	-
	Alumina calcination	800-1200	1	0-50
	Limestone calcination	770	1	Variable
	Gold roasting	650	1	-
	SO_2 from sulphide ores roasting	650-700	1	-
	Pyrite roasting	660-920	1	-
	FeS_2 from sulphide ores roasting	650 - 1100	1	< 3
Drying of solids	Inorganic materials	60 - 110	1	Variable
	Pharmaceuticals	60	1	Variable
Semiconductor Industry	$SiHCl_3$ production	300	1	100
	Silicon production	600 - 800	~1	-
Nuclear Industry	Separation of U-235 from U-238	450	-	-

Despite this, the effects of process conditions on fluidization are still not entirely understood. Design criteria and performance predictions for fluidized bed units working at high temperature have been largely based on fluid-dynamic models and correlations established from tests developed at ambient temperature. Generally, the influence of the working temperature on the dynamic features of the system has been considered by simply accounting for the changes of the gas properties, specifically its viscosity and density. However, extrapolating the results and relationships available at ambient conditions to elevated temperatures can lead to misleading predictions of the fluidized bed performance at high temperature. Drastic changes can occur in the fluidization behavior between low and high temperatures, due to possible modifications induced by the temperature in the structure of the bed. In order to understand the factors responsible for such changes in fluidization behavior, the roles of the interparticles forces (IPFs) and

hydrodynamic forces (HDFs) have been studied, but much controversy still remains to define their relative importance. Although several studies have been carried out on the influence of operating conditions on fluidization, the findings are still controversial and a satisfactory understanding of the phenomena which cause differences between ambient and high temperature conditions has not yet been achieved [2–11]. Temperature can have a considerable effect on particle adhesion, enhancing the role of the interparticles forces (IPFs) on the fluidization quality, if the system is operated at temperatures close to the minimum sintering temperature of the particles. In addition, an increase in temperature may enhance the Hamaker constant, which is related to the van der Waals' attractive forces.

It is universally recognized that, with regard to the effect of temperature on fluidization conditions, a clear correlation for the evaluation of operating parameters, such as minimum fluidization velocity, average particle size distributions of the fluidized particles, terminal velocity, has not yet been identified.

1.2 Objectives of the work

The present work is aimed at investigating the flow properties of fluidized particles of industrial interest under realistic process conditions. Particular emphasis was given to the effect of particle size, operating temperature and different amount of impurities on the same mother particles. Within this framework, powder rheology represents an appealing tool to evaluate indirectly the effects of the interparticle forces on fluidization.

In order to better assess on this point, the High Temperature Annular Shear Cell (HT-ASC) was used to characterize the flow properties of the powder samples with different particle size distributions and different amounts of impurities between ambient temperature and 500 °C.

The final goal of the project is aimed at investigating through a multidisciplinary approach the link between the behavior of fluidized beds operated at high temperature and the rheological measurements. In particular, the main objective is to investigate the influence of high temperature, particle size distribution and composition on the flow behavior of different silicon powders and mixtures with different amounts of impurities.

1.3 Methodology

In order to address the problem of assessing the fluidization behavior of powders at high temperature, the two-fold approach schematically presented in Figure 1 is adopted in this project. On the one hand, the investigation of the fluidization behavior at process conditions is carried out by means of standard fluidization tests; on the other hand, the characterization of the flow properties of the same powders is performed by means of rheological tests. The challenge of the project is to link the rheological measurements to the corresponding fluidization behavior of the powders in order to achieve a physical understanding of the effect of process conditions on fluidization.

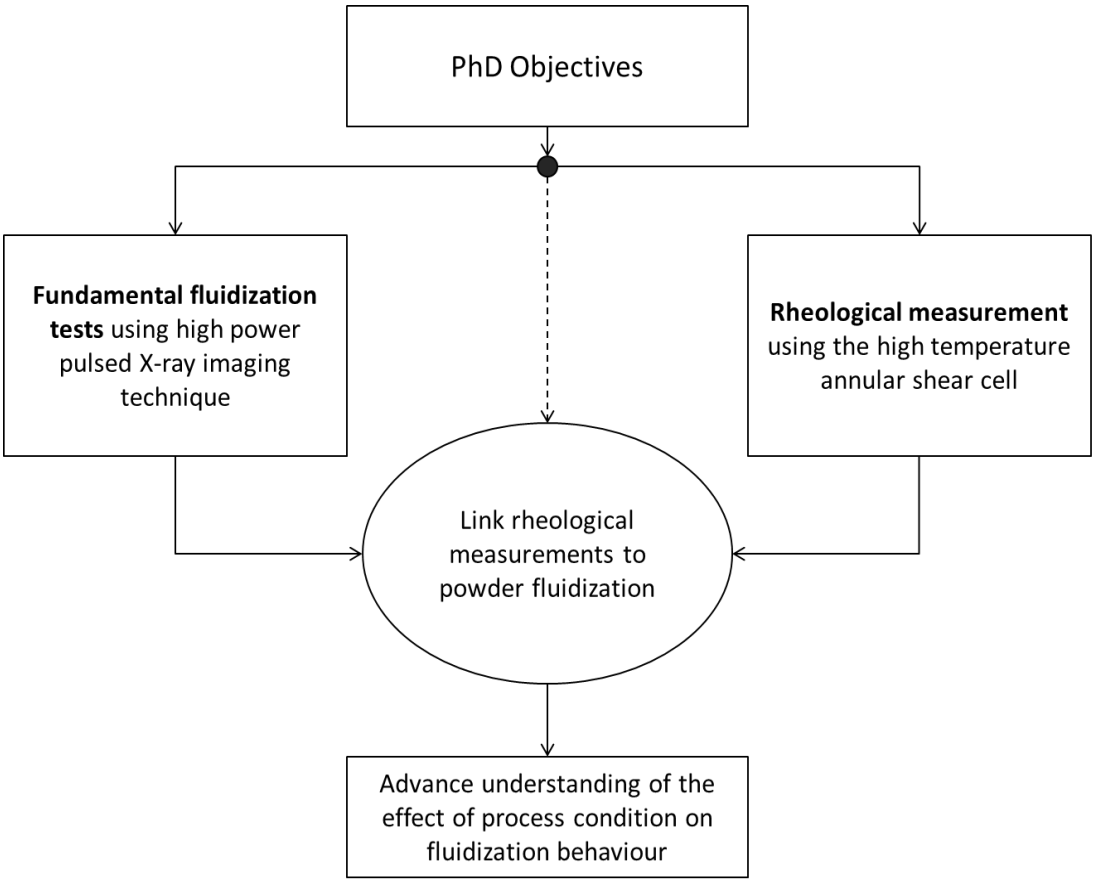

Figure 1 - Schematic representation of the aim and main objectives of the project.

The material chosen for this study was ceramic powder provided by an industrial supplier, where it is used as main material in the production process. The latter process involves a fluidized bed reactor and the operative conditions are 500 °C and 30 bar of temperature and pressure, respectively.

To study the effect of particle size, the silicon powders were sieved into five different size ranges (A1, A2, A3, A4, and A5). The effect of temperature was investigated in the range of temperature between ambient and 500 °C. Finally, the influence of surface impurities deriving from the process of these powders was analyzed testing two different samples of the same mother material but with different amount of impurities.

The fundamental fluidization parameters were measured for each silicon sample with increasing temperature using a 140 mm diameter x 1000 mm tall heated gas fluidized bed. The parameters measured included:

- minimum fluidization velocity, u_{mf}
- bed expansion profiles:
    - settled bed voidage, ε_s
    - voidage at minimum fluidization, ε_{mf}
    - voidage at minimum bubbling, ε_{mb}
    - Richardson and Zaki profiles (n, u_t)
- dense phase properties (from bed collapse test):
    - dense phase collapse rate, U_{de}
    - deaeration time, t_s
    - bed expansion ratio, BER
    - standardized collapse time, SCT
- dense phase voidage, ε_d
- minimum bubbling velocity, u_{mb}
- non bubbling ratio, u_{mb}/u_{mf}

The scope of this part of the work was to characterize the fluidization behavior of the samples with regard to temperature, detecting which of these key parameters of the fluidization behavior is more sensitive to temperature and to particle size distribution. Experimental values of u_{mf}, u_{mb} and U_{de} were also compared with predictions, to evaluate the ability of some of the currently used correlations to predict the behavior of powders at high temperature conditions. The role of hydrodynamic forces (HDFs) on the stability of the fluidized systems was investigated by looking at the applicability of Foscolo and Gibilaro's [12] stability criterion, together with the analysis conducted on the initial settling

velocity of cohesive particles conducted by Valverde et al. [13] and the rheological results. To this end, experimental values of the voidage at minimum bubbling, ε_{mb}, were compared with the prediction given by their model with increasing temperature. The bed collapse technique was used to characterize the areability of powders as a function of temperature. It can be used as a discriminating method of assessing how the materials behave between low and high temperature fluidization. In particular, measurements of dense phase collapse rate, U_{de}, and standardized collapse time, SCT, as a function of temperature, provide a quantitative understanding of the capability of the powders to tolerate sudden changes in the unit. The bed collapse test relies on the foundation that a fast rate of bed collapse is indicative of potential problems in the unit and is therefore capable of characterizing the "fluidizability" and "operability" of materials under operational conditions. Results from bed collapse test were also used to distinguish between systems of powders whose fluidization behaviour was dominated by the HDFs and IPFs (interparticle forces). Along with fluidization test also thermal analyses, such as thermogravimetric (TGA) and differential thermal analysis (DTA) were performed. The purpose was to put in evidence any possible phase transitions or chemical reactions in the range of the temperatures of interest. DTA and TGA were performed in air and nitrogen and the temperature program adopted ensure a linear rate temperature increase, 10 °C/min, from 25 °C to 550 °C. Results obtained from these physical tests were compared with fluidization findings.

The rheological characterization of the powders is part of the work. It was accomplished using the High Temperature Annular Shear Cell (HT-ASC or ASC), which was designed and commissioned by the University of Salerno. The high temperature shear cell is a unique apparatus which allows the evaluation of the flow properties of a bulk of powder for temperatures up to 500 °C. In particular, the experiments carried out in this study investigated the effect of temperature on the failure properties:

- static angle of internal friction, φ
- cohesion, C
- tensile strength, σ_t
- flow factor (ratio of consolidation stress to unconfined yield strength), ffc

The failure properties were measured at very low consolidation level, around 1000−1700 Pa, in order to be close to the minimum fluidization condition.

Finally, the ultimate goal of the experimental campaign was to find correspondences between the rheological and the fluidization behaviour of the various ceramic powder samples analyzed. In particular, a link was found between the voidage of the bed at minimum fluidization conditions and the voidage at fully bubbling conditions and the interparticle forces estimated from the shear experiments. The differences detected by means of the fluidization tests, ε_{mb}, could be explained when including in the predictive equations the adhesion-induced aggregation of fine particles. The latter is a function of the Bond number and of the effective number of the particles per agglomerate. Furthermore, the interparticle forces derived from the shear cell data were compared with the forces calculated in a fluidized bed with the presence of sound field.

1.4 Structure of the thesis

The report starts with a literature survey, chapter 2, on the main interparticle forces involved in the particle processes. Then it moves on the effect that interparticle forces have on the fluidization system and which are the most significant aspects and findings on the effect of temperature on the gas-solid fluidization, such as minimum fluidization, bed expansion, bed voidage and de-aeration rates. Finally, the main techniques used for the characterization and prediction of the flow properties of powders will be also presented. In particular, it will be highlighted how the rheology studies on solid particles can be used as methodology to understand the fluidization dynamics of these systems. Chapter 3 is dedicated to the description of the materials, equipment and experimental methods adopted in this study. Chapter 4 reports the results obtained through analytical measurements, such as laser-light scattering technique, SEM/EDX analyses and thermal analyses. Chapter 5 describes the experimental results obtained for rheological measurement; instead chapter 6 shows the fluidization findings. An entire chapter, number 7, is dedicated to the connection between rheological findings and fluidization behavior. The conclusions and future work are outlined in chapter 8. Graphs and tables summarizing the results of rheological and fluidization tests can be found in the Appendix.

2 Literature review

2.1 Interparticle forces

In all powder handling processes, the adhesive forces between both particles and surfaces might play a relevant role. The particle-particle contact forces can be the result of several mechanisms such as van der Waals forces, electrostatic forces, magnetic forces and capillary bridges, as well as frictional. An extensive review on the subject is reported by Israelachvili [14]. Obviously, these forces may make very challenging to handle the powders.

2.1.1. Van der Waals forces

The Dutch physicist van der Waals was the first to observe the non-ideal behaviour of a gas and he was the first to relate it to an attraction between molecules in the gas [15]. The van der Waals force, or intermolecular force, is a consequence of electrodynamic non-uniformity distribution. It arises from interaction between both uncharged molecules and atoms and it leads to a universal force of attraction between macroscopic bodies. According to Tabor [16], the intermolecular forces include dipole-dipole forces, dipole-induced dipole forces and dispersion forces between non-polar molecules.

Dipole-dipole force is the force between permanent dipoles. In particular, every molecule consists of positive and negative charges which are separated by a small distance (around 0.1 nm) forming an electric dipole. The latter interacts with the adjacent molecule producing an attractive force proportional to z_0^{-7}, where z_0 is the distance between molecules.

Dipole-induced dipole force is the force between a permanent dipole and a corresponding induced dipole. This is the case of interaction of a molecule, which is a dipole, with another which has no natural dipole. The molecule dipole can induce a dipole in the neighboring molecule causing an attractive force still proportional to z_0^{-7}. Dispersion force between non-polar molecules is the force between instantaneously induced dipoles arises from the local polarization produced in molecules by the random fluctuation of electrons. Molecules which are not polar could become polar at any time, given that the configuration of its electrons becomes such that the molecule behaves temporarily as an electric dipole.

In order to the scale up the van der Waals forces for macroscopic bodies, with known volume and numbers of molecules per unit volume, two different approach can be followed: the microscopic theory of Hamaker [17] or the macroscopic theory of Lifshitz [18]. Generally, the van der Waals forces in case of macroscopic bodies are calculated through the microscopic theory. The main assumption of the microscopic theory is that the energy interactions between the isolated molecules are additive and non-interacting, so the total force is computed as sum over all interacting pairs and integrating the molecular interactions over the entire body. This makes the calculations dependent on the shape of the objects. Hamaker performed calculations for different geometries and he found that the attraction force, F_a, between two spherical and rigid particles having diameters d_1 and d_2 is:

$$F_a = \frac{A}{12\, z_0^2} \frac{d_1 d_2}{(d_1 + d_2)} \qquad \text{Eq. 2}$$

Where A is the Hamaker constant; it is a property of the molecules in contact and of any third material between the two bodies.

The microscopic theory considers only pairwise additively and it neglects interactions between molecules and atoms in the presence of other atoms, known as many-body interactions. The macroscopic Lifshitz [18] theory represents a more rigorous approach which consider also the effect of a large number of interacting particles and provides a rigorous method for the calculation of the Hamaker constant as a function of the Lifshitz- van der Waals constant, hw:

$$A = \frac{3}{4\pi} hw \qquad \text{Eq. 3}$$

Values for the Hamaker constant can be found in Israelachvili [14]. The Lifshitz-van der Waals constant depends on the particle and the dielectric constant of the material between the particles. The value of A is significantly reduced for interaction across water. The attractive van der Waals force operates at very short range, and decays rapidly with distance. Van der Waals forces are essentially contact forces. According to Eq. 2 the attractive force increases

when the distance between particles decreases. In principle, it would go to infinity when the distance goes to zero. In other words, the attractive force would be infinite on contact but at very small distances repulsive interaction forces would start to be significant and balance attraction forces. Therefore, it was postulated that there is a minimum distance at which the force reaches a maximum. Generally, the Hamaker constant values in air are about 10^{-20} J [19],and the separation distance z_0 in the Eq. 2 is usually taken as z_0 = 0.4 nm (= 4 Å) in air [20].

Rietema et al. [21] calculated the minimum value for the parameter A, taking into account both repulsive attractive forces and using a net force $F_{attractive}$-$F_{repulsive}$. Following this approach, they evaluated a smaller value for the minimum surface separation of 2.23 Å. Considering this new value of the separation distance, they estimated also the cohesion force due to van der Waals forces for two perfectly spherical and rigid particles having diameters and density of a typical Geldart's Group A material. The result was several orders of magnitude greater than the gravitational force. They also elaborated a fairly complicated model to account for particle deformation when evaluating the cohesive force between particles.

Massimilla and Donsi [22] used a binomial formula for the attractive force caused by particle deformation previously developed by Molerus [23]:

$$F_a = \frac{A}{6\, z_0^2}\left[1 + \frac{A}{6\pi\, z_0^3 H}\right]\frac{d_1 d_2}{(d_1 + d_2)} \qquad \text{Eq. 4}$$

where H represents the material hardness. For non-spherical or for non-perfectly smooth particles it seems reasonable to consider a curvature radius considering asperities and the shape of particles. In the case of rough surface, asperities limit the approach of two particles and the effective separation distance is larger, thereby limiting the van der Waals attraction. For these reasons, the nominal particle diameter often overestimates the characteristic diameter of the contact area. According to these hypotheses, Schubert [24] proposed the Eq. 5:

$$F_a \approx \frac{A\,\delta}{12\,z_0^2} \qquad \text{Eq. 5}$$

Where δ is the value of the mean curvature radius at the contacting surface.

2.1.2. Electrostatic forces

Particles with an electric charge interact with each other. Particle adhesion due to static electricity is generated by the movement of electric charges on the surface of the particles at contact. Electrostatic forces depend on a number of variables difficult to evaluate, such as particle local geometry, surface roughness, presence of impurities, humidity and moisture in the molecular structure. Differently from van der Waals forces, electrostatic forces can be attractive or repulsive, depending on the charge of particles.

The Coulombic force F_{ec} acting between two charged particles can be approximately expressed as function of q_1, q_2, z, ξ_r, ξ_0 by Eq. 6.

$$F_{ef} \approx -\frac{1}{4\pi\xi_r\xi_0}\frac{q_1 q_2}{z^2} \qquad \text{Eq. 6}$$

Where q_1 and q_2 are the total charge of the particles, z is the distance between the centers of the particles, ξ_0 and ξ_r are the dielectric constant of the free space and the relative dielectric constant. Electrostatic interactions can occur also between a charged particle and an uncharged surface because of its own image charge. When a charged particle approaches a surface, it induces an "image charge" in the surface. That phenomenon is explained by Masuda et al. [25]. The image force F_{ei} is:

$$F_{ei} \approx \frac{1}{4\pi\xi_r\xi_0}\frac{q^2}{4z^2}\frac{\xi - \xi_r\xi_0}{\xi + \xi_r\xi_0} \qquad \text{Eq. 7}$$

q and ξ are the particle charge and the dielectric constant of the wall material.

2.1.3. Magnetic forces

As for the electrostatic forces, also the magnetic forces are produced by the motion of charged particles such as electrons. This nature indicates the close relationship between electricity and magnetism. The magnetic force between two particles depends on the shape of the particles, on the level of magnetization, on the orientation and distance of the particles. That force can be either attractive or repulsive and can be expressed as:

$$F_{mf} \approx \frac{\mu\, q_{m1} q_{m2}}{4\pi\, z^2} \qquad \text{Eq. 8}$$

where q_m, μ and z are the magnitudes of magnetic poles, the permeability of the intervening medium and the separation.

2.1.4. Capillary forces

The capillary force arises when a liquid phase is formed in the bulk solid of particles. The liquid phase formation can be assigned to the high relative humidity of atmosphere (>65%) or to chemical components which melt at high temperature. The liquid bridge is formed at the contact point of two particles (Figure 2) and results in an additional component to the van der Waals attraction force.

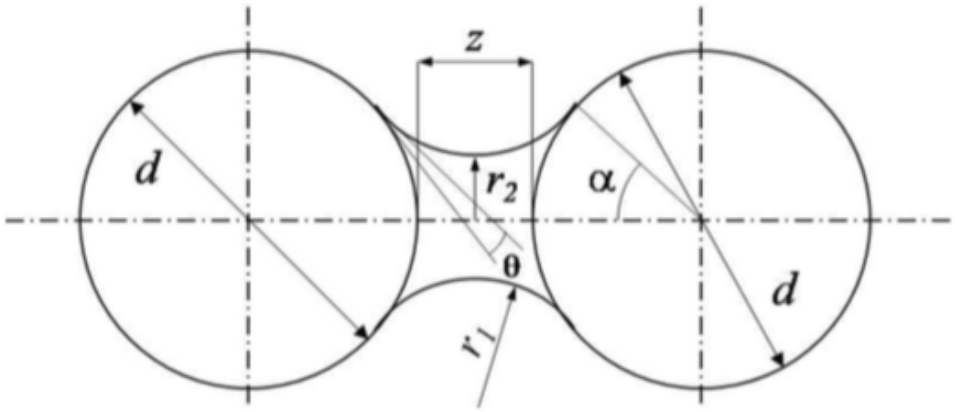

Figure 2 - Schematic representation of a liquid bridge between particles.

Liquid bonding depends on the level of liquid present. Generally, the capillary bridges are classified in four main types of bridging, as shown in Figure 2:

- the *pendular saturation state*, which results from a small point of liquid bridge formation; the liquid present is often due to adsorbed liquid layers
- the *funicular saturation state*, which occurs at higher level of liquid loading; in this case a few of the interstitial voids between the particles are filled
- the *capillary saturation state*, which results from a much thicker liquid layer around the particles, in this case all the interstitial spaces between the particles are filled with liquid
- the *liquid drop*, which forms when just a few particles are suspended in the liquid.

Considering the theory proposed by Fisher [26] in case of two spheres of same diameter d, bound by a liquid bridge of half-angle α at distance z, the total force exerted through the liquid bridge can be considered a combination of two components due to the surface tension, σ_s, acting on the solid-liquid interface and to the capillary pressure, ΔP, arising from the curvature of liquid meniscus at the fluid-liquid interface described by Eq. 9 and Eq. 10, respectively.

$$F_1 = 2\pi r_2 \sigma_s \qquad \text{Eq. 9}$$

$$F_2 = \pi r_2^2 \Delta P \qquad \text{Eq. 10}$$

The total capillary force will be expressed by the sum of these two components:

$$F_{cap} = 2\pi r_2 \sigma_s + \pi r_2^2 \Delta P \qquad \text{Eq. 11}$$

2.1.5. Measurements of interparticle forces at high temperature

A complete understanding of interparticle forces and its role and evaluation is necessary to optimize procedures and to design equipment for industrial plants processing granular

materials. On the other hand, it is equally important to measure the forces acting between two particles.

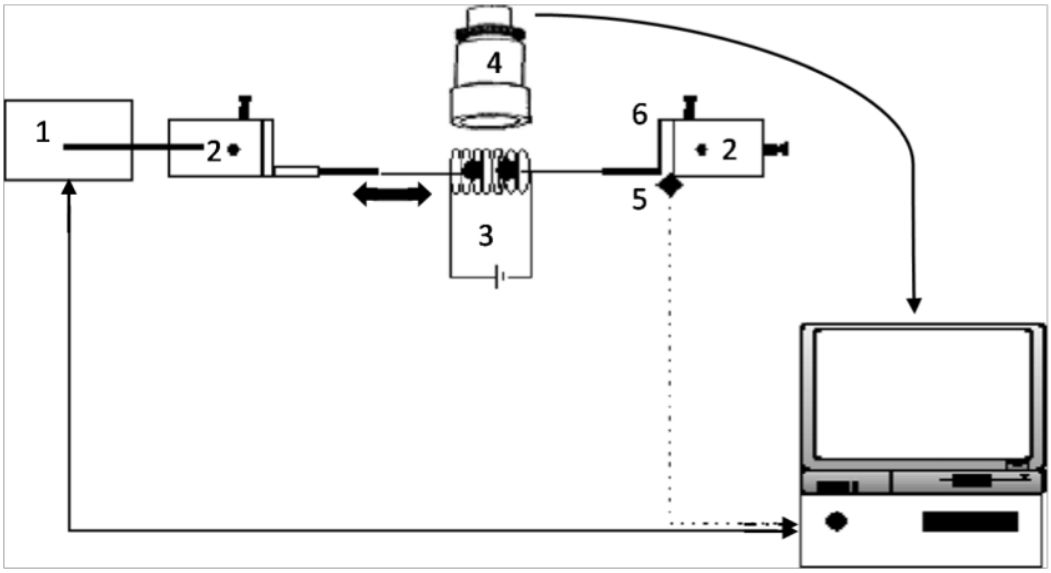

Figure 3 - Schematic representation of the HTMFB: (1) DC motor + axial linear actuator; (2) micromanipulators; (3) heating element + thermocouple; (4) objective + digital camera; (5) LVDT displacement sensor; (6) flexure strip assembly [27].

Most of the devices available are mainly built on the measurements carried out under ambient condition. They are based on the calculation of the displacement caused by these forces on a cantilever system capable to deform for very small forces (10^{-9} N) [28,29]. Moreover, the evaluation of these forces at high temperature is very challenging, mainly because of difficulties related to design heating system operating at the same time of the measurement device.

Pagliai et al. [27,30] developed a novel equipment, named High Temperature Micro-Force Balance (HTMFB), which allows a direct observation of the physical phenomena (Figure 3). Particles are attached on the tips of micropipettes, connected to two micromanipulators, under the focus of the microscope lens. This device measures the strength of a liquid bridge formed between particles, due to addition of a liquid onto the particles or melting the particle surfaces (i.e. as occurs during sintering).

2.2 Fluidization system

Fluidization is one of the most used processes involving granular material. It is a common knowledge that the overall comportment of fluid-particle processes is governed by the

forces acting on individual particles. As the velocity of the fluidizing fluid is increased through a system of solid particles, there comes a point where the drag force on the particles becomes equal to the buoyant weight of the bed. The bed is then supported by the fluidizing gas and possesses fluid-like properties such as: flowing easily, maintaining a horizontal level when tilted and allowing for low-density objects to float on the bed surface. This regime is known as “fluidization”, and the superficial gas velocity at which this happens is called the minimum fluidization velocity, umf. The behavior of the fluid-solid suspension for further increases in fluid velocity depends not only on the physical and geometrical characteristics of the bed particles and on the physical properties of the fluid, but also on the role of the interparticle forces. When the fluid velocity becomes higher than u_{mf} the bed can either show a homogeneous expansion (particulate or homogeneous fluidization) or give rise to the formation of cavities with a solid concentration close to zero, similar to bubbles in a liquid, which rise to the bed surface (aggregative or bubbling fluidization). The velocity at which the first bubble forms is called the minimum bubbling velocity, u_{mb}. At this point, a bubbling fluidized bed occurs as shown in Figure 4C. As the velocity is increased, the bubbles will coalesce and grow as they rise. If the ratio of the height to the diameter of the bed is high enough, the size of bubbles may become almost the same as the diameter of the bed. This is called the slugging regime (Figure 4D). If the particles are fluidized at a high enough gas flow rate, the velocity exceeds the terminal velocity of the particles. The upper surface of the bed disappears and, instead of bubbles, one observes a turbulent motion of solid clusters and voids of gas of various sizes and shapes. Beds under these conditions are called turbulent beds, as shown in Figure 4E. With further gas velocity increases of the fluidized bed becomes an entrained bed in which we have disperse, dilute or lean phase leading to pneumatic transport of solids.

Liquid-solid systems are often characterized by a homogeneous fluidization, while gas-solid systems do so only under special conditions, usually using fine light particles or fluidizing at high pressure.

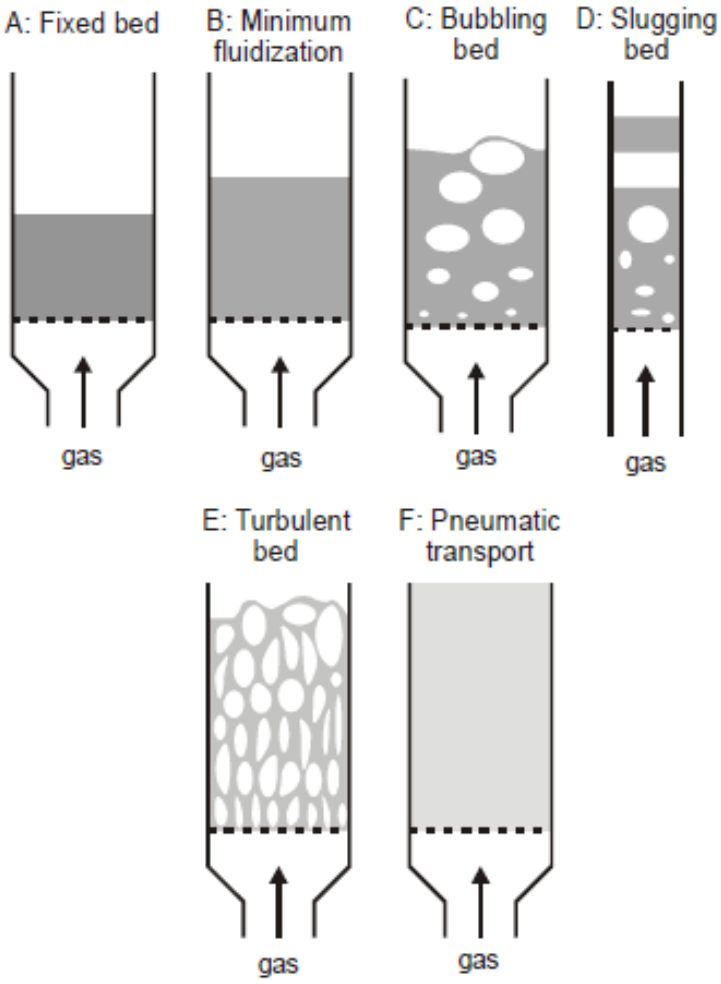

Figure 4 - Schematic representation of fluidized beds in different regimes (based on Kunii and Levenspiel [1]).

The bubbling and slugging regimes can be described as fluidization, because the bed of particles is fully supported by the pressure drop. Spouting and channelling cannot be described as fluidization because the pressure drop during these types of behaviour is less than that required to support the bed. The pressure drop across the bed can also be higher than the bed weight, as in the case when additional forces are present. These have to be overcome in order to achieve fluidization.

2.2.1. Geldart's classification

As it is clear from the previous paragraph, not all the particle systems fluidize in the same way. There are several different factors, which can influence the fluidization quality, such as particle size, shape factor, fines content, temperature and so on. Most of the particles of industrial interest do not show ideal behavior. In some cases, a considerable expansion

of the bed can be observed before the appearance of bubbles or, on the contrary, a difficulty of fluidization phenomena such as channeling and segregation, with a virtually static bed. Moreover, not every particle can be fluidized. The behavior of solid particles in fluidized beds depends mostly on their size and density. Geldart [31], in the attempt to classify the different fluidization behaviors, proposed an empirical classification based on the mean particle size and on the gas and particle densities. Boundaries between these groups were proposed in the form of a dimensional plot of (ρ_p-ρ_g) versus d_p as shown in Figure 5. Moreover, It must be noted that the Geldart [31] classification refers to ambient condition with air as fluidizing medium.

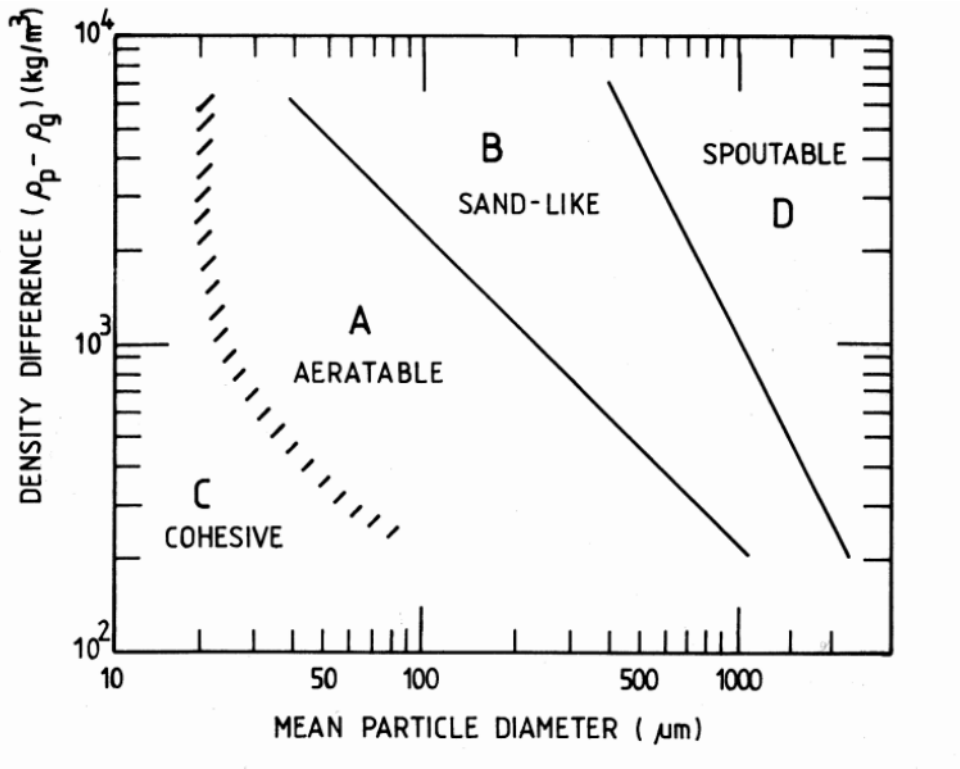

Figure 5 - Geldart classification for air at ambient conditions [31].

Geldart identified four typical fluidization regimes for materials fluidized with air at ambient conditions, which he indicated as A, B, C and D.

Materials belonging to group B or D are characterized by having the same minimum fluidization and bubbling velocity $u_{mf} = u_{mb}$. The difference between the material of the group B and group D powders is that for the first type of particles the bubble velocity is greater than that of the interstitial gas, while for the other, group D particles, bubbles pass through the bed with a velocity lower than that of interstitial fluid.

The powders of the Group A are easily fluidizable. With these particles is possible to observe a homogeneous expansion of the bed for a range of gas velocity between u_{mf} and u_{mb}. Below this velocity range ($u < u_{mf}$) the bed is fixed, while above ($u > u_{mb}$) it has a regime of fluidization in bubbles; the analysis on two-dimensional beds showed that the bubbles break and coalesce frequently and the bubble velocity is greater than that of the interstitial gas.

Finally, very fine particles, with a diameter smaller than 30 µm, belong to Group C. These particles have cohesive properties and their fluidization can be extremely challenging. The behavior of this group of powders is strongly influenced by the interparticle forces, which may be larger than both the gravitational forces and those exerted by the fluidizing gas. As a result, the gas is not able to separate particles and a channeling regime may occur, causing in turn poor particle mixing and resulting into poor heat and mass transfer.

Geldart's classification is clear and easy to use as displayed in Figure 5. For any solid of a known density ρ_s and mean particle size d_p this graph shows the type of fluidization to be expected. However, the boundary regions shown in Figure 5 are not fixed boundaries. As reported by Geldart et al. [32] surface forces such as relative humidity can shift the C-A boundary of the materials. Moreover, Seville and Clift [33] found that the behavior of group B materials change to that of group A adding small amounts of a light oil. Lettieri et al. [8] and, more recently, Chirone et al. [34] showed how process conditions such as high temperature and presence of liquid or the combination of the two, can cause some group A materials to behave like Group C. Therefore, Geldart classification is a simple and powerful tool able to describe the flowability of the powder at ambient conditions, but its applicability became questionable when process conditions, such as temperature, addition of fines or presence of liquids are present in the system.

2.2.2. Different scaling in granular system

The properties of fluidized bed systems are defined by the microscopic properties of the particulate phase and their relationship with the fluid phase. A proper design of unit operations making use of fluidized beds should include consideration of the macroscopic constraints of the fluidized bed. It has been pointed out however that the proper description of a fluidized bed is determined by mesoscale phenomena such as

agglomerates of particles or fluid bubbles that occurs at scales between the microscopic and the macroscopic. The properties of the fluidized system at the mesoscale are a function of the characteristics of the microscopic properties of the system, such as the interparticle forces, and depend on the system fluid-dynamics. In fact, different fluidization conditions identify different mesoscale phenomena somehow affecting the scrutiny scale of interest. The relative weight of interparticle forces and fluid dynamic forces characterizes the different behaviors of the fluidized bed in terms of bubbling formation (stable or instable), bubble size, agglomeration and so on. A great effort in modelling and understanding the role of mesoscale phenomena has been done in the last few years by several Authors [35–39]. In particular, Li et al. [37] explored the multiscale nature of complex systems as a fluidized bed reactor system. They discussed the multiscale and pseudo—particles approaches. They suggest the multiscale approach as a necessary tool to approach the sustainable mathematical description of fluidized bed. They suggest the strategy of structure resolution (particle scale, cluster scale, and unit scale, that is, micro-, meso-, and macroscale, respectively) in describing the heterogeneous structure and mechanism compromise in defining the variational criterion. Differently, the pseudo-particle approach describes the heterogeneous structure by discretizing the fluid into pseudo-particles with a size much smaller than that of the real particles. According to this approach, the particle-fluid interaction is treated as the interaction between real particles and pseudo-particles. More recently, the same researchers [36] reviewed the last decades of their research spanning from the energy-minimization multiscale (EMMS) model specific for gas–solid fluidization to the EMMS principle, that they suggest to be general for all mesoscale problems. They concluded that interdisciplinary collaboration is necessary for addressing this challenge and that engineering disciplines, in particular, can collect evidence by studying actual problems while theoretical disciplines can aid by formulating generality.

Coppens and van Ommen [38] showed how reactor designs, gas distributor designs and controlling the gas inlet dynamics can be used to structure fluidized beds. Different functionalities on bubbles size, bubbles formation and shifting from chaotic to stable were found when applying electric fields, secondary gas injection and oscillating the gas flow respectively. In particular, with fluctuating gas velocity regular bubble patterns were

observed leading to the possibility of intrinsic control and scale-independent hydrodynamics.

In fluidized bed system, the forces acting among particles at single particle scale become fundamental for describing the hydrodynamic behaviour on the mesoscale providing a more comprehensive picture of the relation between micro-scale forces and fluidization characteristics in terms of bubbling formation, size, aggregative fluidization and so on.

Two types of heterogeneous phenomena are possible: single-scale phenomena, generally prevailing in liquid-solid systems in which heterogeneity appears as gradual changes, and multiscale phenomena, mostly occurring in gas-solid systems showing variations at several scales. The study of these phenomena can be approached either from observation in order to infer the intrinsic mechanism in the model or, viceversa, from the assumption of intrinsic mechanism in model to verify that these generate suitable heterogeneities. Generally, heterogeneous structures are significant characteristics of complex systems and represent crucial aspect to be accounted for in scaling up reactors. Three different approaches can be used for their study [37]:

1. the average approach, which is simple but often inadequate to describe structures and transport phenomena. It is the most commonly used but due to the fact that it considers a system to be uniform with average properties it cannot correctly represent particle-fluid interactions in heterogeneous structures;
2. the multiscale approach, which is promising because of its simplicity and effectiveness in approximating structures. It considers the variation of the particle-fluid interaction at different scales and in different phases. This approach needs criteria to identify the prevailing steady state or preferred particle arrangement of the heterogeneous structure;
3. the discrete approach, which should receive more attention but requires great computational capacity since it tracks the movement of all individual particles to elucidate the details of particle-fluid interactions.

The multiscale approach was adopted in studying the two-phase structure of gas-solid fluidization [40] and its potential has been indicated in describing the heterogeneous structure, defining three different scales: particle scale, cluster scale, and unit scale, which

represent micro-, meso-, and macroscale, respectively. Different mechanisms of gas-solid interaction prevail in these two phases: particle-dominated (PD) inside the dense-phase cluster and fluid-dominated (FD) inside the dilute-phase. The mesoscale corresponds to the cluster size, which involves interactions between the dilute broth phase and the dense cluster phase. This scale of interaction is responsible for both ordered behaviors and irregular changes, which cause frequent violations of the particle-dominated condition inside the dense phase and the fluid-dominated condition inside the dilute phase, thus giving rise to complicated time series of fluctuations with intermediate states

2.2.3. Role of interparticle forces on fluidization behaviour

The existence of solid-solid interparticle forces such as van der Waals forces, capillary forces and electrostatic forces may explain the non-ideal behavior of the powders during fluidization. These forces hold the particles of the bed together making difficult their free movement and causing a poor fluidized state. It should be noted that the solid-solid interaction forces are always present, but they play a different role depending on the relative importance between gravitational and hydrodynamic forces [3,41–43]. For coarse particles, the interparticle forces are practically irrelevant when compared to the gravitational forces. However, for particles smaller than 50 - 100 µm these forces become comparable. A good quality of fluidization is achieved when the interparticle cohesive forces are negligible compared to the gravitational forces. When the interparticle forces are larger than the gravitational forces, channeling occurs, causing in most cases poor quality fluidization.

Molerus [3] proposed equivalent limiting conditions of the Geldart classification by taking into account the interparticle forces. He proved that interparticle forces play a key role in the separation of Geldart Groups A, C and B. He stated that the separation of Geldart Group A from Geldart Group C is due to the dominance of the cohesion forces, in the type C, compared to the hydrodynamic and gravitational forces. On the other hand, the separation of Geldart group A from group B arises from a less extent of the interparticle forces in the fluidization condition in type B compared to the hydrodynamic and gravitational forces.

On the transition between homogenous and bubbling regime, many works try to define the controlling factor between the hydrodynamic and interparticle forces. However, the question is still now debated. Massimilla and Donsì [22,44] performed experiments on bed expansion in a semicircular transparent column and discovered, through microscopic observations, cavities and micro channels into the bed of the same order as the particle size. They concluded that this manner of bed expansion is caused by an active function of interparticle forces. In particular, they act to stabilize cavities and micro-channels, playing a critical role in the fluidization behavior of fine powders. On the effect of the interparticle forces on the homogenous fluidization, Mutsers and Rietema [41] conducted a study on a tilting fluidized bed. During these experiments, it was possible tilting the bed until a certain angle without the powder sliding. This finding clearly demonstrated the presence of a well—defined powder structure, with a certain mechanical strength in the expanded state of homogenous fluidization because of the no-negligible presence of the interparticle interactions.

Electrostatic forces could also have a role in fluidization processes. For its nature, particles in a fluidized bed are in continuous contact and separation generating friction between both particle-particle and particle-wall of the vessel. Such conditions promote the rolling at the contact point and consequently charging of particles according with the triboelectrification process [45].

Ciborowski and Wlodarski [46] reported that the attraction force generated by particles with opposite charge and conducting bodies can modify the natural hydrodynamic of the bed. They found a qualitative relation between air humidity and the minimum fluidization velocity. In particular, they observed a progressive increase of u_{mf} with decreasing the air moisture. Boland and Geldart [47] state that the accumulation of certain amount of charge can cause a spark discharge in the bed and also an ignition of the dust could in the freeboard region of the fluidized bed. They also studied the electrostatic charging in fluidized beds founding that most of the particle-particle charging in the bed was related with the passage of bubbles. They measured opposite sign voltages at the nose and wake regions of the bubbles. This phenomenon is not totally clear but it suggests that different mechanism of charge transfer takes place at the nose and wake region of the bubbles. Frictional and kinetic effects may be more significant in the wake region where the motion

of the particle is more vigorous and this can generate higher charging of the particles. It was also supposed that a difference in voidage between the nose and the wake regions could be the reason of the change in resistance, resulting in a different mechanism of charging.

Other authors focused on how to control electrostatic forces in a fluidized bed. For instance, Bafrnec and Bena [48] established that particle charging can be decreased in two ways: or by prolonging the time of surface contact or decreasing the electrical resistance of the particle surface. In a fluidized bed system, the only way forward is the second one. In fact, the contact time cannot be controlled in ordinary fluidized system. Instead, it is thinkable reducing the electrical resistance of the particles by increasing the relative humidity of the fluidizing gas and the conductivity of the particles' surfaces. Boland and Geldart [47] studied the effect of relative humidity (R.H.) on the fluidization of a mixture of lead glass ballotini with different diameter ranges and colours. They found that reducing the relative humidity of 15%, the interparticle forces become dominant over the hydrodynamic forces, preventing the larger particles from segregating. Two phenomena are occurring at the same time, on one hand the increase of relative humidity cause the charge generation, on the other hand, the dissipation process became faster because of a decrease of resistivity of the particles. The critical range for the static dissipation is for R.H. values in the range between 50-70% where the resistance of the lead glass ballotini reduced dramatically. However, different materials with different attraction for water may have different critical ranges.

Electrostatic phenomena in fluidization system are far from being completely understood. Whenever it is possible its effect may be minimized by working in appropriate ranges of humidity, but also by making the bed container conducting and grounded, as was suggested by Ciborowski and Wlodarski [46]. However, in some cases this is not enough to dissipate all the charges present in the fluidized bed.

The relative humidity of the system can also be responsible for the formation of liquid bonding. Several authors studied the critical values of the humidity at which condensation first appears. Turner and Balasubramanian [49] reported values from 65-80%. Coelho and Harnby [50] found that the critical humidity is a function of temperature, pressure and the

nature of the solid and liquid. More recently, Tyrrell and Cleaver [51] investigated the influence of humidity on interparticle forces, and confirmed the existence of capillary bridges also for low values of relative humidity, below 50%.

In industries which involve granulation processes, such as pharmaceutical, mineral and fertilizer industries, the mechanism of particle agglomeration due to liquid bridges is particularly important. However, it can also cause serious problems in the handling of sticky particulate materials. In agglomeration processes the capillary forces can become so strong to give place to the phenomenon known as “wet quenching”, in which fluidization can be lost completely. On the other hand, when the liquid bridges evaporate, it gives place to a phenomenon called “dry quenching”, where the particles are permanently agglomerated by means of solid bridges. For many years, the capillary bridge formation has been widely studied given its importance in various industries.

More recently, a critical examination of the effects of relative humidity, RH, on the fluidization and defluidization curves was performed by LaMarche et al. [52]. The cohesion induced by RH was found to affect more the defluidization behavior than the fluidization one. Additionally, a sharp transition from Group A to C behavior of Geldart classification was discovered as RH is increased over the same small range (60–65%). Furthermore, the Authors proposed a theory to predict the capillary force with increasing RH accounting for surface roughness. The novelty of their approach is the incorporation of measurements of the surface roughness and the development of a model which considered two scales in the asperity size. In fact, the theory is able to simultaneously address the effect of small-scale and large-scale roughness. They used AFM to characterize the particle surfaces and estimate the two characteristic asperity sizes. The result was that the predicted capillary interparticle forces could show a change in the intensity of the force with relative humidity, larger than that found by Landi et al. [53] on model materials. Furthermore, the Cohesive Discrete Element Method (CDEM) was used to investigate the internal tensile stress and the tensile strength of fine, cohesive wet granular materials [54].

D’Amore et al. [55] studied the influence of moisture on the fluidization characteristics of non-porous and porous materials. They highlighted that the ability of the materials to keep water without losing their fluidizability characteristics is governed by particle porosity.

They observed that the pore space of the catalyst tested can contain a great amount of water before creating stable capillary bridges and developing agglomerated particles. On the contrary, non-porous materials tend to defluidize at very low water-mass ratio.

Seville and Clift [33] and, later, Wormsbecker and Pugsley [56] reported on the effect of liquid loading on the fluidization of Group B materials. They detected changes in the fluidization behavior. With a progressive addition of liquids in the system and, consequently, increase of interparticle forces generated, the particles shifted through Group A to C. They found that this behavior is qualitatively consistent with Molerus' analysis of the role of interparticle forces in determining fluidization characteristics. Tardos et al. [57] also investigated the destabilization of fluidized beds due to agglomeration. They found that the limiting velocity necessary to fluidize the bed was dependent on both the amount of liquid added and the bed and fluid properties.

Several authors tried to model the agglomeration process in fluidized bed systems. The approach followed was to scale up forces between pairs of particles to systems of multi-particles. Two models were proposed to simulate the behavior of wet agglomerates. The first assumed that the dynamic forces, which are dominated by the viscosity, are the controlling factor. Whereas, the second model assumed that the static forces, dominated by surface tension, are more significant. Ennis et al. [58] studied the granulation phenomena between wet particles finding that if the liquid (binder) is sufficiently viscous, the interaction is dominated by lubrication forces. They followed the first approach and considered that the energy loss during collision of two particles is caused by the viscous dissipation in the liquid layer. They introduced a new dimensionless number, the viscous Stokes number, to calculate the minimum velocity required for two coated spherical particles to rebound:

$$St^{*} = \frac{2mv_0}{3\pi\mu_l R^2} = \frac{8\rho v_0 R}{9\mu_l} = \left(1+\frac{1}{e}\right)\ln\frac{2\delta}{3h_a} \rightarrow \begin{cases} > 1 \text{ rebound} \\ < 1 \text{ adhesion} \end{cases} \qquad \text{Eq. 12}$$

v_o, m and R represent the collision velocity, mass and radius of the particles respectively, h_a is the height of the surface asperity, μ_l and δ are the viscosity and thickness of the liquid layer respectively, and e is the coefficient of restitution.

In dynamic systems, the formation of agglomerates appears to be related to the balance between the rupture energy of liquid bridges and the particles kinetic energy. In addition, the fracturation of the resulting agglomerates involves liquid bridges rupture and its related rupture energy. Although the behaviour of such particles assemblies is still hardly predictable by means of micro-mechanical models, the knowledge of simple expressions able to describe interactions at the microscopic scale is nevertheless of practical interest.

Simons et al. [59,60] derived a simple model able to predict the rupture energy of the pendular liquid bridge, taking account of the capillary static forces and with only knowledge of the liquid volume active to form the liquid bridge itself. The dimensionless rupture energy is:

$$W^* = \frac{W}{\gamma} R^2 = kV_b^{*0.5} \qquad \text{Eq. 13}$$

where V* is the dimensionless bridge volume ($V^*=V_b/R^3$) and k is a constant equal to 1.8. This work was then further advanced by Fairbrother [61].

Wright and Raper [62] reported on the effect of liquids addition, having different viscosity and surface tension, on the fluidization behavior of Group D powders. They demonstrated the significant role of the binder viscosity in the fluidized bed systems. In particular, the most viscous one shows a relevant retardation in the expansion of the bed. A more relevant effect of viscosity was also noted at the minimum bubbling transition. Instead, surface tension or static capillary forces appeared to play a more central role at minimum fluidization conditions. The authors concluded that at low velocities static bounding is dominant, while at higher velocities the influence of dynamic bridging is greater.

2.2.4. Effect of temperature on fluidization

The prediction of the fluid-dynamic behavior of gas-solid systems at high temperature represents a key aspect in fluidization since most of the industrial processes, which involve fluidized bed reactors, operate at temperatures well above the ambient temperature. The prediction of the effects of a temperature change on the quality of fluidization is relevant, therefore, both in the design stage and management of fluidized bed processes.

Design criteria and performance predictions for fluid bed units working at high temperature have been largely based on fluid-dynamic models and correlations established from tests developed at ambient temperature. However, extrapolating results and relationships available at ambient conditions to elevated temperatures can lead to misleading prediction of the fluid bed performance at high temperature.

For many years the operating temperature has been considered an influence only for the gas density and viscosity. Most predictions of fluidization behaviour at high temperatures, such as minimum fluidization and bubbling conditions, have been established merely on considering such changes in the gas properties. However, this approach turned out to be valid only under the condition that hydrodynamic forces control the fluidization behaviour. Nevertheless, temperature can have a relevant effect on particle adhesion, enhancing the role of the interparticle forces on the fluidization quality, resulting, in extreme condition, in unacceptable fluidization [63]. In addition, it must be considered that in the case of high temperature processes, the intensity of interparticle cohesive forces, such as capillary, electrostatic and van der Waals forces, can be different from ambient values. These changes are principally due to the variations of particles hardness, liquid bridge formation and modification of the particle dielectric properties. This means that even materials of the Group A or B may behave like a material of the Group C. As reported by Lettieri et al. [8], the effect of temperature on a fluidized bed is very dependent on particle size defining the type of particle-particle and fluid-particle interaction and determining the stronger or weaker role of the IPFs.

2.2.4.1. Effect of temperature on the minimum fluidization velocity

A central parameter for describing and designing a fluidized bed system is the minimum fluidization velocity, u_{mf}. The latter may be found by measuring the pressure drop across a bed of particles as a function of the gas velocity. At u_{mf}, the weight of the bed is fully supported by the gas flow and the pressure drop becomes constant. Ergun [64] developed an equation describing the pressure drop across a packed bed, which can be used to calculate the minimum fluidization conditions. The Ergun equation is, among the various correlations, one of the most reliable:

$$Ga = 150\ \frac{(1-\varepsilon_{mf})}{\phi^2\varepsilon_{mf}^3}\ Re_{mf} + \frac{1.75}{\phi\varepsilon_{mf}^3}\ Re_{mf}^2 \qquad \text{Eq. 14}$$

Where:

$$Ga = \frac{d_p^3\rho_g(\rho_p-\rho_g)g}{\mu^2} \qquad \text{Eq. 15}$$

$$Re_{mf} = \frac{d_p\rho_g u_{mf}}{\mu} \qquad \text{Eq. 16}$$

Where g is the gravity acceleration, ϕ the particle shape factor, ε_{mf} the bed voidage at minimum fluidization conditions, ρ is the density and μ is the viscosity. The subscripts g and p indicate the fluid and the particle phase respectively. d_p is the particle diameter, in the case of particle size distribution it is used the Sauter mean diameter, d_{sv}, which is defined as the diameter of a sphere that has the same volume/surface area ratio as a particle of interest. Re_{mf}, defined in Eq. 16, is the Reynolds number at minimum fluidization conditions. Ga, defined in Eq. 15, is the Galilei number, also called the Archimedes number. It is a function of the physical properties of the solid-gas system considered, for which at a given temperature is considered to be known. According to the Ergun equation (Eq. 14) the pressure drop depends on particle and fluid properties and it does not consider the effects of interparticle forces. When applying the Ergun equation, the value of the minimum fluidization voidage and the shape factor, ε_{mf} and ϕ, respectively, should be used although they are frequently unknown. A 10% error on ε_{mf} causes an error on u_{mf} of about 38% in the case of laminar flow and 15% in the turbulent flow [65]. This parameter is a function of the shape and roughness of the solid and the size of the particles. It decreases with the increase of the average diameter and for wider particle size distribution. The methods of analysis adopted are essentially based on an indirect measure of ε_{mf} [65]. To eliminate the explicit dependence of u_{mf} from this parameter many researchers have derived the equations substantially similar to the Ergun equation.

Wen and Yu [66] showed that the voidage and shape factor functions in the original Ergun equations can be approximated as:

$$\frac{1-\varepsilon_{mf}}{\phi^2 \varepsilon_{mf}^3} \approx 11 \qquad \text{Eq. 17}$$

$$\frac{1}{\phi\, \varepsilon_{mf}^3} \approx 14 \qquad \text{Eq. 18}$$

And they proposed the following modified form of Eq. 14:

$$Ar = 1650\, Re_{mf} + 24.5\, Re_{mf}^2 \qquad \text{Eq. 19}$$

That may be rearranged to the general formula:

$$Ar = A\, Re_{mf} + B\, Re_{mf}^2 \text{ or}$$
$$Re_{mf} = \sqrt{a^2 + b\, Ar} - a \qquad \text{Eq. 20}$$

where a is A/2B and b is 1/B; the values for these constants proposed by Wen and Yu [66] are 33.7 and 0.0408 and Eq. 20 becomes:

$$Re_{mf} = \sqrt{33.7^2 + 0.0408\, Ar} - 33.7 \qquad \text{Eq. 21}$$

However, predictions using Eq. 21 do not consider possible changes in the voidage, as a result of an increase of temperature, as discussed later.

Pattipati and Wen [67] reported that the correlation proposed by Wen and Yu is capable of predicting changes in u_{mf} when temperature increases for sand material. They did not observe important changes with temperature in the voidage at minimum fluidization and they found good matching between experimental and predicted u_{mf} values.

Generally, the experimental findings on Geldart's Group B and D particles confirmed the trend predicted by the Wen and Yu equation. Nevertheless, absolute values did not always match with experiments. Knowlton [6] stated that one of the reasons lies in the evaluation of the correct mean particle size and shape factor. He suggested that this could be back-calculated from the Ergun equation using previously measured values of u_{mf}. Doing so, an effective value for the particle size and shape factor would be found.

Botterill et al. [68] reported experimental verification of the temperature effect on u_{mf} for some Group B and D powders. They observed a decrease of u_{mf} with increasing temperature for Group B materials, due to the consequent increase in gas viscosity. Comparing their results with predictions from the Wen and Yu equation, they noted that the decrease was less than that predicted since a change in ε_{mf} had occurred. This is not in agreement with the results of Pattipati and Wen [67]. For Group D powders, Botterill et al. observed an increase in u_{mf}, because of the decrease of gas density. They also found that ε_{mf} for the Group D materials did not change with temperature. Their experimental data matched predictions obtained from the Ergun equation, using the values of ε_{mf} measured at the corresponding operating temperatures, and using also an appropriate value of the shape factor, back calculated from the Ergun equation for a given experiment.

Fletcher et al. [69] in 1992 proposed different equations to predict Re_{mf} at ambient temperature, because they reported that applying Eq. 21, a significant error can be introduced mainly due to the difficulty in measuring the shape factor and voidage at minimum fluidization conditions.

Coltters and Rivas [70] in 2004 proposed a new equation to estimate the minimum fluidization velocity without an experimental determination of bed voidage and shape factor. They tested their correlation against 189 experiments reported in the literature on about 90 different materials, and their results showed good agreement with the experimental data. In parallel, Delebarre [71] revisited the Wen and Yu equations for the prediction of u_{mf} without the dependency on the voidage and shape factor.

The relative role of the hydrodynamic and interparticle forces on the minimum fluidization conditions at elevated temperature for Group A and C powders has been analysed by various authors. In 1986, Lucas et al. [72] reported that changes with temperature in ε_{mf} can

be explained on a hydrodynamic basis, contrary to Raso et al. [73] and Formisani et al. [63] who later related such changes to a variation of IPFs with temperature.

Formisani et al. [63] and Lettieri et al. [8] also reported on the effect of temperature on minimum fluidization conditions and they stated that the Ergun equation and Wen and Yu correlation are capable of predicting changes in the minimum fluidization velocity with temperature if, in addition to changes of gas density and viscosity, the dependence of ε_{mf} on temperature is also accounted for.

Group A Geldart classification

Formisani et al [74] studied the dependence on process temperature of parameters that characterize the dense phase of a freely bubbling bed for FCC, silica sand and corundum in experiments covering a temperature field range from ambient up to 700 °C. They demonstrated that the increase of interparticle forces at high temperatures leads to significant modifications of the fluidization dynamics. In particular, they found that the dense phase voidage of a bubbling fluidized bed undergoes a practically linear increase with temperature. Moreover, a non-unique temperature dependency on u_{mf} was found leading to the conclusion that the temperature effect is the product of the combined variation of both gas properties and dense phase voidage with temperature.

Lettieri et al. [75] studied the influence of temperature, up to 600 °C, on the fluidization of various catalyst powder of type A such as FCC, highlighting the conditions under which the hydrodynamic forces or the interparticle forces become dominant. Some of the Group A materials tested show a significant change in fluidization behavior, as the temperature increases, becoming similar to that of the materials of the Group C. This was attributed to an increase of interparticle forces, which turn out to be dominant over the gravity forces. The authors performed some physical analysis, in order to detect possible degradations of the material caused by a temperature increase. It was found that some of the materials undergo irreversible changes in the physical properties. Moreover, the same authors reported in a previous paper [8] comparisons between experimental values and theoretical values of the minimum fluidization velocity for silica catalysts doped with different amounts of potassium acetate (1.7, 7 and 10 $\%_{wt}$) where the theoretical values were calculated with the experimental ε_{mf} and ϕ=1. The experimental values of u_{mf} were higher

than the expected one for the doped materials (7 and 10 $\%_{wt}$), and the values of ε_{mf} at high temperature were higher than those provided at room temperature. They concluded that this experimental evidence can be attributed to the influence of interparticle forces on the quality of fluidization and that purely hydrodynamic equations, developed for ambient conditions, can predict the behavior towards fluidization when the interparticle forces are negligible.

The same authors [10] reported on the homogeneous expansion of three FCC catalysts with increasing temperature from ambient up to 650 °C. Richardson-Zaki parameters, u_t and n, were estimated from the experimental expansion profiles obtained varying the temperature. Comparing these values with the corresponding theoretical values (n was calculated as a function of the Galileo number, while u_t from Stokes law), they found that the experimental values were larger than expected ones by a factor 10 at ambient condition and 3 at high temperature. They justified these findings assuming the presence of homogeneous clusters in the bed, due to the presence of interparticle forces which are not negligible. They also observed that u_t and n were decreasing with temperature. Based on this evidence they concluded that the interparticle forces, for the investigated materials, are more relevant at low temperatures. However, it should be noted that the authors did not indicate the type of forces responsible for this phenomenon

It is common knowledge in the scientific community that high values of the exponent n of the Richardson-Zaki are indicative of a relevant presence of interparticle forces, as reported by Geldart and Wong [76]. They studied the mechanism of expansion of powders belonging to Group A and found that n increases with decreasing dimension and with increasing cohesiveness of the particles. They found values of n between 4 and 60, with the highest values that compete to materials that exhibit high degrees of cohesiveness.

Group B Geldart classification

Lin et al. [77] studied the effect of temperature and of particle size distribution on the minimum fluidization velocity u_{mf}. The material used was sand belonging to the Group B of Geldart classification. The tests were carried out in air at atmospheric pressure between 700 and 900 °C. Regarding the effect of temperature, the experimental results revealed a minimum of u_{mf} around 800 °C. The increase of u_{mf} for T> 800 °C was interpreted as the

effect of the interparticle forces, which, above this temperature, become not negligible. All the theoretical correlations tested overestimate the experimental value and did not predict the minimum of u_{mf}. Botterill et al. [78] reported experimental verification of the temperature effect on umf for some Group B and D powders. They observed a decrease of u_{mf} with increasing temperature for Group B materials due to the consequent increase in gas viscosity. They compared their results with predictions from the Wen and Yu equation and noted that the decrease was less than that predicted since a change in ε_{mf} had occurred. This is not in agreement with the results of Pattipati and Wen [67].

Group C Geldart classification

The processes involve very fine cohesive particles are very attractive for the industries, mainly because these materials have a very high specific surface area. Despite that, handling the particles is very challenging. It has already been said that intensive experimental research was conducted in order to obtain a good quality of fluidization; the results cannot be generalized, since they depend on the technique used.

Zhou and Li [79] have proposed an alternative model to predict the fluid-dynamic behavior of powders that tend to agglomerate. Such a model attempts to estimate the average size of the agglomerates formed in the fluid beds of cohesive particles. The model is based on the forces balance acting on single agglomerate. The forces that are supposed active on the individual agglomerate are: the drag force, the collision force, the difference between the weight force and the buoyancy force, and the cohesive force (van der Waals force). The sizes of the agglomerates calculated with the model agree with the experimental results they found for materials of type C. The authors found that an accurate estimation of the model parameters is necessary, since the results depend significantly on the parameter values such as the Hamaker constant, the distance between particles or agglomerates, the voidage of the bed and the one of the agglomerates, the Poisson and Young modules for the collision force and the relative speed of the agglomerates. Another problem concerning the application of this model is that this has been developed for agglomerates of a single size, while in reality agglomerates of different sizes may be shaped. These considerations constitute the limits for the application of this model in real cases.

Some conclusions from the analysis of the literature panorama can be done:

1. There are several experimental evidences that highlight the influence of temperature on the extent of interparticle forces and, consequently, on the quality of fluidization of particles not only of type C, but also of type A and B.
2. The model of Zhou and Li has limitations for its real applicability.
3. An appropriate diameter and average value of bed voidage at minimum fluidization must be used in order to better describe this condition. Temperature can affect both parameters and are still missing alternative relationships to those classical which account for these changes when working with a fluidized bed reactor at high temperature. In the literature, there are numerous correlations for calculating u_{mf}, proposed by different authors; it is appropriate, however, to remember that these were developed considering only the active hydrodynamic forces and that the coefficients differ substantially from one derived from the comparison with the experimental results.

2.2.4.2. Effect of temperature on the minimum bubbling velocity and on the bed expansion

Many studies focus on fluid dynamic properties of fluidized bed systems. Particular attention was paid to the transition between the particulate, a stable region of non-bubbling expansion, and bubbling regime of Geldart's Group A powders. The findings are rather controversial. Uniform expansion of the bed and, in turn, the bubble delay, is the main difference between gas and liquid fluidization. Also in the case of gas fluidized beds it is generally accepted the Richardson and Zaki [80] equation strictly valid for liquid fluidized beds:

$$u = u_t \varepsilon^n \qquad \text{Eq. 22}$$

With u, u_t representing the liquid velocity and the terminal velocity, and n is a parameter between 4.65 and 2.4.

Massimilla and co-authors [22], on the basis of some experimental observations on the bubble free expansion of gas fluidized beds of fine particles, interpreted bed expansion connected to nucleation and growth of cavities in the bed as a results of a broad distribution of interparticle forces.

However it must also be noted that a delay in bubbling regime was observed with large particles fluidized under high pressure conditions [7] and in magnetized assisted fluidization of large particles [81,82].

Even the voidage at minimum bubbling, ε_{mb}, is considered affected by HDFs and IPFs. Different mathematical approaches have been proposed: i) a criterion based on the assumption that hydrodynamic forces are the controlling factor (Jackson [83]); ii) a criterion based on the assumption that interparticle forces prevail on the hydrodynamic forces.

The first approach, contrary to the experimental evidence obtained for Geldart's Group A powders, is not able to predict a homogenous expansion of fine particles fluidized beds. Other theoretical approaches are those proposed by Verloop and Heertjes [84], which re—formulated the hydrodynamic model applying Wallis stability criterion [85]. Foscolo and Gibilaro [12], on the basis of Verloop and Heertjes model, proposed the Particle—Bed Model, to predict the onset of bubbling ε_{mb} in a fluidized bed. The model has been validated on the basis of experimental data obtained at both ambient and high pressure conditions. Furthermore, Brandani and Foscolo [86] defined the different fluidization behaviors through the analysis of the discontinuities arising from the one-dimensional equations of change of the Particle-Bed Model.

An important contribution on the role of interparticle forces in bed expansion behavior is given by Rietema and co-workers [21,41,87,88]. They proposed a stability criterion which accounts for the effect of these additional forces, i.e. IPFs, to the fluid-dynamic forces and gravitational weight. The main argument is the possibility that interparticle forces between particles may result into a three-dimensional powder structure characterized by a certain mechanical strength even in the homogeneous fluidization regime. Only gas velocities sufficiently high may destroy this mechanical structure. Similarly to Foscolo and Gibilaro [12], Mutsers and Rietema [41] used the approach proposed by Wallis and gave expressions for both the kinematic and dynamic wave velocities. Contrarily to the criteria exclusively based

on the hydrodynamic forces, Mutsers and Rietema assumed that the bed elasticity and so, the theoretical concept behind it, is the essential property which determines the dynamic behaviour of the bed, and this, in turn, is strictly related to Van der Waals forces effective between the solid particles. However, the formulation proposed by Rietema and co−workers, differently from Foscolo and Gibilaro correlation, is not able to predict minimum bubbling voidage, a priori.

A validation of the Foscolo and Gibilaro criterion to predict ε_{mb} for 65 and 103 μm FCC powders from ambient conditions up to 900 °C is provided by Rapagna et al. [89]. They observed a decrease in the average bubble size and a delay of the onset of bubbling with increasing temperature. Strictly related to that is also the increase of the voidage at minimum bubbling with temperature. The effect is greater for the finer materials. Figure 6 reports a comparison between experimental data and Foscolo and Gibilaro's Fluid-Bed correlation predictions.

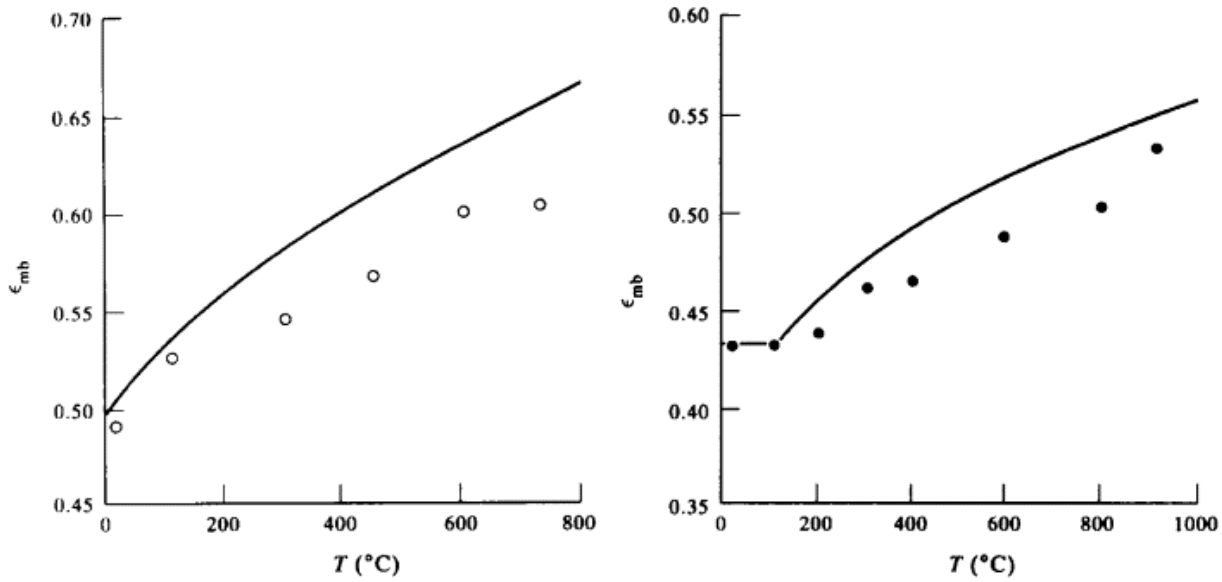

Figure 6 - Experimental and calculated values of bed voidage at minimum bubbling condition as a function of temperature for commercial cracking catalyst (on the left) and a fraction of the same sample obtained by sieving (on the right) [89]**.**

Differently, Xie and Geldart [90] observed no significant change in ε_{mb} with increasing temperature for any of the FCC catalysts investigated. They also reported that predictions of ε_{mb} given by Foscolo and Gibilaro [12] and later, by Jean and Fan [91] well match the experiments at ambient temperature for FCC powders larger than 60 μm, but over-predict ε_{mb} at ambient temperatures for the finer powders. Furthermore, their models also

predicted significant changes in ε_{mb} with temperature, in contrast to the experimental results reported. Failure of the hydrodynamic models to predict correctly the transition between the particulate and bubbling regime was assumed to be the result of ignoring the interparticle forces.

The onset of bubbling regime was also investigated by Formisani et al. [63]. They measured changes in the minimum bubbling velocity of FCC catalysts and silica sand with increasing temperature from ambient up to 800 °C in a 55 mm i.d. quartz column by visual observations. For all material tested they observed an increase of u_{mb} with increasing temperature with a trend very similar to the increase observed for u_{mf}. Unlike Rapagna' et al. [89], they observed a very small bed expansion increase with increasing temperature.

Lettieri et al. [75] in 2001 explored the fluid-bed stability of three fresh FCC catalysts both experimentally and theoretically as a function of increasing temperature. Values of the voidage at minimum bubbling conditions were obtained in the range of 20-650 °C, and compared with predictions given by the Foscolo and Gibilaro correlation. They found a small increase of ε_{mb} with increasing temperature for all FCC catalysts tested. The comparison shows that the predicted values carried out with Foscolo and Gibilaro equation were lower than those found experimentally, see Figure 7.

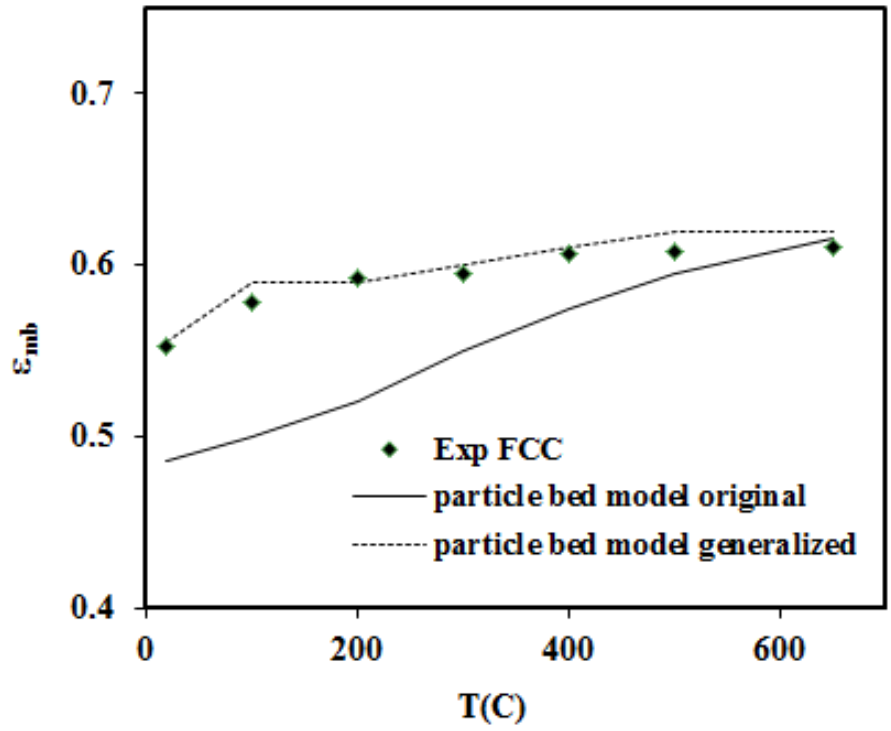

Figure 7 - Comparison between measured ε_{mb} values and predictions using the original and generalized Foscolo-Gibilaro particle-bed model for an FCC catalyst [75].

The disagreement between predicted and experimental ε_{mb} values was related to the large discrepancy between the values of n and u_t in the Richardson and Zaki equation, obtained from the experimental bed expansion profiles and the calculated ones. For all FCC catalysts, the highest values of the experimental n and u_t were found at ambient conditions. The authors started from the procedure followed by Foscolo and Gibilaro, and proposed a generalized expression of their criterion which was able to predict ε_{mb} values within 5% for all FCC catalysts. It must be noted that even if the particle-bed model was originally developed on the assumptions that the hydrodynamic forces are responsible of the fluid-bed stability, the analysis proposed by Lettieri et al. [75] suggested that contribution of the interparticle forces to bed stability of the materials studied cannot be ignored.

As a follow up study, in 2008 Lettieri and Mazzei [92] analysed the effect of temperature on the fluid-bed stability of the same three FCC catalysts used in Lettieri's previous work, but this time through considerations on the fluid-bed elasticity. They reported experimental findings on the effect of temperature on the elasticity modulus at minimum bubbling conditions, calculated according to the theory of Foscolo and Gibilaro [12] and also adopting the criterion of Mutsers and Rietema [41]. In accordance with the theoretical postulation of

Mutsers and Rietema, the results from bed expansion presented by Lettieri and Mazzei [92] and previously by Lettieri at al. [93], showed that the role played by the IPFs can affect the stability of Group A powders. However, the sensitivity analysis conducted by the authors revealed that the parameter which dominates the effect of temperature on the elasticity modulus was the gas viscosity, as shown in Figure 8. This result highlighted the relevance of both HDFs and IPFs on the stability of Group A powders and the need for a correct and complete description of both contributions.

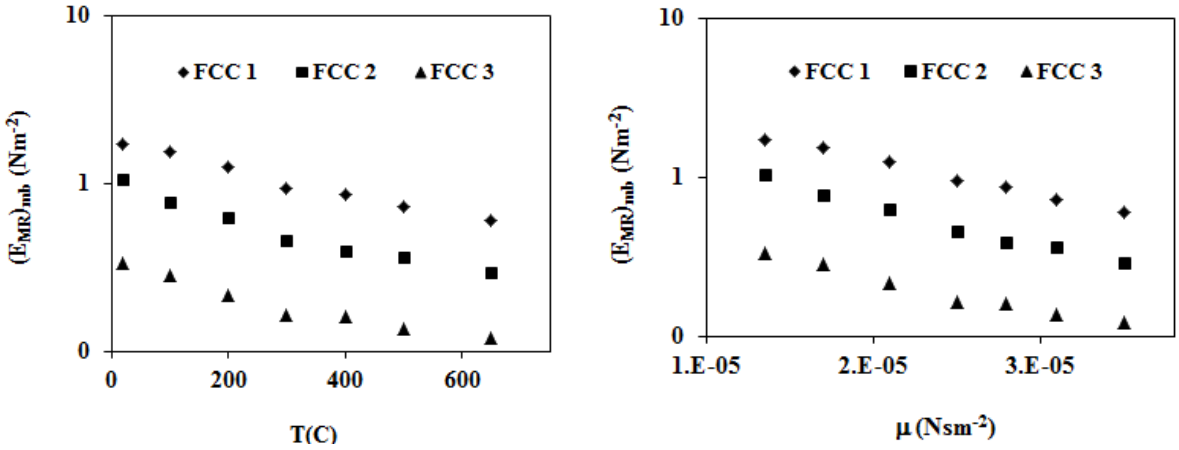

Figure 8 - Influence of temperature and gas viscosity on the elasticity modulus at ε_{mb} according to Mutsers and Rietema criterion, for all fresh FCC [92].

In line with this finding, Valverde and co-workers [13] emphasized the main role played by the interparticle forces on the settling and particulate fluidization of fine powders. They proposed an extension of the Richardson and Zaki correlation and the theoretical Mills—Snabre [94] model. The latter was originally developed for the settling of non-cohesive spheres and it was modified by Valverde et al. [13] in order to predict the settling of agglomerates which may form when the interparticle forces exceed several orders of magnitude the particle weight. Valverde et al. [95] extended the previous study investigating, from both macroscopic and local measurements, the transition between the solid-like, fluid-like, and bubbling fluidization of gas-fluidized fine powders. They showed that the transition between the solid-like and the fluid-like regimes takes place along an interval of gas velocities in which transient active regions alternate with transient solid networks. Using optical probe for local measurements, they emphasised the existence of meso-scale

pseudo-turbulent structures and short-lived voids, in the fluid-like state, which make the prediction of the transition between the different regimes a complicated task.

Castellanos [96] observed that the onset of fluidization of fine and ultrafine powders was characterized by the presence of agglomerates which give place to a highly expanded state of uniform fluid-like fluidization. Valverde and Castellanos [97] proposed in 2008 an extension of the Geldart's classification of powders to predict the gas-fluidization behaviour of cohesive particles which combine the role of the interparticle and hydrodynamic forces on the existence of a non-bubbling regime. In the new phase diagram proposed by Valverde and Castellanos, the boundaries between the different types of fluidization are defined as a function of fluid viscosity, particle density, the fractal dimension of the agglomerates and the powder's compaction history, as reported in 2006 by the same authors [39].

Girimonte and Formisani [98] presented a study on the influence of operating temperature on the transition to the bubbling regime for samples of FCC, silica and corundum sands, at temperatures ranging from 30 to 500 °C. They determined the minimum bubbling velocity using four different methods and obtained different results for u_{mb} with increasing temperature. The first method was based on the direct observation of the velocity at which the first bubble erupted on the free surface of the bed. The second method was based on the measurement of the pressure drop across the whole bed, and u_{mb} as taken at the point where a shallow minimum of the ΔP vs. u curve occurs. The last two methods were derived from the analysis of the "fluidization map", namely the examination of the expansion behaviour of the bed over a range of fluidization velocities from the fixed bed state to the bubbling regime. They found that the optical method and the method based on the detection of the minimum pressure drop were unreliable for correctly determining the starting point of bubbling. They stated that only the analysis of bed expansion as a function of the gas velocity allows reconstructing the emerging of the bubbling phenomena. More recently, they reported on new experiments on the effect of temperature on the fluidization of FCC particles [99]. They used a non-invasive optical technique for acquiring images of bubbles' eruption at the free surface and results from bed collapse tests. Their experiments showed that high temperature influences the quality of bubbles producing a

smoother regime of bubbling, which they attributed to the thermal enhancement of IPFs that leads to higher porosity and lower interstitial flow in the emulsion phase.

In summary, high temperature clearly affects the stability of fluidized beds of Group A powders; well established theories and models fail to predict correctly the voidage at minimum bubbling with increasing temperature. Models corrected on the basis of experimental data are capable to reproduce correct trends; however a priori predictions of the fluid bed stability with increasing temperature still need to be achieved. The main challenge here is in the ability to describe the forces that determine the transition from particulate to bubbling fluidization. Hence, some kind of quantification of the effects of the IPFs on fluidization is needed in order to advance the understanding of fluidization at high temperature.

2.2.4.3. Effect of temperature on the bed collapse test: dense phase

The bed collapse test (BCT) was first introduced in 1967 by Rietema [100] and was subsequently used by Sutton and Richmond [101] to test the capability of a powder bed to retain aeration gas. Initially this technique was used as tool to improve the storage of fine powders in aerated hopper. Since then it has been adopted with different purposes. It was used to compare Geldart Group A and C powder behaviour [102], to assess the effects of fines distribution [103–105], to evaluate changes in catalyst properties and to help diagnose commercial operational problems [106], but mostly to characterize dense phase properties [8,63,74,75,99,100,105,107–109], such as the dense phase voidage ε_d, the dense phase collapse rate U_{de}, the bubble escape rate U_b, the standardised collapse time SCT and the bed expansion ratio BER.

When the fluidizing gas is suddenly shut off, the bed materials will exhibit different collapse profiles depending on the powder properties. Figure 9 reports a typical collapse profile for a gas-solid system with Geldart Group A powder in which three main stages can be observed:

- bubble escape stage: the initial rapid collapse due to the bubbles leaving the system
- hindered sedimentation stage: the dense phase collapses linearly with time until the bed approaches the height at incipient fluidization

- solid consolidation stage: the final consolidation of the solid materials.

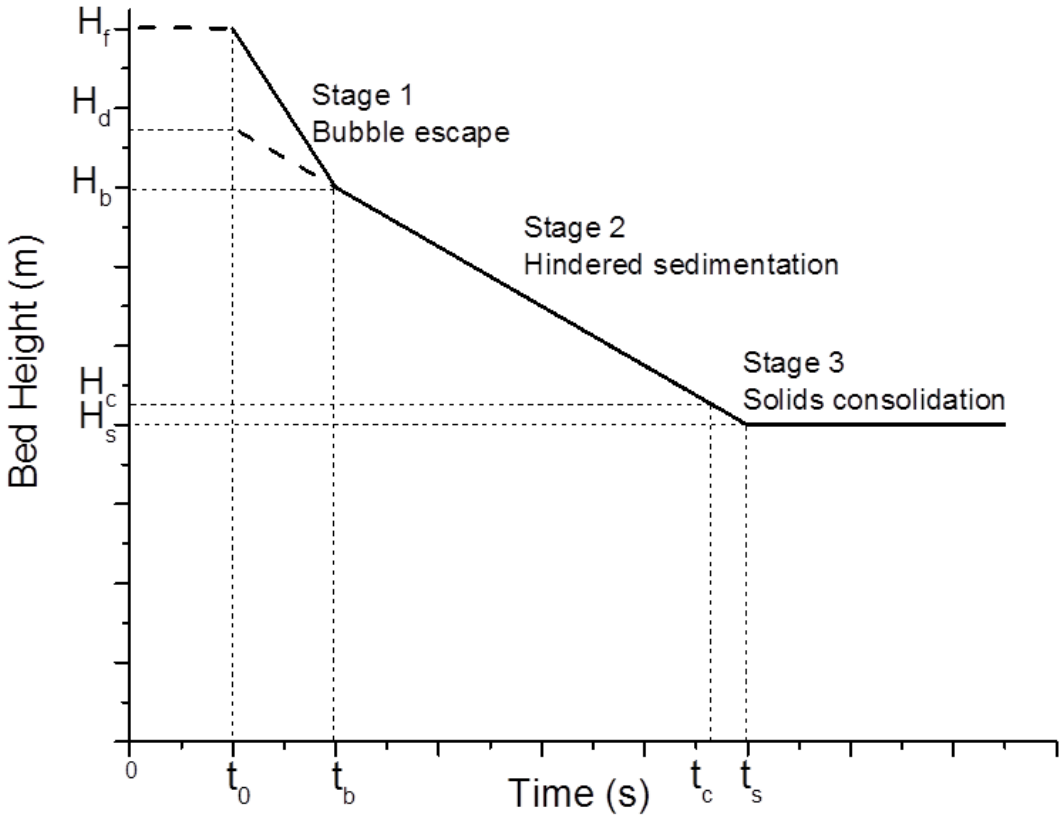

Figure 9 - Typical collapse profile for Geldart Group A powders.

From the BCT several parameters, describing the dense phase, can be derived:

$$\varepsilon_d = 1 - \frac{M}{A_c\, \rho_p H_d} \qquad \text{Eq. 23}$$

$$U_{de} = \frac{H_d - H_s}{t_s - t_0} \qquad \text{Eq. 24}$$

$$U_b = \frac{H_f - H_b}{t_b - t_0} \qquad \text{Eq. 25}$$

$$BER = \frac{H_d - H_s}{H_s} \times 100 \qquad \text{Eq. 26}$$

$$SCT = \frac{BER}{U_{de}} = \frac{t_s - t_0}{H_s} \qquad \text{Eq. 27}$$

In Eq. 23-Eq. 27, t_0 and t_s represent the time when the gas supply to the fully bubbling bed is switched off and the time when the collapse is complete and the bed is settled. H_s is the height of the settled bed, whereas H_d is the extrapolated value of the dense phase height at time t_0.

However, particles with different sizes and properties exhibit different BCT profiles. For Geldart Group B and D powders, which show aggregative fluidization for gas velocities above u_{mf}, the bed collapse curve consists only of the first stage because the solid materials reach the final static bed height as soon as the bubbles are expelled. For these powders, the hindered sedimentation and the final consolidation stage does not usually appear, thus their collapse rate is faster than for Group A materials (Figure 10).

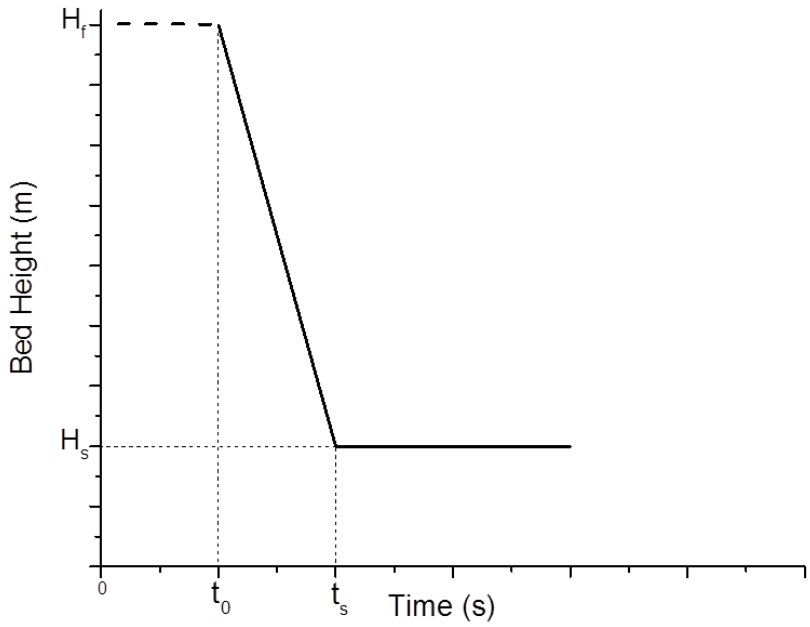

Figure 10 - Typical collapse profile for Geldart Group B and D powders.

Geldart Group C materials reveal a different collapse curve from either A or B and D powders. There is not a hindered sedimentation stage, but only consolidation, as shown in Figure 11.

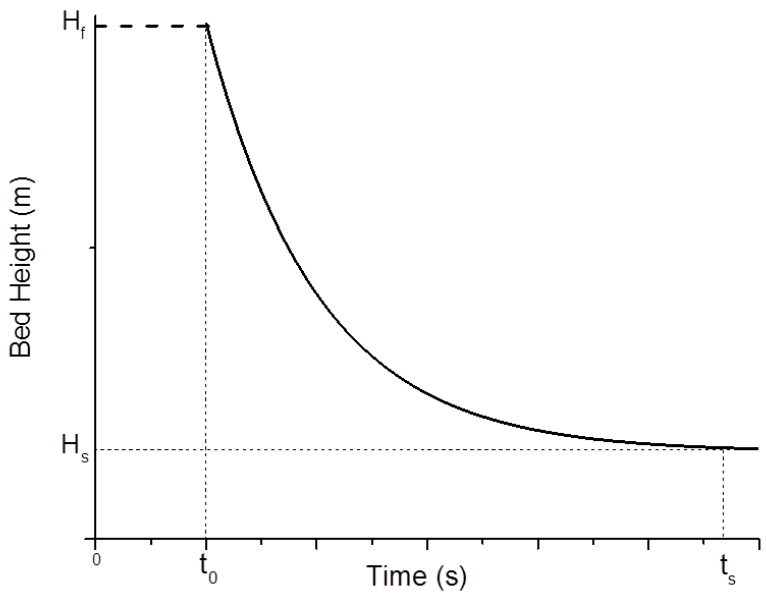

Figure 11 - Typical collapse profile for Geldart Group C powders.

Geldart and co-workers reported that Group C bed expansion is caused by the presence of cavities and cracks [102,110]. They reported that when the gas is cut off, the largest cracks close up quickly and further collapse proceeds more slowly, and then the rate of collapse is controlled by the rate at which gas can escape from vertical channels. In addition, they observed that the bed height decreases exponentially with time.

Barreto et al. [108] studied the dense phase voidage in bubbling beds comparing the results obtained using the BCT technique and those directly observed with the X-rays absorption technique. They found good agreement between the two techniques.

Abrahamsen and Geldart [107] reported that the BCT parameters can be influenced by the starting fluidizing velocity when the superficial gas velocity at the beginning of the collapse is below 6 cm/s. Moreover, they found that in beds of Geldart Group A powders the voidage of the dense phase increases as:

- the particle density decreases
- the mean particle size decreases
- the fraction of fines < 45 mm (F45) increases
- the gas viscosity (temperature) increases
- the gas density (pressure) increases

They also developed a correlation at ambient temperature to predict the dense phase collapse rate U_{de} (Eq. 28). According to this correlation, U_{de} should decrease with increasing temperature meaning that the dense phase should collapse at a slower rate as temperature rises.

$$U_{de} = \frac{0.314\ \rho_g^{0.023}\left(\rho_p - \rho_g\right)^{0.271} d_p^{1.282} e^{0.50\ F_{45}}}{\mu_g^{0.5} H_s^{0.244}} \qquad \text{Eq. 28}$$

Lettieri at al. [8,75,111] and Formisani et al. [63,74,99] used the BCT to study the influence of temperature on the dense phase properties of FCC catalysts fluidized beds.

In 1999, Lettieri et al. [111] observed that despite the sensitivity of the fluidization parameters on the initial gas velocity, it did not affect the trends of these parameters with temperature. This finding suggests that, as long as the experiments are performed in a consistent manner, i.e. at the same initial fluidizing velocity, an important assessment of the influence of process conditions can be achieved.

Furthermore, later they obtained a good agreement between Eq. 28 and the experimental values for U_{de} measured for FCC catalysts at temperatures ranging from ambient up to 650 °C. Within this range of temperature, they reported a decrease of 25-50% for the FCC catalysts. In addition, they found that the SCT was the most discriminating parameter to distinguish between systems of powders dominated by the interparticle forces (IPFs) or the hydrodynamic forces (HDFs). The SCT increased with increasing temperature for those powders dominated by the HDFs (the fresh FCC catalysts), while it decreased with increasing temperature for those materials for which the increasing influence of the IPFs caused formation of agglomerates within the bed (E-Cat catalyst).

In 2014, Girimonte and Formisani [99] highlighted the significant influence of operating temperature on the quality of bubbling. They focussed the study on the volumetric bubble fraction δ_b, also called “bubble hold-up” and defined by the following relationship:

$$\delta_b = \frac{H_b - H_d}{H_b} \qquad \text{Eq. 29}$$

Their results indicated that bubble hold-up increases with increasing temperature due to the greater difficulty encountered by the gas passing through the dense phase and in the bubble diameters. The authors related these phenomena to the thermally induced IPFs, which increased the cohesiveness of the dense phase, making the fluidized behaviour very similar to that typical of the beds of fine particles fluidized at ambient condition.

2.3 Rheology applied to solids

As it appears clear from the previous chapters, the flow behavior in multi-particle systems is strictly linked to the role of interparticle interactions between particles. It is also clear that their quantification in aerated system is still an open quest. Within this general picture, powder flowability represents an appealing tool to evaluate indirectly the effects of the interparticles forces on fluidization.

Two approaches can be followed for a macroscopic analysis of the rheological behavior of powders. The first consists of measuring the interparticle interactions acting on the single particle and integrating them on all the population of particles. This approach is considerably problematic. In particular, it must consider many factors which are difficult to correctly evaluate, such as particle size distribution, shape and surface properties of particles. On the other hand, the second approach consists of direct characterization of the rheology of powders treated as a bulk solid. The latter is more commonly used in engineering science and industries.

2.3.1. The Mohr-Coulomb failure criterion: linear yield locus

Following the second approach, the flow behavior of granular materials is generally described by using a continuum mechanics approach. In particular, the stress distribution inside a bulk solid is described with the Mohr-Coulomb analysis. In the latter, the local state of stresses is represented by Mohr's circle on normal stress, σ, and shear stress, τ, plane, in which the yield condition is represented by a line of slope tan φ_i and intercept C as shown in Figure 12. In this analysis φ_i and C represent the static angle of internal friction and the powder cohesion.

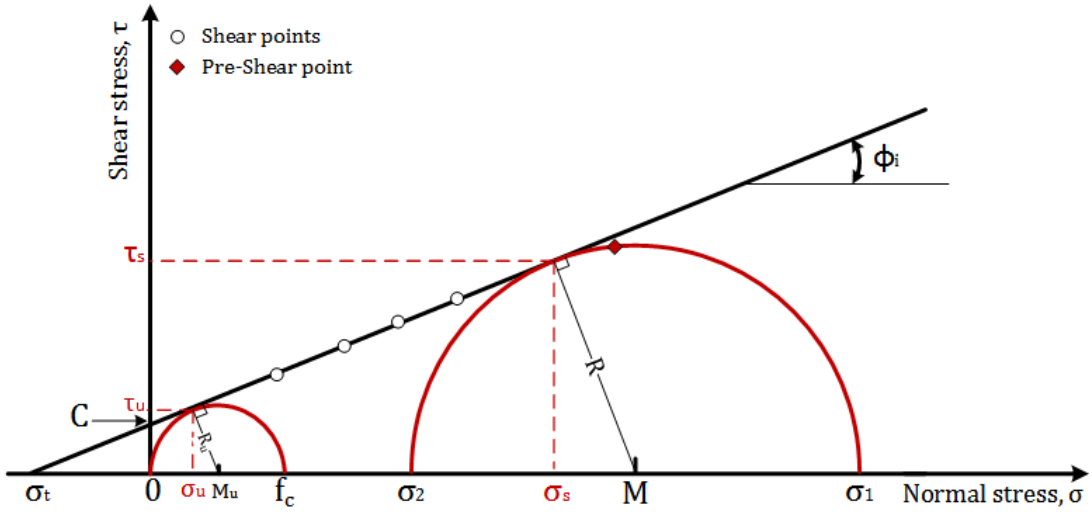

Figure 12 - Mohr-Coulomb failure criterion: linear yield locus.

Furthermore, in the Mohr-Coulomb analysis, the granular material is assumed to be a solid in the failure condition, which is a solid where the Mohr circle is always tangent to the Coulomb yield locus [112,113]. Following the Mohr-Coulomb analysis, the stress distribution within the powder [114–116] can be estimated for the design, handling and storage equipment [117,118], provided that powders are appropriately characterized. For design purposes, the most used powder characterization devices are translational and rotational shear cells [119–121]. The major principal stress, σ_1, is the one occurring during consolidation. It is usually considered that the Mohr circle representing the state of stress during the material consolidation in the critical state shear closes the yield locus on the consolidation side. Therefore, σ_1 is estimated from the largest intercept on the σ axis of the Mohr Circle tangent to the yield locus and passing through the consolidation point. The unconfined yield strength f_c is the material strength under unconfined uniaxial compression and, therefore corresponds to the finite intercept on the σ axis of the Mohr Circles, which is tangent to the yield locus line and passes through the origin of σ-τ Plane. As it is known, particle properties, such as size and shape, [122,123], and mechanical properties [23,124–127] affect the flowability of powders. In fact, the powder flowability is related to the type and magnitude of the interactions between particles acting at the microscopic scale.

$$\tau = m\,\sigma + C = \left(\frac{C}{\sigma_t}\right)\sigma + C = \tan\varphi_i\,\sigma + C \qquad \text{Eq. 30}$$

2.3.2. The Warren-Spring equation

However, the Coulomb Equation is often not adequate to fit the shear data because the shear points not necessarily belong to a straight line. Sometimes a convex curve is used in order to describe the shear data. The linear approximation can bring to larger deviations which then are likely to be transmitted to both the consolidation and the unconfined yield Mohr circles. It is possible to fit empirical curves between the shear points.

Another possibility is to use line segments to connect the points as implemented on the software procedure in support of the Schulze apparatus. However, in order to avoid excessive deviations due to error in single points, this procedure requires a certain number of repetitions of each for the shear points. Another possibility is to use the Warren Spring equation (Figure 13):

$$\tau = C\left(1 + \frac{\sigma}{\sigma_t}\right)^{\frac{1}{n}} \qquad \text{Eq. 31}$$

which introduces the parameter n. The latter is a measure of the yield locus curvature. The problem with the application of the Warren Spring equation is that the regression procedure of this nonlinear equation is much more complicated than that for the Coulomb equation.

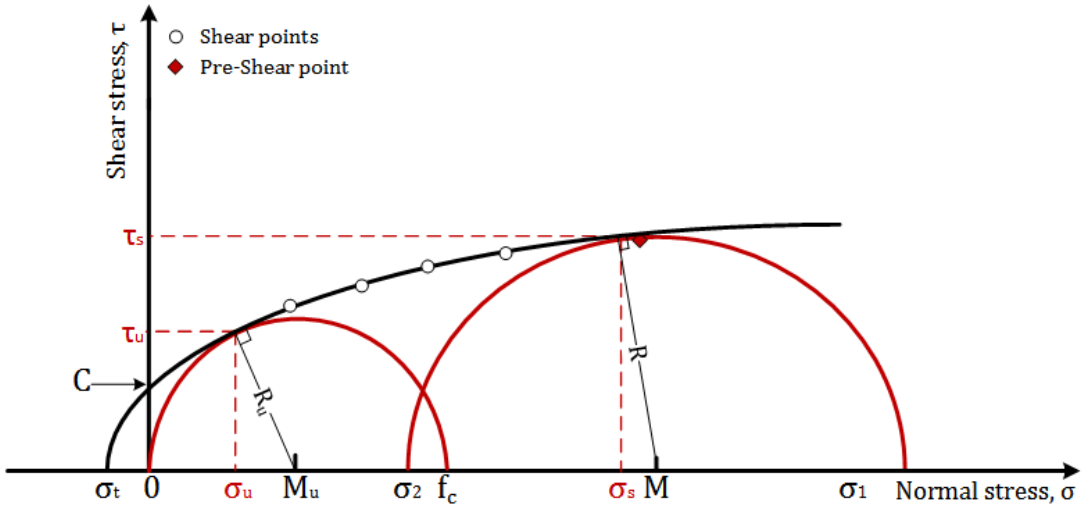

Figure 13 - General curved YL and flow properties according to Warren-Spring equation.

2.3.3. Measure of the failure and flow properties of powders in stationary status

Different types of equipment and procedures can be used to evaluate the failure properties of granular materials at ambient condition [121].

Early in 1965, Carr [128] developed a classification system capable of predicting the flow characteristics of particulate solids. He assigned a numerical value to the results of several tests producing a relative flowability index for that particular bulk material. In 1970, the author defined the main parameters used in model [129]:

- The *angle of repose* defined as the constant angle to the horizontal assumed by a cone like pile of the material. It is a direct indication of the potential flowability of a material: materials with good flowability are characterized by low angles of repose.
- The *angle of fall* is determined by dropping a small weight on the platform on which an angle of repose has been formed. The fall causes a decrease of the angle of repose that is called angle of fall. The more free-flowing is the material the lower is the angle of fall.
- The *angle of difference* is the difference between the angle of repose and the angle of fall. The greater this angle, the better the flow.
- The *angle of internal friction* is defined as the angle at which the dynamic equilibrium between the moving particles of a material and its bulk solid is achieved. This is of particular interest for flows in hoppers and bins. The *angle of spatula* is a quick measurement of the angle of internal friction. It is the angle that a material assumes on a flat spatula that has been stuck into the dry material and then brought up and out of it. A free-flowing material will have formed one angle of repose on the spatula's blade. A cohesive material will have formed several angles of repose on the blade, the average of these is taken. The higher the angle of spatula of a material the less it is flowable.
- *Cohesion* is defined as the apparent cohesive forces existing on the surface of fine particles or powders. The cohesion test consists of passing the material through

three vibrating sieves in series. The material left on each sieve is weighted and a cohesion index is determined from the relative amounts retained.

In addition, other parameters were used to characterize the cohesiveness and, consequently, the flow properties of the materials, such as the Hausner Ratio (HR) and the compressibility [130,131]. The Hausner Ratio is the ratio between the loose and the packed bulk density and is used as an indication of the cohesiveness of the materials [130]. The loose bulk density (ρ_{BDL}) is measured by gently pouring a sample of powder into a container, whereas the packed or tapped bulk density (ρ_{BDP}) is determined after settling and deaerating of the powder has occurred due to tapping of the sample. The powder compressibility is expressed as 100 (ρ_{BDP}-ρ_{BDL})/ρ_{BDP}.

Performing these tests is very easy, that makes them an appealing tool to determine powders flowability and it explains their wide use in industry and academia. However, it is very challenging to standardize the procedures and the results are that these tests are barely reproducible [132]. Furthermore, Bruni et al. [133] stated that the link between the fluidization behaviour and static properties is not so straightforward. This come out mainly to the uncertain relationship between the IPFs and the HDFs involved when gas passed through a bed of particles. The use of static methods to predict the fluidization behaviour of powders, despite being widely employed, is therefore questionable, especially when the fluidization behaviour needs to be assessed at process conditions.

An indirect shear test is the uniaxial test. In this kind of test, the sample is filled into a cylinder with frictionless walls and is consolidated under a normal stress σ_1 leading to a bulk density ρ_b. After removing the walls, the sample is loaded with an increasing normal load up to the failure point. The stress at failure is defined as the unconfined yield strength f_c. The unconfined yield strength is a measure of cohesiveness of the sample, in other words, greater is the value of the unconfined yield strength, greater is the cohesive behavior and worse is the flowability of the material. The plot of the unconfined yield strength f_c vs. the normal stress σ_1 is generally known as *flow function*, FF. This parameter is a key parameter in the design of hoppers and silos. According to Jenike [119], consolidated powders can be classified with respect to their flow behaviour using the flow factor defined "ffc=σ_1/f_c". The larger ffc is, i.e., the smaller the ratio of the unconfined yield strength, σ_c,

to the consolidation stress, σ1, the better a bulk solid flows. In particular, Jenike [134] introduced 5 different regions of flowability, those of hardened materials (ffc<1), very cohesive powders (1<ffc<2), cohesive powders (2<ffc<4), easy flowing powders (4<ffc<10) and free flowing powders (ffc>10). These regions and the corresponding separation lines are reported in Figure 14. The main limit of the uniaxial test is that only cohesive powders can be characterized since they do not yield after the walls have been removed.

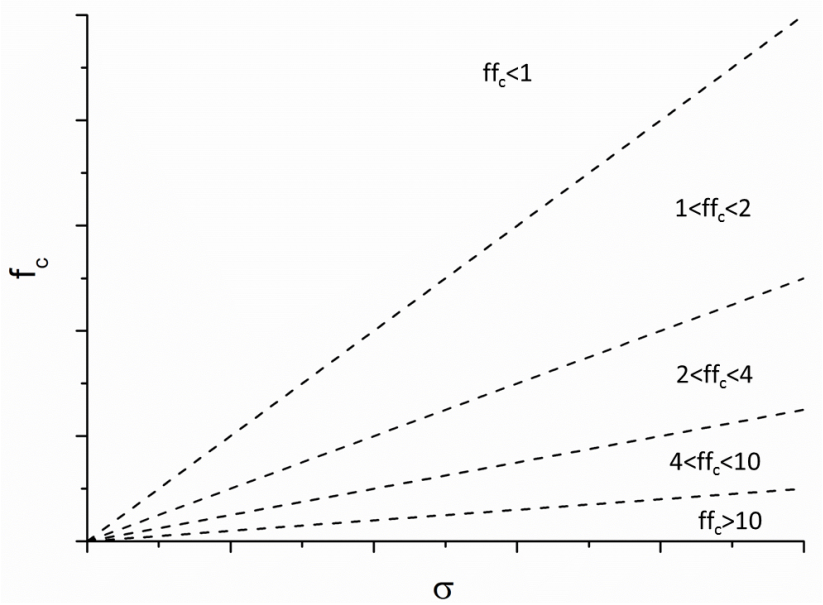

Figure 14 - Jenike classification [119].

2.3.4. Shear cells

More recently, other facilities have been developed in order to evaluate the failure and flow properties of cohesive and non-cohesive powders. The most common apparatus are the shear cells. This apparatus can measure the force (F) necessary to generate a slip plane inside a sample of granular material while a specified normal load N is applied on the same plane. Shear cells can be translational or rotational shear cells depending on how the shear plane is generated (for translation or for rotation of the parts of the shear cell). The most known translational shear cell is the Jenike shear cell (Figure 15).

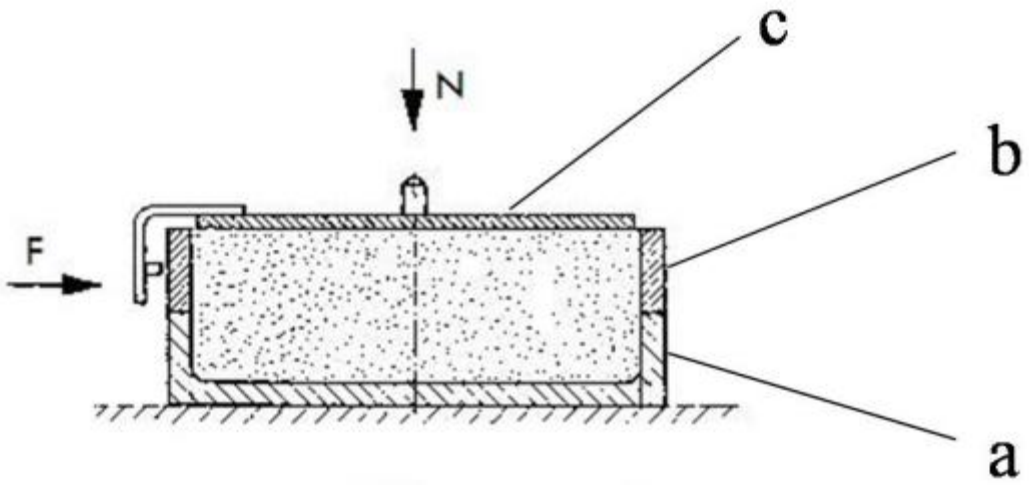

Figure 15 - Schematic representation of the Jenike shear cell. (a) base; (b) ring; (c) lid [119].

After filling the cell with the powder sample, the procedure of the test mainly follows two steps: pre-shear and shear. The pre-consolidation or pre-shear step, consists in applying a horizontal shear in the sample by moving forwards the ring at a specified consolidation load, σ_c, applied on the lid hold fixed. The shear is applied until steady state conditions are reached and detected by a constant value of measured shear force, τ_c, and necessary to hold the lid in steady position. The second step, known as shear, consists of applying again a shear within the sample applying lower normal load (σ) on the lid, lower than the pre-consolidation step. The maximum of the registered shear force measured on the lid allows calculating the incipient shear stress of the material, τ, as a function of the applied normal load. Repetition of these steps with decreasing normal loads during shear steps allows evaluating the internal yield locus. The detailed experimental technique was developed by the Working Party on the Mechanics of Particulate Solids in the European Federation of Chemical Engineering [135]. A comprehensive description can be found in the "Standard Shear Testing Technique for Particulate Solids using the Jenike Shear Cell" [135]. Figure 16 reports a schematic representation of the experimental procedure to calculate the internal yield locus.

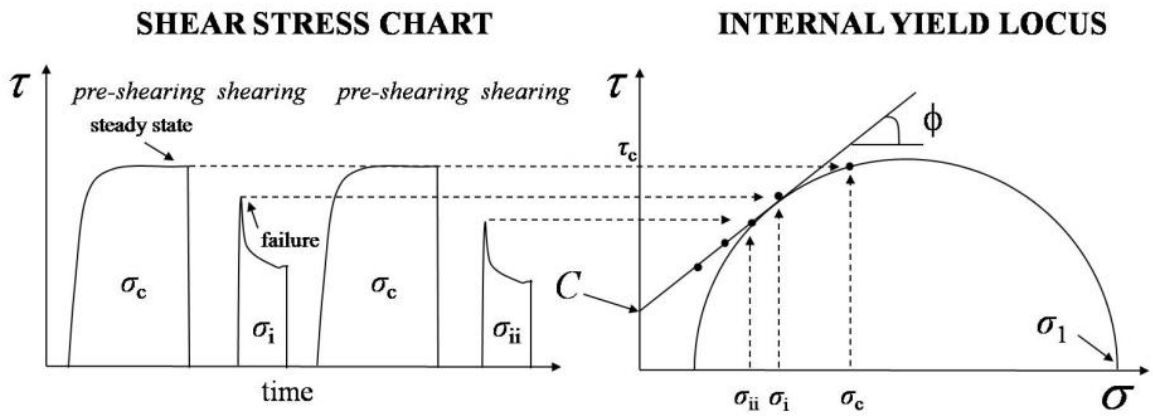

Figure 16 – Measurement of the yield locus with a shear cell: schematic of the experimental procedure.

According to Figure 16 the major principal stress σ_1 of the pre-consolidation is evaluated by the intersection of the σ-axis and the Mohr's circle tangent to the yield locus and passing through the point of consolidation (σ_c, τ_c). Each yield locus is parametric with the consolidation level of the bulk solid, defined by the major principal stress σ_1. With higher values of the pre-consolidation loads, the bulk density ρ_b increases and the yield locus moves upwards. The unconfined yield strength f_c is estimated by the intersection of the σ-axis and the Mohr's circle tangent to the yield locus and passing to the origin. Each yield locus gives one pair of values of the unconfined yield strength f_c and the major consolidation stress σ_1 from which it is possible to evaluate and plot the flow function. Another relevant parameter is the effective angle of internal friction φ_e, the angle between the tangent to the principal Mohr's circle and the σ-axis. It is an indication of the inner friction at steady state flow and it is used for the design of hoppers and silos. A less intuitive concept for granular materials is the tensile strength σ_t. It characterizes the resistance force necessary to separate two layers of material by means of a tensile force. It is mathematically derived by the intersection of the negative σ-axis and the yield locus, through Eq. 32.

$$\sigma_t = \frac{C}{\tan \varphi} \qquad \text{Eq. 32}$$

Generally, it differs from zero when interparticle attractive interactions are present in the system tested. Translational shear cells, as the Jenike shear cell, show the following limits: tests at low consolidation levels are not possible, small strain and very time consuming.

To overcome these disadvantages, the rotational shear cells have been developed. The most common rotational cell is the Schulze Ring Shear Tester [136] which is schematically represented in Figure 17. The latter provides comparable results with the Jenike shear cell, but does not have limits of strain, and is able to perform measurements at small normal stresses (< 1 kPa). The experimental procedure mainly follows the same procedure of the Jenike shear cell, with repeated steps of pre-shear and shear. In this case, the measured variable is the torque needed to the rotation of the lid from which the shear stress τ is derived. It must be highlighted that the shear measurements occur in static regime. For completeness, a brief reference to other equipment will be presented in the following section that could help elucidate the inertial regime.

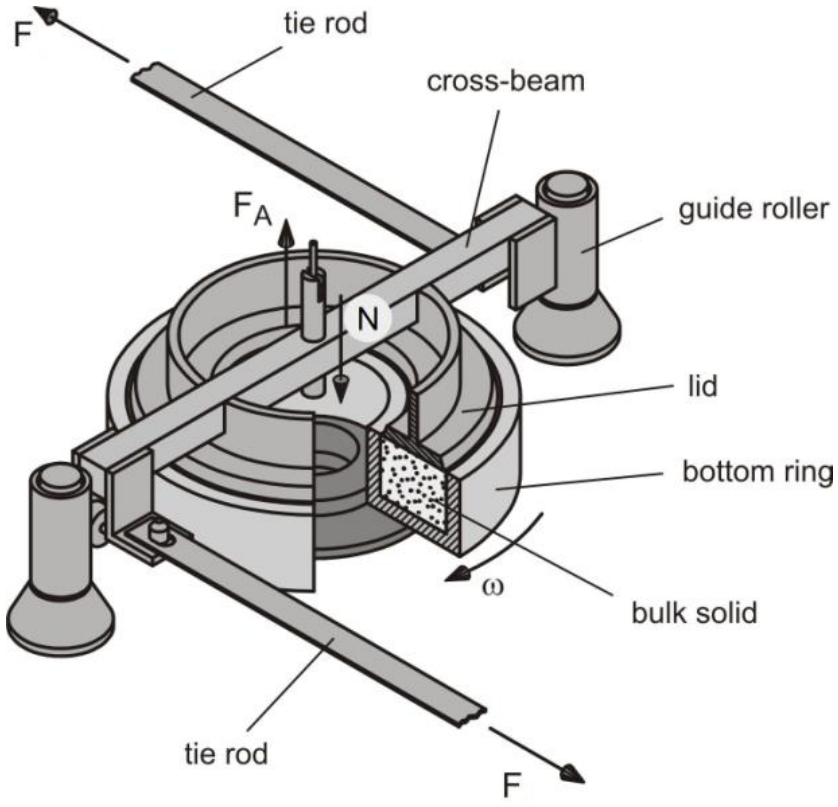

Figure 17 – Schulze Ring Shear Tester [136].

2.3.5. Rotational rheometer

Shear tester are used for silo design and adopt quasi static measurements. Among rotational shear tester, such as the Schulze tester described above there is the Powder F low Tester (PFT Brookfield Engineering Laboratories, USA) [137] the FT4 [138,139] (Freeman Technology, UK) in its tester configuration. Similarly to the Schulze tester, the PFT uses an annular cell geometry. The FT4 shear cell utilizes the entire circular area. Differently from the Schulze that measures force on attached tie rods, the FT4 and the Brookfield both measure torque on a sensitive axis. The Schulze and Brookfield both measure the applied normal force at the top of the powder bed while the FT4 measures this force at the bottom of the powder bed. Each shear cell is characterized by the capability to test a specific range of sample sizes.

Differently from shear testers, rheometers can characterize material under dynamic conditions. different apparatuses for dynamic measurements have been developed. The most established powder rheometer is the FT4 [138,139] (Freeman Technology, UK) rheometer that has a different set up from the shear cell. The rheometer is provided with an helical impeller and measures both the torque necessary to rotate the impeller and the axial force in the impeller shaft. The flow energy, which is the energy necessary to make the impeller penetrating in to the powder that is a function of the impeller speed, is at the base of the evaluation of a series of indexes that are used to classify the powder flowability and its stability with time

Recently, a mechanically stirred fluid-bed rheometer (msFBR) was developed by Bruni et al. [133] to study the rheology of aerated and fluidized powders. This apparatus was able to measure powder flow properties at low levels of consolidation stress, thanks to the combined actions of material weight and vertical aeration, as well as to the different depth at which the impeller can be placed. Later, Anton Paar Company developed a similar instrument for measuring powder flowability in partially or totally suspended conditions in presence of vertical air flow. However, further research should be addressed to directly correlate the rheometer measures to the powder flow properties [140].

2.3.6. Shear cell at high temperature

Few studies available in the literature have addressed the experimental evaluation of powder flow properties at high temperature. The first attempt was carried out by Smith et al. [141], who preheated powder samples of $MgSO_4$ and $CaSO_4$ up to 750 °C, moved them into a Jenike shear cell and performed shear tests instantly without any control of the temperature. Pilz and Loeffler [142] tested the flow behavior of fine quartz powders in the heated chamber with the Jenike cell. They observed an increase of cohesiveness with temperature. Kanaoka et al. [143] performed measurements up to 950 °C and at low consolidation level (<1 kPa) on fly ash particles by means of a Powder Bed Tester. The instrument was placed in a heated chamber to control the testing temperature and it measured the stress able to generate the shear of a moving plate on a pre-consolidated powder sample packed in a fixed plate. This tester allowed performing flow measurements at very low consolidation stresses and evaluated the adhesion of the sample with respect to a specific wall sample. In other words, it did not allow estimating the internal flow properties.

More recently, Ripp and Ripperger [144] designed a temperature controlled annular shear cell for the Schulze shear tester operating from 80 °C to 220 °C. An electric heater was used to heat up the upper part of the lid while the vertical walls and the bottom of the cell were provided with a double casing through which a heating or a cooling medium can flow. A notable experimental campaign was conducted and wall friction and internal friction at different temperature were evaluated for different kinds of powders and temperature. From this work, a uncertain effect of temperature was determined for all the types of powders.

Besides shear testers, split cells were also used to evaluate the flow properties of granular materials up to 1000 °C [145,146]. This kind of cell measures the tensile strength necessary to separate the movable part from the fixed part of the cell filled of powder in horizontal direction. Firstly, Kamiya et al. [147] placed this apparatus in a heated chamber and performed measurements on ashes and silica powder up to 900 °C. The results showed an increment of the tensile strength with increasing temperature up to 800 °C. For higher temperature, the authors noticed for the ashes a faster increase of the tensile strength

caused by the formation of both liquid bridges and sintering phenomena. Below 800 °C, they justified the increase of the cohesive behavior with modification of the surface properties of particles, which was also confirmed with IR spectroscopy analysis on the experimental materials. Later, Hurley et al. [146] reported on the effect of temperature on the adhesive properties of dusts, obtained through combustion, in order to quantify its role on the efficiency of candle filters. A split cell with a porous metallic bottom through which air was pulled, was used for the measurements. Different results were observed. For one type of dust, a decrease of the tensile strength with the temperature increase was observed up to 400 °C. However, when altering the chemical composition, a different behavior was observed and chemical aspects have to be considered for a correct interpretation of the phenomena occurring at high temperature.

Zimmerlin et al. [148] measured the torque necessary for rotating of an impeller into a bed of different samples of cohesive powders up to 700 °C. Experimental results showed an increase of the unconfined yield strength with increasing temperature for all the powders tested. More recently, a High Temperature Annular Shear Cell (HT-ASC) was developed at the University of Salerno. The HT-ASC is suitable to measure powder yield loci up to 500 °C [149,150]. This cell was used to assess the temperature effect on flow properties of samples of fluid catalytic cracking catalyst (FCC powder), fly ashes, natural corundum and synthetic porous α-alumina and glass beads. However, experimental evidences did not reveal a univocal effect of temperature in the tested range. The findings showed that, in spite of the hardness of the ceramic material tested, plastic behavior of the material at the contact point was necessary to justify all the experimental observation. However, the wide particle size distribution of the samples and the lack of knowledge of the effect of temperature on the materials' yield strength did not allow a complete proof of this finding.

2.3.7. Link between rheological measurements and fluidization

Direct measurement of interparticle forces as a function of temperature is difficult to perform and it is affected by significant uncertainty [29]. Alternatively, it is possible to measure bulk properties such as the powder cohesion as a function of temperature and to correlate the cohesion change with interparticle forces variations. Moreover, it is also possible to link measured flow properties and fluidization behavior of powders [133,151,152].

Powder cohesion, in fact, is related to the intensity of interparticle forces such as van der Waals, capillary and electrostatic forces. These forces, in turn, can be affected by temperature as a result of changes of particle hardness, liquid bridge formation or variations of the particle dielectric properties. Mikami et al. [153] studied the fluidization of a bed of metal particles exposed to temperatures producing particle sintering by surface diffusion. They found a good correlation between interparticle forces estimated applying the Rumpf [154] approach on the measured compressive strength of agglomerates and the fluidization overpressure necessary to break the sintered bed. Later, Seville et al. [155] approached the agglomeration process of metal particles at high temperature by comparing the sintering characteristic times assuming a viscoplastic behaviour of the particles and the characteristic times for quiescent motion of particles in the fluidized bed. In that case it was deduced that the compressive interparticle forces estimated with the Rumpf [154] approach do play a significant role in particle agglomeration by sintering at high temperature.

3 Materials and experimental methods

3.1 Materials

The experimental campaign was performed on ceramic powders of industrial interest provided by a private company. In particular, the materials tested were fresh ceramic powder and used ceramic powder used in their production process. The fresh material is the virgin material which is used for the reactive process; instead, the used one was obtained from different batch of the production process where the impurities have been accumulated during a reactive treatment. A small representative amount of each sample was used for analytical analyses, such as particle size distribution, shape and composition analyses. In addition, also thermal analyses were performed.

In particular, in order to study the effect of the particle size distribution five powders of the same material characterized by different particle size distributions were used. Samples of each powder of several kilograms were obtained by sieving the same fresh mother powder, so that each sample was characterized by a narrow particle size distribution. Each of these samples was mixed and the quantities produced for each sample were sufficient to carry out all the experiments described in the following. In particular, the five cuts were sieved by using standard nets with nominal mesh size of 20, 38, 63 and 88 μm. In this way, the materials obtained cover Group B, A and C of Geldart's classification. Particle size distributions by volume of the samples obtained were measured by means of a laser scattering particle size analyser Mastersizer 2000 (Malvern Instruments).

Two different samples of the used material were tested. In particular, the samples have the same kind of mother particles with different particle size ranges and different amounts of impurities, accumulated during a reactive treatment process. The first sample ("S1") and the second sample ("S2") contain an intermediate and a high level of impurities respectively.

The physical properties of all materials prior to experiments are reported in Table 2. Results are reported for both the fresh and the used samples, in terms of the Sauter mean diameter, d_{32}, that is the surface weighted mean size, the volume weighted mean size, d_{43},

and the sizes corresponding to the 10th, the 50th and the 90th percentile of the volumetric distribution, named d_{10}, d_{50}, and d_{90}, respectively. All the materials tested during this work are characterized by a broad particle size distribution, as shown by the analytical diagrams reported in Chapter 4.

Table 2 – Characteristic sizes of the samples tested.

Sieving range	A1	A2	A3	A4	A5	Sample "S1"	Sample "S2"
d_{32}, μm	7.0	22	29	65	104	14	21
d_{43},μm	14	37	63	89	227	37	76
d_{10}, μm	3.0	18	38	55	90	7.0	13
d_{50}, μm	12	35	61	87	184	25	44
d_{90}, μm	28	61	95	130	423	85	180
σ_{dp}	1.54	1.34	0.66	0.29	0.01	1.10	0.67
F_{45}, %	99	76.7	24.4	4.7	0	70	51
Geldart Group	C	A/C	A	A/B	B	A/C	A/C

3.2 SEM/EDX analysis

A Scanning Electron Microscope (SEM) was used to observe the sample's surface topography. The SEM is a kind of microscope which uses an electron beam to generate a magnified image of the specimen. The basic principle of this system is that the beam is emitted by an electron gun, and it is focused by one or two condenser lenses before passing through deflection coils deflecting the beam, so that, the SEM provides a raster scan of the sample. Detectors of secondary and backscattered electrons necessary to produce the image of the sample complete the equipment. When the electron beam interacts with the specimen several phenomena occur. The "secondary electrons" or the low energy electrons give the usual SEM image. Instead, the electrons from the primary beam penetrate into the sample and are scattered by the atoms of the material. When they are scattered out of the materials, they are detected by a different detector and the "back-scattered electron image" is produces. The contrast is mostly caused by the changes in the average atomic number of the sample regions. Light atoms scatter a small number of electrons and appear dark in the image; contrarily to this, denser atoms scatter more

electrons and appear bright. All these phenomena allow producing SEM images up to magnification from around 10 to 500000 times and so, to make evaluations regarding morphology and topography of the sample.

Energy-dispersive X-ray spectroscopy (EDX) is an analytical technique used for the elemental analysis and chemical characterization of a material. It is based on an interaction between the X-ray excitation and the material sample. The fundamental working principle is that each element has a unique atomic structure corresponding to a unique set of peaks on its electromagnetic emission spectrum. The beam of X-rays is focused into the specimen to stimulate the emission of characteristic X-rays from its. The number and energy of the X-rays emitted from a specimen can be measured by an energy-dispersive spectrometer. The X-ray detector used is a Si crystal, cooled to liquid nitrogen temperature, fitted with a thin polymer window. This allows measuring the elemental composition of the specimen.

In this work, SEM/EDX magnification of samples of experimental materials was performed by a SEM–EDX FEI – Ispect S, available at the Istituto di Ricerche sulla Combustione (IRC−CNR), in Naples, in order to analyze the shape and surface of the particles and to evaluate their role on the magnitude of interparticle interactions.

3.3 Thermal analyses

In this study, the thermal analyses were performed with the TA-Q600 instruments available at the University of Salerno. The device provides simultaneous measurement of weight change (TGA) and thermal information (DTA) on the same sample from ambient to 500 °C. It features a highly reliable horizontal dual-balance mechanism that supports precise TGA and DTA measurements.

3.3.1 Differential Thermal Analysis (DTA)

Differential thermal analysis (DTA) is a technique that measures the energy necessary to maintain a nearly zero temperature difference between a specific sample and an inert reference material. The two materials experience identical thermal regimes in an environment heated or cooled at a controlled rate. The differential temperature is registered and plotted over the temperature. Thus, physical or chemical transformations,

such as glass transitions, crystallization, melting and sublimation, can be detected comparative to the inert sample, for either exothermic or endothermic processes.

3.3.2 Thermal Gravimetric Analysis (TGA)

Thermogravimetric analysis or thermal gravimetric analysis (TGA) is a technique through which changes in physical and chemical properties of materials are measured as a function of temperature (with constant heating rate), or as a function of time (with constant temperature and/or constant mass loss). This analysis provides information about both physical phenomena including vaporization, sublimation, absorption and chemical phenomena such as desorption, chemisorptions, desolvation, decomposition, and solid-gas reactions (e.g., oxidation or reduction). Generally, TGA is used to determine selected characteristics of materials that exhibit either mass loss or gain due to decomposition, oxidation, or loss of volatiles (such as moisture).

3.4 The High Temperature Shear Cell (HT-ASC)

In this work, the HT-ASC was used to perform measurements (shear testing) of the powders at ambient and at 500 °C. A Schulze shear cell was modified at the University of Salerno in order to perform measurements of the powder flow properties at high temperature [150]. Figure 18 shows a schematic representation and different pictures of the high temperature shear cell (HT-ASC).

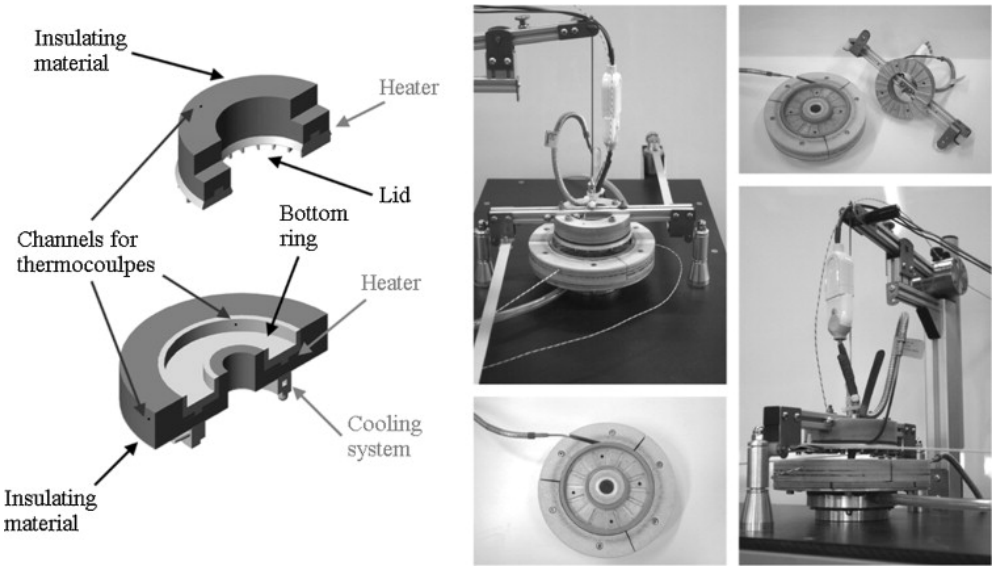

Figure 18 - Schematic representation (a) and pictures (b) of the High Temperature Annular Shear Cell (HT-ASC).

The materials used for the construction of the High Temperature-Annular Shear Cell (HT—ASC) allow a safe operation of the system up to 550 °C. The main geometrical data of the modified shear cell are listed in Table 3. The annular shear cell operates on the same workbench as the original Schulze Ring Shear Tester developed for shear test at ambient temperature.

Table 3 – Geometrical data of HT-ASC.

	HT-ASC	
	Bottom ring	Lid
Internal volume, cm^3	95	-
Inner diameter, mm	60	62
Outer diameter, mm	120	118
Nominal height, mm	10	-
Heating power, W	600	260

In particular, the HT-ASC consists of a bottom annular rig containing the powder specimen and an annular lid placed on the top of the sample like an annular Schulze shear cell. The lid is fixed at a crossbeam connected by two tie-rods to two load beams which allow measuring the shear force acting on the shear plane developed inside the powder sample. The shear plane is caused by the rotation of the bottom ring relative to the lid for a specified normal load, applied by weight pieces placed on a hanger connected to the crossbeam. The powder sample in the cell is heated by electric heaters placed in the

bottom ring and in the lid. In order to minimise the temperature gradient of the sample inside the cell and to reduce the heat flow from the cell to the environmental ambient an insulating material was placed on the lid and around the trough of the cell. Furthermore, a cooling system was designed to cool the cell base where it is in contact with the gears of the rotation mechanism of the tester. Indeed, in order to keep the cell base in contact with the instrument gears at room temperature, the insulating material below the trough of the cell was placed over metal disk. Such a disk is cooled by a water steam flowing inside a cavity in the ring at the base of the cell that is in contact with the rotating gear. A temperature control system is used to achieve a constant temperature in the powder sample. In particular, the temperature vertical uniformity inside the powder sample is verified and controlled by two different PID temperature control systems. These systems consist of two "J" thermocouples measuring one the temperature just above the base and the other just below the lid. A third thermocouple is placed at an intermediate height between the base and the lid to verify the temperature homogeneity inside the sample. Further details are reported by Tomasetta et al. [150].

3.5 Procedure with the HT-ASC

The experimental procedure to measure the yield loci of the samples at high temperature mainly followed the standard procedure for the shear test with the annular Schulze shear cell. After filling the bottom ring of the cell and positioning it on the desk of the Ring Shear Tester, thermocouples were set and the lid and the weights for consolidation were placed according to the standard procedure. In order to achieve the desired operating temperature, before starting the shear test, heaters were activated and the necessary time was waited to let the temperature reach the desired steady state value. The remaining part of the experimental procedure, used to evaluate the yield loci of the material, at the set temperature with the HT-ASC, mainly followed the standard procedure for shear tests with the Schulze Ring Shear Tester proposed by Schulze [135]. In the Schulze tester, an electrical motor is used to rotate the bottom ring. The shear velocity depends on the radius of the shear cell. Instead, the lid is held in place by two tie-rods. Two load cells measure the torque necessary to keep the lid in place. The height of the vanes present on the lid defines the shear plane inside the sample. The weight of the lid, crossbeams and hanger is

balanced by counterbalance system. A vertical normal stress is exerted on the shear plane by loading the lid with a certain weight, through a hanger connected to the crossbeam. Therefore, the normal stress is calculated as the weight loaded defined by the cell surface. The shear stress is determined by the torque necessary to keep the lid in place and the surface of the shear plane. It is calculated as average forces measured by the two load cells.

The shear experiments were carried out with the same specimen of powder to measure four different yield loci and in turn to obtain a flow function with four points. To obtain a single yield locus two steps were followed, as described in section 2.3.1. The first step is the pre-shearing or consolidation step. Bulk solid specimen is sheared at normal vertical stress until the constant shear stress steady state condition is attained. In the second step, shearing, powder is sheared at a lower stress than the stress in the pre-shearing step until the shear stress has reached its maximum value. The maximum shear stress is the point at which the powder starts to flow at the corresponding normal stress,

Figure **19**. Repetitions of these steps in series with decreasing normal stresses during shear steps allow evaluating the internal yield locus relevant to the powder consolidation attained in the pre-shear phase.

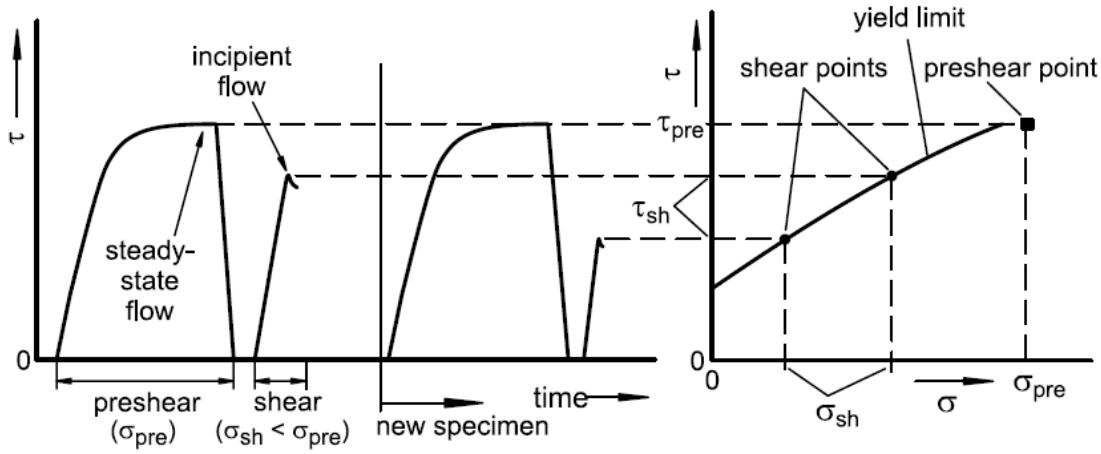

Figure 19 - Determination of Yield Locus through the evaluation of the shear stress.

For Coulomb materials, the internal yield locus is calculated as the best fitting line through the (σ, τ) experimental points and it is defined by the cohesion C and the angle of internal friction φ_i.

The angle of internal friction, φ_i, is a measure of the friction between particles and it

indicates the resistance to flow. It is the slope of the yield locus. The major principal stress, σ_1, acting on the sample during consolidation, is determined by the consolidation Mohr circle in the σ, τ diagrams (yield locus). It is calculated by the intersection of σ-axis and the Mohr's circle tangent to the yield locus and passing to the pre-shear point (σ_{pre}, τ_{pre}). The unconfined yield strength, f_c, of the powder, is the stress that cause failure in a consolidated powder sample loaded under a vertical compressive stress without any walls that supports the sample and relieve stress. It is defined by the smallest Mohr circle in the yield locus and it is estimated by the intersection of the σ-axis and the Mohr' s circle tangent to the yield locus and passing to the origin of the axis, Figure 20.

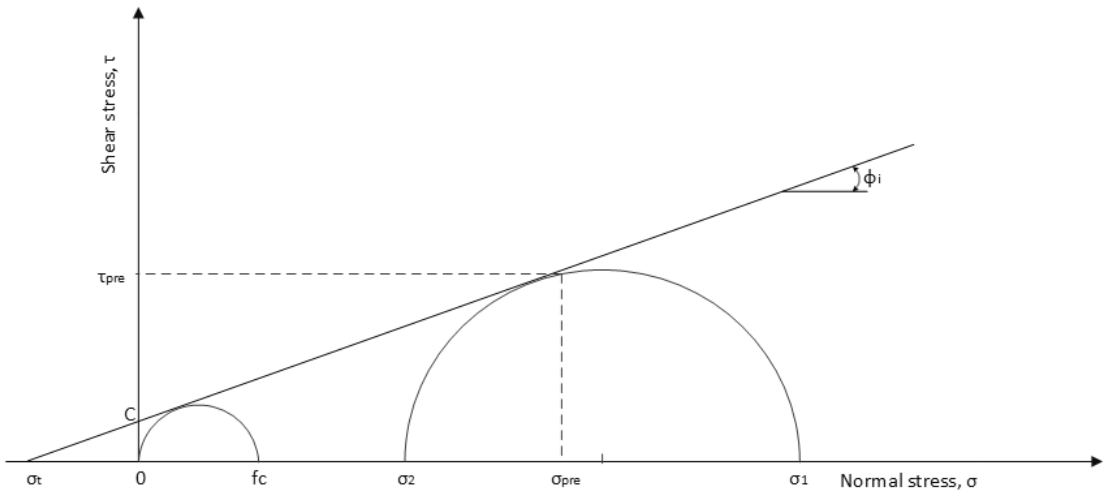

Figure 20 - General internal YL and flow properties for a Coulomb material.

All the powder samples were tested at room temperature and high temperature (500 °C). Due to a possible long-term sensitivity of the powder to oxidation and to avoid air humidity condensation in preparing the samples, especially handling heated samples the powder samples were filled and removed from the cell inside a glove-bag in nitrogen atmosphere. It was assumed that once in the cell closed by the lid, the sample could only marginally be affected by the environment air and therefore all the tests were carried out in laboratory environment without controlling the air humidity. Four shear points were used to derive each yield locus. Each shear experiment was repeated four times in order to increase the statistical significance of the results in terms of yield loci. Furthermore, yield loci obtained at different consolidation stresses provide couples of values (σ_1, σ_c) that can be plotted to represent the so-called material flow function. The plane σ_1, σ_c is divided in regions bounded by lines corresponding to constant values of the ratios σ_1/σ_c, the so-called

''flow factor, ff_c''. These regions correspond to different classes of flowability according to the Jenike classification, as explained in section 2.2.3.

In particular, in this study the experiments were performed for a major principal stress, σ_1, in the range 1200-1700 Pa**.** Such low normal stress values were adopted in order to approach a consolidation state relevant to fluidised powders.

3.6 Experimental fluidization rig

The experimental apparatus is shown in Figure 21. The reactor was made of 3 mm thick Inconel. It consists of a vessel of 140 mm in diameter and 1000 mm in height. The vessel was fitted with a very fine (i.e. pore size of 40 µm) Hastelloy X distributor plate to ensure a high pressure drop and, thus, a good fluidization in the reactor. The windbox, below the distributor plate, was made in Inconel. The windbox height is 150 mm and it was packed with 10 mm ceramic balls in order to improve the temperature uniformity. The upper disengaging section fitted on top of the vessel was made of stainless steel; 500 mm height with a freeboard diameter of 250 mm. Connected to the side of the disengaging section was another stainless-steel pipe line that acts as a pressure relief valve. The latter is connected to a stainless-steel cylindrical tank (1700 mm tall x 130 mm diameter) containing water. The height of the column of water was worked out, so as to give a pressure drop of 150 cmH_2O, which means that any pressure higher than this would lead the gas to bubble through the water. Moreover, a system of two solenoid valves are fitted on the rig, one (SV1) is used to cut the gas supply to the bed, the other (SV2) to vent the gas trapped in the windbox section. This system of solenoid valves was implemented during the bed collapse experiments. The two valves were operated remotely from outside the X-ray room, where the fluidization rig is located and were synchronized to switch position simultaneously: when the fluidizing gas was shut off by closing valve SV1, valve SV2 was opened allowing the gas trapped in the windbox to be vented. A horizontal pointer made of material opaque to X-rays was connected to the solenoid valves so that when the valves were switched over the pointer changed position from horizontal to vertical. This pointer, externally mounted next to the vessel, can be moved to be always in the field of view of the X-ray image and therefore provide a visible indication of the start of the bed collapse test (time zero).

Fluidizing gas, nitrogen or air, was measured with rotameters (CT Platon). To maximize the heat rate, the fluidizing gas is preheated while passing through the preheating section and the windbox section was wrapped with 800 W heating tape. The vessel was surrounded by two flexible ceramic heaters wrapped around the vessel, and capable of providing an operating temperature up to 900 °C. The two ceramic heaters covered 900 mm of the vessel height. All the system was packed with two layers of 1.5 cm thick Super-wool, covered by a 7 cm thick layer of Rockwoll wrapped with silver tape, in order to insulate heat loss. A pressure tap was located above the distribution plate to measure the pressure drop profile across the bed as a function of the fluidizing gas velocity. Seven thermocouples were used to monitor and control the temperature in the fluidized bed system. The temperature was controlled by three different PID controllers at experimental conditions of 25, 100, 200, 300, 400 and 500 °C. Further details are reported by Lettieri [111].

Figure 21–- Experimental apparatus for fluidization tests.

3.7 The X-ray technique

The X-ray system is a non-intrusive tool which allows qualitative and quantitative real-time information on the internal structure and on instantaneous changes in three dimensional systems. Providing a sufficient amount of power, the pulsed high energy X-ray beam passes through the vessel causing attenuation phenomena due to the amount and distribution of the fluids and solids in the vessel. The X-ray facility used in this work is available in the Department of Chemical Engineering at University College London.

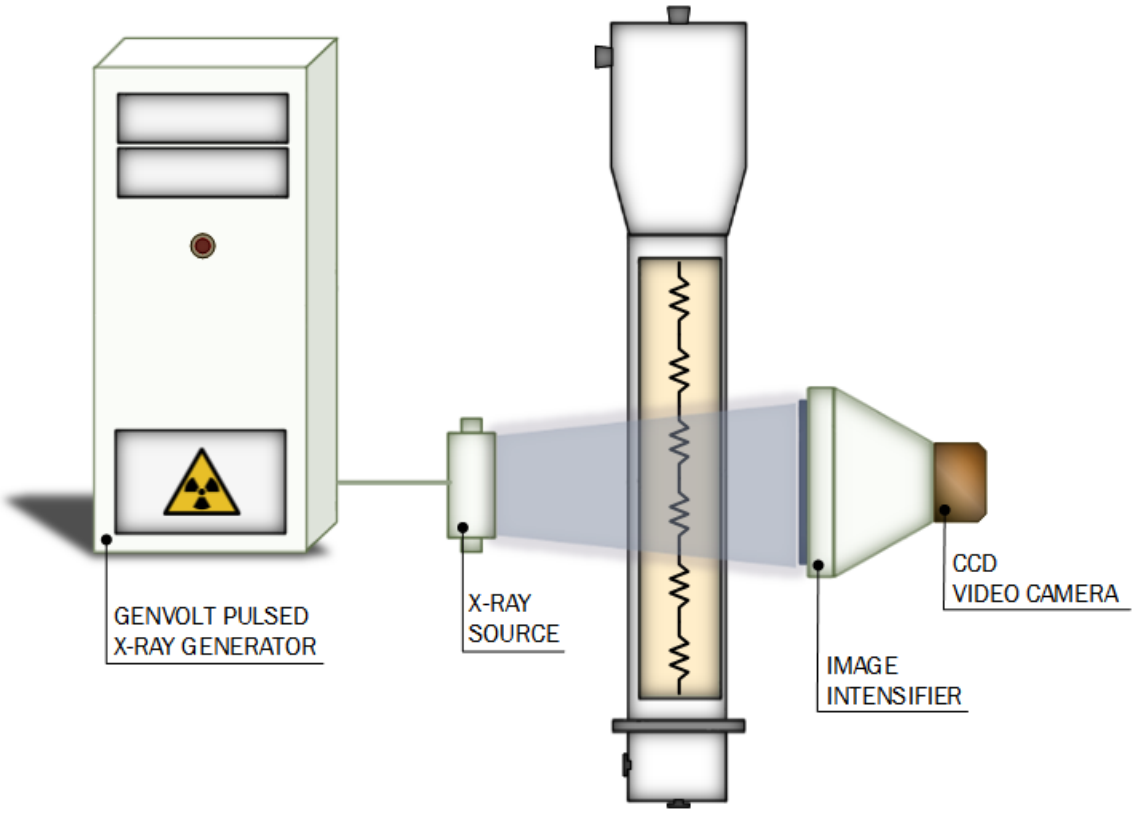

Figure 22 - Scheme of the X-ray system unit.

3.7.1 X-ray unit

The X-ray unit consists of a generator, X-ray source and image intensifier. The X-ray source, or tube, and image intensifier are mounted on a twin column ceiling suspension unit as shown in Figure 21 and Figure 22. The two columns can be moved laterally and vertically

allowing that both the distance between the tube and the image intensifier and height from the ground can be changed. This solution offers the possibility of moving the system along the length and height of the room either independently or synchronized. The system is motorized and can be remotely controlled from outside the room. The X-ray generation system, developed in collaboration with General High Voltage Industries Ltd. (Genvolt), provides X-ray pulses down to 200 µs width with an intensity of up to 450 mA at a voltage variable from 50 kV to 150 kV. It is coupled to a rotating anode X-ray tube with the capacity of up to 1 million heat units and 68 kW peak loading allowing sustained X-ray pulse streams of several minutes. Two focal spots can be selected (0.6 mm and 1.2 mm) and the target can be rotated at either 50/60 Hz or 180 Hz, depending on the power required. The X-rays are detected on a 30 cm Industrial X-ray Image Intensifier optically coupled to a 1024 x 1024 pixel high speed digital CCD camera. The camera is triggered by the control software, which itself is triggered by the X-ray generator at frame rates from 24 to 72 frames per second (fps). Both the X-ray tube and X-ray detector have motorised X-ray masking to ensure the best quality images with the minimum of scatter. All X-ray operations were carried out from the main control console located outside the radiation proof room. For further information see Lettieri and Yates [156].

3.7.2 Image recording system

Images are captured, displayed and stored using powerful acquisition software. The software handles image processing/corrections, lossless image storage and playback up to 72 fps in either real-time or frame by frame. An extensive set of analysis tools allows for off-line data analysis and for measurements to be made.

3.8 Fluidization measurements

3.8.1 Minimum fluidization velocity: u_{mf}

The minimum fluidization velocity, u_{mf}, was experimentally measured at increasing temperature. At each temperature, the u_{mf} was graphically obtained from the diagrams of the pressure drop profile across the bed over the fluidizing gas velocity. The fluidizing gas, nitrogen, was controlled by calibrated rotameter. The pressure drop profiles were obtained first by increasing the gas flow rate until the bed was well fluidized, and then by

decreasing the flow rate until the bed settled down. A typical pressure drop profile for Geldart Group A is shown in Figure 23. The minimum fluidization velocity was calculated from the pressure drop profile as the intersection of a diagonal line and the horizontal line obtained when decreasing the gas flow rate as shown in Figure 23. The measurements were repeated, from 3 to 5 times, to verify the precision and consistency of the measurement itself. The experimental value of the pressure drops across the bed, ΔP_m, was compared with the predicted, ΔP_c.

$$\Delta P_c = \frac{Mg}{A_c} \qquad \text{Eq. 33}$$

where M, A_c and g are the bed material weight, the cross-sectional area occupied by the material and the acceleration due to the gravity.

Generally, particles belonging to different groups of Geldart classification exhibit different pressure drop profile. In particular, for Group B and D particles, initially the pressure drop increases linearly with the gas flow rate till the minimum fluidization velocity, then its value remains constant and the ratio $\Delta P_m / \Delta P_c$ is 1. When the pressure drop curve is derived starting from high flow rate and gradually reduced to zero, the curve mainly follows the same trend as for the previous case. Differently, Group A and C particles show different behaviour. When increasing the flow rate, it may occur an overshoot in the pressure drop curve before reaching the fluidization conditions ($\Delta P_m / \Delta P_c = 1$) as shown in Figure 23. This phenomenon can be associated to an active role of interparticle forces compared to the hydrodynamic ones. In other words, for these particle systems it takes to break the strongest interaction among particles before reaching the fluidization conditions. Conversely, when decreasing the gas flow rate until the bed settled down, the transition between fluidization regime and static bed is much smoother.

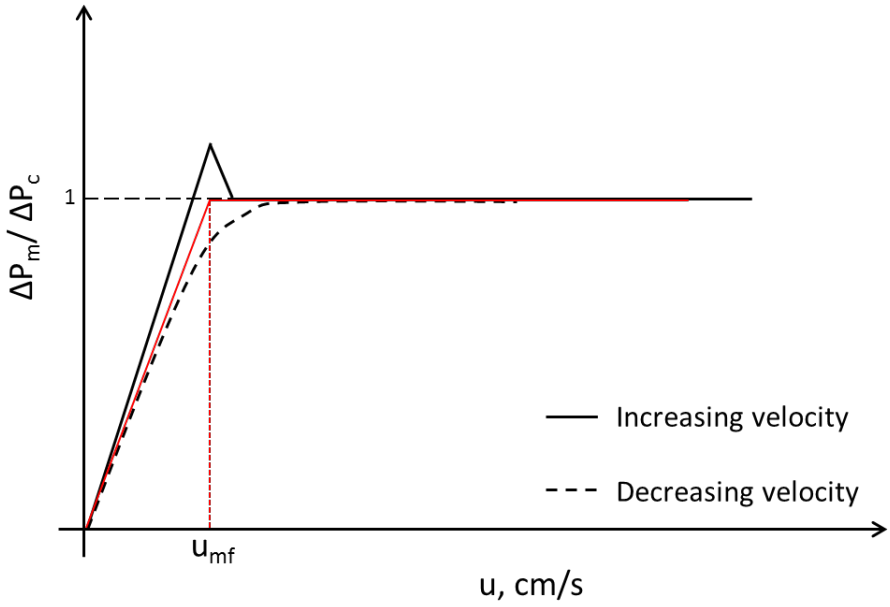

Figure 23 - Typical pressure drop profile for Group A of Geldart classification.

3.8.2 Minimum bubbling velocity: u_{mb}

In this work four different methodologies were used to determine the minimum bubbling velocity [98]. The first method used was the visual analyses of the VHS images on a frame by frame basis, from the X-ray imaging technique, and noting the velocity, $u_{mb,\,v}$ at which the first bubble was seen breaking the bed surface. The second procedure followed the idea proposed by Rapagna' et al. [89]. The authors assumed that the u_{mb} has to be taken where the shallow minimum of pressure drop profile occurs as shown in Figure 24.

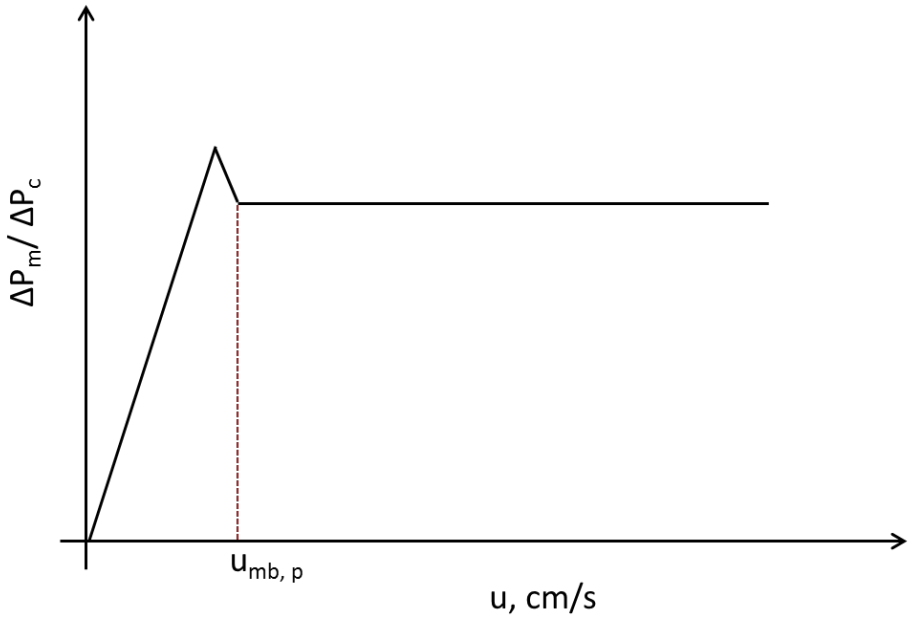

Figure 24 - Minimum bubbling velocity calculated according to Rapagna et al. [89].

The other two methods use the ε vs u plots, namely "fluidization map" of the system [157,158] to identify bubbling velocity. In particular, the plot reports the overall bed voidage, ε_b, and the dense phase voidage, ε_d as a function of the gas flow rate. The overall bed voidage values were obtained from the bed height, during fluidization experiments, for relatively low gas velocity and from the bed collapse test for higher velocity. Instead, the dense phase voidage values were measured from the bed collapse tests. One of the possible fluidization map profiles have been reported as example in Figure 25. Increasing the gas velocity over the minimum fluidization condition, the bed starts to linearly expand until either a peak (as in Figure 25) or an evident variation of slope occurs. In both cases, these points identify u_{mb} as the end of the homogeneous expansion of the bed and the starting point of the bubbling regime ($u_{mb,e}$). A second option is to consider the point where the values ε_b and ε_d start to diverge ($u_{mb,s}$). These values of the minimum bubbling velocity were calculated and compared with the predictive equation available in the literature.

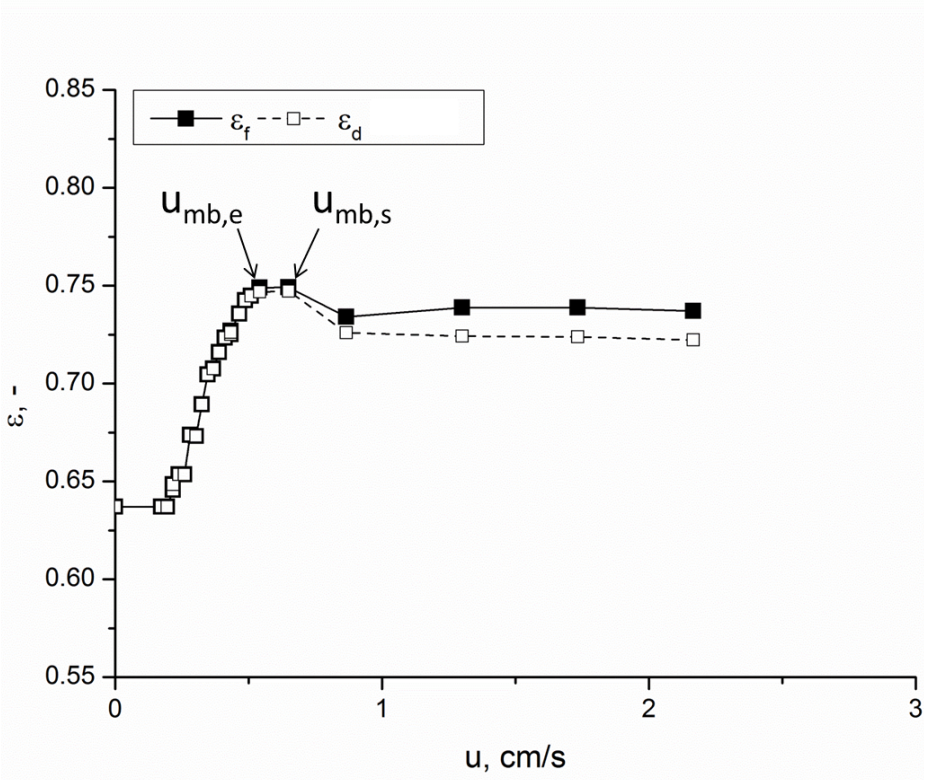

Figure 25 - Fluidization map: the overall and dense phase voidage as function of the gas velocity.

3.8.3 Bed voidage: ε

The bed expansion profiles in this work were obtained using the X-rays imaging technique. The bed material was initially vigorously fluidized to allow the good mixing of particles, and then the expansion profiles were obtained by slowly re-fluidizing the powder and recording the bed height at each gas velocity. Before recording the bed height some time was waited in order to stabilize the bed fluidization. The expansion profiles were calculated between ambient temperature and 500 °C. From each height, the corresponding average bed voidage was calculated with Eq. 34.

$$\varepsilon = 1 - \frac{\mathrm{M}}{\mathrm{A}_c\ \rho_\mathrm{p}\ \mathrm{H}} \qquad \text{Eq. 35}$$

3.8.4 Bed collapse test: BCT

The bed collapse experiments were performed at different flow rate of the fluidizing gas, predetermined chosen from u_{mf} to value above u_{mb}, and suddenly shutting off the gas supply to the bed. The bed heights were recorded using the X-rays technique described in section 3.7. Abrahamsen and Geldart [107] found that the bed collapse parameters depend on the starting fluidizing velocity. In particular, they report that the parameters were affected by the initial gas velocity for values larger than 6 cm/s. Lettieri [159] showed that despite the sensitivity of the fluidization parameters on the initial gas velocity, the trends of these parameters as a function of temperature do not change. In this study the dependency of the BCT parameters from the initial gas velocity was not analyzed. The maximum superficial gas velocity was set 6 times larger than the minimum fluidization velocity in order to minimize fine particles elutriation from the reactor. This velocity was the highest velocity which would keep the visually observed elutriated fines to a minimum.

The bed collapse tests were operated using the double-drainage method, as described in section 3.6, where the fluidizing gas trapped in the windbox is vented out as the gas supply to the bed is cut off. This choice was made according with the results proposed by Park et al. [160]. They showed that in the single-drainage method, the measured voidage and gas velocity in the dense phase depends on windbox volume, gas flow resistance of distributor and gas velocity, whereas in the dual-drainage method, the dense phase properties are independent of the distributor resistance and windbox volume.

4 Analytical results

In this chapter, results from PSD, SEM/EDX and thermal analyses are presented. The characterization of the material tested in term of particle physical properties laid the basis for a better understanding of the dynamic behavior of the powders when operated in fluidized bed reactors.

4.1 Fresh material

4.1.1 PSD analysis

In order to study the effect of particle size distribution with temperature, the fresh silicon powders were sieved in five different ranges (A1, A2, A3, A4 and A5). Figure 26-Figure 30 show the particle size distribution for each different fresh sample prior to fluidization and rheological tests of A1, A2, A3, A4 and A5 respectively. The finest sample, A1, A2 and A3 powder samples are characterized by a very wide PSD, with a relative diameter spread (σ/d_{50}) of 1.5, 1.3 and 0.65 respectively, as previously reported in Table 2. Moreover, the A2 powder sample contains about 72 $\%_{wt}$ of fine fraction (diameter below 45 μm) and the A3 sample contains about 20 $\%_{wt}$. The A4 and the coarsest sample, A5 are characterized by a fairly wide and very narrow PSD, with a relative spread diameter of 0.29 and 0.01. The fine fractions are 3.8 and 0 respectively.

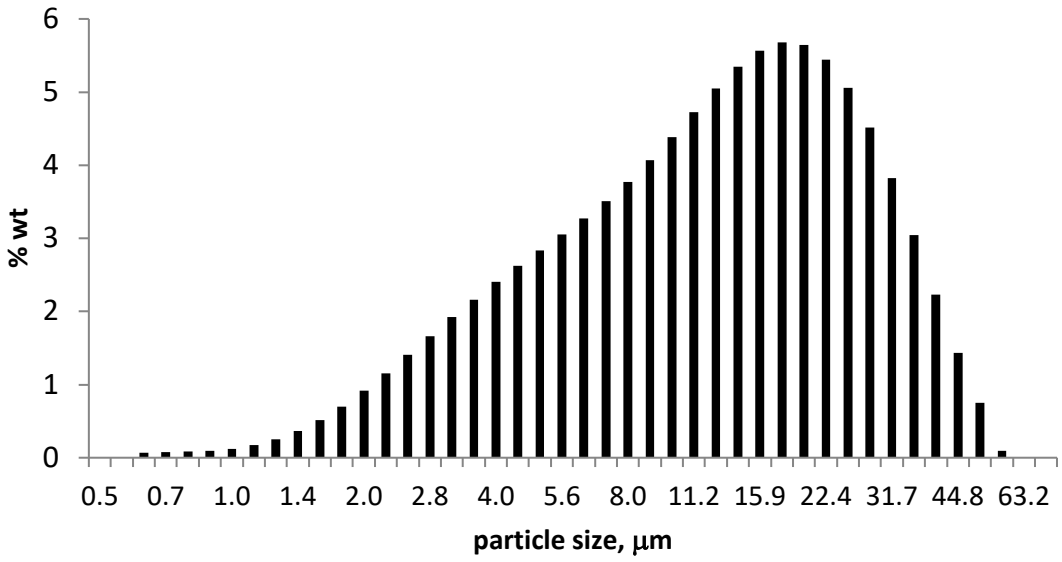

Figure 26 - Particle size distributions of A1 powder sample.

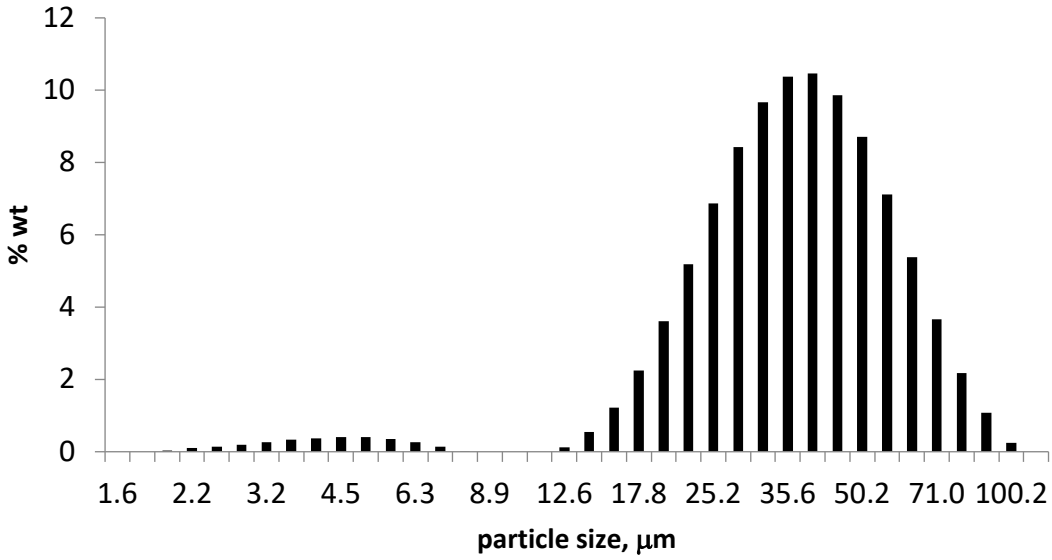

Figure 27 - Particle size distributions of A2 powder sample.

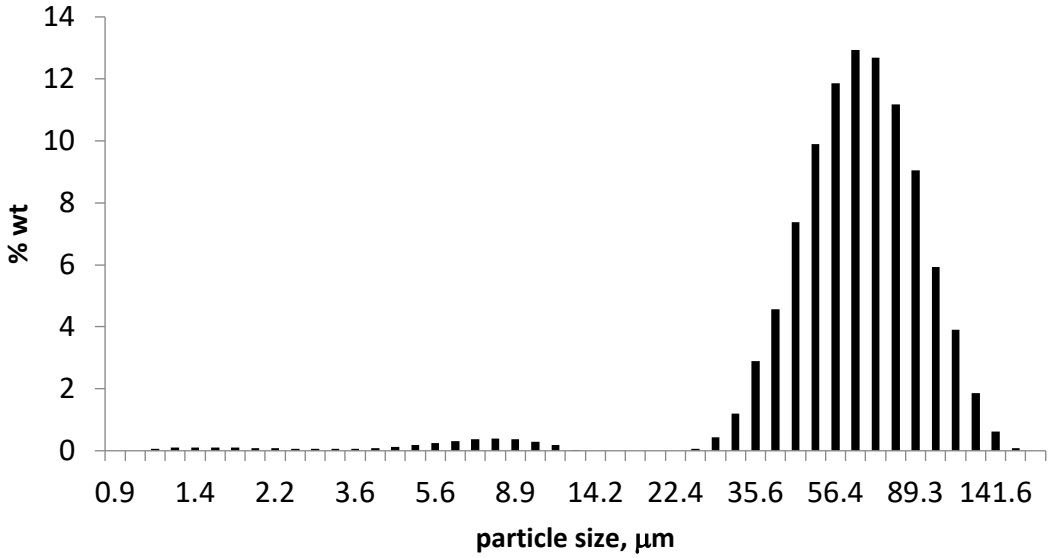

Figure 28 - Particle size distributions of A3 powder sample.

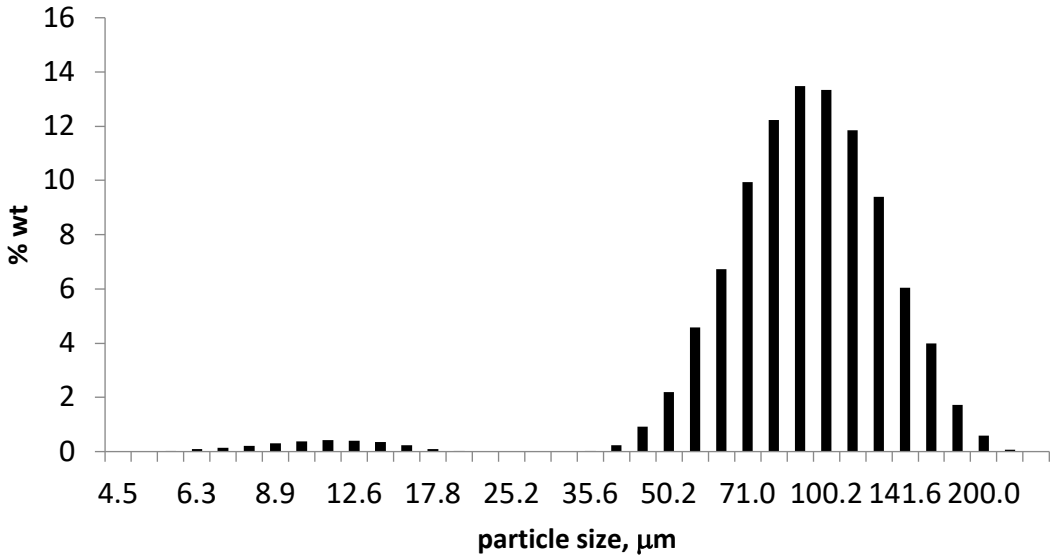

Figure 29 - Particle size distributions of A4 powder sample.

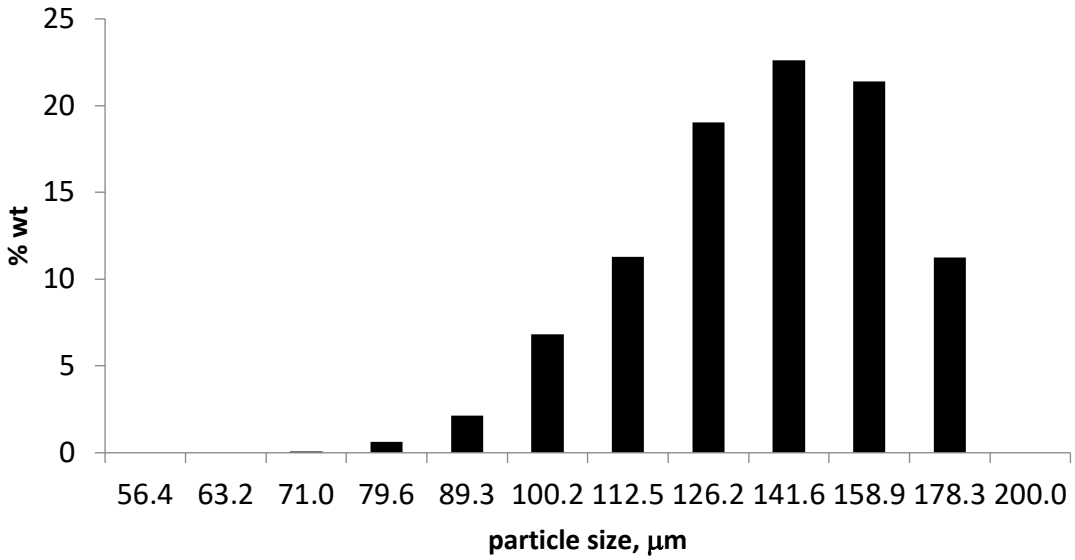

Figure 30 - Particle size distributions of A5 powder sample.

4.1.2 SEM/EDX analysis

Figure 31 reports typical pictures obtained by SEM analysis for fresh samples of the powder. Analysis of the pictures shows some similar features for all the size cuts analyzed. In particular, it can be observed large quantities of fines adhering on the surface of larger particles, irregularly shaped particles with flat surfaces and sharp edges.

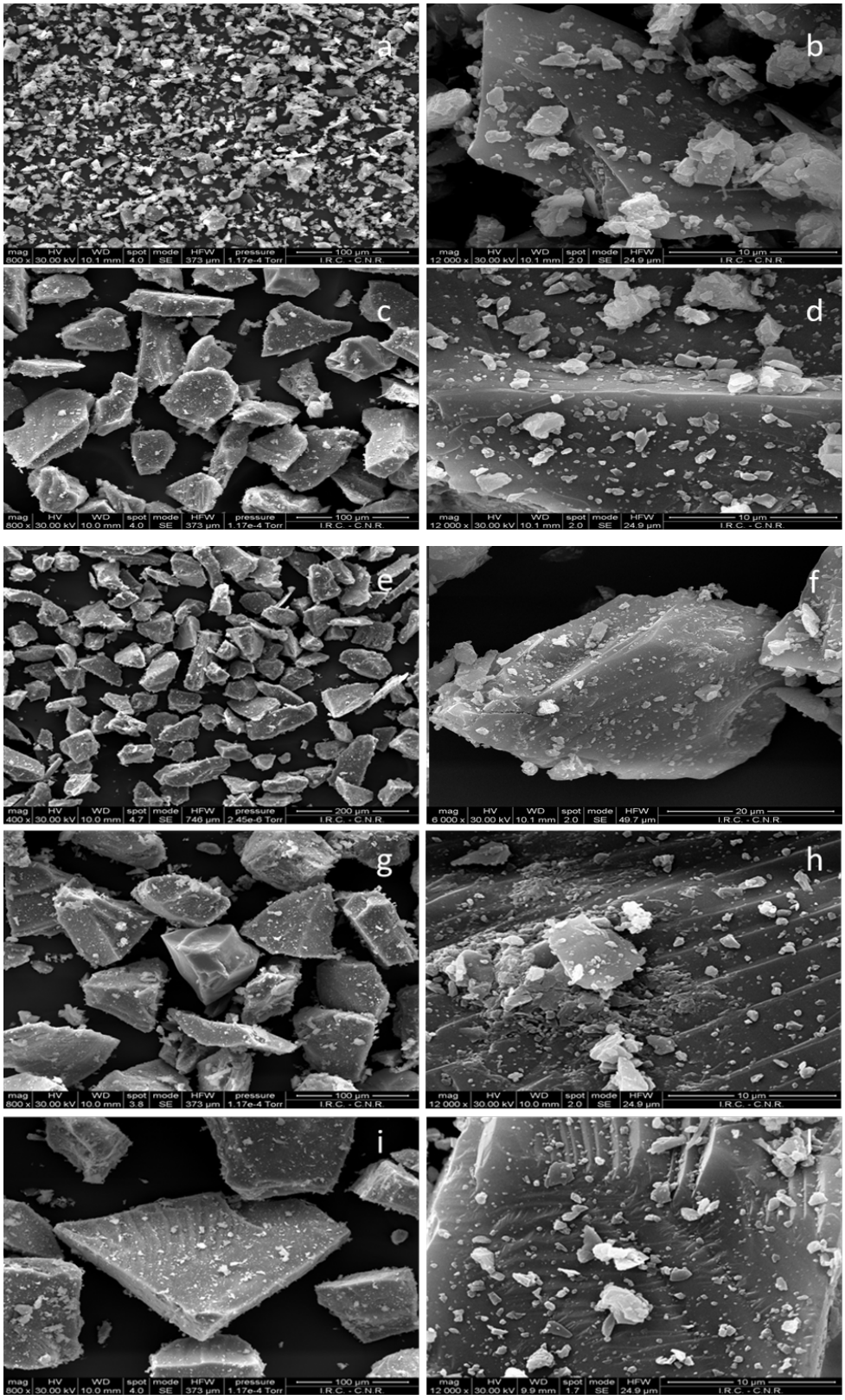

Figure 31 - SEM pictures for the sample smaller than A1 (a, b), A2 sample (c, d), A3 sample (e, f), A4 sample (g, h) and A5 sample (i, l).

Together with the SEM analysis also the EDX examination was performed. Most of the particle samples showed only the emission lines of the mother particles in the EDX

diagram. However, some particles showed the presence of metals probably due to metallic impurities deriving from the ball milling process. Unfortunately, other details of the material cannot be provided for confidentiality reasons.

4.1.3 Thermal analysis

A SDTQ600 (TA Instruments) was used to carry out both Differential Thermal Analysis (DTA) and Thermal Gravimetric Analysis (TGA). The purpose was to put in evidence any possible phase transitions or chemical reactions in the range of the temperatures tested with the HT-ASC. DTA and TGA were performed in air and nitrogen and the temperature program adopted ensure a linear rate temperature increase, 10 °C/min, from 25 °C to 550 °C. Unfortunately, it was not possible to have heat calibrated signal for the DTA, whose response in terms of heat exchanged has to be taken only qualitatively. In Figure 32 the heat flow and the sample weight change, related to the weight at ambient temperature, are reported as a function of temperature for all the fresh samples. All measured heat fluxes are positive, that is they are intended towards the sample. Phase changes should be visible with fluxes larger in modulus as negative peaks. Accordingly, inspection of the figure reveals a similar thermal behavior of the powder samples. A change of weight is detected around 100 °C and it is possibly related to some condensed moisture evaporation. The constant weight of the sample above 100 °C indicates that chemical reactions (e.g. oxidation) can be excluded in that range. The thermal behaviour observed for all the other samples was qualitatively similar. The absence of significant physical or chemical changes seems to be confirmed also by SEM images of the materials taken after the 500 °C test. An example is reported in Figure 32, that shows for the A2 sample exposed to 500 °C the same features of the fresh material.

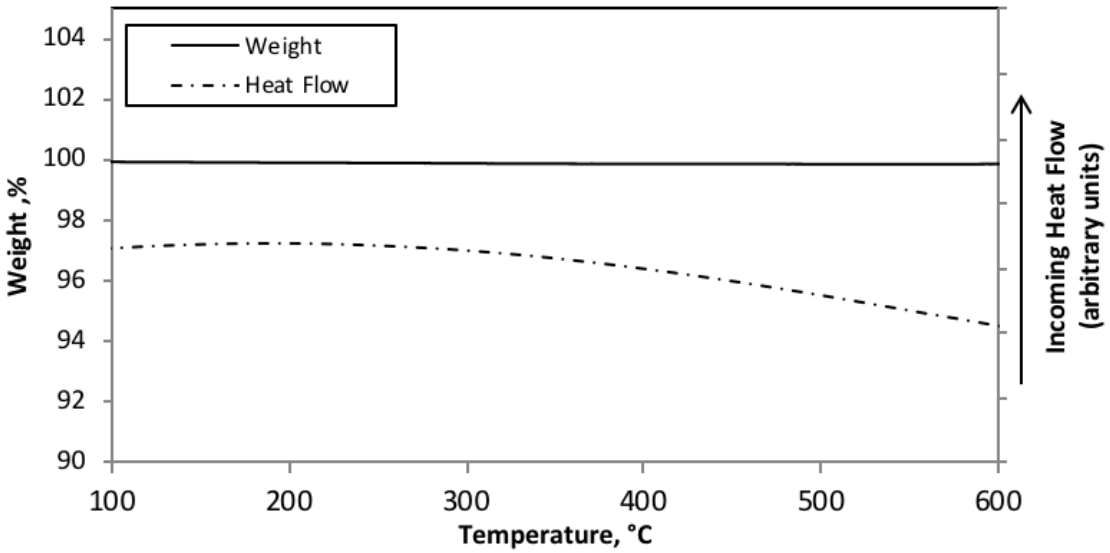

Figure 32 - Heat flow and weight vs temperature obtained by DTA and TGA.

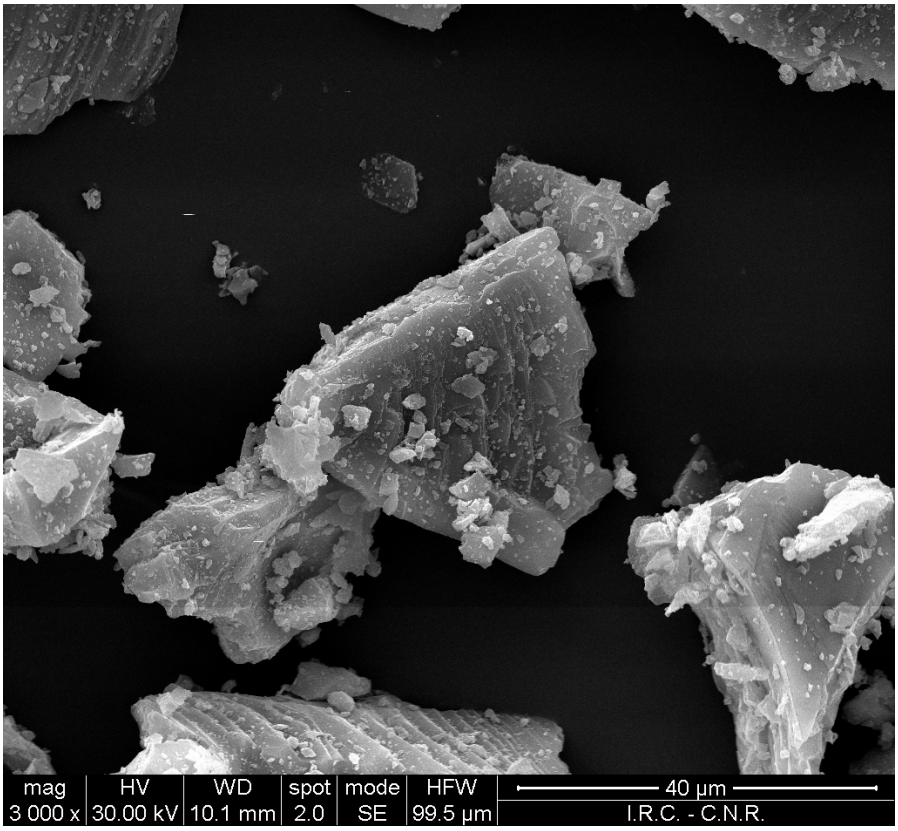

Figure 33 - SEM picture for the A2 sample after exposure to 500°C.

4.2 Reacted material

Two batches of approximately 500 g were taken during the reactive production process in the fluidized bed reactor of the company. During the reactive process the particles accumulate increasing amounts of impurities. These impurities were then characterized using different techniques.

4.2.1 PSD analysis

The samples have the same kind of mother particles with different particle size ranges and different amounts of impurities. The first sample ("S1") and the second sample ("S2") contain an intermediate and a high level of impurities, respectively. Unfortunately, other details of the material cannot be provided for confidentiality reasons. PSD results are reported in Figure 34 and Figure 35 and previously in Table 2. The amount of fine fractions decreases with the increase in impurities concentration, from 70% to 51%, and they are characterized by a very wide PSD (σ/d_{50} changes from 1.1 to 0.67). Both materials belong to the Group A of the Geldart classification for fluidization behaviour.

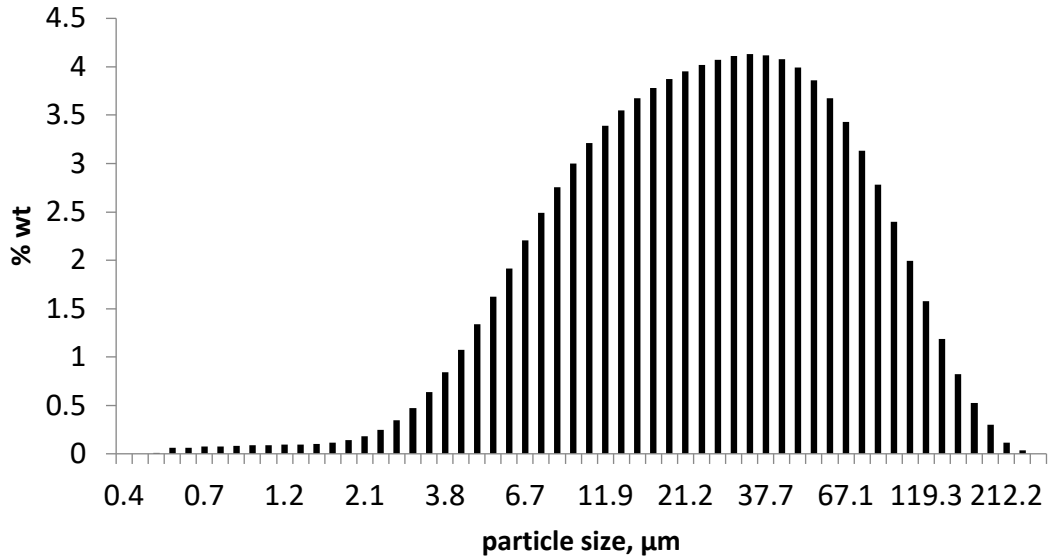

Figure 34 - Particle size distributions of powder sample "S1".

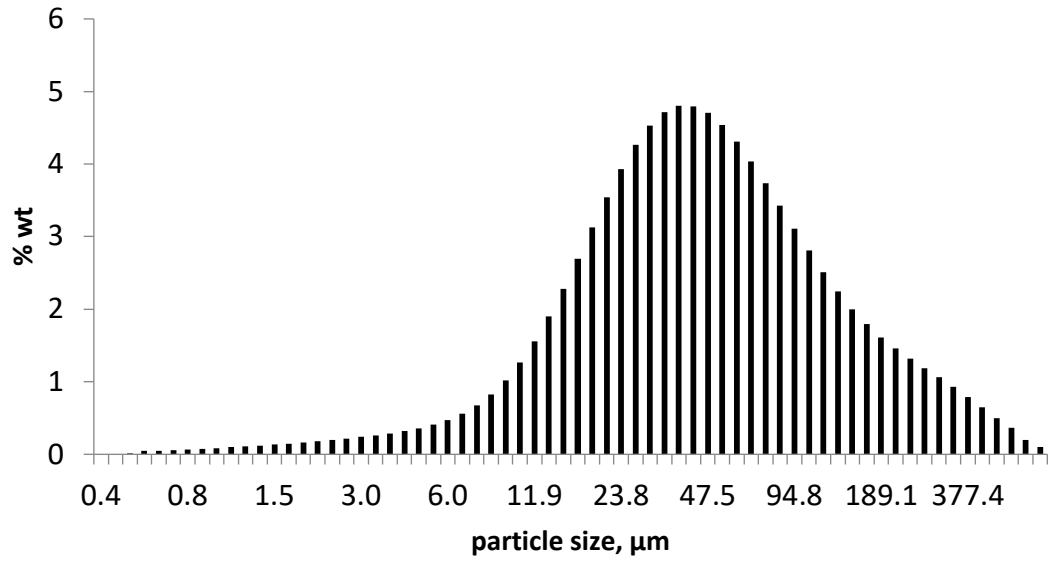

Figure 35 - Particle size distributions of powder sample "S2".

4.2.2 SEM/EDX analysis

Figure 36 reports the SEM images obtained on the different reacted samples. Both samples show comparable aspects such as large amounts of fines adhering on the surface of larger particles, irregularly shaped particles with flat surfaces and relatively sharp edges. Moreover, the specimen S2, richer in impurities, exhibits a great number of sticking particles, which seem to be partially sintered on the larger particles.

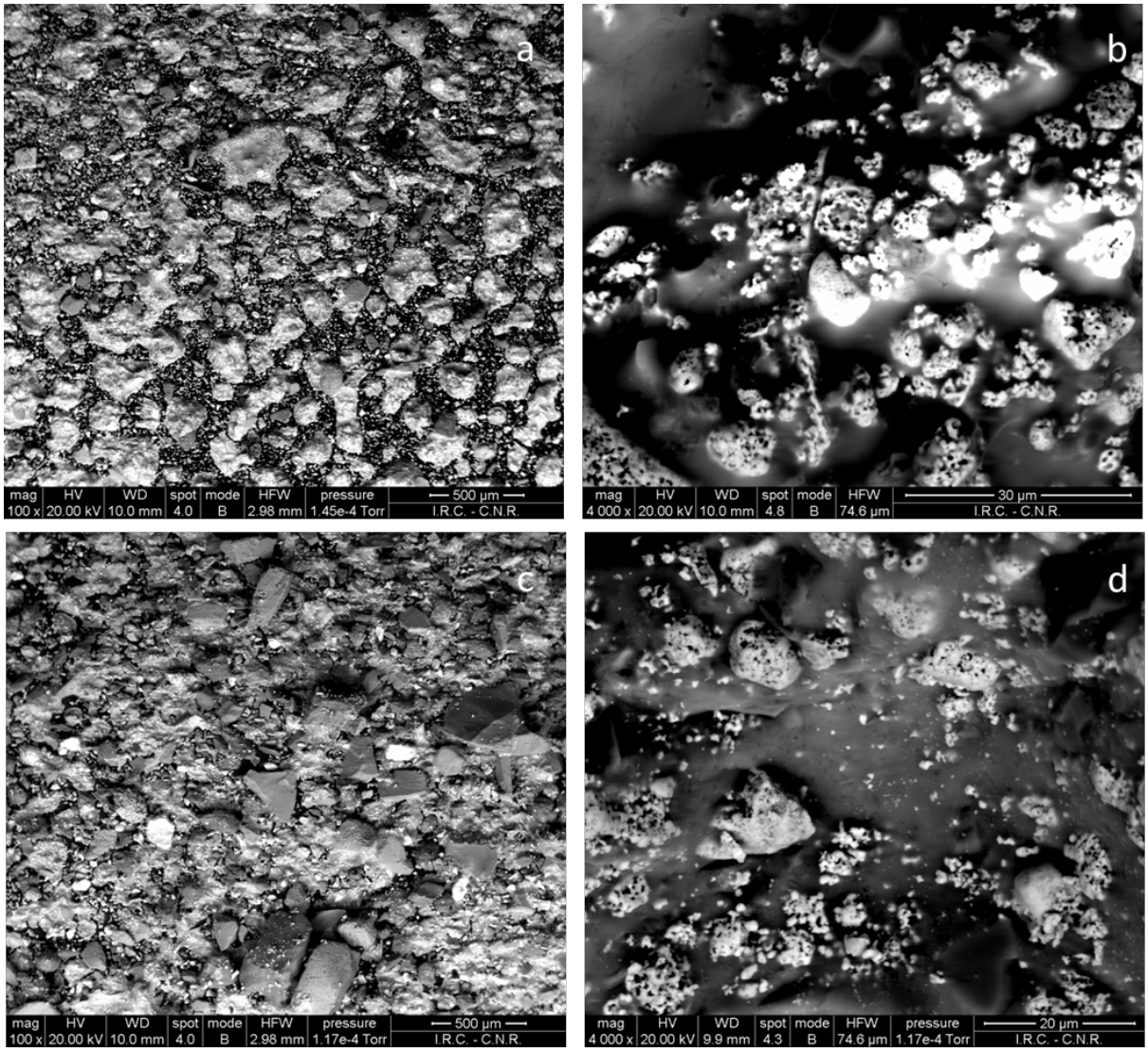

Figure 36 - SEM pictures for the reacted materials: sample "S1" (a, b) and sample "S2" (c, d).

Unfortunately, the results of the EDX analysis and more specific details of EDX spectrum cannot be provided for confidentiality reasons. Moreover, several impurities were found in the two samples, such as aluminum, chlorine, calcium, iron, magnesium. Among all those the most abundant elements are Al, Cl and Ca. Based on the process characteristics, it is assumed that the three are present in form of aluminum chloride ($AlCl_3$) and calcium chloride ($CaCl_2$). Moreover, impurities in Figure 36 appear as a separate solid phase on the particle surface. As a result, the melting temperature of the impurities should not be affected by their amount in respect to the mother ceramic powders. Details on the composition of the impurities are provided and discussed in the Model Results, section 5.6.1 below.

4.2.3 Thermal analyses

The thermal behavior of the two samples is similar, thus in Figure 37 are reported the heat flow and weight of the sample as function of temperature for only one sample S1. In particular, it can be observed that it is not possible to detect any significant phase change, either melting or solid phase transition, also above 300 °C where the materials tested show the largest effect of temperature in the industrial process. A change of weight is detected around 100 °C and it is possibly related to some condensed moisture evaporation. The constant weight of the sample above 300 °C indicates that chemical reactions (e.g. oxidation) can be excluded in that range.

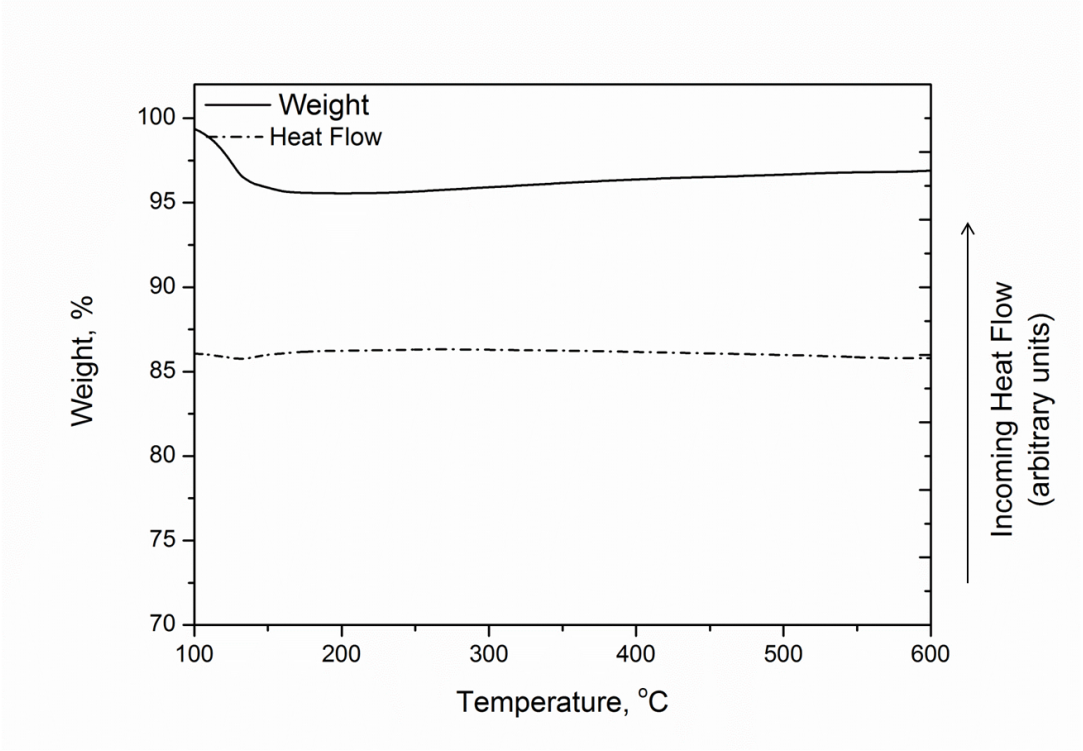

Figure 37 - Heat flow from DTA and sample weight from TGA plotted as a function of temperature: Sample "S1".

5 Shear testing results

Previous chapters have outlined the importance of understanding the influence of temperature on the fluidization behaviour of solid particles, given the importance of its applications in various industrial processes operated at high temperatures. However, findings are still questionable and an adequate understanding of the phenomena that control changes in flow behaviour between ambient and high temperature has not yet been fully achieved. Many questions arise from the relative importance and role of interparticle forces (IPFs) and hydrodynamic forces (HDFs) on the flow behaviour. Moreover, the interpretations of the experimental results are challenging, mainly because the complexities to recognise and quantify the nature of the IPFs involved in each case. Within this framework, powder rheology represents an appealing tool to evaluate indirectly the effects of the interparticles forces on fluidization.

This chapter reports on the experimental results of rheological tests performed on all the samples tested. Firstly, the effect of particle size distribution, temperature and amount of impurities on the flow properties of the material has been studied. Subsequently, the experimental results have been critically analyzed in order quantify the interparticle forces active on the systems.

Powder flow properties were measured using a single specimen for the calculation of four yield loci, which refer to four different loads of consolidation, in order to obtain four points of the flow function. Furthermore, each test was repeated four times. Four shear points were used to derive each yield locus. Yield Loci were measured at 20 °C and 500 °C for each sample. In order to increase the relevance to fluidized bed conditions, shear tests were carried out at low consolidation level for major principal stress σ_1 from about 1000 to 1700 Pa. These values represent the very limit operative value of the modified Schulze shear cell. By using smaller values, unquantified mistakes can occur.

5.1 The effect of particle size on the Yield Loci, fresh materials

Following the procedure described in section 3.5, the Yield Loci of all the samples were calculated at ambient temperature for the different samples. Typical shear data obtained

with the Schulze machine are reported in Figure 38. The latter represents a single repetition for the calculation of three Yield Loci and each of them was calculated with four different shearing steps. Black dotted lines represent the series of various pre-shearing and shearing steps at different consolidation levels. Before starting the measurements, the consolidation stage was repeated two or three times in order to achieve a constant value of the measured shear stress. The shear stress profile and the displacement of the sample calculated during the test are reported with solid black and blue lines, respectively.

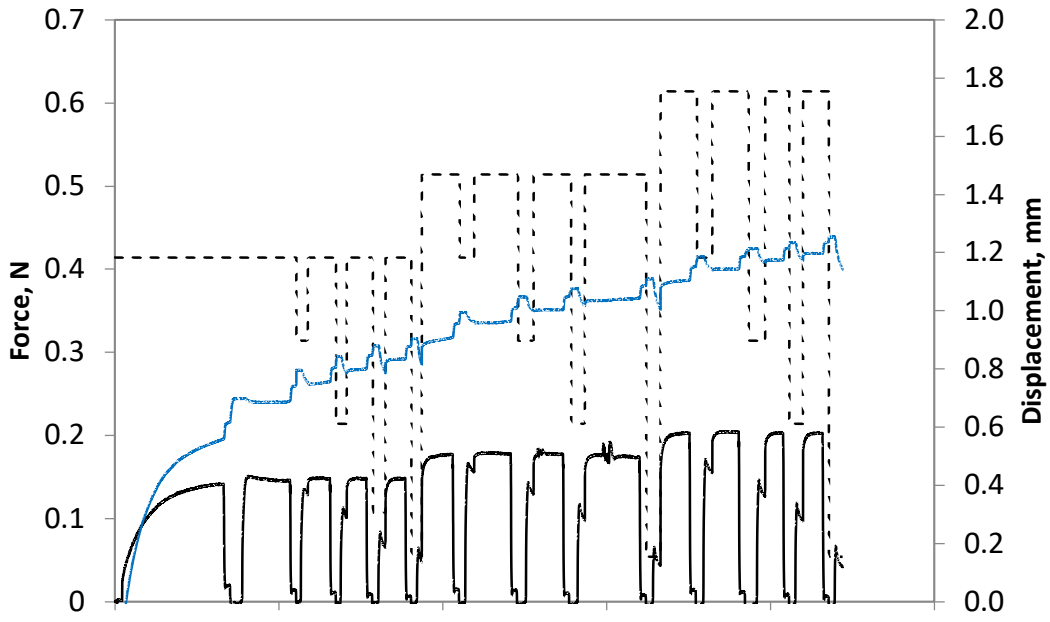

Figure 38 - Shear stress (black line) as a function of pre-shear load (dotted line) and of the displacement of the lid (blue line).

In the pre-shearing steps, an average value of the shear stress is taken, differently in the shearing the maximum shear value is needed, together with the values of the displacement. All these data were used to calculate the yield loci and the bulk density with RSV95 program developed by Schulze. The series of pre-shearing and shearing used in this work are reported in Table 4. In particular, the tests were carried for major principal stress, σ_1, in the range 1000–1700 Pa. Such low normal stress values were adopted in order to approach a consolidation state relevant to fluidised powders

Table 4 - Pre-shearing and shearing load for the experimental test.

Pre-shearing load, g	Shearing load, g				
414	314	214	107	0.054	black
514	414	314	214	0.054	red
614	414	314	214	0.054	blue
714	514	414	214	107	violet

The Yield Loci obtained from shear tests are reported in Figure 39-Figure 43. In all of the plots, different colour lines identify the yield locus at specific consolidation value as reported in Table 4. The numerical results of the shear experiments at ambient temperature in terms of major principle stress (σ_1), unconfined yield strength (f_c), cohesion (C), angle of internal friction (φ_i) and the flow factor (ff_c) are listed in Table 5.

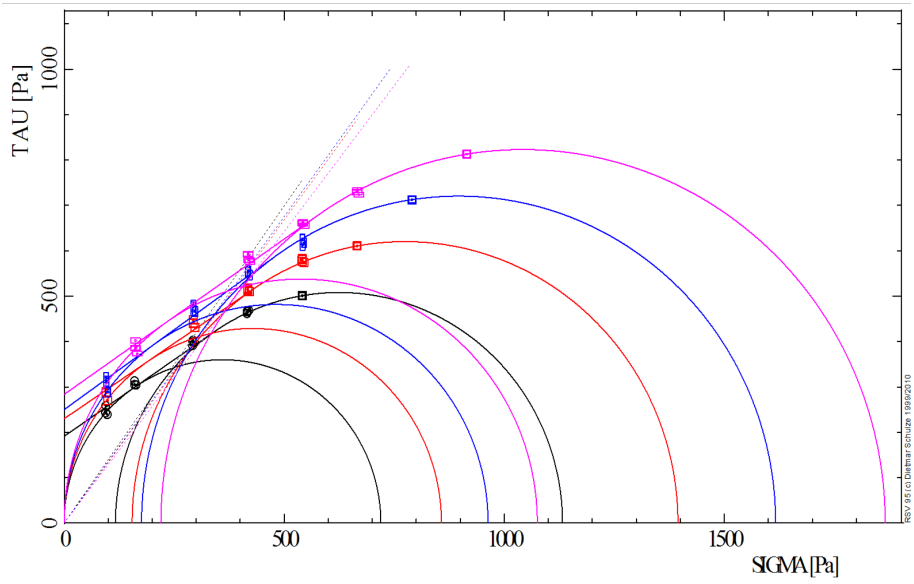

Figure 39 - Yield Loci at ambient temperature for sample A1 (Group C of Geldart classification).

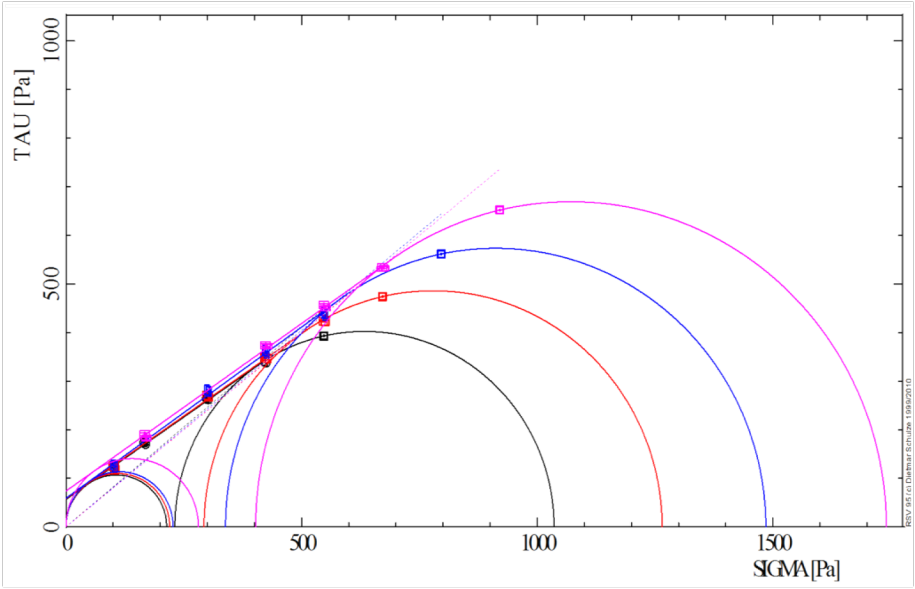

Figure 40 - Yield Loci at ambient temperature for sample A2 (Group A/C of Geldart classification).

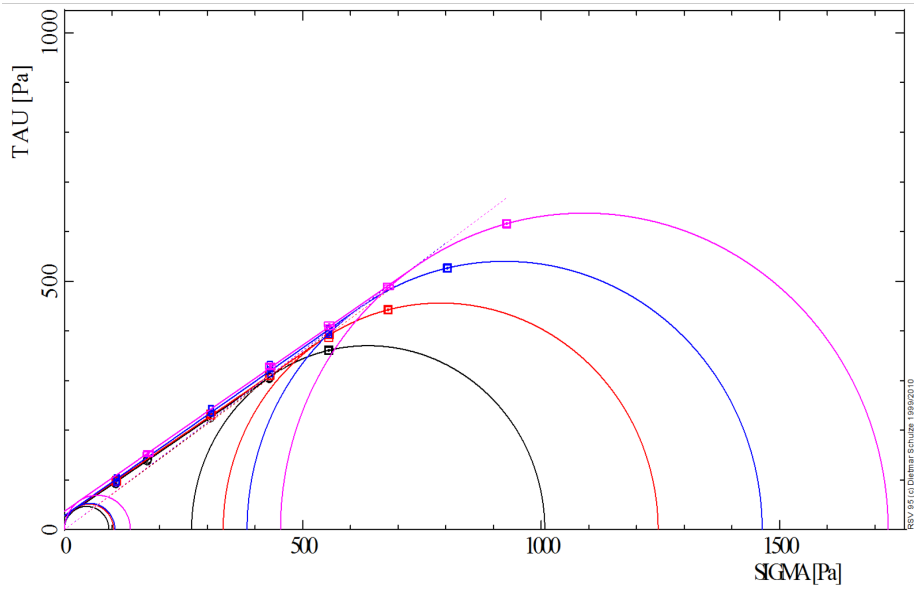

Figure 41 - Yield Loci at ambient temperature for sample A3 (Group A of Geldart classification).

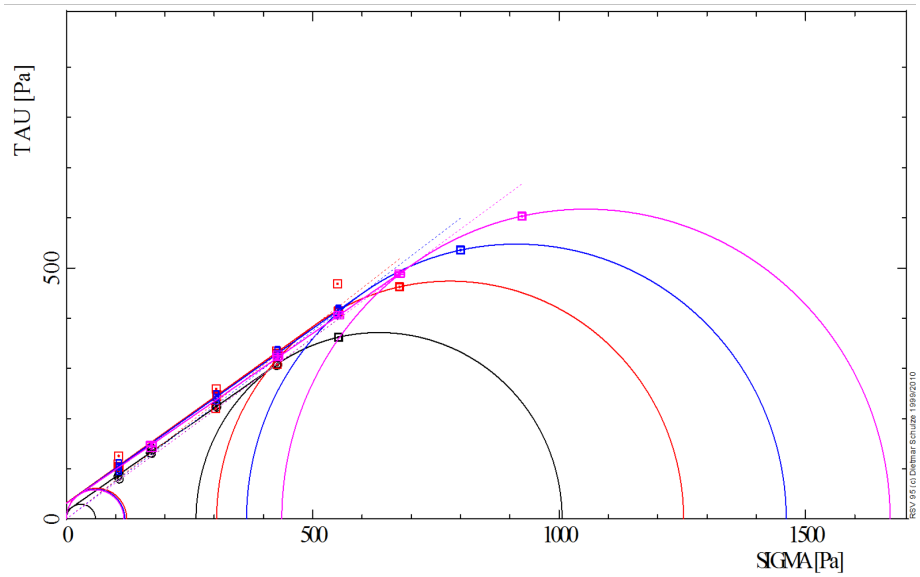

Figure 42 - Yield Loci at ambient temperature for sample A4 (Group A/B of Geldart classification).

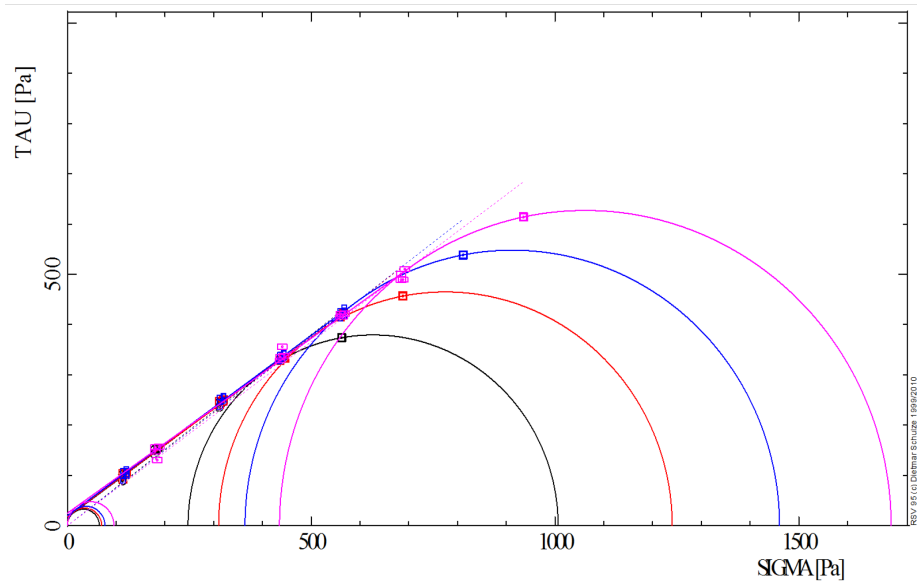

Figure 43 - Yield Loci at ambient temperature for sample A5 (Group B of Geldart classification).

Table 5 - Results of the shear experiments for the fresh material at ambient condition.

	Geldart	Yield Locus	σ_1, Pa	f_c, Pa	ff_c, -	C, Pa	φ_i, °
A1	C	1	1132	720	1.57	191	34
		2	1395	857	1.63	230	33.6
		3	1617	963	1.68	250	35.2
		4	1866	1075	1.74	283	34.4
A2	A/C	1	1036	214	4.85	57	34.1
		2	1265	220	5.75	58	34.2
		3	1485	227	6.53	59	35.2
		4	1741	281	6.19	74	34.6
A3	A	1	1007	93	10.78	25	33.2
		2	1245	103	12.08	28	33.3
		3	1463	106	13.8	28	34
		4	1728	138	12.48	37	33.8
A4	A/B	1	1006	59	17.06	16	34.4
		2	1279	142	9.02	38	34.1
		3	1461	119	12.32	31	34.9
		4	1672	117	14.34	31	34.1
A5	B	1	1006	66	15.34	17	35.7
		2	1240	70	17.63	18	35.5
		3	1460	77	18.95	20	35.7
		4	1689	96	17.68	25	34.8

The results at ambient condition suggest that the cohesion and the unconfined yield strength increase with decreasing the particle size. A slight change of such parameters with the consolidation levels was detected, as shown in Figure 44 and Figure 45. According to Figure 46, the angle of internal friction seems to be independent from both the particle size and the consolidation load and its value is about 35°.

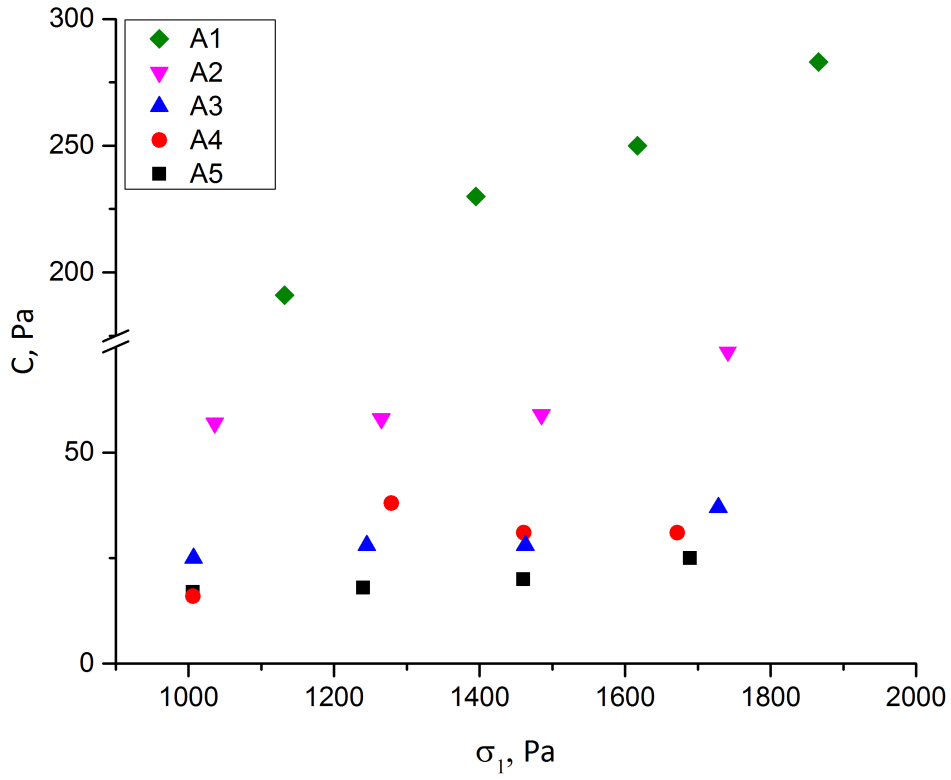

Figure 44 - Cohesion vs major principle stress.

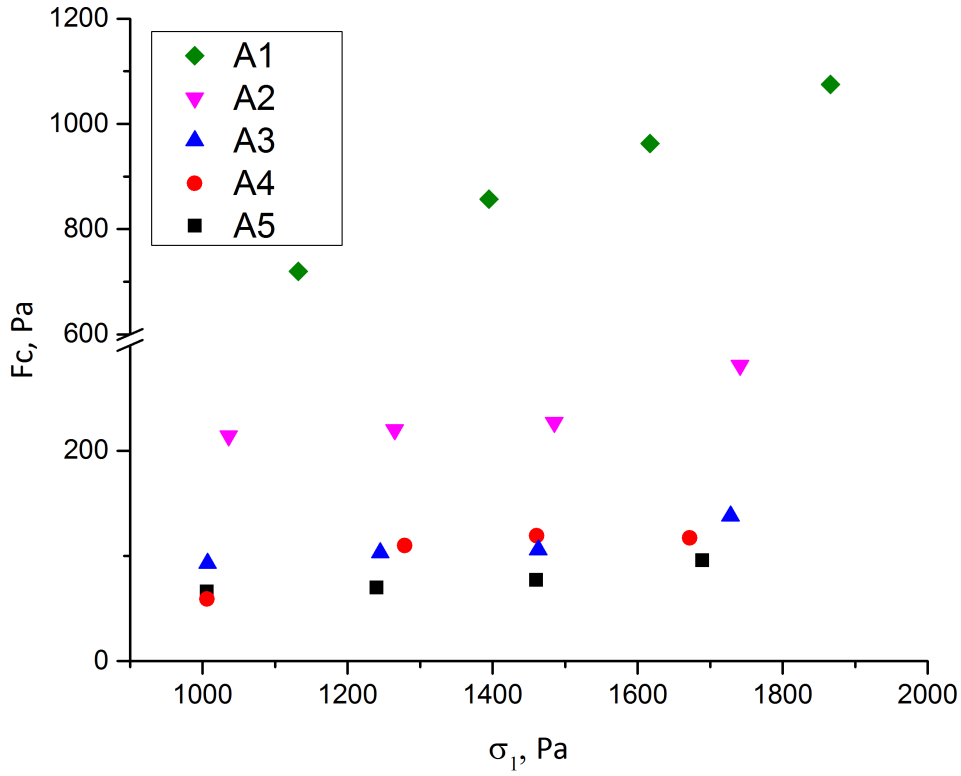

Figure 45 - Unconfined yield strength vs major principle stress.

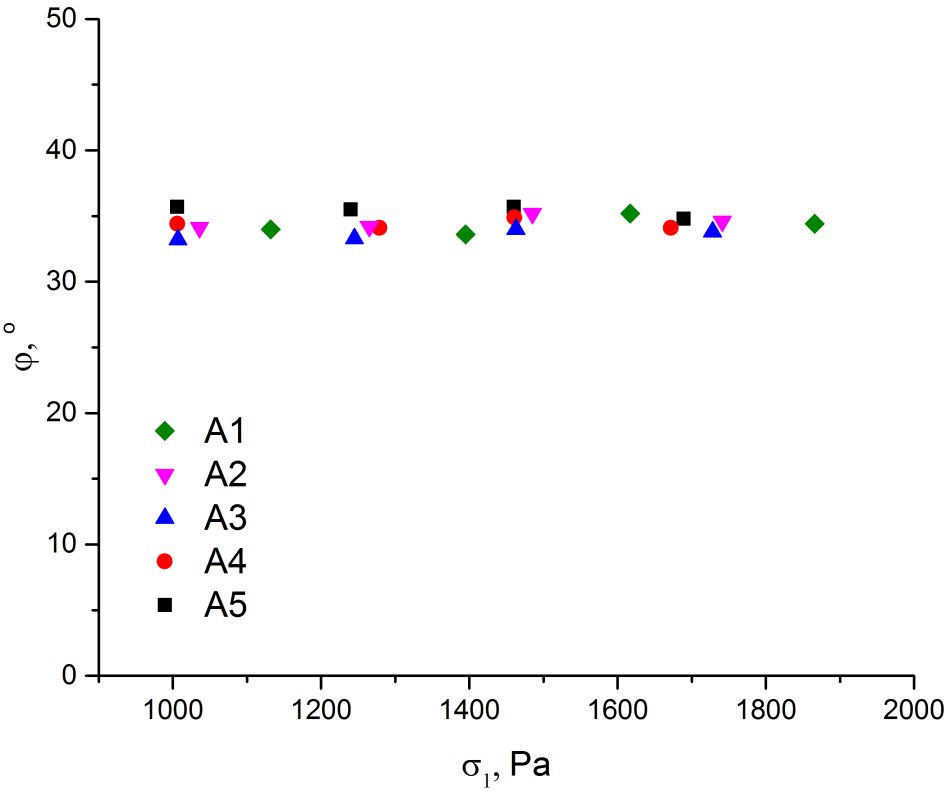

Figure 46 - Angle of internal friction vs major principle stress.

The flow functions (i.e. the unconfined yield strength fc vs the major principal stress σ_1, see section 2.1.6) of the five powder samples at ambient temperature are reported in Figure 47. Inspection of the figure confirms the expected dependence of flowability on the particle size distribution [105]. In particular, according to the Jenike classification of flowability, the finest sample (A1) belongs to the very cohesive class; A2 sample belongs to the easy-flowing class; the flow functions of A3 and A4 samples lay on the border between easy-flowing and free-flowing classes; the coarsest sample (A5) belongs to the free-flowing class.

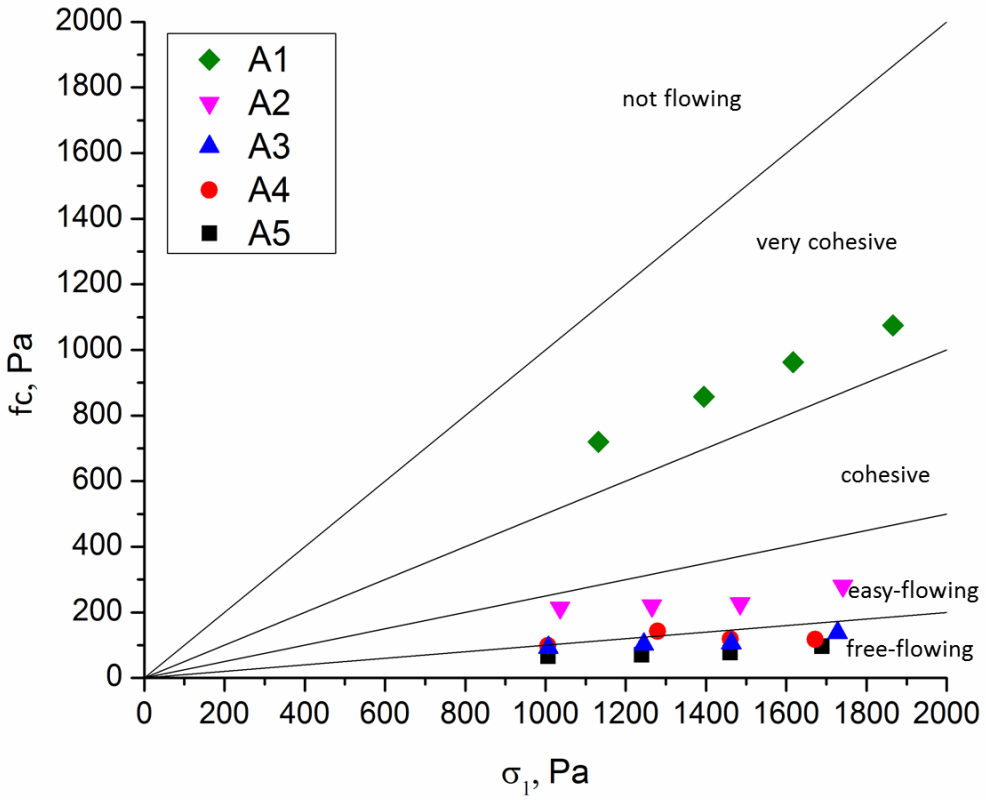

Figure 47 - Flow functions of all fresh samples measured with the HT-ASC at 20 °C.

5.2 The effect of temperature on the flow properties

In order to address the role of temperature on the flow properties of the fresh material the shear tests were performed at ambient and at 500 °C. The Yield Loci calculated from the experimental shear data at 500 °C for each sample tested can be found in the Appendix A3.

Figure 48 and Figure 49 report the yield loci of the A5 sample tested at 25 °C and at 500 °C for $\sigma_1 \approx 1000$ Pa (Figure 48) and $\sigma_1 \approx 1700$ Pa (Figure 49), as an example of the results obtained for all the samples. Dotted lines passing through the origin and tangent to the consolidation Mohr circle, define with their slope the effective angle of internal friction, used in many design procedures. More specific details on yield loci and their derived powder flow properties are available elsewhere [136,161]. It must be stressed that the yield loci estimate in Figures were obtained combining the shear data coming from all the 4 independent repetitions of the test. From the yield locus graph, it is possible to determine

the static angle of internal friction as the slope of the linear yield locus and the cohesion as the intercept of the yield locus with the shear stress axis. Comparing the yield loci, there is a noticeable increase of the cohesion with both consolidation and temperature. Differently, the static angle of internal friction, φ_i, is independent of the consolidation and of the temperature. As a result, the increase of the unconfined yield strength, f_c, is mainly related to the cohesion. All the numerical values of the major principal stress (σ_1), unconfined yield strength (f_c), flow factor (ff_c), cohesion (C) and angle of internal friction are reported in Table 6.

Table 6 - Results of the shear tests performed on the fresh samples with HT-ASC.

	T, °C	σ_1, Pa	f_c, Pa	ff_c, -	C, Pa	P_b, kg/m^3	φ_i, °
A1	25	1132	720	1.57	191	698	34.0
	25	1395	857	1.63	230	719	33.6
	25	1617	963	1.68	250	737	35.2
	25	1866	1075	1.74	283	752	34.4
	500	1141	807	1.41	211	608	34.8
	500	1391	895	1.55	225	629	36.7
	500	1619	979	1.65	238	646	38.1
	500	1873	1109	1.69	284	658	35.8
A2	25	1036	214	4.85	57	855	34.1
	25	1265	220	5.75	58	869	34.2
	25	1485	227	6.53	59	882	35.2
	25	1741	281	6.19	74	894	34.6
	500	1040	338	3.07	90	782	33.9
	500	1265	370	3.42	99	799	33.5
	500	1495	414	3.61	113	797	32.7
	500	1729	413	4.18	112	805	33.2
A3	25	1007	93	10.78	25	1027	33.2
	25	1245	103	12.08	28	1044	33.3
	25	1463	106	13.8	28	1056	34.0
	25	1728	138	12.48	37	1067	33.8
	500	1056	186	5.02	47	990	37.4
	500	1305	210	5.37	58	997	35.5
	500	1538	220	6.26	57	999	36.4
	500	1843	240	6.57	67	1003	35.9
A4	25	1006	98	17.06	29	981	34.4
	25	1279	142	9.02	38	976	34.1
	25	1461	119	12.32	31	971	34.9
	25	1672	117	14.34	31	987	34.1
	500	1009	177	5.71	47	965	33.7
	500	1238	168	7.35	45	924	33.3
	500	1421	161	8.82	43	930	33.7
	500	1653	175	9.43	47	1011	33.6
A5	25	1006	66	15.34	17	1243	35.7
	25	1240	70	17.63	18	1283	35.5
	25	1460	77	18.95	20	1279	35.7
	25	1689	96	17.68	25	1269	34.8
	500	1003	120	8.37	31	1159	35.7
	500	1238	128	9.71	33	1167	35.6
	500	1467	152	9.68	39	1186	35.5
	500	1697	182	9.3	47	1181	35.8

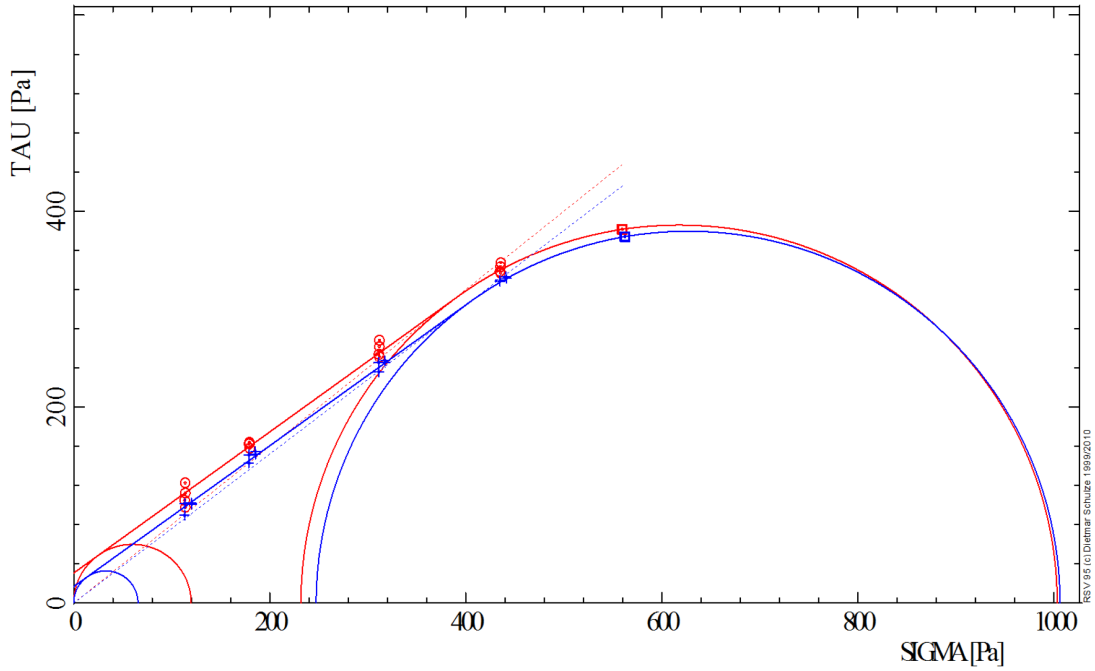

Figure 48 - Yield Loci for the A5 sample measured with the HT- ASC at 25 °C (blue line) and 500 °C (red line), at lowest consolidation load (σ_1≈1000 Pa).

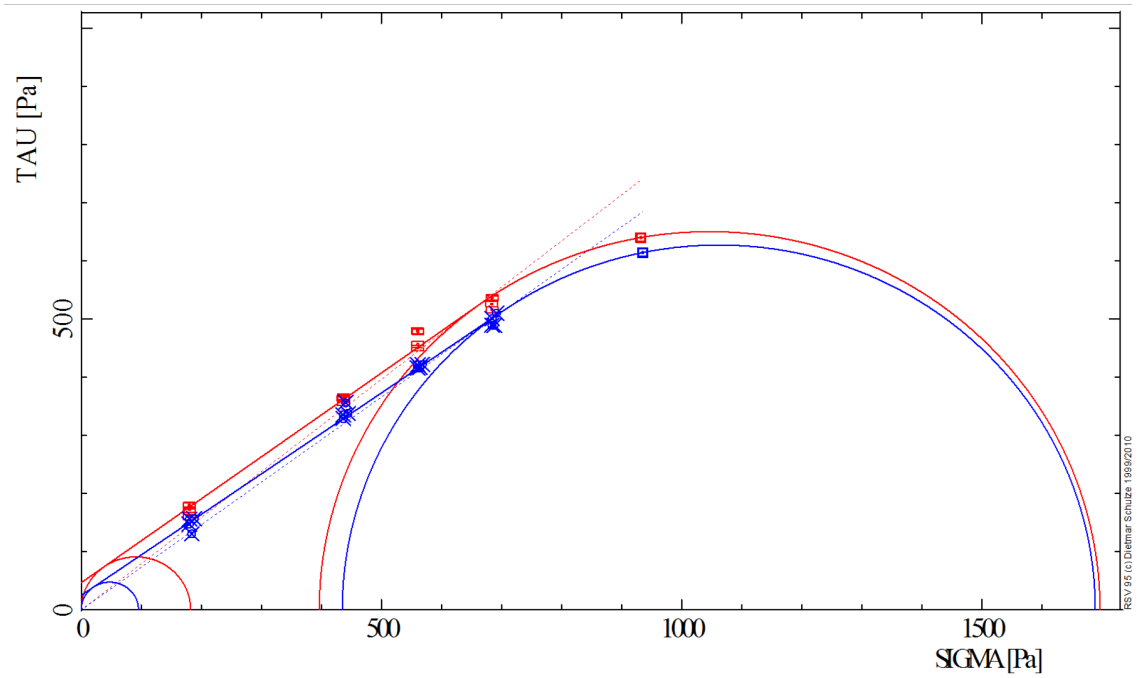

Figure 49 - Yield Loci for the A5 sample measured with the HT- ASC at 25°C (blue line) and 500 °C (red line), at highest consolidation load (σ_1≈1700 Pa).

The effect of temperature on the angle of internal friction Figure 50 reports the angle of internal friction vs the consolidation level as a function of temperature for all the fresh samples. The angle of internal friction is independent from both consolidation and temperature with an almost constant value of 34-37° for all the samples. A common feature of this material is the rather little effect of consolidation on the unconfined yield strength. This is typical for incompressible powders such as these used for our experiments. Powder incompressibility is likely to be a consequence of the narrow size distribution which does not allow a significant particle spatial reorganization, bringing a change in the number of particle contact points. This change can be experienced in powders with a broad particle size distribution, but in powders made of narrowly sized and relatively coarse particles, consolidation can only change cohesion by changing the intensity of the interparticle contact forces. A very slight increase of the angle of internal friction was observed for the finest sample, A1, with both temperature and consolidation (Figure 50_A2 and A3).

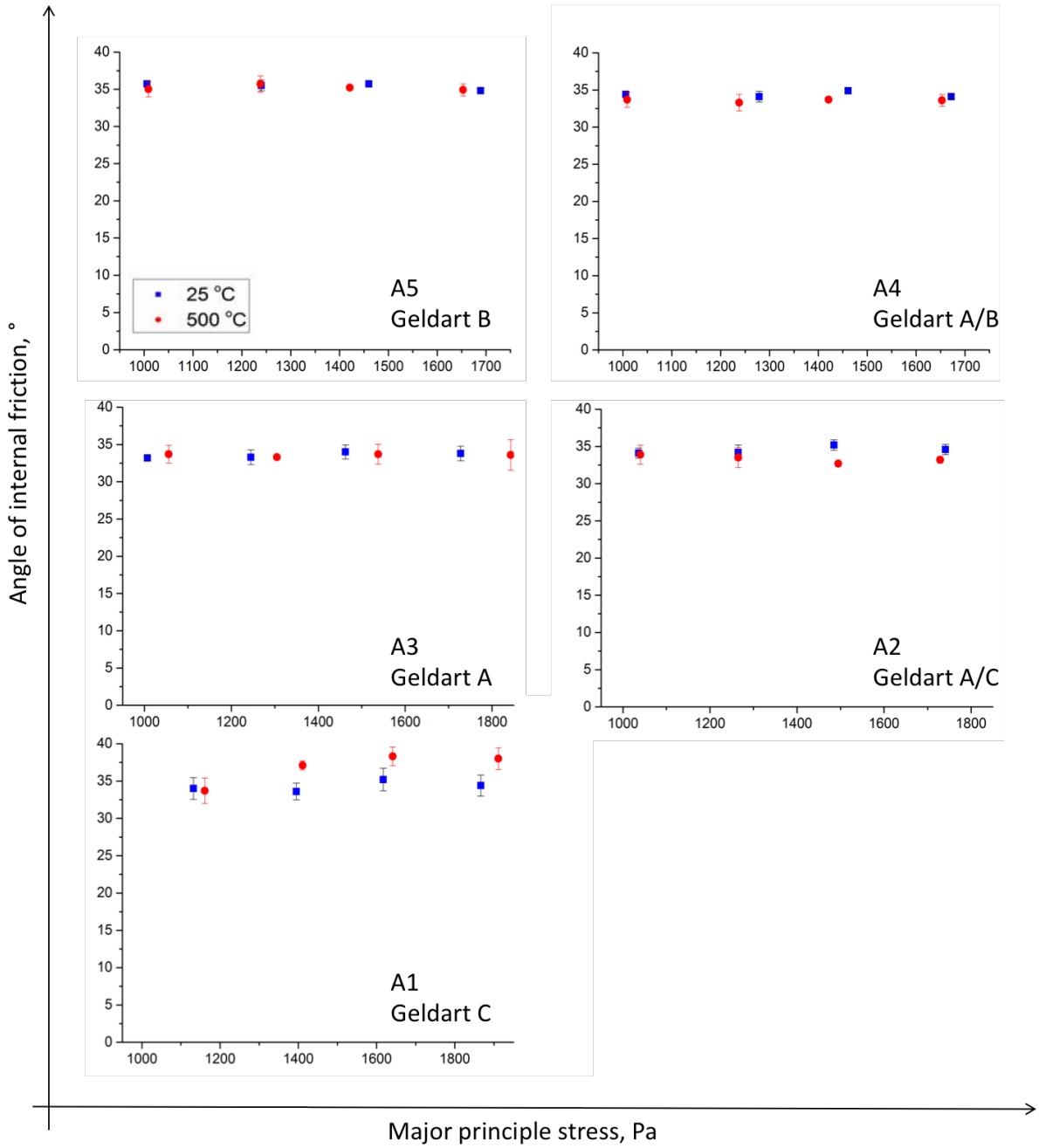

Figure 50 - Angle of internal friction vs consolidation load fresh samples at 25 °C and 500 °C.

5.2.1 The effect of temperature on the cohesion

The effect of temperature and consolidation on the cohesion is shown in Figure 51. The cohesion weakly depends on consolidation level for samples A5 and A4; a larger dependency can be observed for the other samples, A3, A2 and A1. On the other hand, the increase of temperature results into an increase of cohesion of about 60 to 80% for all the

tested samples except for the finest one, A1. In this case, the cohesion remains almost constant when increasing temperature.

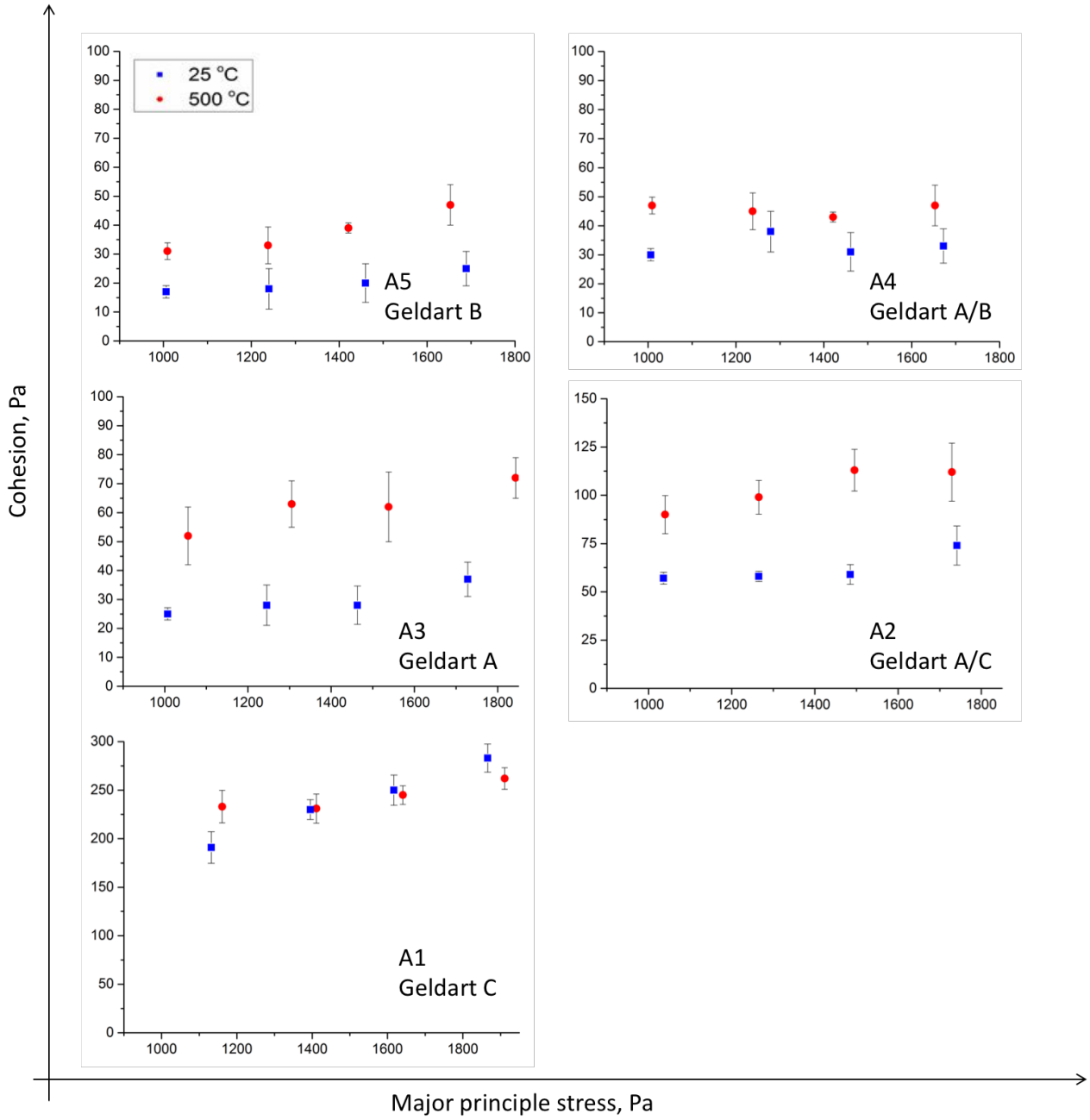

Figure 51 - Cohesion vs consolidation load fresh samples at 25 °C and 500 °C.

5.2.2 The effect of temperature on the unconfined yield strength

The increase of the unconfined yield strength, shown in Figure 52, with consolidation and temperature is mainly due to the increase of cohesion since the angle of internal friction has a weak dependency on the temperature.

The increase of cohesion with temperature results in an upward shift of the flow function, σ_1/σ_c, which moves from the free-flowing class to the easy-flowing class for sample A5, A4 and A3 and from easy-flowing class to cohesive class of the Jenike classification for sample A2 (Figure 52). The flow faction of sample A1 seems not to be affected by temperature. According to the flow Function diagram (Figure 52), the powder behaviour is that of a very cohesive powder at both room and high temperature.

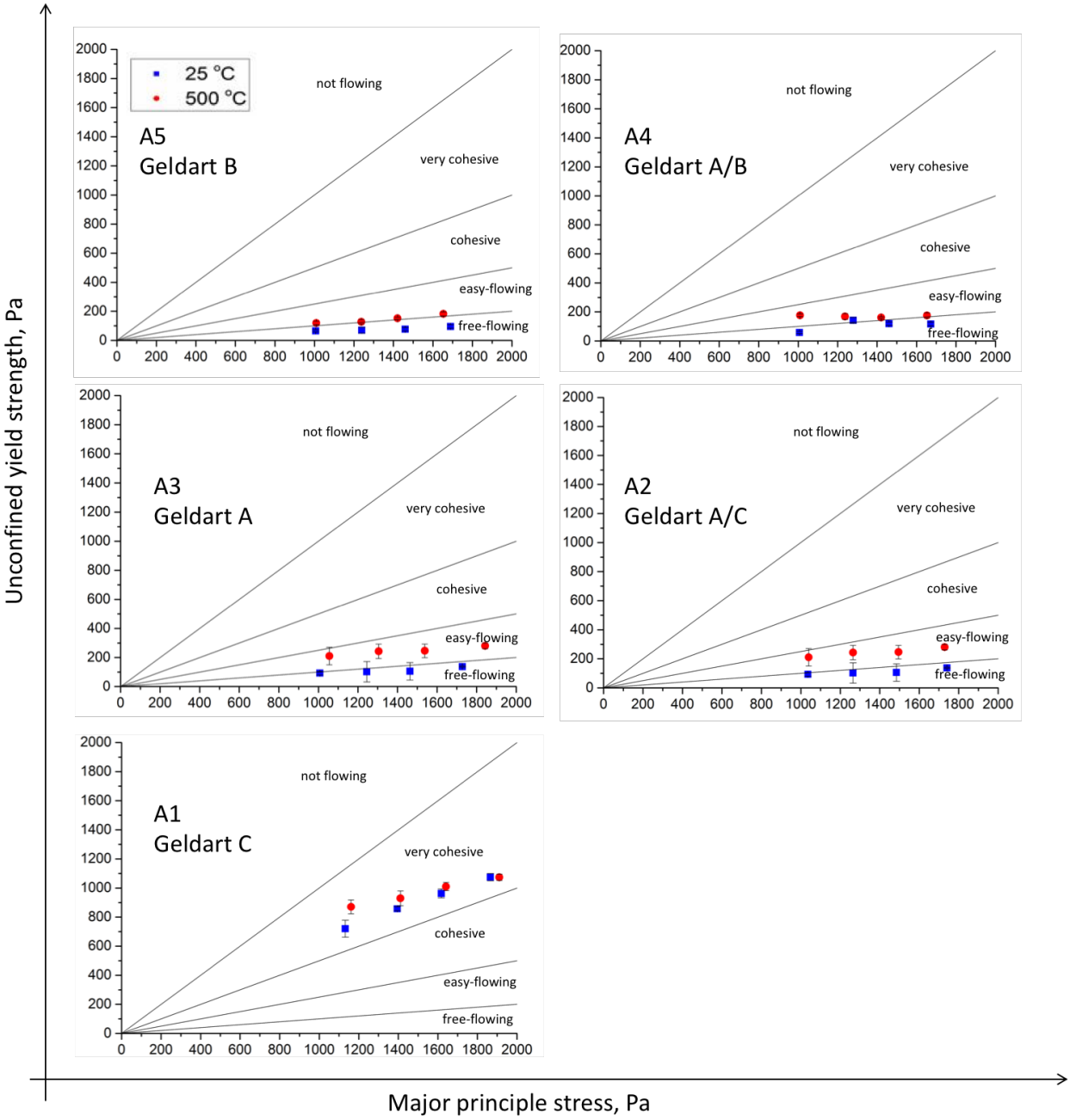

Figure 52 - Unconfined yield strength vs consolidation load fresh samples at 25 °C and 500 °C.

5.3 Rumpf and Molerus model

In order to correlate bulk flow properties to interparticle interactions at ambient and high temperature a model based on the microscale approach provided by Rumpf [154] and by Molerus [23] can be used. Such model is based on the possibility to relate consolidation and non-rapid flow of particulate solids with adhesion forces in particles contacts.

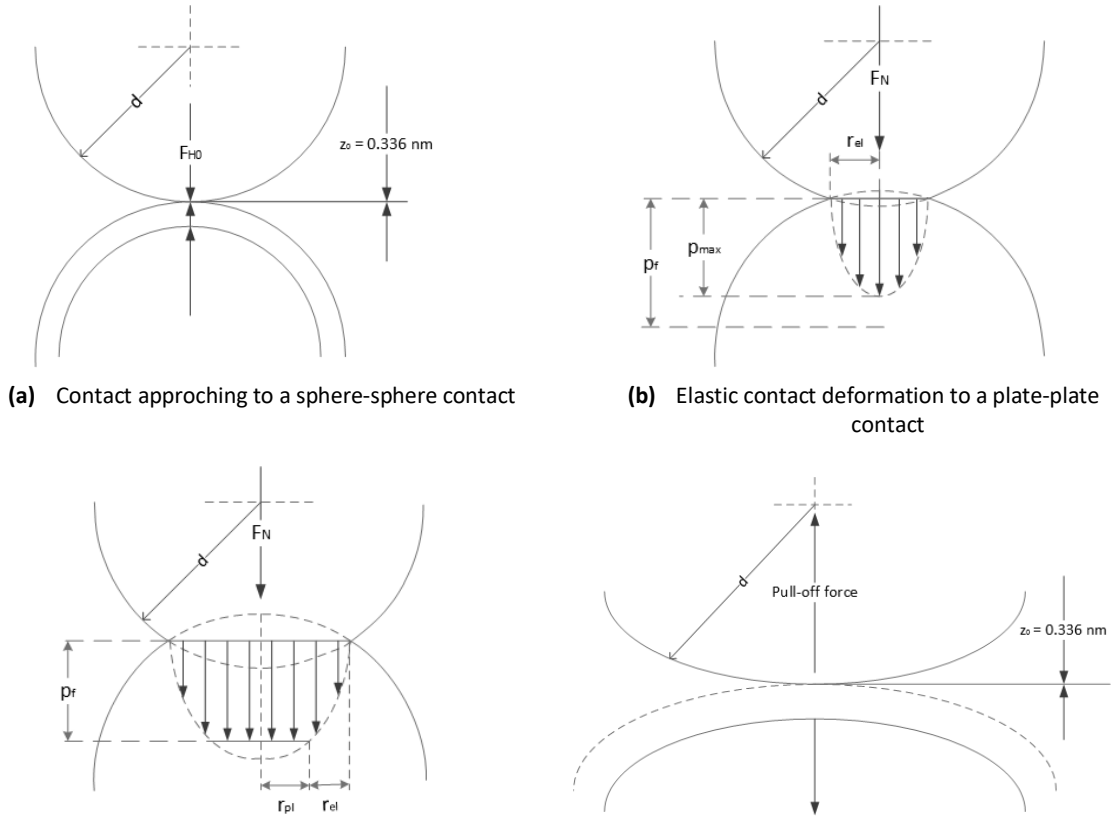

(a) Contact approching to a sphere-sphere contact

(b) Elastic contact deformation to a plate-plate contact

(c) Elastic-Plastic contact deformation to a plate-plate contact

(d) Plate-plate contact removing

Figure 53 - Particle contact approaching, deformations and removing.

It is important to consider which kind of mechanical deformation occurs when an external compressive normal force F_N is acting on particles that are very close to each other. In particular, according to Tomas [125,126,162,163] there are four different kinds of mechanical interaction in particle surface contacts, and their physical behavior can be identified as follows:

1. Reversible elastic, in which deformation rate and consolidation do not bear time effects; these are generally valid for all particulate solids at least in a limited portion of the interparticle approach;

2. Irreversible plastic, in which deformation rate and consolidation are time invariant; these are typical for mineral powders;
3. Reversible viscoelastic, in which deformation rate and consolidation change with time; these are distinctive for cut post-consumer waste particles;
4. Irreversible viscoplastic, in which deformation rate and consolidation change with time variable; these apply to fine particle fusion.

In this work, the hypothesis of plastic deformation was assumed according to the results obtained by Tomasetta et al. [149]. That study, in fact, indicated that the assumption of plastic deformation provides the correct order of magnitude values of tensile strength and its dependence on consolidation.

The main underlying assumptions of the Rumpf [154] and Molerus [23] approaches are:

1. Particles are organized in a randomly packed assembly.
2. Particles are spherical and monodisperse.
3. The contact areas between particles are small enough in comparison with the particle surface and therefore contact areas can be assumed as contact points.
4. The contact points are distributed over the particle spherical surface with equal probability.
5. The packing structure is isotropic.
6. The transmission of an isostatic state of compressive stress with three equal principal stresses is assumed.
7. The coordination number (i.e., the mean number of contacts of a particle with the adjacent neighbors), k, and assembly porosity, ε, follow the correlation $k\varepsilon \approx 3.1 \approx \pi$ [20,135].
8. The particle Sauter mean diameter, d_{sv}, is used as the representative particle size.

Van der Waals' forces F_{vdW} are the only interparticle forces assumed following the results of the particle thermal analysis.

Starting from these hypotheses, Rumpf and Molerus derived the following equation relating the isostatic stress with the contact forces, F_c, for monodisperse particles with a characteristic diameter, d, and bed porosity, ε:

$$\sigma = \frac{F_c}{d^2}\frac{1-\varepsilon}{\varepsilon} \qquad \text{Eq. 36}$$

EquationEq. 36 is very simple but rather comprehensive in considering the reasons behind the strength of a powder. This latter, in fact, is mainly given by two factors, 1) the strength of the interparticle contacts and 2) the "intensity" of the fabric of inter-particle contacts. In simpler words, the intensity of the fabric is the number of binary interparticle contacts per unit surface area. Eq. 36 consider two contributions to this number, one is the particle size, the smaller the particles the larger the number of contacts per unit surface, the other is the system voidage. In fact, decreasing the voidage increases this number.

Strictly speaking Eq. 36 was derived for spherical particles. The sphericity of the particles allowed to easily bring in the derivation simplifications due to particle symmetry. However, the results of such consideration may hold also for non-perfectly spherical particles randomly oriented since in that case forces can be in average be similarly balanced over a group of particles. Also, the coordination number assumed between particles in deriving Eq. 36 is considered approximately to be equal to π/ε. Such number is near to 6-8 and reasonably it cannot be so different even for non-spherical particles, provided that they are isometric, that is they do not show 1 or 2 prevailing dimensions.

Considering conditions where electrostatic and capillary forces do not occur and van der Waals forces play a dominant role, Eq. 36 can be used to link the tensile strength, σ_t, with a mean isotropic contact force, F_{vdW}:

$$\sigma_t = \frac{F_{vdW}}{d_{sv}^2}\frac{1-\varepsilon}{\varepsilon} \qquad \text{Eq. 37}$$

where d_{sv} is the particle Sauter mean diameter. This gives the best estimate diameter of a sphere that has the same volume/surface of the powder. This diameter is most sensitive to the presence of fine particles and provides the most accurate volume concentration of interparticle contact points that represents a fundamental variable.

In principle, due to the experimental conditions, in which the samples were handled and prepared under dry nitrogen environment, capillary forces can be excluded. Also, in principle, instead, it is not possible to exclude the formation of electrostatic forces in the tested systems. The fact that both in shear test experiments and in fluidization experiments the vessel wall were made in metal and were electrically grounded should minimize the possibility of build-up of charges in the particulate material. Furthermore, the experiments did not provide evidence of the onset of significant electrostatic forces, and also, the intensity of the forces suggests that the only interparticle forces acting in the system were van der Waals forces. Therefore, in the following the assumption will be maintained that van der Waals forces are the only kind of forces present in the proposed experiments, when capillary forces can be excluded.

According to Eq. 37, the isostatic tensile strength σ_t of a bulk solid sample, extrapolated from the powder experimental yield locus, is the tensile stress corresponding to the contact separation force equal to the attractive interparticle force at the contact point F_{vdW}.

Eq. 37 was used to relate the tensile strength extrapolated from the powder yield locus to the binary interparticle forces. Assuming a plastic irreversible deformation at contact points, Molerus developed an equation for the adhesion van der Waals force at consolidated contacts:

$$F_{int} = F_{vdW} = \frac{A^* r}{12 z_0^2} \frac{1+\left(2F_N/\pi p_f r z_0\right)}{1-\left(A^*/6\pi p_f z_0^3\right)} \qquad \text{Eq. 38}$$

where A^* is the Hamaker constant, r is the mean curvature radius at contact points (which is not necessarily related to the particle size because of the local curvature due to the asperities of the particle surface and it would correspond to the radius of the particles only in case of two interacting spheres with the same size), and z_0 is the separation distance that is usually taken as z_0=0.4 nm in air [20]. F_N is the compressive force transmitted at the contact during consolidation and p_f is the plastic compressive yield strength of the particle material at the contact point. Therefore, the combination of Eq. 37 and Eq. 38 provides with an estimate of the tensile strength, given the parameters A^*, r and z_0. According to

Eq. 38, the magnitude of the van der Waals interparticle force is affected by a factor accounting for the flattening of the contact point, which is a function of the local normal force F_N. The latter is indirectly related to the external consolidation load at the bulk level. Therefore, these equations can be used to relate the powder tensile strength to powder consolidation. These equations account for powder porosity changes and for changes in the intensity of the binary interparticle interactions.

To calculate the effect of consolidation on the intensity of the binary interaction, the normal contact force F_N that occurs during consolidation must be estimated. Assuming a consolidation stress σ_p, it follows from Eq. 36 that:

$$F_N = \sigma_p d_{sv}^2 \frac{\varepsilon}{1-\varepsilon} \qquad \text{Eq. 39}$$

The assumption of uniform distribution of powder consolidation at contact points could be criticized by arguing that not all of the contact points are equally loaded. According to Tomasetta et al. [164] a non-uniform distribution of consolidation forces at contact points F_N does not introduce variations in the estimates of the tensile strength σ_t with the above-proposed procedure.

Particles within the strong force network are usually correlated in a line–line mode over distances of several particle diameters leading to the so-called “force chains” [165,166]. The results of shear experiments provide an average value of the forces. In previous paragraphs Figure 38 shows the shear profiles coming directly from experimental shear tests. According with the figure the value of the forces is not constant during the time of the measurements. These peaks can be attributed to repeated excitations of the existing force chain. Generally, a force chain consists of a set of particles within a compressed granular material that are held together and jammed into place by a network of mutual compressive forces [167]. Force chains arising from grain-scale interactions may also induce non-local behavior that is largely observed at meso- and macro-scales in number of flow configuration [168]. An improved understanding of force chain dynamics and nonlocal constitutive theories might therefore provide new insight into the multi-scale physics of granular media. Furthermore, mesoscale properties such as effective friction play an

important role in solid-like, fluid-like, and gas-like behavior and transitions at the macro—scale. It must be stressed that the forces estimated with the approach proposed by Rumpf [154] are derived with the assumptions of random powder packings and isostatic states of stress, thus, changes in the local force directions tend to compensate in the average. However, despite the connections between the scales studied in this thesis, the influence of chain forces on the granular material is out the scope of this thesis. However, previous studies suggest force chains are only able to transmit large loads a certain distance into a granular medium before the forces split into different paths and decay, a theory proposed in past work [169,166]. This phenomenon, and other phenomena involving interparticle forces are the subject of ongoing research and should be discussed in more depth in future work.

5.4 An insight in the Rumpf and Molerus assumptions

The continuum approach is often used to describe powder mechanics in order to avoid the excessive complication and often the impossibility of describing the system by following the statics or the dynamics of the many single particles. For many technological applications it is useful, however, to understand and relate the properties of the material approached as a continuum with averaged particle-particle interactions. While it is easy to recognize that assumptions 1, 4 and 5 can be easily verified for fine powders made of sufficiently stiff particles. All the other assumptions deserve a more comprehensive discussion in order to be accepted with some confidence. In our case, the assumption that seems to be most strikingly in contrast with the real particles of the material used is the number 2, regarding the particle shape. In particular, the spherical shape of the particles, together with the isostatic state of stress allow to assume that all forces acting on the particles are normal to the particle surface and directed towards or from the particle center. This condition is likely to be not verified in single cases of non-spherical particles. However, we have to recall that the Rumpf analysis approaches the stress description in terms of averaged interparticle forces. Therefore, it can be easy to recognize that, with random powder packings and isostatic states of stress, changes in the local force directions tend to compensate in the average, in the sense of leaving to a finite average value only the components directed towards the centre of mass of the particle. Similarly, since the

particle size play the most important role in defining the number of interparticle contact points per unit volume, it can be easily acknowledged that violations of assumption 3 can be easily overcome by using the Sauter mean diameter as the average particle size. In fact, the Sauter averaging has the characteristic of keeping the same surface to volume ratio of the distribution and, therefore, also the same number of contact point per unit volume, that coincides also with the average number of interparticle forces contributing to the stress, the resulting force per unit area. Of course, the particle shape can affect also the how the number of contact points change with the porosity. However, it has to be recalled that the number of contact point per particle k, estimated by means of the relation $k\varepsilon=\pi$ [20,135], suggest numbers around 6 and 7 for powder porosities between 0.4 and 0.5. With the random packing of rather isometric particles, that is without any prevailing dimension such as those used in our systems, it is hard to think that deviation of k from π/ε may overcome the value of 1. According to Eq. 36, this would imply <15% error in the force/stress estimation. A fairly reasonable precision within the range of approximation of our calculations. The most complex assumption to discuss is the number 7 (see previous section), that indirectly supports also assumptions 5 and 6. In fact, Molerus [23] suggested that, since any isostatic tensile stress can be considered the combination of three uniaxial state of stress, and since any state of stress can be represented by three uniaxial state of stresses, then Eq. 36 can be applied to any state of stress. We suspect a flaw in this reasoning due to the fact that the first condition is necessary but not sufficient and, therefore, cannot be used as an equivalence, as the unflawed reasoning would require. In spite of that, we believe that Eq. 36 is still able to provide reasonable values of average normal stresses even in slightly non-isostatic conditions. This is the case of powder preshear, for which Eq. 36 is used to relate the normal consolidation stress (a value close to the average stress represented by the centre of the consolidation Mohr circle) and the normal force consolidating the interparticle contacts. Therefore, the approach proposed by Rumpf [23], in spite of the many assumptions required to find the extraordinary simple result reported in Eq. 36, still represents a reasonable and rather robust relation between average interparticle forces and local material stresses or strength that can be used also in systems with particles significantly differing from the assumed properties for his derivation.

5.4.1 Model results

The model described in section 5.3 was applied to the experimental materials. A unique value of the Hamaker constant was assumed for all samples and temperatures [170]. Instead, accounting for thermal expansion and thermal effects on mechanical properties of the particle material, different values of particle density ρ_p and compressive strength p_f [171] were adopted at 25 °C and 500 °C, as reported in Table 7. Furthermore, sample porosity ε was derived from experimental values of bulk density, ρ_b, measured during shear tests and from the particle density.

$$\varepsilon = 1 - \frac{\rho_p}{\rho_b} \qquad \text{Eq. 40}$$

The evaluation of the sample porosity is affected by some inaccuracies, because of the leakage of the powder from the cell during shear testing. This leakage may entail an overestimation of the effective mass of the sample, and a resulting underestimation of the relevant porosity, which is calculated from the bulk density (i.e., the ratio between the initial sample mass and the current sample volume). Moreover, the estimated porosity is an averaged value and is not necessarily representative of the local porosity in the shear zone, which is more relevant to the measured stresses. In fact, powder dilation in the shear zone makes the local porosity value larger than the sample average. However, as reported by Tomasetta et al. [164], changes in this parameter slightly affect the model results.

Table 7 - Particle properties used in the model at ambient and high temperature.

T, °C	ρ_p, kg m^{-3}	A*, 10^{-20} J	p_f, GPa
25	2330	20	12
500	2320	20	4.5

p_f and A* are taken from literature [170,171].

The isostatic tensile strength is evaluated from the experimental measurement, assuming the hypothesis of a Coulomb material. According to this assumption the isostatic tensile strength is given by the intersection of the negative σ-axis and the linear extrapolation of the yield locus, or in algebraic terms:

$$\sigma_t = \frac{C}{\tan \varphi_i} \qquad \text{Eq. 41}$$

Substituting this σ_t value in Eq. 37, the experimental σ_p value in Eq. 39 and combining Eq. 37 to 40, the mean curvature radius r was evaluated for all samples and experimental conditions.

The use of the extrapolation in the traction plane of the Coulomb yield locus is a rather strong assumption in spite of the fact that powder yield data align rather well in the compression half plane. Therefore, it has to be recognized that this extrapolation not necessarily reflects reality and may overestimate the real tensile strength of the material. It has to be considered, however that, without any data in the traction half-plane, any other assumption, together with the Coulomb yield locus would have been equally arbitrary. Furthermore, for the sake of completeness, it should be mentioned that also the use a Warren-Spring type of equation has been tested in order to correlate that data and estimate the isostatic tensile strength. The use of this type of equation, however, brings to much lower values of σ_t and correspondingly of the van der Waals Forces estimated with by the use of Eq. 37. With some of the size cuts, these force values are so small that are even smaller than the smallest force that can be predicted from Eq. 39 with a curvature radius tending to zero. For this reason, the Warren-Spring approximation was not considered in the analysis of the data in this work, as unable to produce realistic data. Furthermore, a MatLab App named cYield was developed by using Matlab's Graphical User Interface Design Environment (GUIDE). This tool enables to calculate both straight line (Coulomb) and curved line (Warren-Spring) yield loci as the best fitting of the σ-τ experimental shear points. The different features of such a tool are presented and the important steps for the execution of its calculations are illustrated in the appendix section.

Results in terms of interparticle forces, mean curvature radius and other bulk properties are reported in Table 8. Inspection of this table indicates that the mean curvature radius value generally varies with the particle size of the sample and with temperature, however a mean curvature radius of about 1 µm is found for almost all powder samples, while it is around 0.3 for the smallest size cut A1. For this reason, in order to verify if the equations

developed by Rumpf and Molerus are able to predict the main temperature effects, a mean curvature radius constant with temperature was assumed. In particular, r=0.35 μm was assumed for the finest sample (A1), while r=1.06 μm was used for all the other samples. Given the curvature radius, the model can predict the tensile strength by using Eq. 39, Eq. 38 and Eq. 37 in sequence.

Table 8 - Mean results of the mathematical model.

sample	T	σ_c	ρ_b	ε	σ_t	F_{VdW}	F_n	r
	°C	Pa	kg m^{-3}	-	Pa	nN	nN	µm
A1	25	541	682	0.71	271	311	622	0.29
	25	666	704	0.70	346	380	731	0.35
	25	790	721	0.69	354	377	840	0.35
	25	915	737	0.68	413	425	942	0.39
	500	538	605	0.74	349	472	727	0.41
	500	633	623	0.73	305	396	820	0.34
	500	787	638	0.73	310	389	988	0.33
	500	912	653	0.72	335	408	1109	0.34
A2	25	547	983	0.58	84	584	3793	0.50
	25	672	999	0.57	85	575	4530	0.48
	25	796	1014	0.56	84	549	5227	0.45
	25	921	1028	0.56	107	688	5904	0.57
	500	544	899	0.61	134	1071	4351	0.84
	500	669	919	0.60	150	1155	5165	0.88
	500	793	917	0.60	176	1365	6148	1.04
	500	917	926	0.60	171	1305	6992	0.96
A3	25	554	1027	0.56	38	799	11586	0.60
	25	679	1044	0.55	43	865	13787	0.64
	25	803	1056	0.55	42	826	15969	0.57
	25	928	1067	0.54	55	1078	18107	0.78
	500	552	970	0.58	63	1441	12664	0.88
	500	676	982	0.58	73	1650	15183	0.99
	500	800	980	0.58	72	1620	18032	0.86
	500	924	984	0.58	83	1865	20680	0.99
A4	25	553	1128	0.52	28	772	15383	0.53
	25	677	1119	0.52	46	1287	19133	0.96
	25	801	1117	0.52	44	1261	22727	0.89
	25	801	1354	0.42	46	862	15089	0.62
	500	553	1110	0.52	70	2007	15749	1.30
	500	675	1063	0.54	68	2117	20858	1.22
	500	800	1070	0.54	64	1969	24426	0.96
	500	927	1163	0.50	71	1839	24097	0.85
A5	25	559	1243	0.47	24	2246	53077	1.42
	25	685	1283	0.45	25	2236	60694	1.31
	25	808	1279	0.45	28	2483	72091	1.39
	25	612	1269	0.46	29	2612	55557	1.74
	500	560	1159	0.50	37	4027	60911	1.57
	500	684	1167	0.50	46	4945	73380	1.98
	500	809	1186	0.49	55	5677	83992	2.28
	500	932	1181	0.49	65	6824	97600	2.86

In the parity plot reported in Figure 54, the tensile strength values obtained by the application of the model with these further assumptions were compared with the tensile strength values, obtained from the experiments assuming the Coulomb hypotheses and extrapolating results. The comparison shows a very good match between model values and extrapolated values over a significantly large range of diameters and temperature range tested. This result allows concluding that, assuming a reasonable value of the mean curvature radius at the contact points, the model is able to predict the correct order of magnitude of the tensile strength.

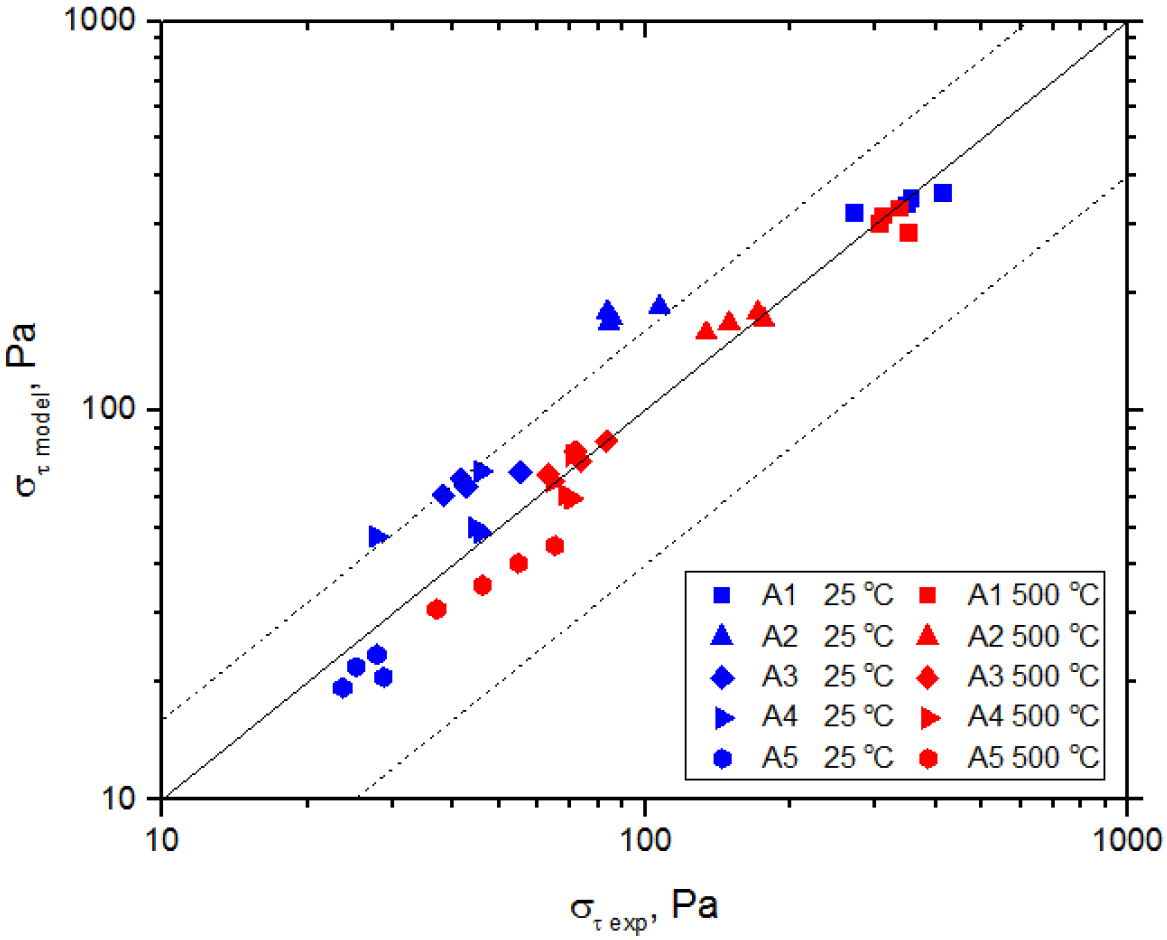

Figure 54 - Extrapolated tensile strength vs tensile strength model predictions; dotted line ±60%.

5.5 Reacted material Yield Loci

The Yield loci of the reacted material were calculated by following the same procedure used for the fresh materials. Because of the limited availability of the material, only 500 g for each sample, a different use of the samples was required with respect to the previous

procedure, in which fresh sample was used every time the cell was re-filled. In fact, each flow function test required about 100 g of material (without repetitions) and therefore a sample "regeneration procedure" was necessary, in order to use the same powder in more than a single test. According to this procedure, the sample was removed from the cell and brought inside a glove-bag in a nitrogen atmosphere. The purpose was to minimize the time exposure of the powder to oxygen. In the glove bag, all the clumps were broken up (or sieved out) by using two sieves (200 and 90 μm) through which the powder was let flow. The material obtained was re-used for other shear experiments at the same temperature or higher than the previous experiment. This procedure tended to minimize the effects of the sample cooling in the compacted state that had been reached within the cell in the previous experiment, and to bring it back to a condition that should be more similar to the loosely compacted state at which these powders were generated. In any case, memory effects should be limited for the reuse of powder from tests at temperatures in which there was no evidence of capillary bridging. With each material, a first set of experiments was performed by repeating at spaced temperature increments (25→150→300→340→380→420→460→500 °C) a binary sequence of a single pre-shear step at 600 Pa of normal load and a single shear step at 500 Pa of normal load. This test is useful in order to provide information on the temperature at which the rheological properties would change. The increments are set closer, at 40 °C differences, above 300 °C in the range of temperature where the industrial application of the tested material provided indication of significant temperature effects. The results of these preliminary tests are reported in Figure 55 and Figure 56. Sample S1, the one with low level of impurities, shows that the pre-shear and shear values at the same temperature differ for temperature below 400 °C. At temperatures between 400 °C and 500 °C, these values are practically overlapped and a clear trend can be observed. This change is an indication of the fact that the nature of the interparticle interactions is changing with the temperature. As it is widely discussed below, it is hypothesized that this change is due to the onset on capillary bridges between particles. In fact, the reduced effect of consolidation on the shear is in agreement with previous research [172] on the presence of capillary forces. A phenomenological interpretation of this finding can be guided by Eq. 36. This can be strictly applied to relate the material tensile strength with the average set of interparticle

forces, Fc. In this simple limit, it is clear from Eq. 36 that the strength of the material with consolidation can increase either because of the increase of the average forces F_c holding together two neighbouring particles, or because of the increase of the number of contact points per unit volume $\propto(1-\varepsilon)/\varepsilon$, as a consequence of powder densification. Considering van der Waals forces in which $F_c=F_{vdW}$, it is clear from Eq. 38 that consolidation can activate both the increase of the number of contact points and the increase of the contact force, due to the importance effect of plastic deformation of the contacts points caused by the consolidation force (F_N) on the resulting value of F_{vdW}. Instead, for capillary forces $F_{in}=F^*_c$, following the model used by Rabinovich [173] the physics of the capillary bridge suggest that the binary interparticle forces are not directly affected by the normal consolidation forces F_N. Therefore, for capillary forces, the powder consolidation can change only as a result of a change in the powder porosity.

As mentioned above, Eq. 36 is not valid for shearing. However, it is reasonable to hypothesize that the qualitative dependencies found above between consolidation and material strength can apply to the shear experiments reported in Figure 55 and Figure 56. Assuming that in these experiments the system porosity is not changing significantly during the test, the observed changes of shear stress are likely to mostly depend on changes in the interparticle forces. In particular, the increase of shear stress at certain temperature, as well as the reduced dependency of shear stress with the pre-shear consolidation, are both coherent with the onset of capillary forces, stronger than van der Waals forces and less affected by consolidation.

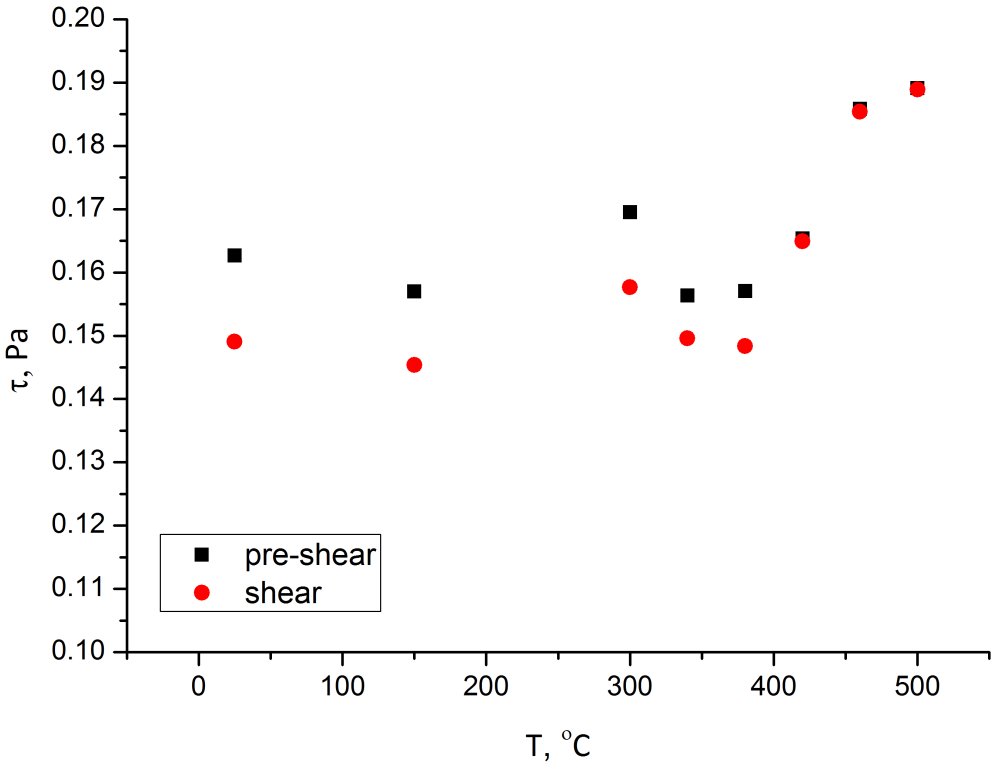

Figure 55 - Tests provided at each temperature by a single pre-shear step at 600 Pa of normal load and a single shear step at 500 Pa of normal load for Sample "S1".

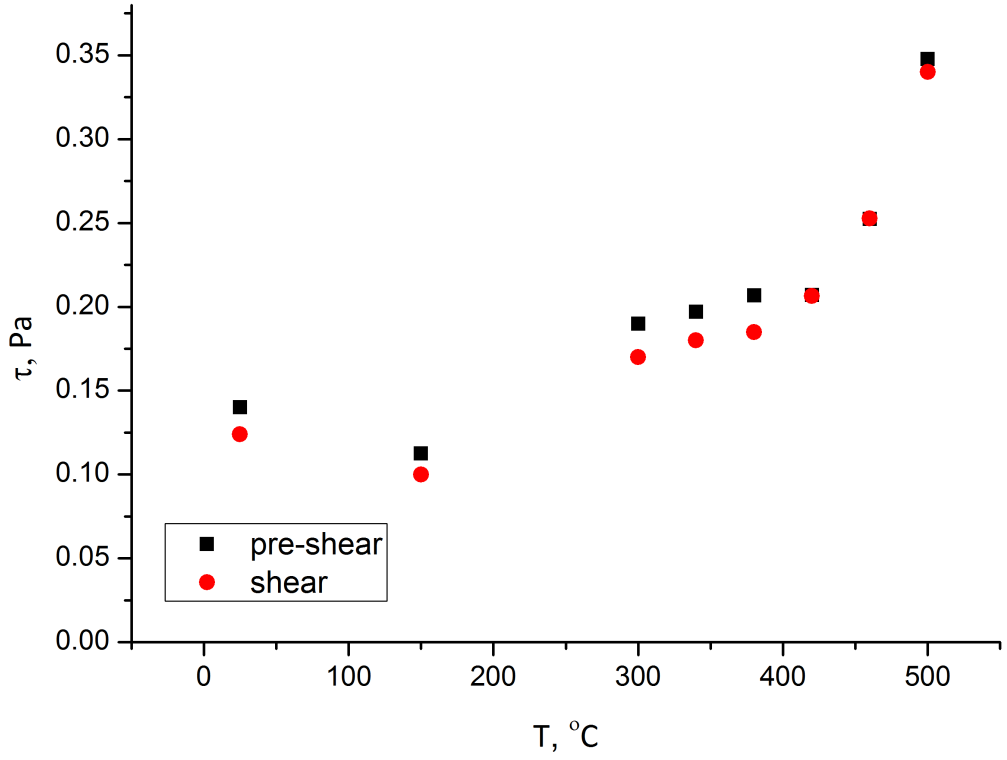

Figure 56 - Tests provided at each temperature by a single pre-shear step at 600 Pa of normal load and a single shear step at 500 Pa of normal load for Sample "S2".

Taking the indication provided from these experiments, material yield loci and flow functions were measured at 25, 350, 450 and 500 °C in order to better describe the effect of temperature.

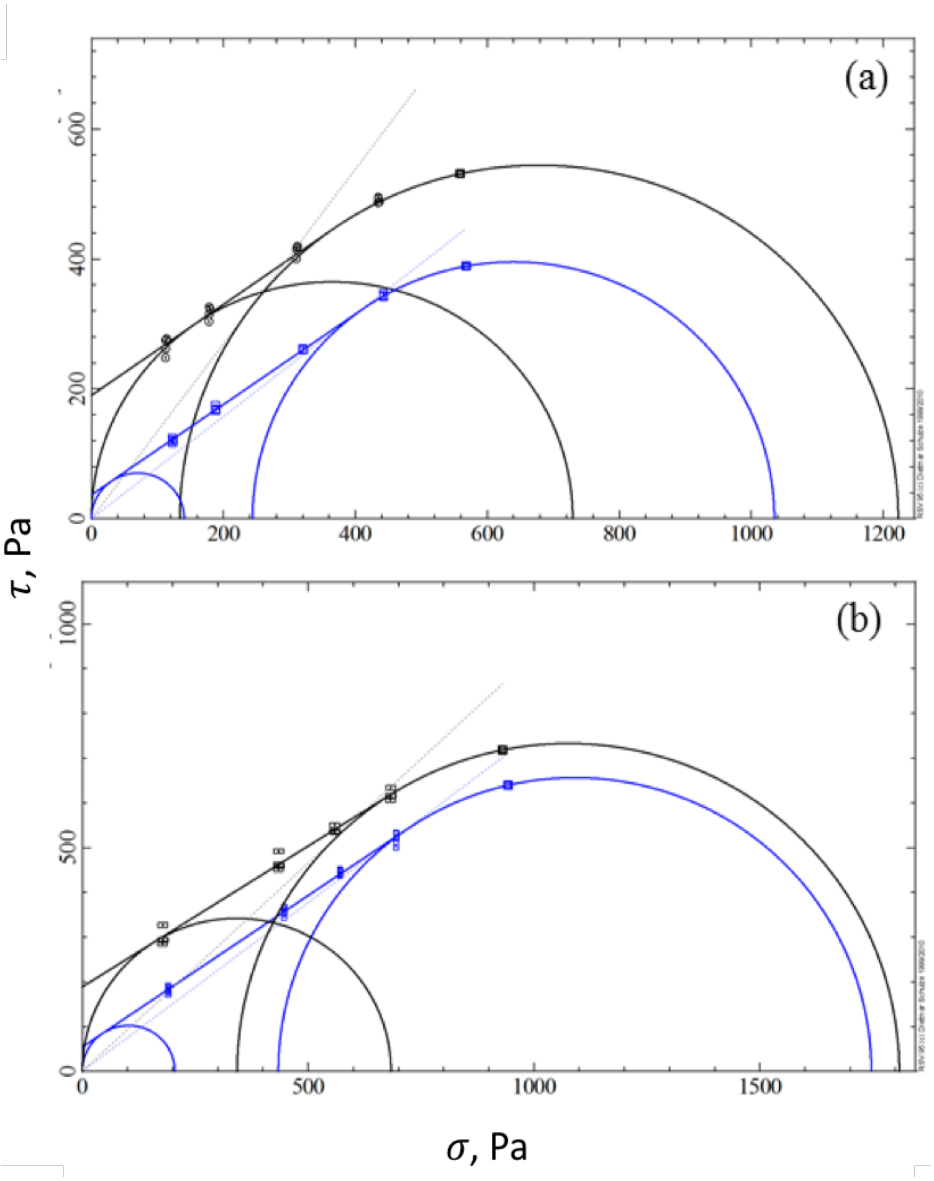

Figure 57 - Yield loci for the "S2" sample measured with HT-ASC at 25 °C (blue line) and 500 °C (black line): (a) $\sigma_1 \approx 1000$ Pa; (b) $\sigma_1 \approx 1700$ Pa.

An example of the observed effect of temperature on the yield loci is reported in Figure 57. For the sake of clarity, the figure reports results for a single material (sample S2), two consolidation levels and two temperatures. All the other measured yield loci are available as additional in the Appendix A1.3. In order to visualize the yield loci, the simple line description of the yield locus of Coulomb materials has been used. Different yield loci were found when varying temperature and it can be noted that the cohesion is significantly

affected by both consolidation and temperature. On the contrary, the static angle of internal friction φ_i turns out to be almost independent of both consolidation and temperature, as it was observed for the fresh materials. This behaviour is typically shown by powders showing prevailing capillary forces with amounts of liquid corresponding to the pendular state [53,172]. In these conditions, capillary forces are able to affect cohesion due to the increase of the adhesion forces between particles but are not able to affect significantly the powder friction. Therefore, the observed increase of the unconfined yield strength, f_c, with both consolidation and temperature is to be attributed to the changed cohesion for both the samples tested. Table 9 reports the flow properties (namely, the cohesion C, the angle of internal friction φ_i, the unconfined yield strength f_c and the flow factor ffc) obtained as a function of temperature for both samples. Data in the table are limited to the lowest and the highest consolidation level.

Table 9 - Results of the shear tests performed at different temperatures for sample S1 and S2.

Sample	T, °C	σ_1, Pa	C, Pa	φ_i, °	f_c, Pa	σ_t, Pa	ffc, -
S1	20	1069	46	37	187	60	5.76
	300	988	46	35	173	67	5.70
	400	1074	79	36	316	105	3.40
	500	1156	139	37	568	179	2.03
	20	1798	71	37	289	92	6.22
	300	1596	58	35	219	85	7.28
	400	1777	118	37	470	158	3.78
	500	1844	180	36	706	247	2.61
S2	20	1037	37	35	142	53	7.28
	300	1254	144	37	585	187	2.73
	400	1223	190	35	729	271	1.68
	500	2626	269	38	1118	344	2.05
	20	1747	54	34	205	79	8.52
	300	1881	156	34	586	233	3.21
	400	1808	189	33	684	300	2.65
	500	3684	280	35	1067	407	3.45

5.5.1 The effect of temperature on the angle of internal friction

Figure 58 summarizes all the values of the angle internal friction derived from the material yield loci obtained for both the materials at all the consolidation levels and temperatures at which the yield loci were determined. Error bars are also provided in Figure 58. These were calculated as the maximum deviation of the values of the internal friction calculated separately for each of the 4 test repetitions. The same approach to calculate the error bars was used with the other flow parameters reported in the following. The angle of internal friction is almost constant with temperature and its value is about 35±3°. For the sake of clarity, it must be said that an irregular upward motion of the lid of the shear cell was observed, as shown in Figure 59, when performing shear experiments at 500 °C and very low σ_1 (around 1000 Pa) for the sample S2 (the one with a larger amount of impurities). As it can be seen from the pictures in Figure 59 a compacted structure of powders was caused by a significant increase of the interparticle forces acting on the system resulting in a tensile force not on the same plane. The presence of these forces dramatically affects the measurements at low values of normal load, thus the tests were performed at larger value of σ_1 (2600-3600 Pa).

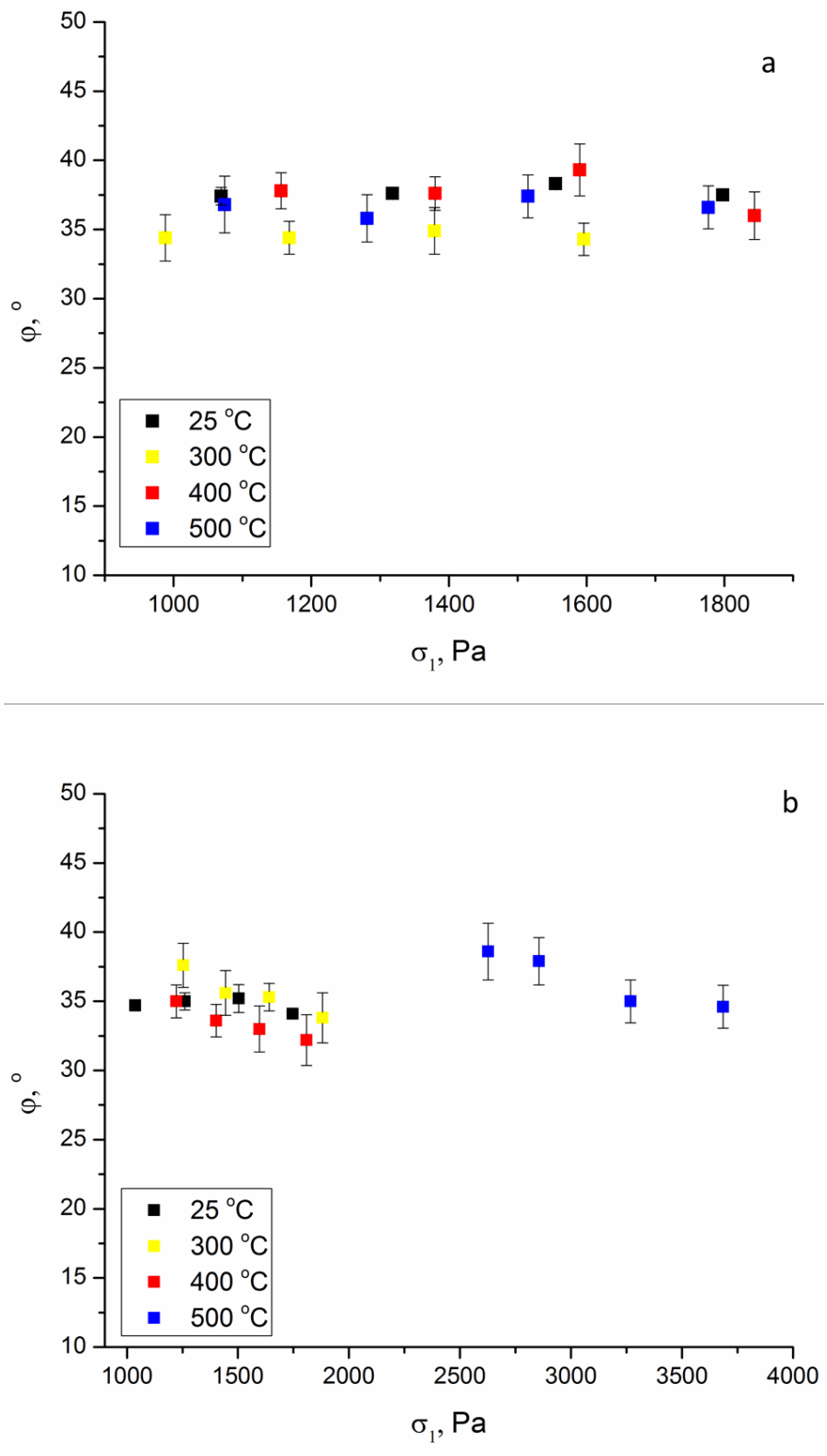

Figure 58 - Static angle of internal friction as a function of the consolidation stress and of the test temperature for: (a) sample “S1” and (b) sample “S2”.

Figure 59 - Images of the cell during a test at a value of 1900 Pa of applied normal stress. On the left the lid lifted during the test. On the right the caked material in the lid vanes after the cell cooling.

5.5.2 The effect of temperature on the cohesion

Figure 60 regroups the results for the cohesion as function of temperature. With reference to the sample S1, lower amount of impurities, the increase of temperature up to 300 °C does not produce any significant effect. At these temperatures, the cohesion is rather stable and its value is around 52±7 Pa. Increasing the temperature up to 500 °C, two changes occur. At 400 °C, the cohesion rises to 87±10 Pa and at 500 °C it rises up to 205±15 Pa. The other powder sample, the one with higher amounts of impurities exhibits a qualitatively similar behaviour. According to Figure 60b, three different increases of cohesion can be observed by increasing the temperature up to 500 °C. Its value at ambient temperature is around 42±5 Pa, then 142±70 Pa at 300 °C and 183±7 Pa at 400 °C. Finally, at 500 °C, the results show a very high cohesion equal to 288±17 Pa. Tests performed at 300/400 °C, for both samples, exhibit a large scatter between data. This scatter is coherent with the interpretation of incipient formation of liquid capillary bridges that, close to the material melting condition, may make the measurement strongly variable between tests. In fact, shear stress results might be differently affected by the effective amount of the liquid phase formed.

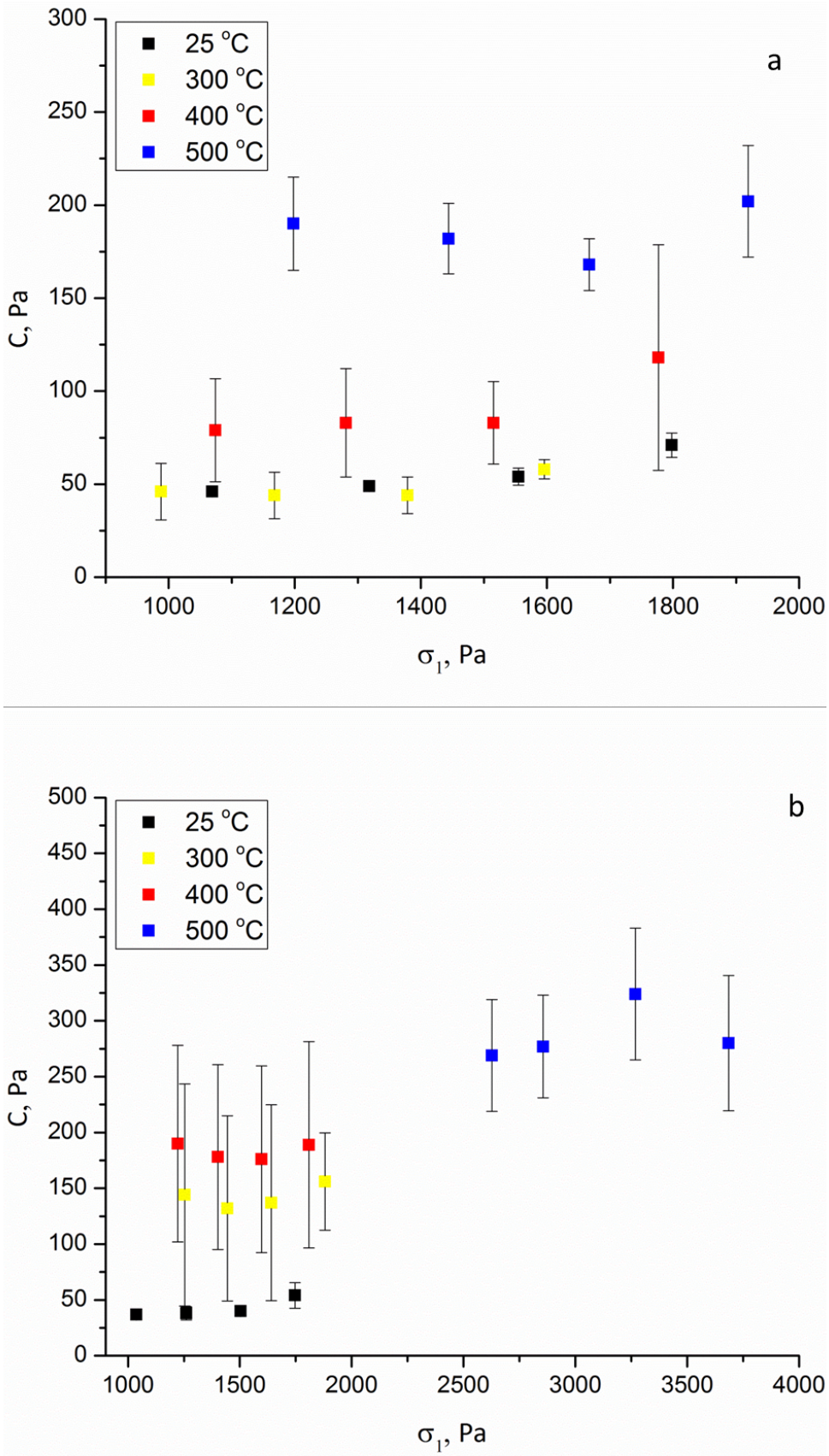

Figure 60 - Powder cohesion as a function of the consolidation stress and of the test temperature for: (a) sample "S1" and (b) sample "S2".

5.5.3 The effect of temperature on the unconfined yield loci

Figure 61 reports the complete flow functions at different temperatures for both reacted materials. In case of sample “S1”, inspection of Table 9 and of Figure 61a indicates that the yield loci at ambient and 300 °C are almost coincident. This suggests that temperature changes have a minor effect on the powder cohesion in this range. Such values of the flow function, for temperatures up to 300 °C, classify the powder as an easy flowing material. A significant increase of cohesion, around two times, is registered with increasing temperature up to 400 °C. As a result, the upward shift of the flow function determines a classification change of the powder flow from easy flowing to cohesive material. A further increase of temperature up to 500 °C produces an even larger cohesion and, therefore, a further upward shift of the flow function. For the sample “S2”, an increase of temperature from ambient to 300 °C involves an increase of cohesion of about four times its ambient value, resulting in an upward shift of the flow function from the easy flowing class to the limiting region between very cohesive and cohesive classes, as reported in Figure 61b. The yield loci at 300 °C and 400 °C are almost coincident. At 500 °C a strong powder bulk agglomeration was observed as reported in Figure 59.

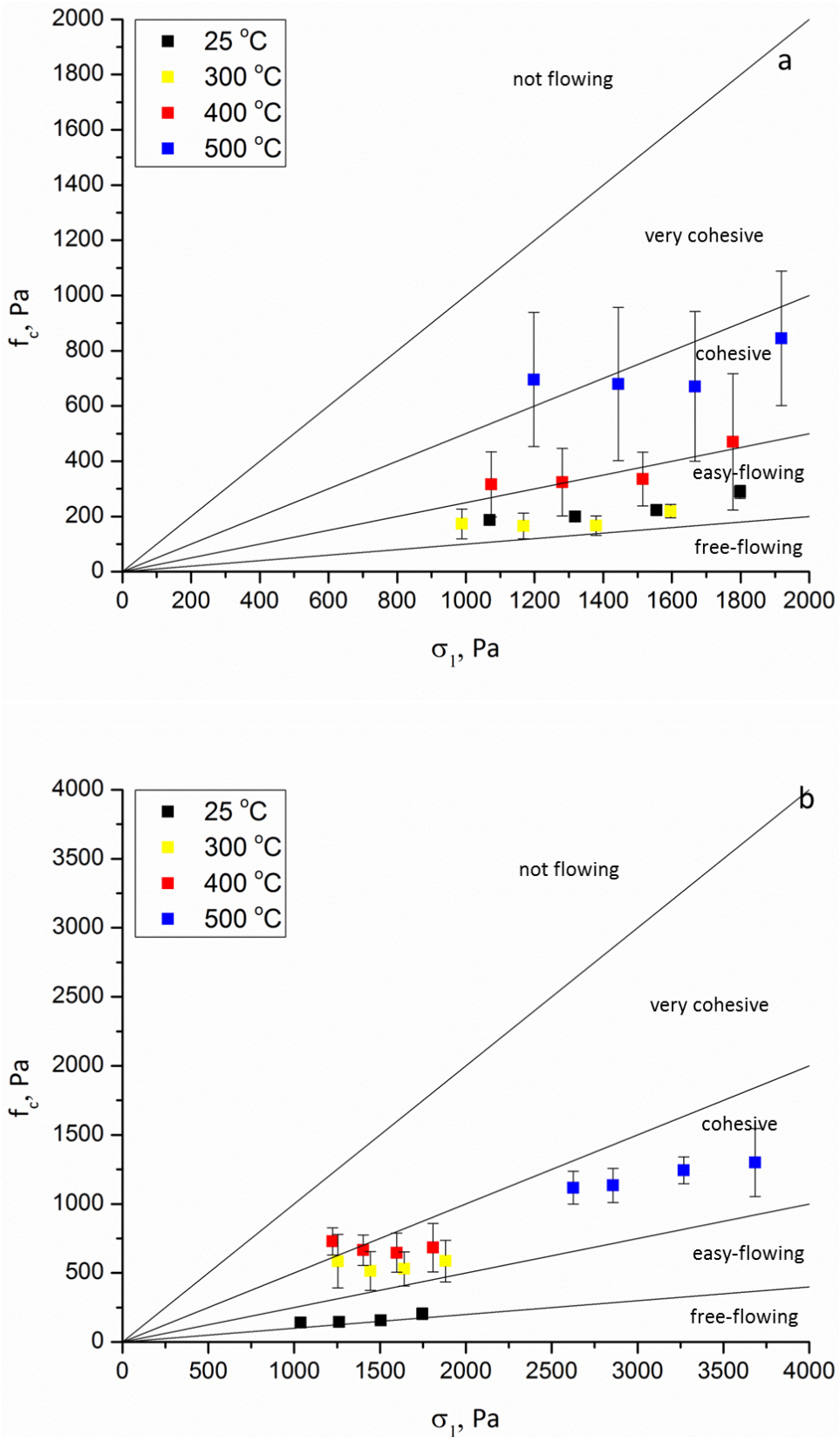

Figure 61 - Flow functions measured at different temperatures: (a) sample “S1”; (b) sample “S2”.

5.6 Capillary model

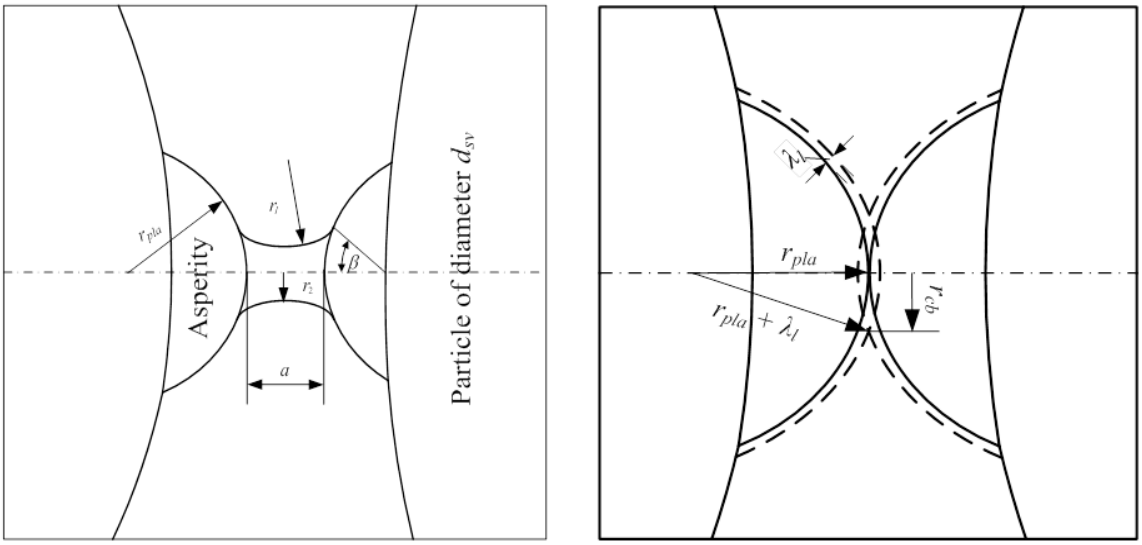

Figure 62 - Scheme of a capillary bridge between particles with the nomenclature used accounting for particle asperities.

In case of presence of a liquid phase, surface tension may determine the formation of connecting links between the particles, named capillary bridges, that result in attractive forces between particles (see for example Fayed and Otten [174]). These forces depend on the local particle curvature. Therefore, with perfect spheres, they depend on the particle size. Instead, with rough particle surfaces, liquid bridges form between particle asperities and the asperity size should be properly considered for the estimation of the effective curvature radius at contacts. Pierrat and Caram [175] developed a model in order to predict the tensile strength of wet granular materials. They also proposed a theory for describing the effect of moisture on the flow properties of granular materials with a reduced number of tests to be performed [172]. The latter was used to study the effect of moisture on the flow properties of glass beads of 93 µm diameter and a correlation that fitted well with experimental measurements was found. The same Authors suggested the theory of shift [172]. According to this theory it is possible to determine the yield locus of a powder at any moisture content by shifting the original failure function in the region of positive normal stresses. Lately, Landi et al.[53] used the bridge model proposed by Pierrat and Caram [175] but introducing consideration on the roughness of the particles. Their model was based on the hypotheses of capillary condensation and allowed the correct determination of the capillary forces. Besides, the model prediction of the powder

tensile strength agreed well with the estimates of the tensile strength, derived from direct powder shear tests carried out at air relative humidity up to 80%. A similar model was very recently applied by La Marche et al. [52] to estimate capillary forces in beds of glass beads fluidized with humid air.

Following the approach proposed by Landi et al. [53], it is possible to describe the characteristics of the formed capillary bridge according to the simplified approach used by Rabinovich et al. [173].

$$r_1 = r_{pla}\left[\left(1+\frac{a}{2r_{pla}}\right)\sec\beta - 1\right] \qquad \text{Eq. 42}$$

$$r_2 = r_{pla}\left[\left(1+\frac{a}{2r_{pla}}\right)\tan\beta - \left(1+\frac{a}{2r_{pla}}\right)\sec\beta + 1\right] \qquad \text{Eq. 43}$$

$$r_1 = r_{pla}\left[\left(1+\frac{a}{2r_{pla}}\right)\sec\beta - 1\right] \qquad \text{Eq. 44}$$

$$V_b = 2\pi[r_1^2+(r_1+r_2)^2]r_1\cos\beta - \left(\frac{2\pi(r_1^3\cos^3\beta)}{3}\right) - 2\pi r_1^2(r_1+r_2)\left[\cos\beta\sin\beta\left(\frac{\pi}{2}-\beta\right)\right] - \frac{2\pi r_{pla}^3(2+\cos\beta)(1-\cos\beta)^2}{3} \qquad \text{Eq. 45}$$

where r_{pla} is the radius of the asperity, a is the gap between the bridge asperity and β is the angle of the wet spherical cap of the contact measured from the centre of the curvature radius as defined in Figure 62. Rearranging Eq. 43 to Eq. 44, the volume of the bridge is a function of a single parameter, which is the angle β. Inversely, if the volume of the bridge is set, as well as the radius of the contact point, then it is possible to evaluate the bridge geometrical characteristics, r_1, r_2, and β. In turn, according with the theoretical model of capillary bridges proposed by Pierrat and Caram [175], these parameters allow to derive the tensile force of the bridge, F_c^*. In particular, this force can be considered as the sum of the direct action of the surface tension σ_s in the axial direction of the bridge and in its indirect effects through the pressure difference generated by its action on the capillary bridge surface. If capillary forces are present, generally these are much larger than van der Waals forces [174] and, therefore, it is possible to neglect these latter and assume that $F_{int}=F_c^*$.

$$F_c^* = 2\pi r_2 \sigma_s + \pi r_2^2 \sigma_s \left(\frac{1}{r_1} - \frac{1}{r_2} \right)$$ Eq. 46

5.6.1 Model results

The particles used for this study have an irregular shape and, therefore, the effective curvature radius at the contact point that enters in the estimation of both van der Waals and capillary forces is not necessarily related to the particle size as, instead, it would happen for spherical particles. In order to overcome this system indeterminacy, the effective curvature radius at the contact was determined at ambient temperature using the approach previously described in section 5.3, by making the hypothesis that in these conditions the capillary forces can be neglected. The curvature radius obtained with this procedure was then used to calculate the forces at other temperatures. For the sake of clarity, the details of the procedure are reported below.

The isostatic tensile strength of the material was estimated from the Coulomb Yield locus:

$$\sigma_t = \frac{C}{\tan \varphi}$$ Eq. 47

The values of σ_t obtained from Eq. 47 are reported in Table 9. These values are used to evaluate the interparticle forces F_{int} from Eq. 36, considering the experimental values of the bed porosity ε and the powder mean Sauter diameter d_{sv}. According to Molerus [176], the consolidation force at the contact point is estimated from the major principal stress during consolidation σ_1, reversing Eq. 36:

$$F_N = \frac{d_{sv}^2 \, \sigma_1 \varepsilon}{1 - \varepsilon}$$ Eq. 48

Figure 62 reports the values of F_{int} as a function of F_N calculated according to the above procedure for both materials and at the different temperatures. At high temperature, interparticle forces increase of an order of magnitude with respect to ambient conditions.

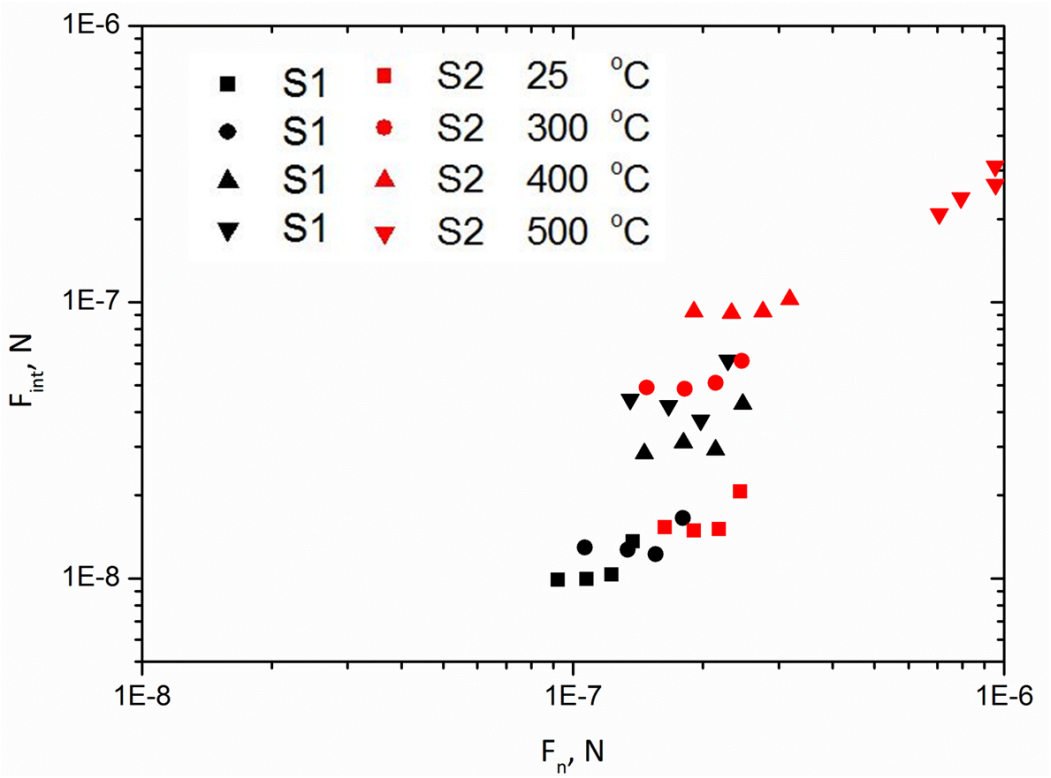

Figure 63 - Values of interparticle forces F_{int} calculated from experimental data according to Eq. 36 and 46 as a function of the Normal Force F_N calculated according to Eq. 48 for the two materials at all different temperatures.

Considering only results at ambient temperature, Eq. 38 is used to calculate the average particle curvature radii at the contact point from the previously calculated value of $F_{int}=F_{vdW}$. The values of the material parameters used in Eq. 38 are listed in Table 10. The curvature radii obtained at ambient temperature for powder S1 and powder S2 are $8.85 \cdot 10^{-2}$ µm and $1.29 \cdot 10^{-1}$ µm, respectively. Following the same procedure used for the fresh material, the model proposed by Rumpf and Molerus was applied for these samples. The results of the model were not able to produce satisfactory predictions as it is shown in Figure 64.

Table 10 - Materials parameters used in the model calculations for samples S1 and S2.

Sieving range	T, °C	A^{*}, 10^{-20} J	p_f, GPa	ρ_p, kg/m^3
S1	25	20	12.0	2330
	300	20	10.5	2324
	400	20	9.0	2322
	500	20	4.5	2320
S2	25	20	12	2330
	300	20	10.5	2324
	400	20	9.0	2322
	500	20	4.5	2320

This result suggests that in this particular case the only van der Waals forces are not able to explain the great increase of the cohesiveness of the particles with temperature. Therefore, a different procedure was followed to describe the effect of temperature which made use of capillary interparticle forces. The fundamental hypothesis behind this approach is that the liquid phase on the surface is generated by the partial melting of the salt impurities present on the particle surfaces itself as described above in the material section 4.2.2. In fact, the salts making the impurities, depending also on the composition of the mixture, can melt at temperatures that are much lower than the particle melting temperature that, in turn, is much higher than the tested temperatures. Therefore, it can be excluded that any liquid phase might contain the mother particle material. Moreover, these impurities appear as a separate solid phase on the particle surface thus the melting temperature of the impurities should not be affected by their amount in respect to the mother silicon powders as it will be seen in the next chapter. Necessary information to predict the capillary forces is the average volume of the liquid bridge V_b. Once V_b is known, the set of Eq. 42 to Eq. 44 can be solved for r_1, r_2 and β, which in turn can be used to calculate the capillary force with Eq. 46.

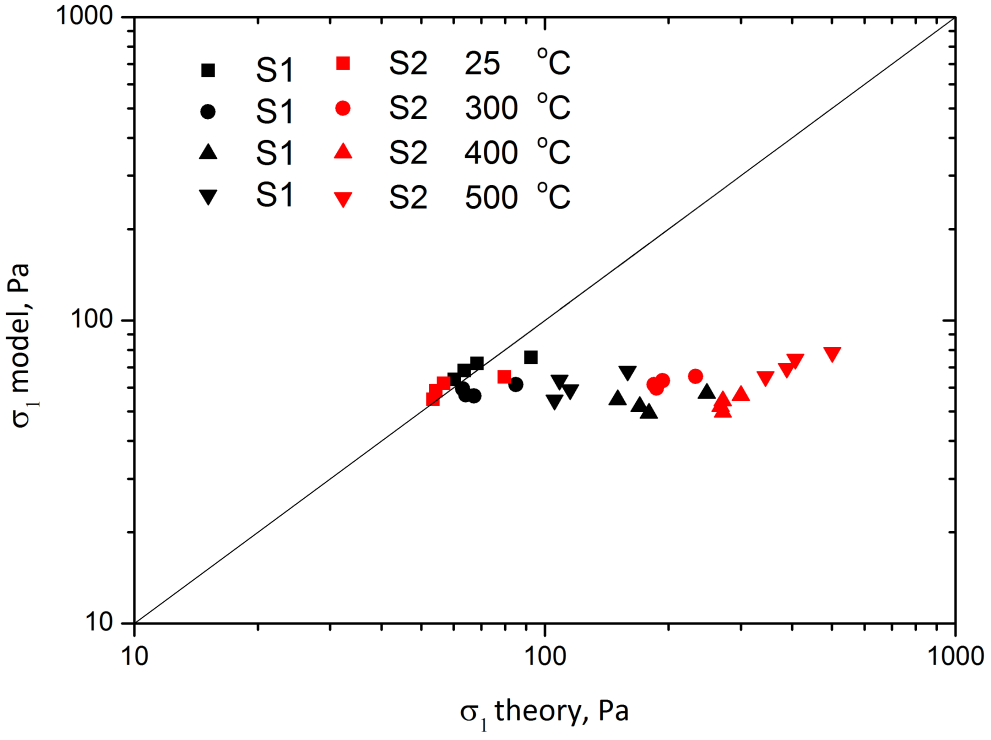

Figure 64 - Extrapolated tensile strength vs experimental tensile strength with the hypothesis of only van der Waals forces active for sample S1 and S2.

The volume of the bridge was estimated using the quantitative analysis on the salt content of these powders. The weight fraction of the total salts in the samples, as well as the salt composition is reported in Table 11. The impurities were characterized by the company using the X-ray Fluorescence (XRF) and X-ray Diffraction (XRD) analyses. They found that the largest amounts of impurities are in form of aluminum chloride ($AlCl_3$) and calcium chloride ($CaCl_2$), finding which are confirmed by the results of the EDX analysis reported in section 4.2.2.

The outcomes are reported in Table 11, in the columns in which the salt concentration base is "100 g of oxidized powder" columns. Due to the high tendency of Aluminum Chloride to be oxidized during the sample preparation procedure for the analytical determination, it is assumed that all the aluminium present in the quantitative analysis as alumina is present as Aluminum Chloride ($AlCl_3$). This assumption allows calculating the mass and the mole contents of the most abundant salts in 100 g of powder as reported in columns called "100 g of reduced powder" of Table 11. Aluminium Chloride is a low melting salt that alone sublimates at 180 °C and mixed with $CaCl_2$, is able to melt at temperatures between 120 and 460 °C as shown in the phase diagram of the mixtures of the two salts,

Figure 65. In order to use the diagram, the mole fractions of the salt binary system $AlCl_3$+$CaCl_2$ have been evaluated and they are reported, for the two samples, in the columns named "$AlCl_3$+$CaCl_2$ in reduced powder" of Table 11.

Table 11 - Salt composition in the reacted powder samples.

	Sample "S1"				Sample "S2"			
Base	100 g of oxidized powder	100 g of reduced powder		$AlCl_3$+$CaCl_2$ in reduced powder	100 g of oxidized powder	100 g of reduced powder		$AlCl_3$+$CaCl_2$ in reduced powder
Mass	g	g	mol	mole fraction	g	g	mol	mole fraction
Al_2O_3	1.8	-	-	-	3.1	-	-	-
$AlCl_3$	-	4.71	0.0353	0.247	-	8.11	0.0608	0.327
$FeCl_2$	2.3	0.35	0.0027	-	5.2	0.98	0.0077	-
$CaCl_2$	78.7	11.96	0.1078	0.753	73.4	13.87	0.1250	0.673
Salt/Powder, wt %	15.2	17.0	17.0	16.7	18.9	22.3	22.3	22.0

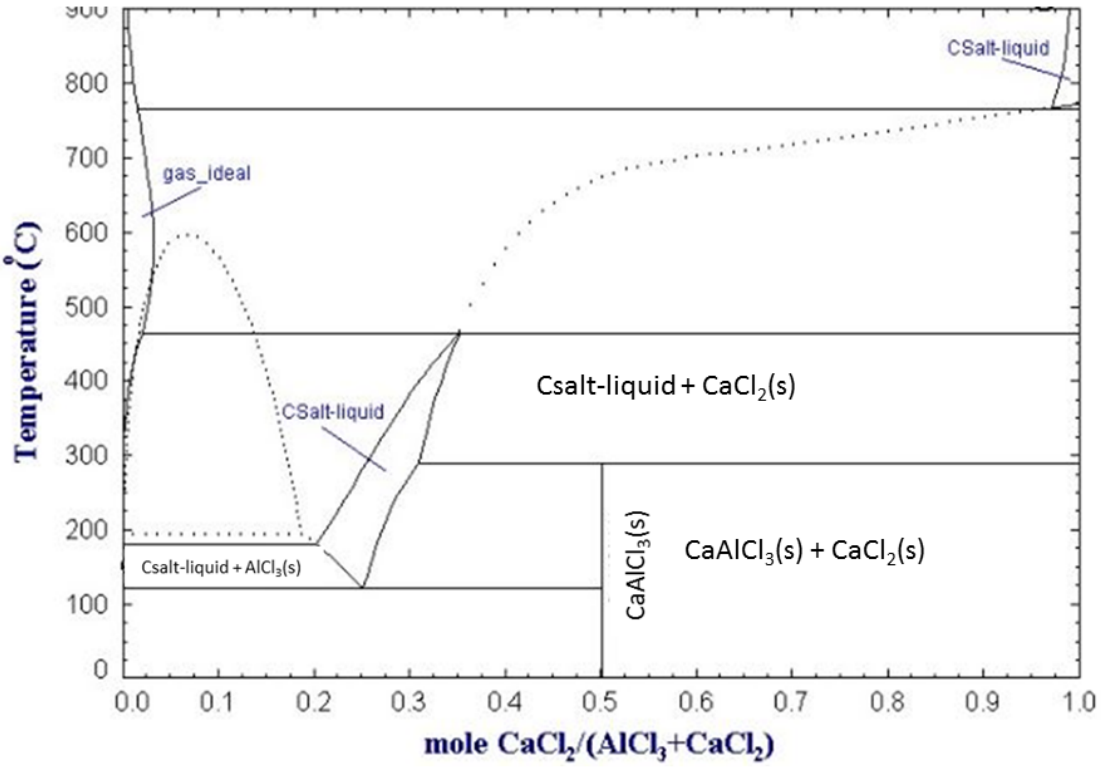

Figure 65 - Phase diagram of the salt binary system $AlCl_3$+$CaCl_2$ [177].

With these compositions it is possible to use the phase diagram of Figure 65 [177] and it is possible to calculate the liquid weight fraction (X_l) of the $AlCl_3$+$CaCl_2$ systems, reported in Table 11. Provided the total salt weight fraction S_{tot} calculated for the system ($AlCl_3$+$CaCl_2$) and given in the columns "$AlCl_3$+$CaCl_2$ in reduced powder" of the last line of Table 11 it is possible to calculate the liquid volume per unit mass of the sample, V_l.

$$V_l = \frac{X_l \; S_{tot}}{\rho_{l\,a}} \qquad \text{Eq. 49}$$

Consequently, the amount of liquid per particle, L_p, can be calculated as:

$$L_p = V_l V_p \rho_p \qquad \text{Eq. 50}$$

and the average liquid volume per unit surface, λ_l, evaluated using the mean Sauter diameter, d_{sv}, is

$$\lambda_l = \frac{L_p}{A_p} = V_l \frac{d_{sv}}{6} \rho_p$$ Eq. 51

Resulting values for V_l, L_p and λ_l are reported in Table 12. In order to estimate the amount of surface liquid that is available to for each bridge, we assumed that the bridge is able to collect the liquid on the portion of the asperity surfaces on which the liquid layer is able to contact the surface of both particles. According to Figure 62 this assumption defines an area of radius r_{cb} such that:

$$r_{cb} = \sqrt{\left(r_{pla} + \lambda_l\right)^2 - \left(r_{pla}\right)^2}$$ Eq. 52

and, in turn, it allows estimating the volume of the liquid that can form the liquid bridge V_b:

$$V_b = \lambda_l \pi r_{cb}^2$$ Eq. 53

According to Eq. 52 and Eq. 53, V_b can be calculated from λ_l once a certain asperity radius is assumed. The asperity radius calculated by the application of Eq. 52 and Eq. 53 is reported in Table 12. The latter was used to evaluate r_1, r_2 and β solving the set of Eq. 52 to Eq. 53 and to calculate the tensile force of the bridge F_c^* trough Eq. 46. Values of F_c^* are reported in Table 12. The surface tension of the mixture has been evaluated as the weighted average over the density of the single liquid components. Table 12 reports the value of the surface tension and liquid density for the two samples at different temperatures [178–181].

Table 12 - Results of the model calculation for capillary forces.

	T °C	r_{pla} µm	X_{lCaCl2} -	X_l -	ρ_{la} kg/m^3	σ_s N m^{-1}	V_l 10^{-5} m^3 kg^{-1}	λ_l µm	V_b 10^{-2} µm^3	F_c^* N
S1	25	8.9 E-2	-	-	-	0.14	-	-		9.9 E-9
	300		0.27	0.39	1330	0.05	5.06	0.25	8.5	1.8 E-8
	400		0.29	0.40	1080	0.17	5.17	0.26	9.6	4.4 E-8
	500		0.31	0.41	700	0.16	5.26	0.27	10.5	4.4 E-7
S2	25	12.9 E-2	-	-	-	0.14	-	-		1.5 E-8
	300		0.27	0.51	1330	0.04	6.68	0.55	76.0	3.7 E-8
	400		0.29	0.53	1080	0.16	6.82	0.56	80.4	8.9 E-8
	500		0.31	0.54	700	0.16	6.94	0.57	84.2	3.1 E-7

The tensile strength values obtained by using Eq. 46 with assuming $F_{int}=F_c^*$ were compared with the values obtained with the experimental tensile strength values in the parity plot of Figure 66. The comparison shows a very good match between model values and experimental values for the two samples over a significantly large range of temperature tested, in spite of the large number of assumptions made. These results allow concluding that, by assuming that capillary bridges are formed between two particle asperities and a reasonable value of the surface tension of the mixture, the model is able to correctly predict the order of magnitude of the tensile strength and its variations with temperature.

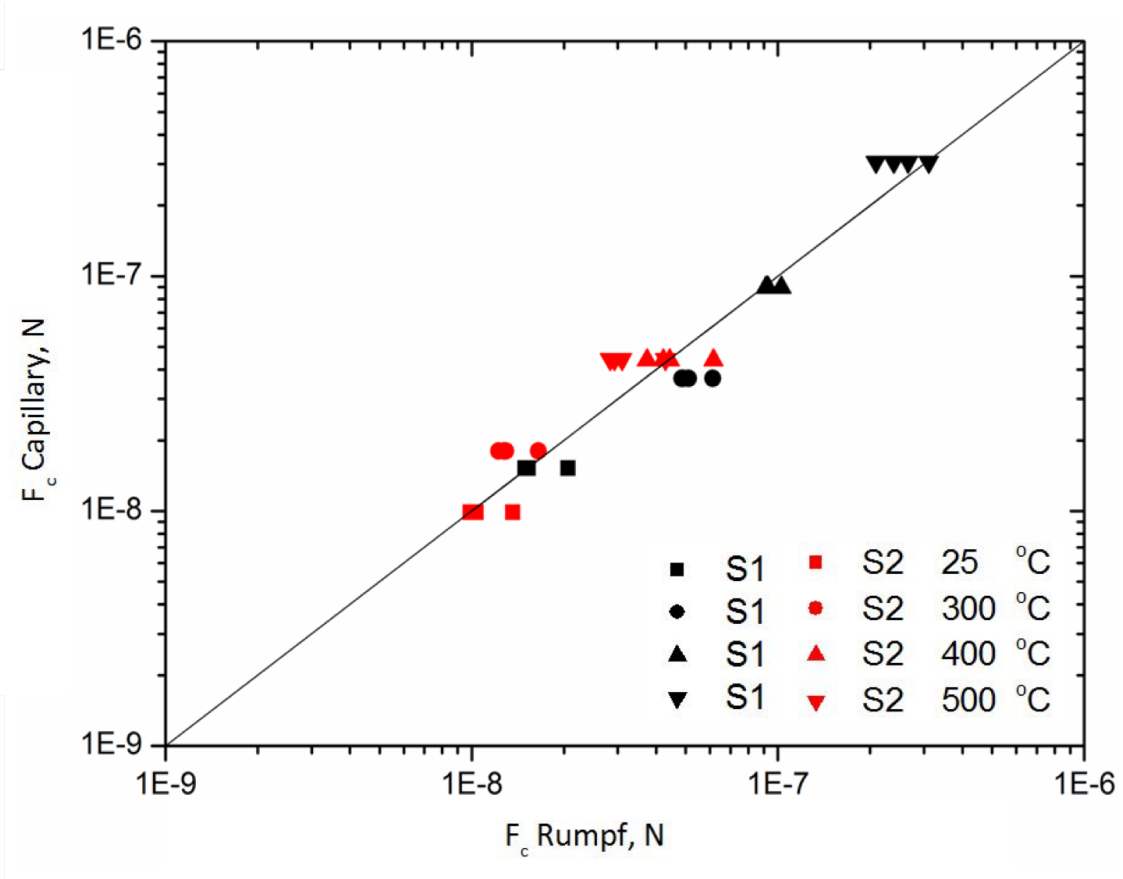

Figure 66 - Tensile strength of the liquid bridge calculated from the theory of capillary bridges vs the tensile strength of the liquid bridge estimated from the flow properties using Eq. 36.

5.7 Summary of the rheological tests

In summary, some concluding remarks can be drawn from the rheological tests conducted on the fresh material:

- A significant increase of powder cohesion at 500 °C was observed for different cuts of the same powder with particle size larger than 20 µm. This translated into a lower flowability of the samples;
- Thermal analysis conducted on the powder samples revealed that the effect of temperature on the powder flow properties is only due to van der Waals forces;
- The model developed which combines the continuum approach with the particle–particle interaction, is able to predict the correct order of magnitude of the tensile strength, based on the assumption that plastic deformation occurs at the contact

points and when using a reasonable value of the mean curvature radius at the contact points.

The analysis of the flow behavior of the reacted material showed:

- The powder cohesion is the parameter which appears to be mostly affected by temperature;
- The shear stress becomes almost independent of the consolidation state when increasing temperature;
- The observed changes are due to the occurrence of capillary bridges between the particle asperities, even if DTA and TGA are not able to detect any significant phase changes. However, the small amounts of liquid phase formed and confined to the particle surface are sufficient to considerably change the powder flow properties;
- The estimation of the amount of liquids present in the capillary bridges based on geometrical consideration, together with a reasonable estimate of the liquid surface tension allows to correctly predict the capillary interparticle forces and the tensile strength of the material.

6 Fluidization results

Previous chapters have outlined how the process conditions, such as temperature, particle size distributions and amount of impurities, may affect the flow behaviour of solid particles. In particular, shear experiments highlighted a significant increase of powder cohesion at 500 °C for different cuts of the same powder with particle size larger than A1. This resulted in a lower flowability of the samples. Thermal analysis on the powder samples revealed that the temperature effect on powder flow properties is mainly due to van der Waals forces.

In this chapter the fluidization results carried out on the same material and in the same range of temperature of the rheology experiments are reported and discussed. The aim of this work was to provide a better understanding of the factors responsible for changes in the fluidization behaviour between ambient and high temperature, highlighting the conditions under which either HDFs or IPFs dominate and control the fluidization behaviour.

6.1 Pressure drop profile and minimum fluidization velocity

The minimum fluidization velocity was measured from ambient temperature up to 500 °C, in steps of 100 °C. In order to guarantee a good mixing of particles the bed material was fluidized in bubble regime for around 20 minutes before any measurements was made. As described in section 3.8.1, the minimum fluidization velocity, u_{mf}, was experimentally measured from pressure drop profiles obtained first by increasing the gas flow rate until the bed was well fluidize, and then by decreasing the flow rate until the bed settled down. The minimum fluidization velocity was calculated from the pressure drop profile as the intersection of diagonal line and the horizontal line obtained when decreasing the gas flow rate.

6.1.1 The effect of temperature on pressure drop profile and u_{mf}

The pressure drops in Figure 67 and Figure 68 are plotted for samples A5 and A4 as ratios $\Delta P_m/\Delta P_c$, where ΔP_m is the measured pressure drop and ΔP_c is the calculated pressure drop when full bed support is achieved, as defined by Equation 34. Figures (a) report the pressure drop profile obtained decreasing the gas flow rate at all temperatures; on the other hand, the comparison between fluidizing and defluidizing pressure profile is shown in figure b. For flow rate above the minimum fluidization condition, the ratio $\Delta P_m/ \Delta P_c$ was constantly equal to unity for all the temperature range analysed. These results indicate a good fluidization quality and a negligible effect of interparticle forces on this parameter. According to Figure 67, the pressure drop profile moves on the left, meaning that the bed is fully supported by the gas for lower velocity. The results show a decrease of experimental u_{mf} with increasing temperature for both samples.

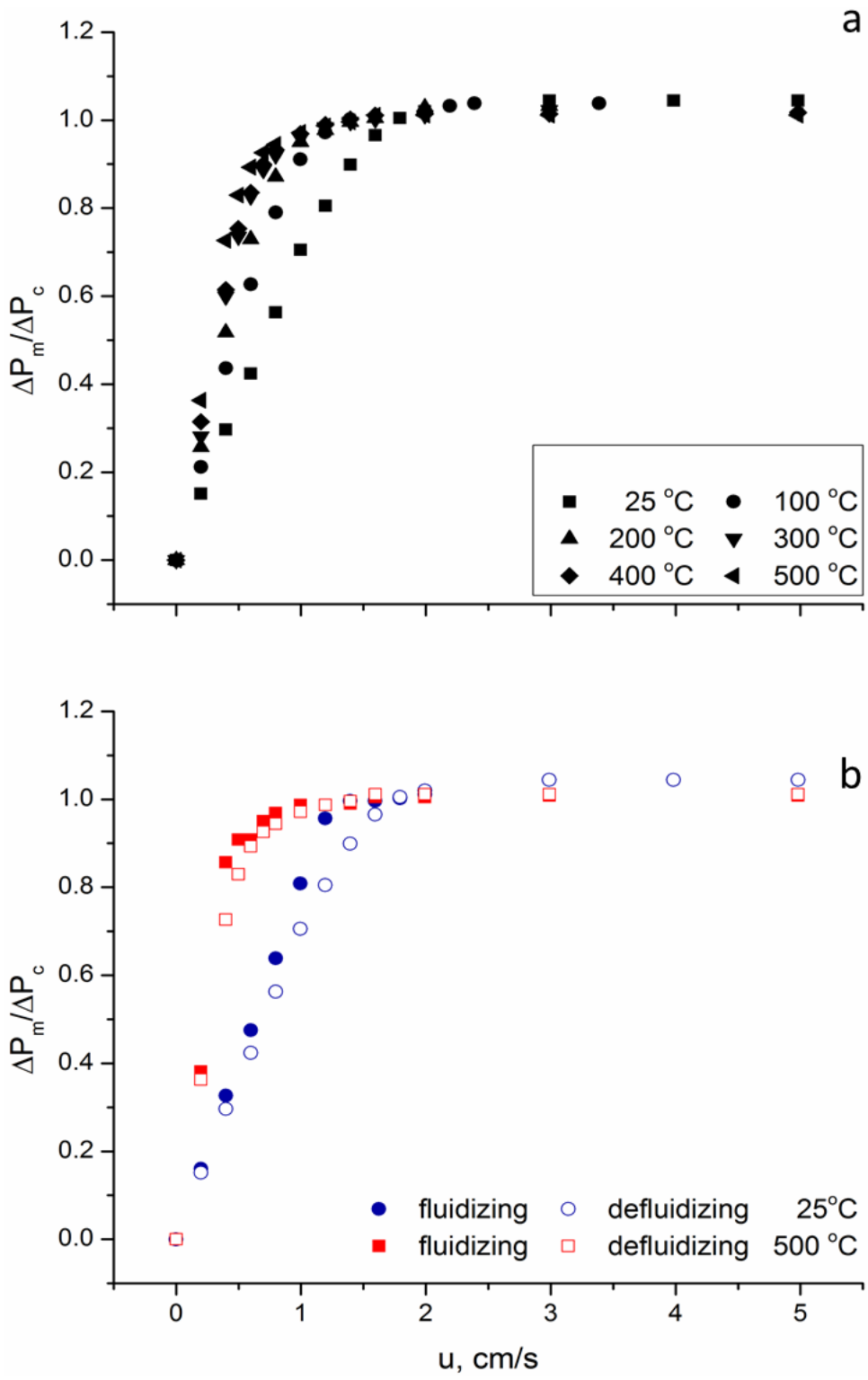

Figure 67 - Sample A5 (Geldart B): a) measured over calculated pressure drop profile in defluidization with increasing temperature; b) measured over calculated pressure drop profile when fluidizing and when defluidizing with increasing temperature.

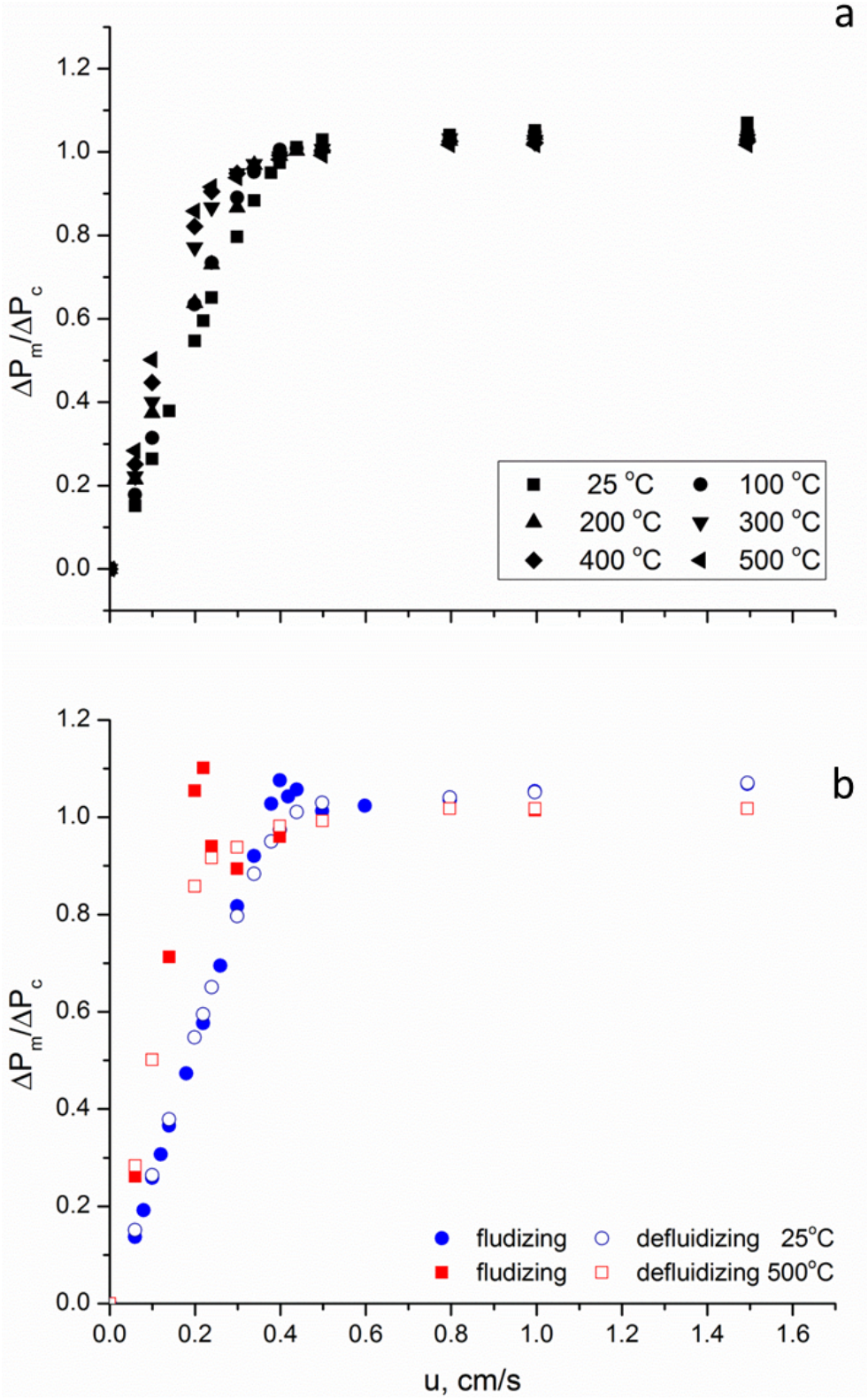

Figure 68 - Sample A4 (Geldart B/A): a) measured over calculated pressure drop profile in defluidization with increasing temperature; b) measured over calculated pressure drop profile when fluidizing and when defluidizing with increasing temperature.

The experimental values of u_{mf} were compared with the empirical correlation used to predict the minimum fluidization condition. In particular, the experimental values were compared with the Baeyens and Geldart [182] equation:

$$u_{mf} = \frac{0.0009\left(\rho_p - \rho_g\right)^{0.934} g^{0.934} d_p^{1.8}}{\rho_g^{0.066}\mu^{0.87}} \qquad \text{Eq. 54}$$

and the viscosity term of the Wen and Yu [66] equation:

$$u_{mf} = \frac{\left(\rho_p - \rho_g\right) g\, d_p^2}{1650\,\mu} \qquad \text{Eq. 55}$$

and the viscous flow term of the Ergun equation:

$$u_{mf} = \frac{\left(\rho_p - \rho_g\right) g\left(\phi d_p\right)^2}{150\,\mu}\frac{\varepsilon_{mf}^3}{1-\varepsilon_{mf}} \qquad \text{Eq. 56}$$

It is worth noting that while the Wen and Yu [66] and the Baeyens and Geldart [182] do not require a value of the bed voidage, the Ergun equation, instead, include voidage and the shape factor. In this latter case, estimates will be carried out both with the tapped bed voidage measured before any fluidization experiments at ambient temperature and the one measured from the X-ray observation of voidage at the minimum for fluidization. The results, reported in Figure 69, for samples A5 and A4 show that the Baeyens and Geldart equations and the Ergun with the predetermined $\varepsilon_{s,tapped}$ well describe the effect of temperature on the minimum fluidization condition but underestimate the experimental values. The experimental values are reported in Appendix A4.

The pressure drops profile of sample A3 and A2 are plotted in Figure 70 and Figure 71. For flow rate well above the minimum fluidization condition, also for these samples, the ratio $\Delta P_m/\Delta P_c$ was constantly equal to one for all the temperatures. In this case, the pressure drop profile moves to the left for temperature up to 400 °C and 300 °C for sample A3 and A2 respectively. A further increase of temperature had a limited effect on the pressure drop for sample A3 (Figure 70b) which remains almost constant and, thus so u_{mf}. A

significant effect on the sample A2 was instead observed where a further increase in temperature beyond 400 °C had caused an increase in u_{mf} (Figure 71b). It should also be noted that when increasing the temperature, the reproducibility of the experimental measurements became much lower, meaning larger error bars.

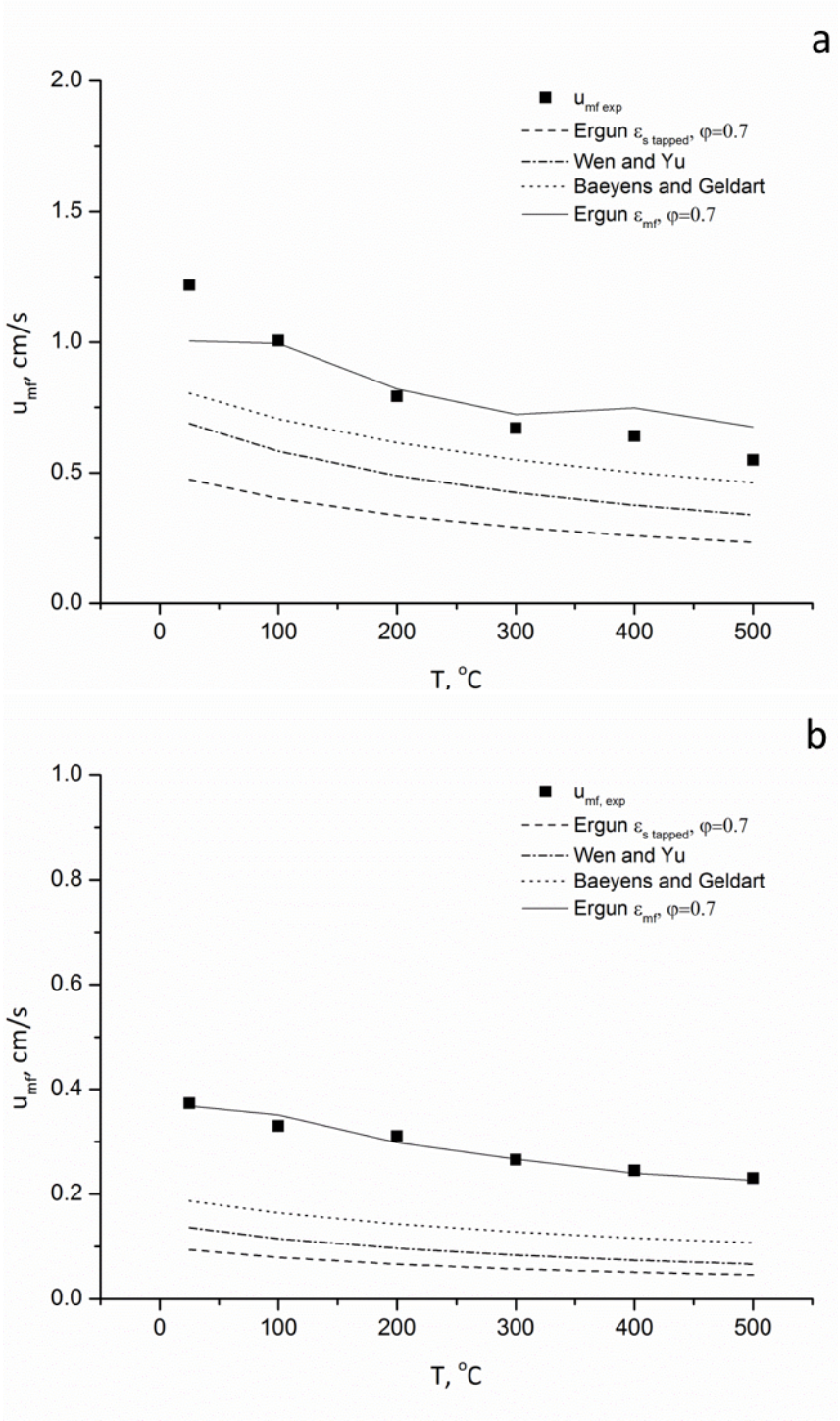

Figure 69 - Comparison between experimental and predicted u_{mf} values with increasing temperature: a) sample A5; b) sample A4.

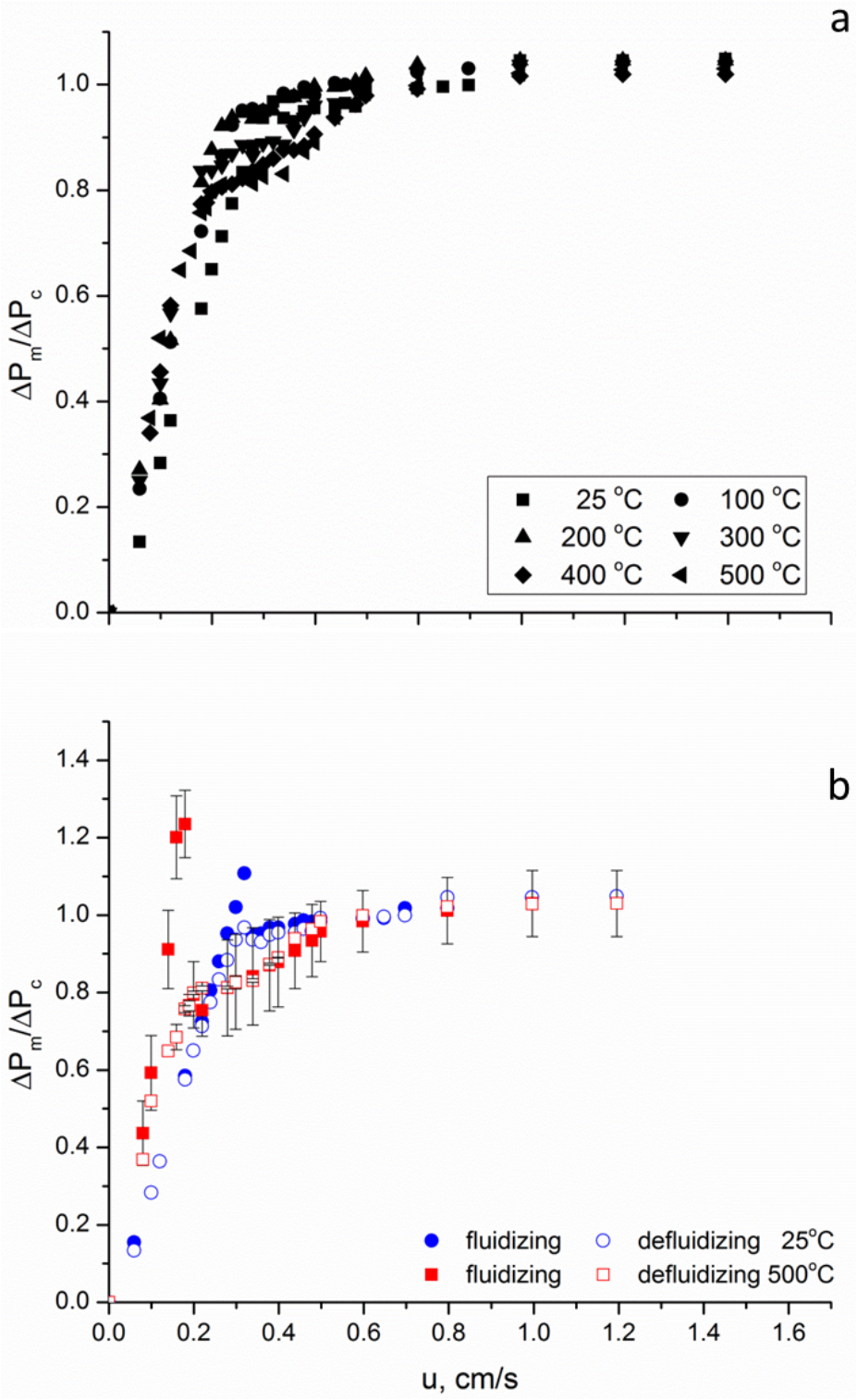

Figure 70 - Sample A3 (Geldart A): a) measured over calculated pressure drop profile in defluidization with increasing temperature; b) measured over calculated pressure drop profile when fluidizing and when defluidization with increasing temperature.

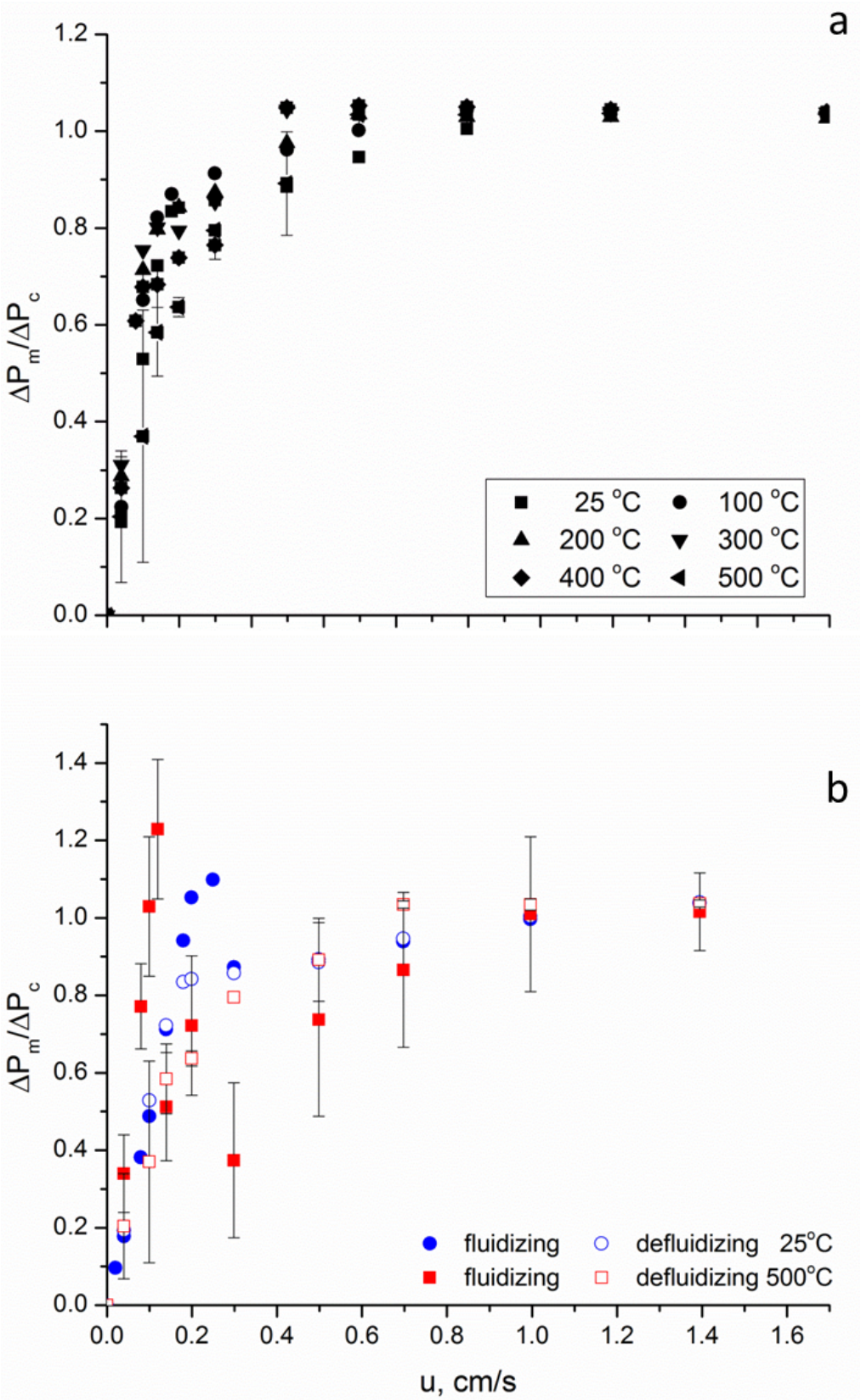

Figure 71 - Sample A2 (Geldart A/C): a) measured over calculated pressure drop profile in defluidization with increasing temperature; b) measured over calculated pressure drop profile when fluidizing and when defluidization with increasing temperature.

While increasing the gas flow rate, four different stages were notable for both samples:

- Stage 1: at low gas velocity, ΔP increases almost linearly with the flow rate
- Stage 2: increasing the gas velocity, ΔPm/ΔPc reaches its maximum value, larger than 1.
- Stage 3: small bubbles were seen breaking the surface and travelling through the bed in instable channelling. ΔPm/ΔPc ratio remained below 70-80% for sample S3 between ambient and 500 °C and below 70-50% for sample S2. Increasing the flow rate the pressure drop ΔP_m began to approach ΔP_c breaking the formed channels, as shown in Figure 73.
- Stage 4: for a further increase of the gas velocity, larger bubbles were seen all over the surface and the ratio ΔPm/ΔPc=1.

During stage 3, the fluidization behaviour was mainly characterized by instable channelling fluidization, very instable values of ΔPm/ΔPc, as shown in Figure 72. To better explain the fluidization behaviour, Figure 73 shows an instant picture of the flow pattern inside the reactor, using X-rays, for sample S2. The pictures are taken at four different gas velocities, 0.12, 0.3, 0.4 and 0.8 cm/s. An analysis of the images suggests that the unstable pressure drop profile between 0.15 and 0.6 cm/s is due to vertical channel is forming. Inspection of the images suggests that the unstable pressure drop profile between 0.12 and 0.6 cm/s is due to irregular by-pass of the gas through the bed particles causing vertical channels. Figure 73a shows a fixed bed for $u<u_{mf}$. Increasing the gas flow rate, the pressure drop starts to fluctuate and, according with Figure 73b, a non-horizontal bed surface can be observed. In video sequences, corresponding to the depression of the bed surface, it is possible to observe local variations of bed density, visible as fluctuation of grey scales, and of the bed surface, that can clearly be attributed to high gas velocity in the region due to channelling. A further increase of the flow rate causes an expansion of the channel, lower non-horizontal bed surface, with a consequent linear increase of the pressure drop (Figure **73**c).

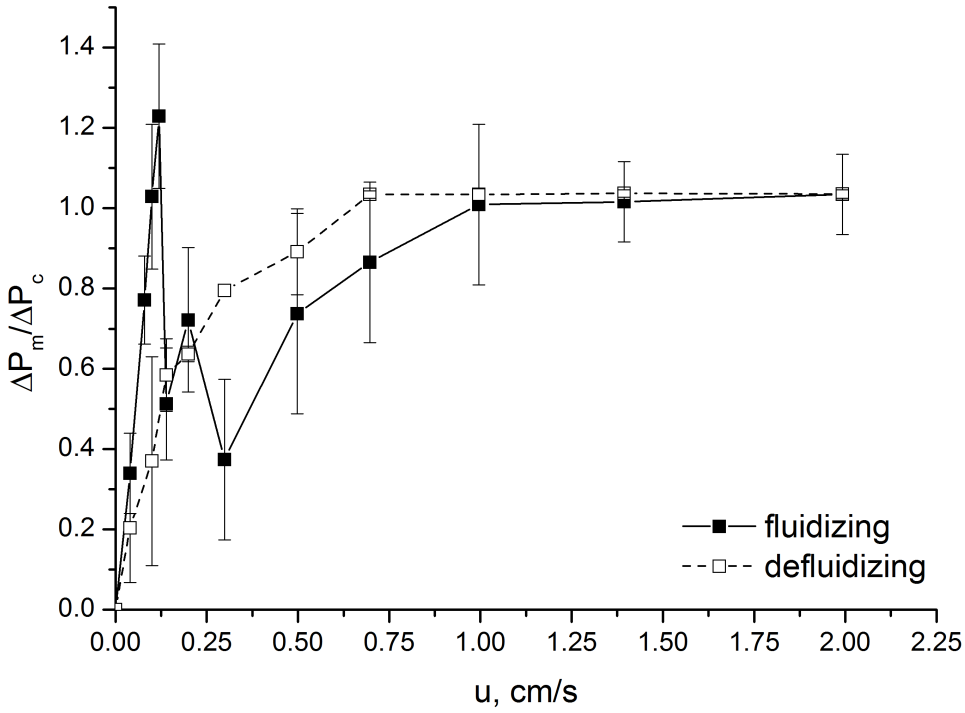

Figure 72 - Sample A2: measured over calculated pressure drop profile in fluidization and defluidization at 500 °C.

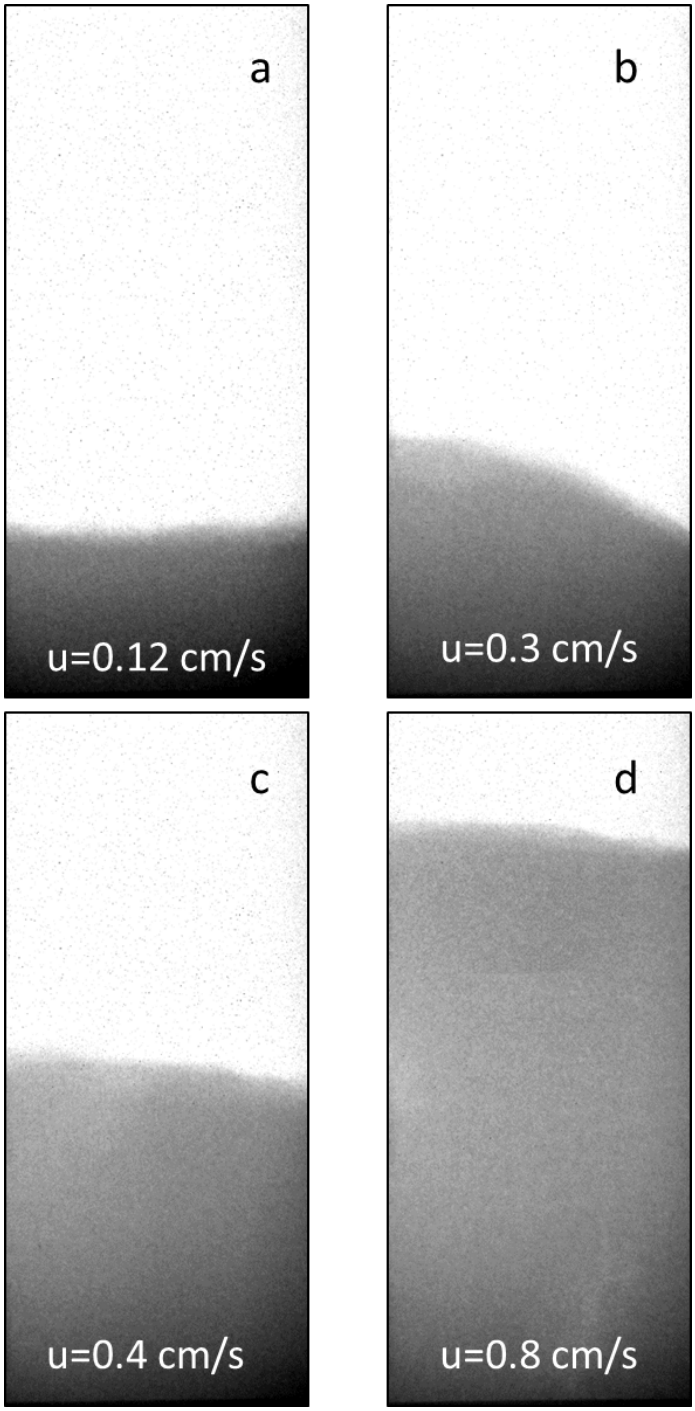

Figure 73 - X-rays images of the reactor for sample A2 at different flow rate at 500 °C.

The overshoot in the measured pressure drop reveals a slight degree of cohesiveness of the particles. The values of the overshoot in the pressure drop curve when increasing the gas velocity is noticeable at each temperature and are reported in Figure 74 for both samples. The plot shows an increase of the ratio up to 300 °C, between 300 °C and 500 °C the ratio is almost constant.

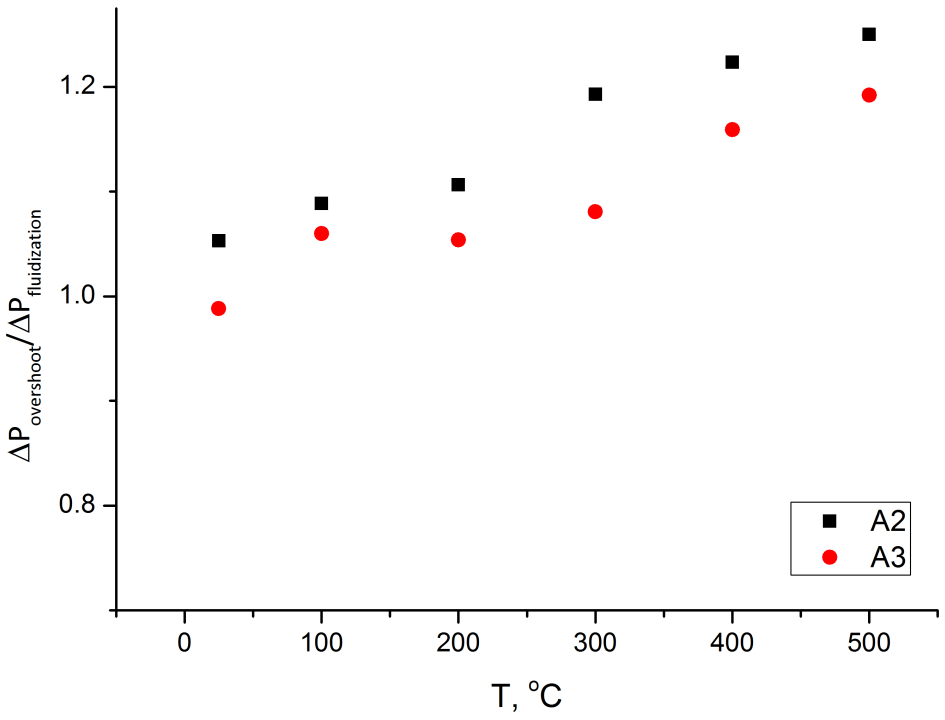

Figure 74 - Effect of temperature on the overshoot, ratio $\Delta P_{overshoot}/ \Delta P_{fluidization}$, for sample A3 and A2.

It should also be noted that a hysteresis phenomenon forms when increasing temperature, which was particularly more relevant for sample A2 (Figure 72). Several researchers found this phenomenon associated with the fluidization of nanoparticles [183,184]. The comparison between experimental minimum fluidization velocity against predictions is shown in Figure **75** and Table A3 in Appendix. In the case of samples A3 and A2, the comparison shows that the predictions underestimate u_{mf} and they are not able to follow the trend of the experimental u_{mf} at high temperature.

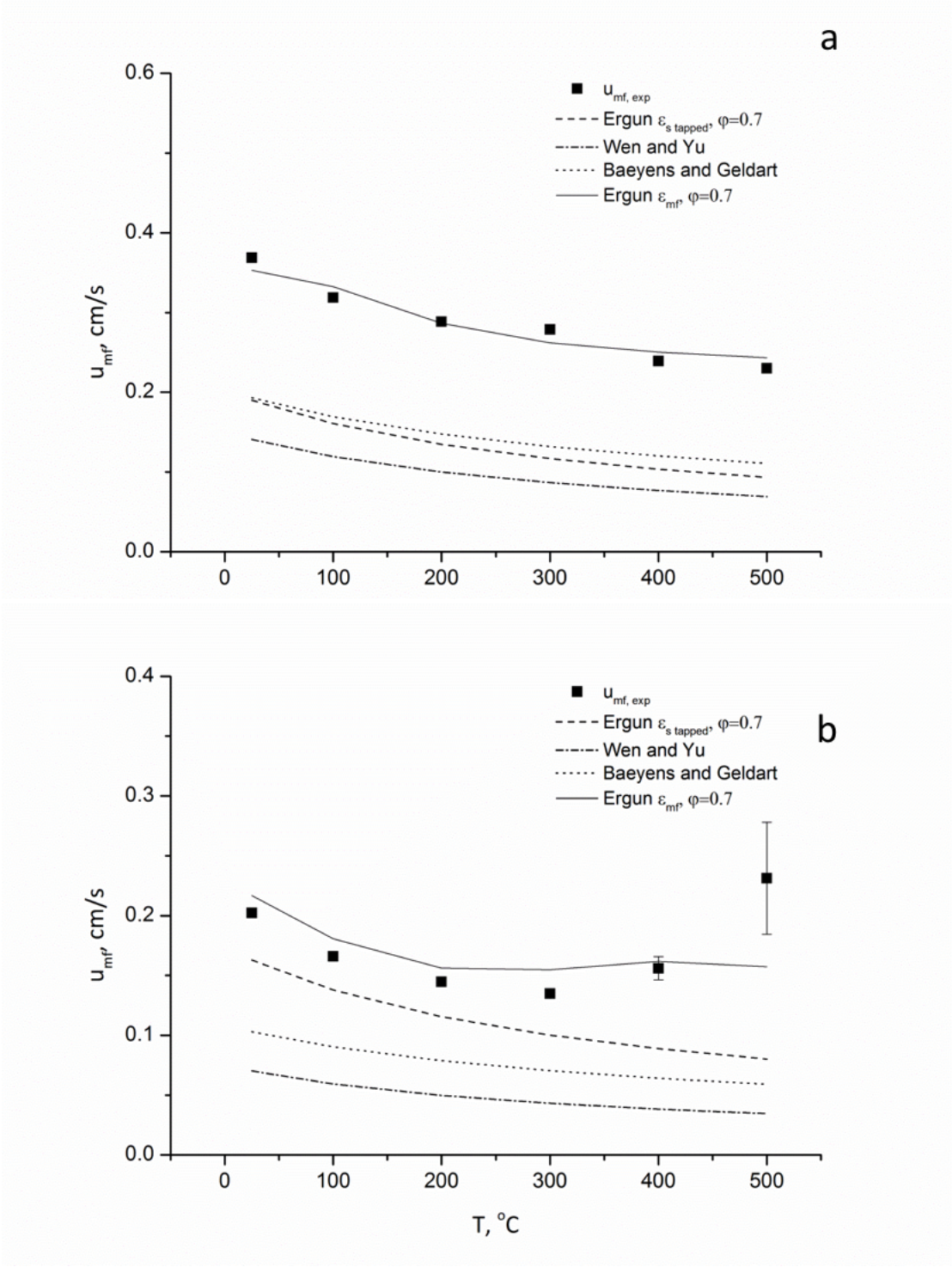

Figure 75 - Comparison between experimental and predicted u_{mf} values with increasing temperature: a) sample A3; b) sample A2.

The minimum fluidization conditions were also analysed in term of the voidage of the bed in such instant, ε_{mf}. Once the minimum fluidization conditions were achieved, the X-ray facility was used to take images of the bed at each temperature. Then the voidage of the

bed was calculated using Eq. 35, see section 3.8.3. The data are reported in Figure 76. A maximum of 15% relative increase in ε_{mf} was observed for the finest sample A2.

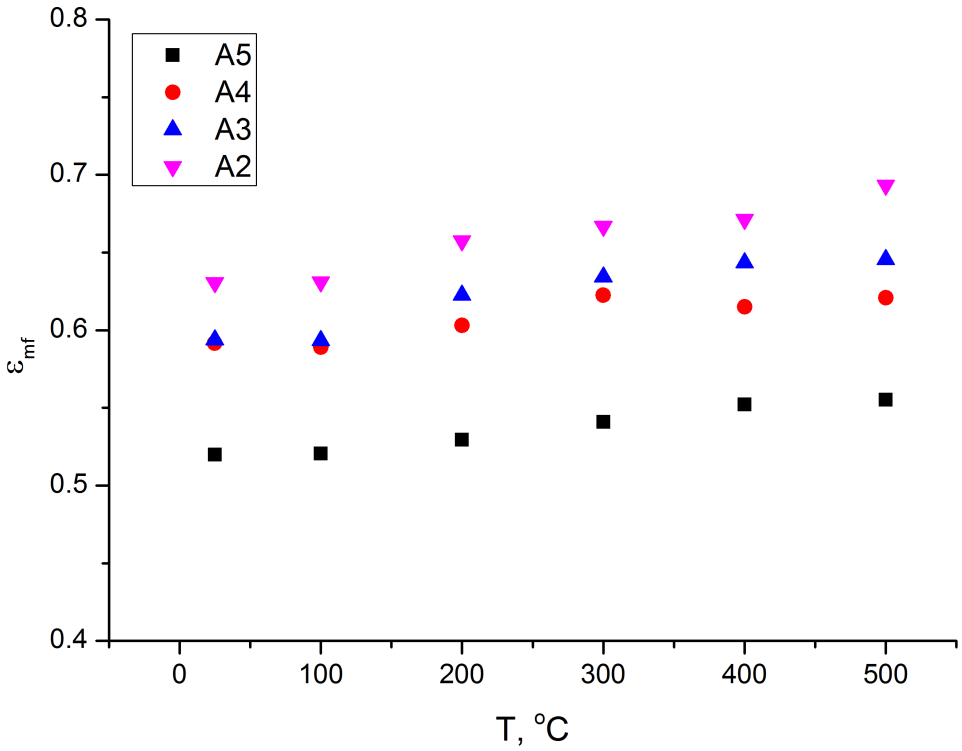

Figure 76 - Effect of temperature on the bed voidage at the minimum fluidization condition experimental values in Table A2, in Appendix.

The Ergun correlation (Eq. 56) was used to calculate the particle shape factor, ϕ, of each samples using the experimental values of u_{mf} and ε_{mf}, as suggested by Knowlton [6]. The values obtained at ambient condition are reported in Table 13. The results show that the shape factor varies between 0.7 and 1.2. Values larger than 1 do not have any physical meaning, thus it represents just a coefficient needed to adjust the mean particle diameter. For this reason, the shape factor of the particles was geometrically estimated using the SEM pictures and considering a parallelepiped shape of the particles. In particular, it was considered a prevalent dimension of the parallelepiped and the results show values of ϕ between 0.68 and 0.75. Thus, a constant value of ϕ=0.7 was chosen. The applicability of the Ergun correlation was also tested using the experimental values for the voidage at minimum fluidization velocity and the values of the shape factor estimated from the SEM pictures. Results are in solid lines in Figure 75. A better fitting among experimental and predictive data was achieved by considering the changes in the voidage of the bed with temperature.

Table 13 - Shape factor back-calculated from the Ergun equation.

	A5	A4	A3	A2
ϕ	0.7	0.5	1.1	1.2

The finest sample tested A1 belongs to Group C of Geldart classification. This particle sample was characterized by a very high degree of cohesiveness. Fluidization conditions could not be achieved at any temperature between ambient and 500 °C. An irreversible defluidization occurred due to the dominant effect of interparticle forces over hydrodynamic forces. Figure 77 and Figure 78 report the pressure drop curves at ambient condition and the snapshot of the flow in the reactor between 0 and 6.5 cm/s. From the X-rays images, the structure of the bed can be observed at the different flow rate. According to Figure 78, channelling phenomena occur and, increasing the flow rate, it became much clearer that the channels develop as horizontal cracks leading to solid plugs rising and braking.

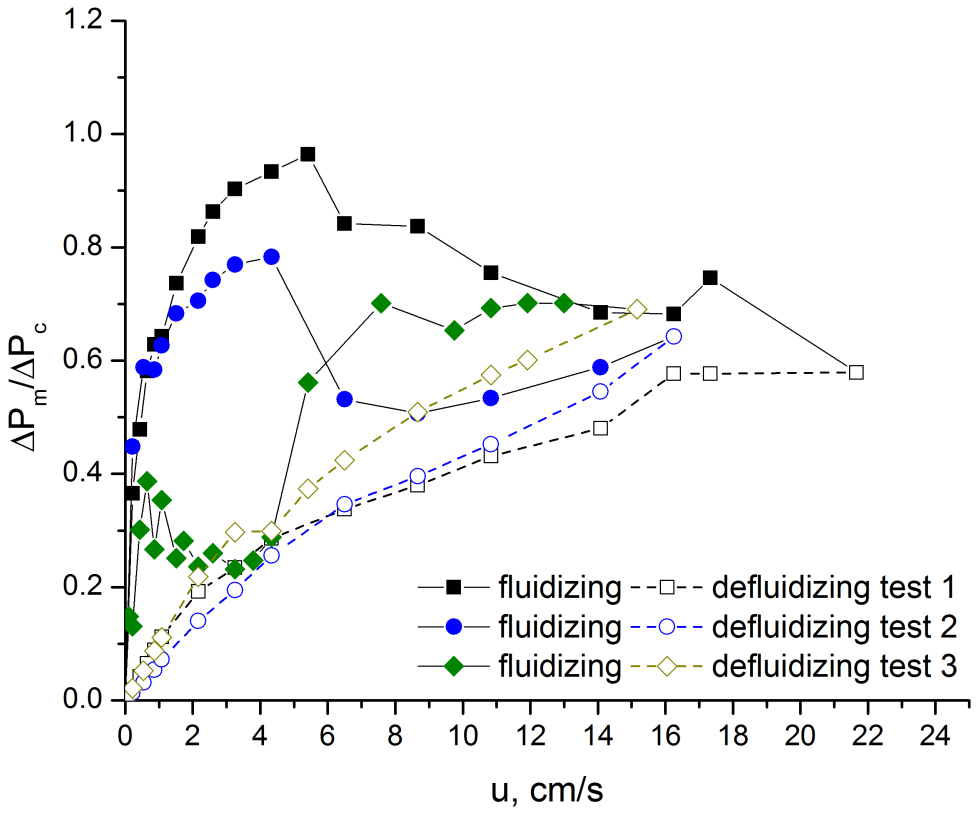

Figure 77 - Pressure drop profile for sample A1 (Geldart C) at ambient condition.

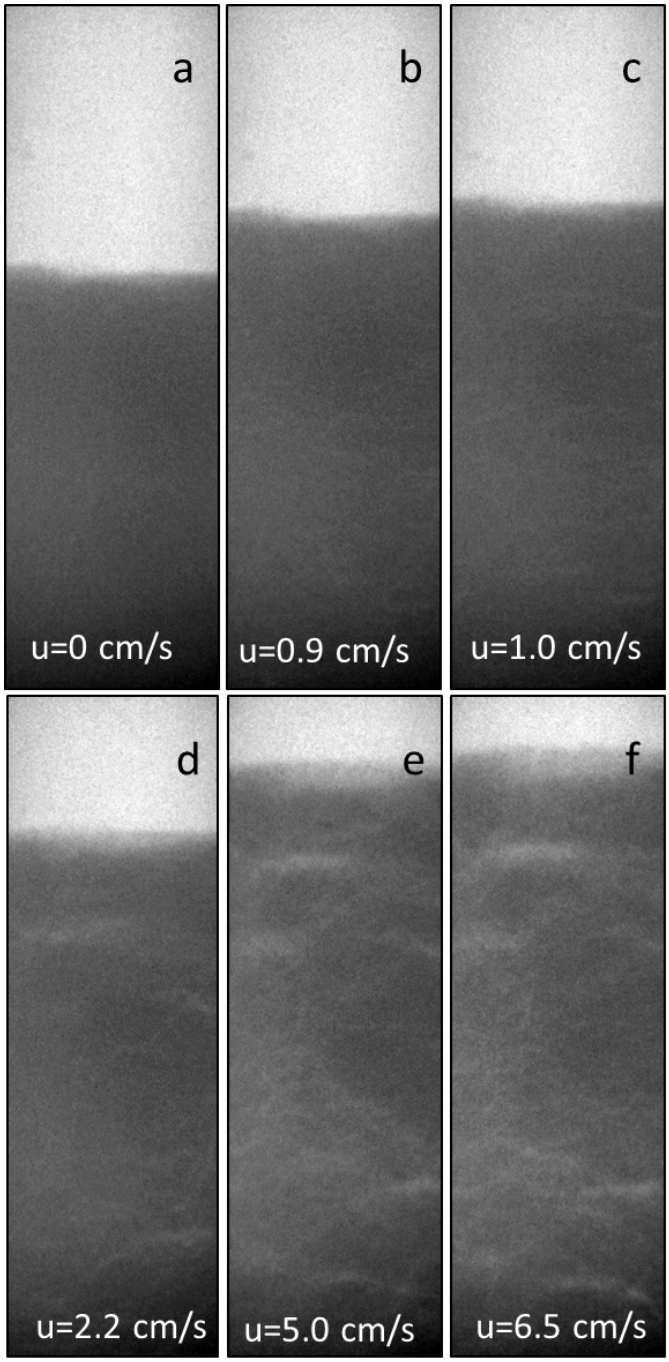

Figure 78 - Snapshot inside the reactor of sample A1 at ambient condition at different flow rates.

6.2 The effect of temperature on bed expansion profile

The bed expansion profile was determined from the X-ray imaging technique and following the experimental procedure described in section 3.8.4. It is also worth pointing out that the expansion profiles were obtained with several repeated experiments. The profiles

obtained for all samples at each temperature are reported in Figure 79. It reaches a maximum value at around 300 °C, a further increase of temperature has a negligible effect on the bed expansion. Thermogravimetric analysis, described in chapter 4, showed no weight loss at the temperature range investigated for all powder samples, thus this behaviour cannot be justified with changing in weight sample. Diversely it can be on the basis of the relative weight of the temperature effect between the gas properties and the particle compressive strength p_f [171]. In particular, for temperatures between 25 °C and 300 °C, the temperature mainly affects the gas properties (density and viscosity), instead, for temperatures higher than 300 °C, these particles show a significant decrease of the compressive strength [171] with a relative increase of interparticle forces.

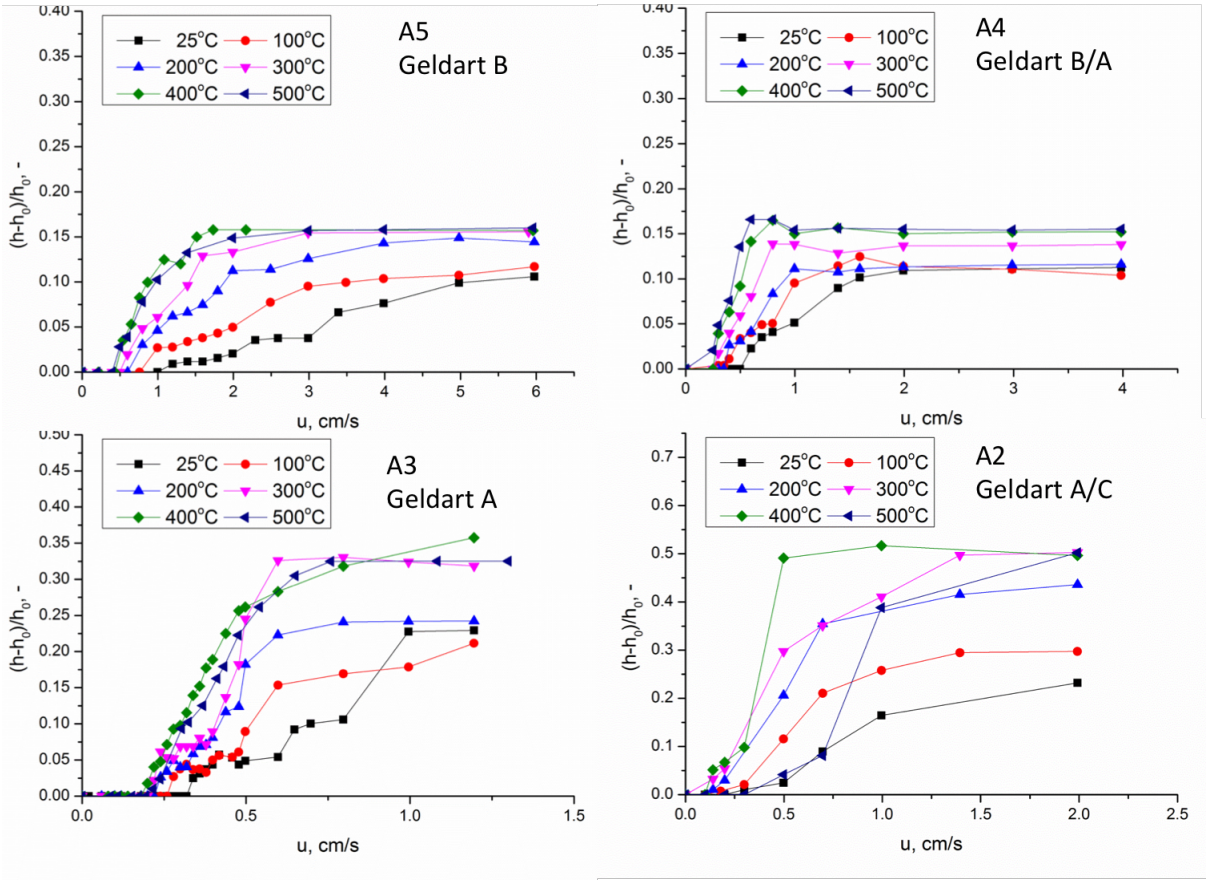

Figure 79 - Effect of temperature on bed expansion profile of sample A5, sample A4, sample A3 and sample A2.

Expansion appeared to be affected by temperature, and similar qualitative features were observed for all samples. The starting velocity for the bed expansion decreased with temperature, while the magnitude of the expansion increased with temperature and with decreasing the particle size distribution, as shown in Figure 80.

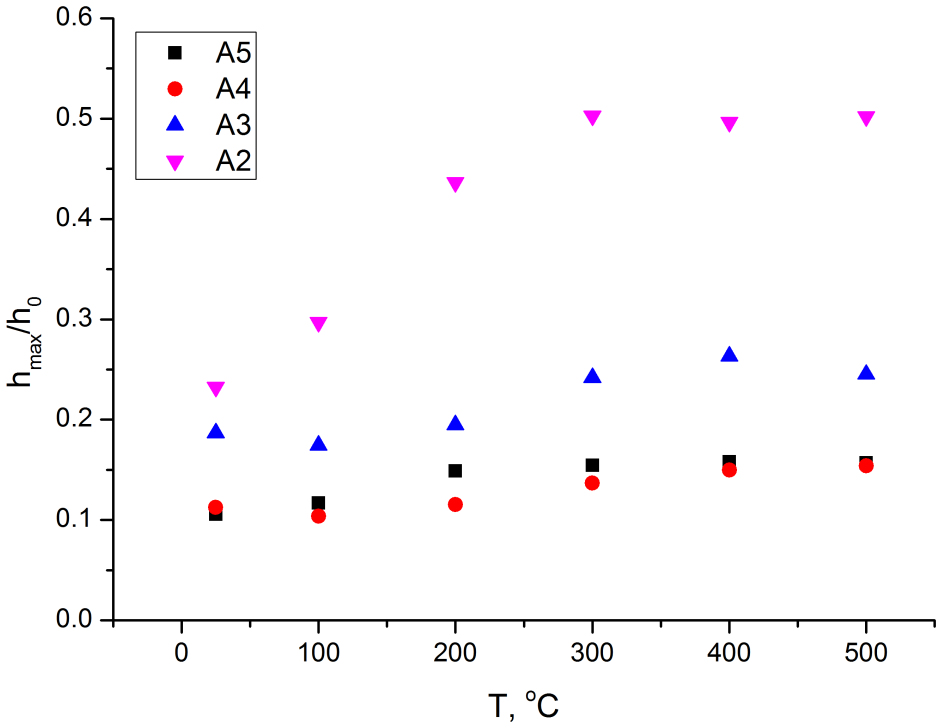

Figure 80 - Effect of temperature on the ratio h_{max}/h_0 for all the materials.

A considerable increase of the bed expansion occurred for all the samples from 20 °C up to 300 °C: a 15% relative increase was observed for samples A5 and A4, about 24% for A3, and a relative increase of up to 50% was observed for A2.

Figure 81 shows the comparison of the bed height recorded while increasing and decreasing the flow rate. A slightly hysteresis can be observed at high temperature for samples A3 and A2. The higher height of the bed in defluidizing condition compared with the one in fluidizing condition, is due to the fact that when the gas velocity breaks all the interaction among particles (fluidizing condition) the excess gas goes to increase the bed voidage of the dense phase, hence changing the structure of the bed. More specifically, as the average particle size decreases, larger cohesion occurs between particles, resulting in increased frictional forces (since friction is proportional to the normal force). The increased friction causes a resistance by the particle bed to compaction under its own weight. A similar behaviour was found by LaMarche et al. [52] in their experiments in presence of high air relative humidity.

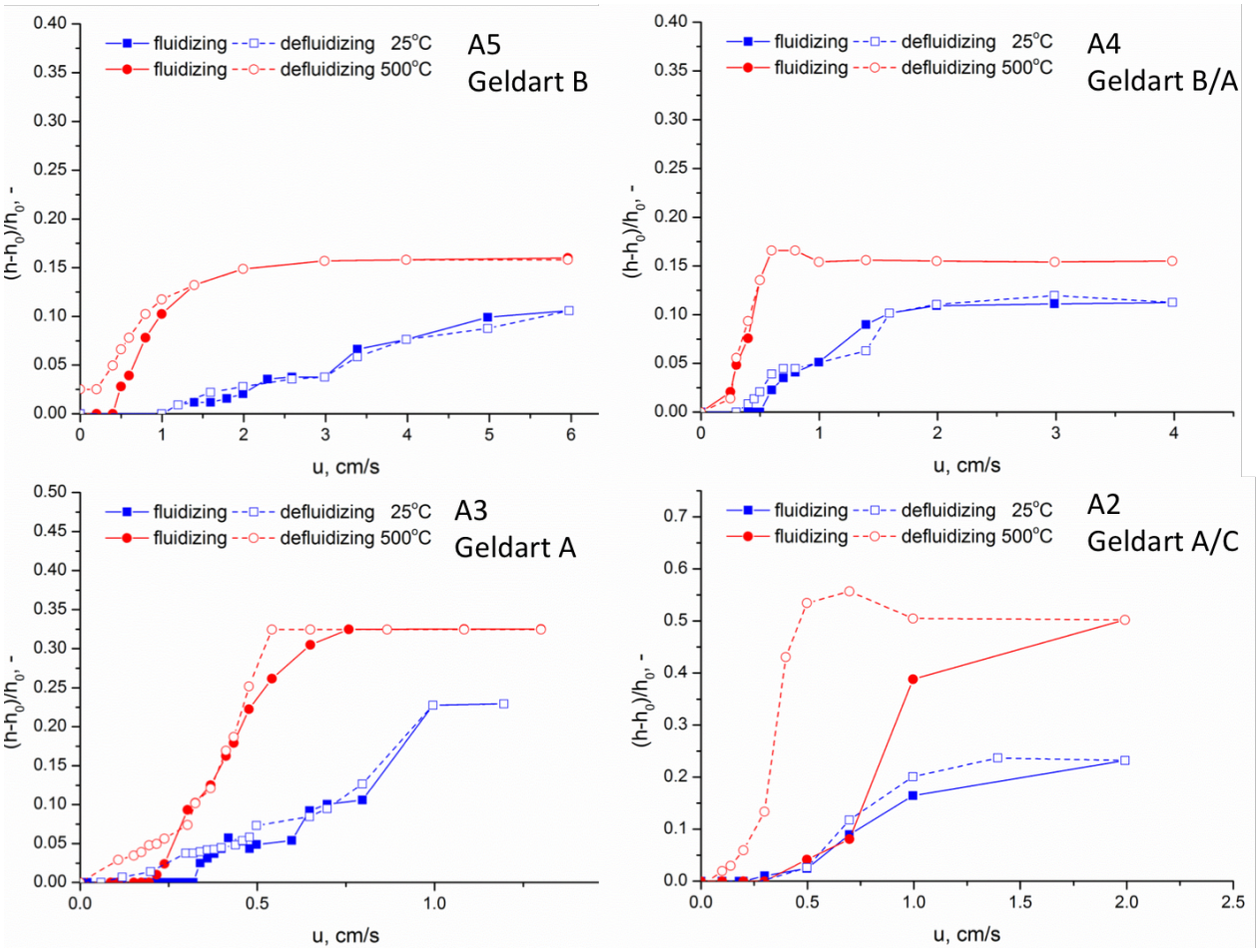

Figure 81 - Comparison fluidizing and defluidizing profile for sample A5, sample A4, sample A3 and sample A2.

6.2.1 The settled bed voidage

Figure 82 reports the settled bed voidage (ε_s) calculated in slow and fast (Bed Collapse Test) defluidization as a function of temperature for all the powders tested. ε_s was found to increase by about 9% with increasing temperature for both cases, slow and fast defluidization. This trend is in agreement with previous findings by Lettieri in experiments carried out on FCC powders [159]. The values obtained from bed collapse measurements were found to be a little higher for all fresh materials than those measured after slow defluidization.

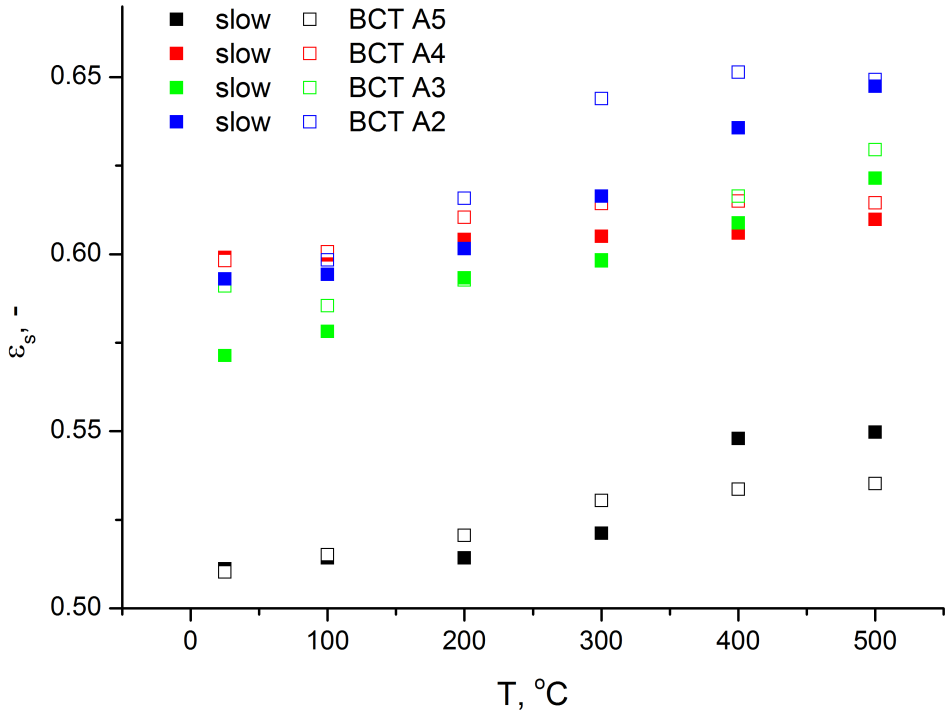

Figure 82 - Effect of temperature on the settled voidage of the bed.

6.2.2 The expansion profile in Richardson-Zaki form

The expansion profiles were also analysed using the Richardson-Zaki [80] equation, Eq. 57, for homogeneous bed expansion.

$$u = u_t \varepsilon^n \qquad \text{Eq. 57}$$

u_t represents the terminal velocity of a single particle and n is the index of the R-Z equation. Experimental values of u_t and n were extrapolated from the expansion profiles as a function of temperature and are denoted as n* and u_t*. Typically, the Richardson-Zaki equation plots the fluidizing velocity as a function of the voidage, on logarithmic scales. Figure 83 shows the expansion profile of all the samples in the R-Z form.

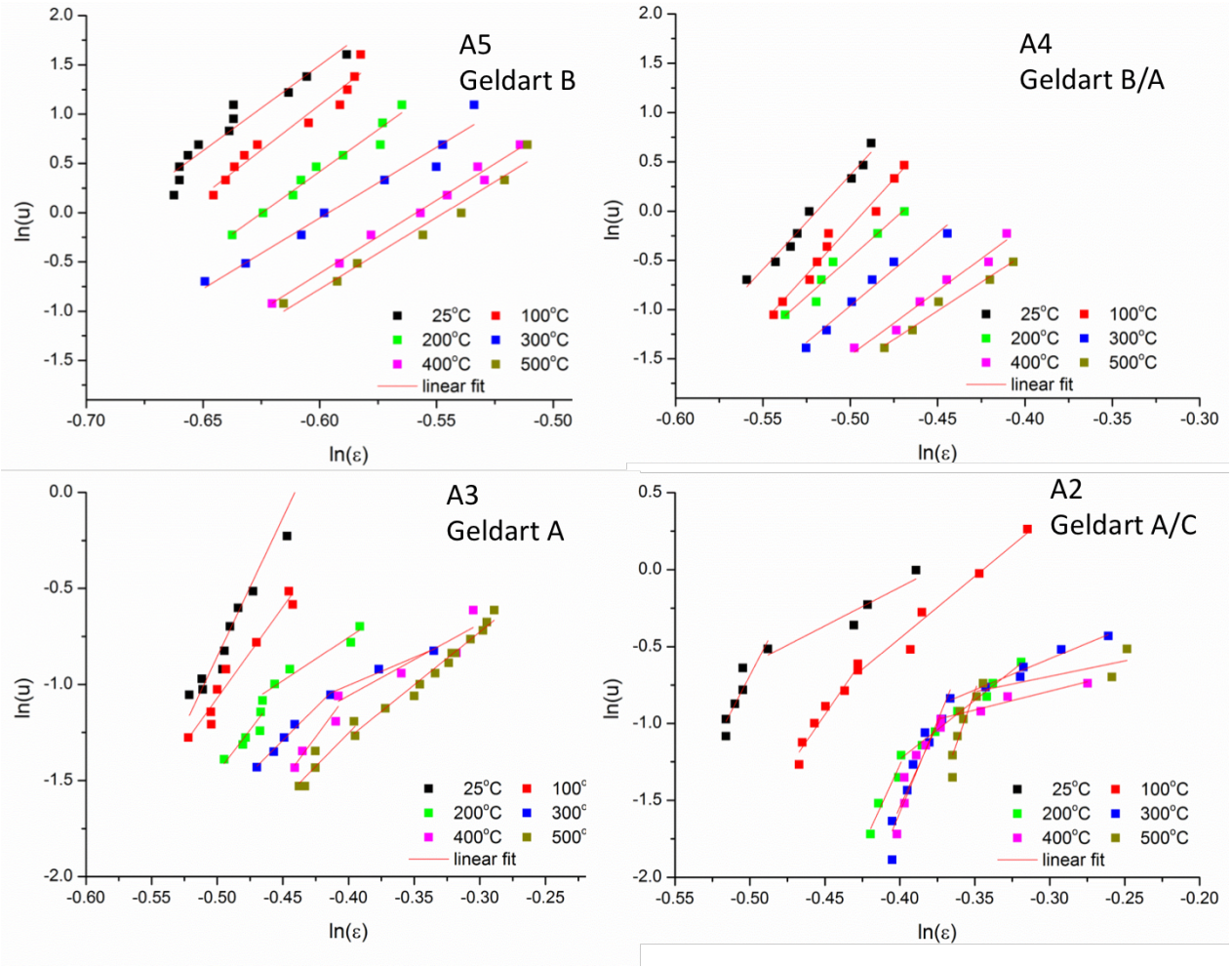

Figure 83 - Bed expansion in the Richardson-Zaki form profile for sample A5, sample A4, sample A3 and sample A2.

Different bed expansion profiles were found for samples A5 and A4 compared with sample A3 and A2. In particular, the two largest particle size distributions, samples A5 and A4, show a single slope, n*, for a large range of gas velocity. Diversely the bed expansion profiles of the finest powders, samples A3 and A2, are described by two different lines with two different slopes, one for lower bed voidage and another for higher bed voidage, as shown in Figure 83a-b. The Richardson-Zaki parameters were estimated for each curve and reported in Table 14. The values of the voidage where the slope change occur, $\varepsilon_{changing\ slope}$, are reported in Figure 84. An increase of $\varepsilon_{changing\ slope}$ with temperature was observed. This parameter can identify the point at which the IPFs became dominant compared with the HDFs.

Both n and u_t were found to decrease with increasing temperature. These results are in agreement with Lettieri et al. [93]. These experimental values were also compared with the

prediction values obtained using the drag equation for the settling velocity of a single particle. The Stokes Law was used to determine u_t and the following relations were used to estimate the index n:

$$\mathrm{Ga} = 18\mathrm{Re_t} \quad \text{for } \mathrm{Ga} \leq 3.6$$

$$\mathrm{Ga} = 18\mathrm{Re_t} + 2.7\mathrm{Re_t}^{1.687} \quad \text{for } 3.6 \leq \mathrm{Ga} \leq 500 \qquad \text{Eq. 58}$$

$$\mathrm{n} = 4.8 \quad \mathrm{Re_t} \leq 0.2$$

$$\mathrm{n} = 4.6\mathrm{Re_t}^{-0.03} \quad 0.2 \leq \mathrm{Re_t} \leq 1 \qquad \text{Eq. 59}$$

$$\mathrm{n} = 4.6\mathrm{Re_t}^{-0.1} \quad 1 \leq \mathrm{Re_t} \leq 500$$

Table 14 reports the mathematical and experimental values of n and u_t for all sample tested and temperatures. The calculated value for n is constantly 4.8, because of the smaller particles and thus smaller Re_t. The calculated u_t decreases with temperature, as it is observed in the experiments, except for the finest sample A2. However, the calculated values of u_t are greater than the experimental ones for sample A3, while they are smaller for sample A2.

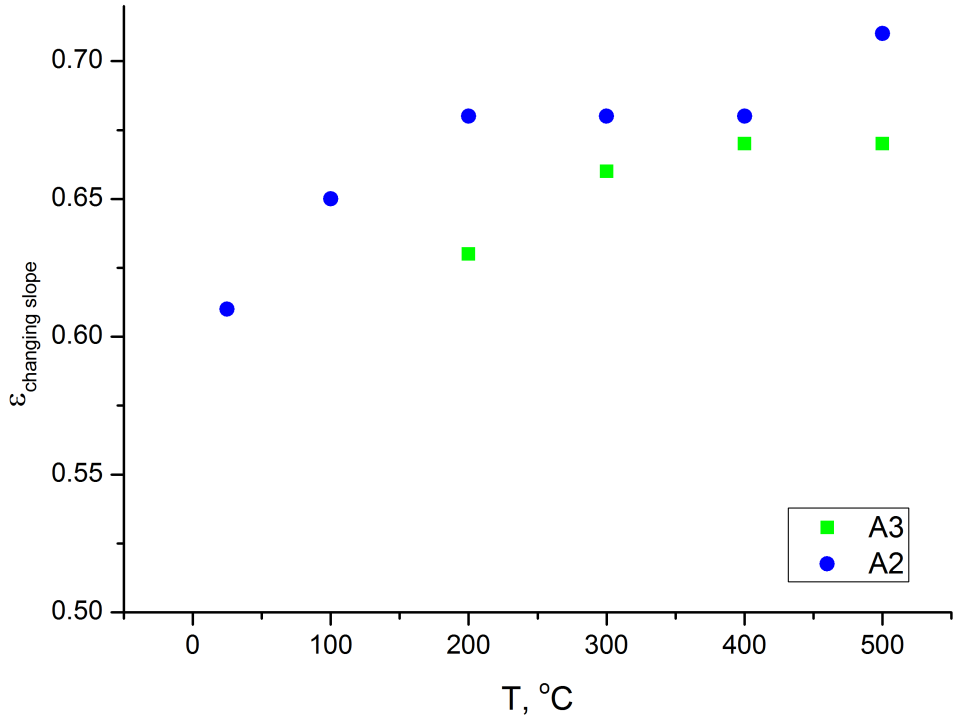

Figure 84 - Effect of temperature on the voidage at which the slope changes for the R-Z equation.

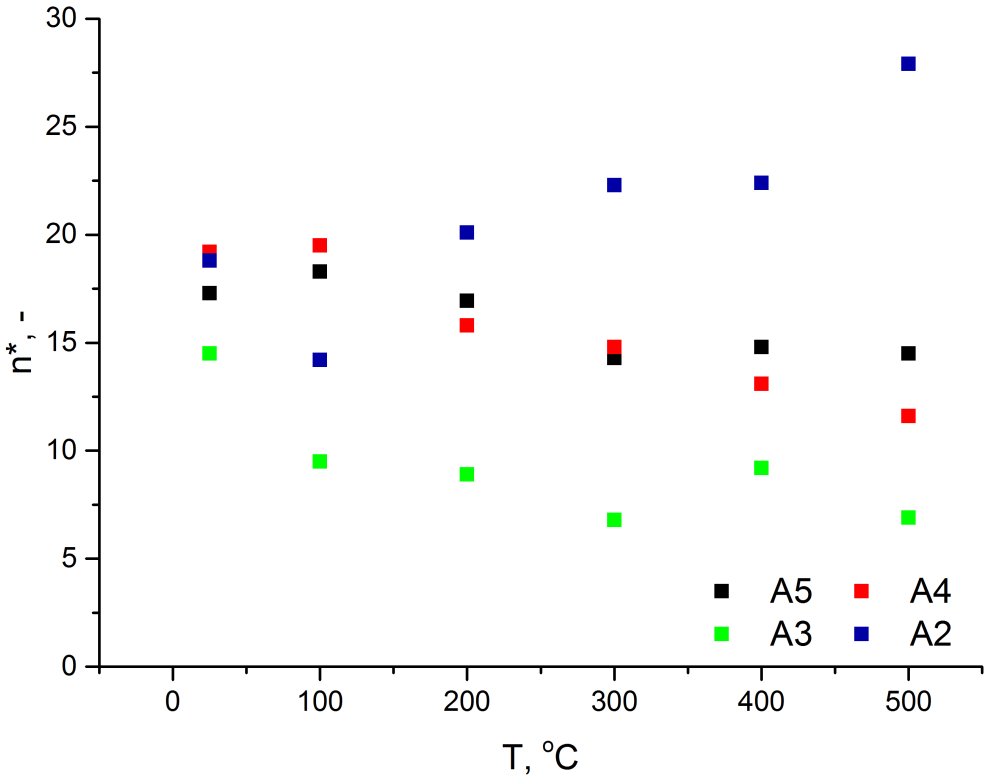

Figure 85 - Effect of temperature on the index n* of the Richardson-Zaki equation.

Table 14 - Comparison of the mathematical and experimental values for n and u_t of the R-Z equation.

	A5				A4			
T, °C	u_t*	u_t	n*	n	u_t*	u_t	n*	n
25	11.6	75.0	17.3	4.1	9.8	27.0	19.2	4.8
100	12.0	63.5	18.3	4.4	9.6	22.9	19.5	4.8
200	10.6	53.3	17.0	4.6	7.4	19.2	15.8	4.8
300	8.6	46.2	14.3	4.7	6.4	16.6	14.8	4.8
400	8.3	41.0	14.8	4.7	5.1	14.8	13.1	4.8
500	7.9	37.0	14.5	4.8	4.2	13.3	11.6	4.8
	A3, $\varepsilon > \varepsilon_{changingslope}$				A2, $\varepsilon > \varepsilon_{changingslope}$			
	u_t*	u_t	n*	n	u_t*	u_t	n*	n
25	6.4	5.8	14.5	4.8	8.7	3.5	18.8	4.8
100	3.7	4.8	9.5	4.8	5.4	3.0	14.2	4.8
200	3.0	4.1	8.9	4.8	7.0	2.5	20.1	4.8
300	1.8	3.6	6.8	4.8	7.9	2.2	22.3	4.8
400	2.7	3.2	9.2	4.8	7.0	1.9	22.4	4.8
500	1.5	2.5	6.9	4.8	9.0	1.7	27.9	4.8
	A3, $\varepsilon < \varepsilon_{changingslope}$				A2, $\varepsilon < \varepsilon_{changingslope}$			
	u_t*	u_t	n*	n	ut*	ut	n*	n
25	6.4	5.8	14.5	4.8	1.9	3.5	5.0	4.8
100	3.7	4.8	9.5	4.8	2.8	3.0	8.0	4.8
200	0.8	4.1	4.1	4.8	1.9	2.5	7.8	4.8
300	0.2	3.6	2.9	4.8	0.9	2.2	4.9	4.8
400	0.4	3.2	3.7	4.8	2.4	1.9	2.4	4.8
500	0.9	2.5	5.5	4.8	1.6	1.7	1.6	4.8

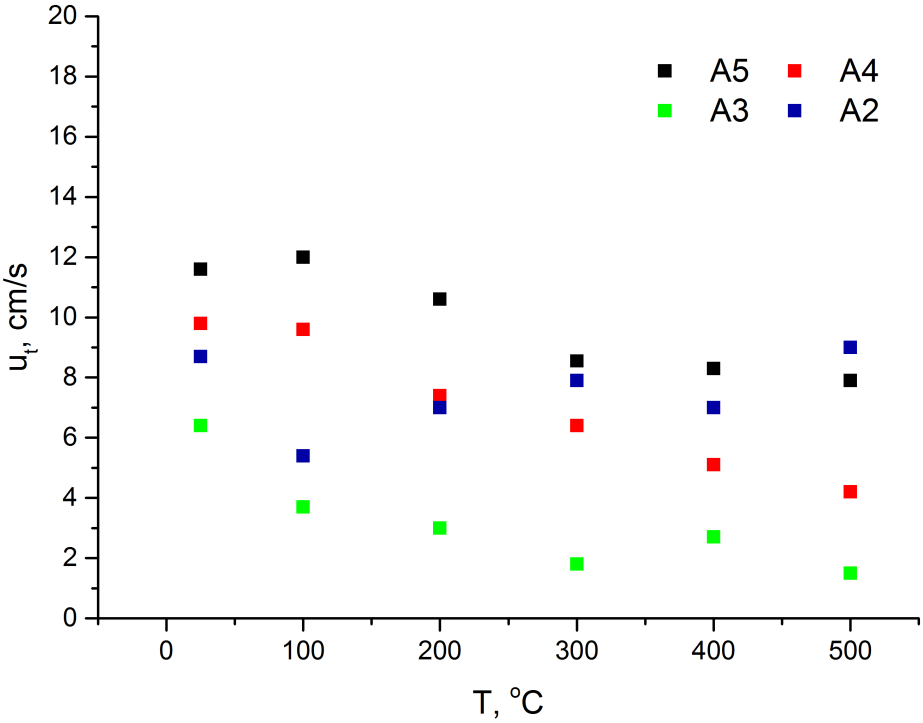

Figure 86 - Effect of temperature on u_t of the Richardson-Zaki equation.

6.3 The effect of temperature on the aereability of the particles: BCT

In this work the bed collapse tests are used to compare the collapse parameters obtained for all the samples tested with increasing temperatures. The same initial gas velocity was chosen for all the experiments, with respect to the minimum fluidization velocity in order to produce meaningful results. A velocity six times the minimum fluidization condition was chosen as the initial gas velocity for all the powders at all the temperatures investigated [111,185]. Therefore, it must be said that the results obtained by the BCT technique are valid only for the initial gas velocity chosen. However, the BCT can be used to make comparisons between the aeratability of the different powders under analysis and to assess the role of the process conditions, i.e. temperature and mean particle size, on the powders' flowability. All the experimental values are reported in Appendix A4.

6.3.1 Experimental bed collapse profiles

Figure 87 shows the bed collapse profiles obtained for all the samples and for all the temperatures at the same initial fluidizing velocities. The collapse profiles were found to change both with particle size and temperature.

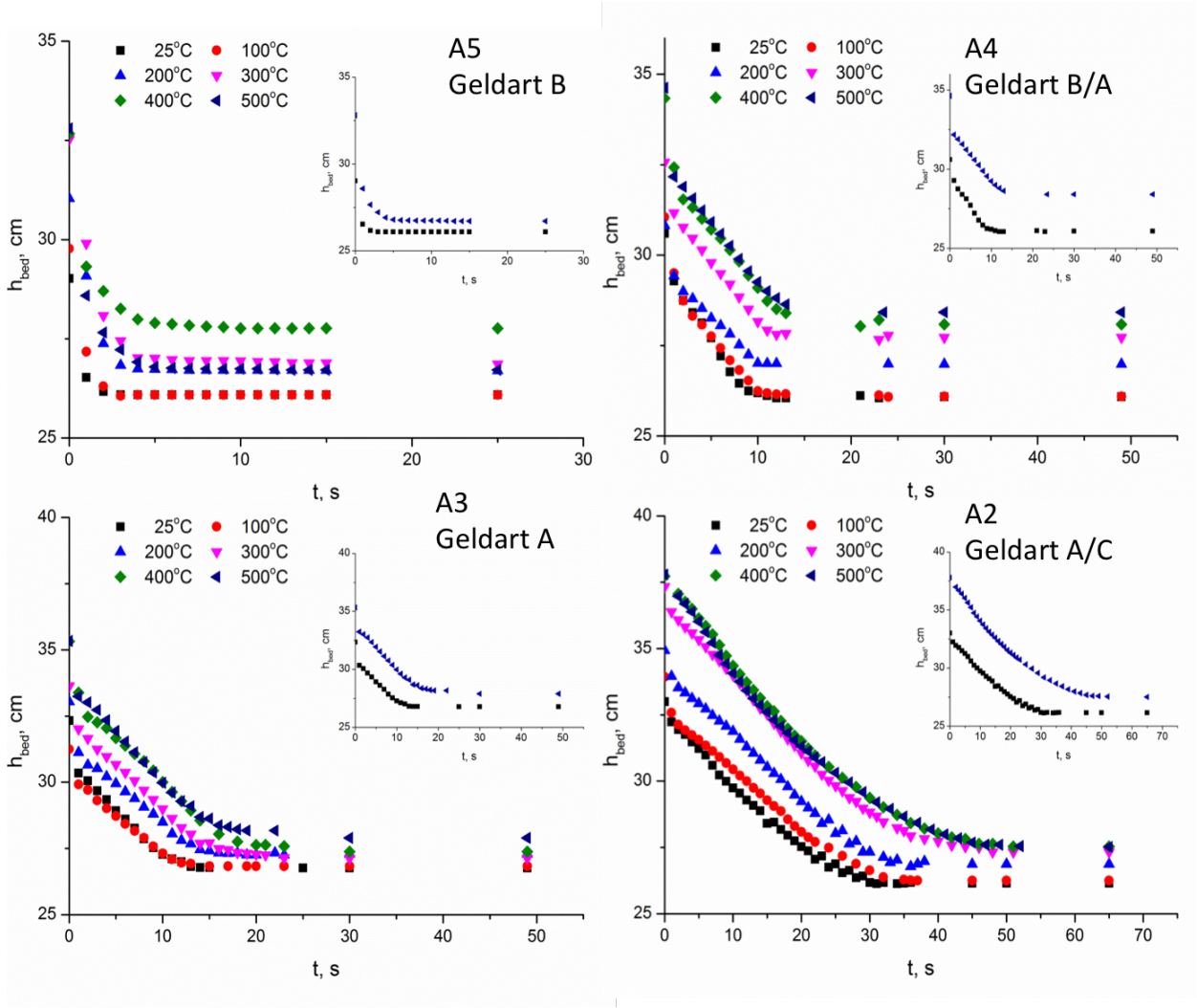

Figure 87 - Effect of temperature the bed collapse profiles for samples A5, sample A4, sample A3 and sample A2.

In particular, the largest samples, A5, at ambient condition behave like a typical sample B Geldart classification. The collapse profile is characterized by only the bubbling escape stage, thus as soon as the bubbles are expelled the solids reach the final static bed height. Differently, for temperature above 300 °C, the bubbling escape stage follows two slopes, meaning two velocities can be observed. The comparison of bed collapse profiles, with the X-rays images, shows that in the very first second the largest bubbles were seen to vanish,

after that, a couple of seconds were needed to expel the smaller bubbles (Figure 88). Figure 89 shows an elaboration of the X-rays images of the bubbles in the first 2.5 seconds. It is clear that the size of the bubbles initially expelled is larger than that of the bubbles expelled in the second step (1< t <2.5 s). The collapse profiles for sample A4 and A3 show three different stages, Figure 87b-c. First a very fast bubbling escape occurs, less than couple of seconds, then the hindered sedimentation takes place at constant rate, finally solids consolidation can be observed. The latter became more prominent when increasing the temperature and with smaller mean particle size. Figure 87d reports the collapse profiles for the finest sample tested, A2. The findings reveal a typical behaviour of a Group A material up to 300 °C. When increasing temperature, the bubbling escape stage became less noticeable and the profile is very similar to that of Group C material, as it can be seen in Figure 87d. The comparison with the X-ray images reveals that bubbles are present also at high temperature, thus the experimental findings suggest that the bubbling escape rate is very similar to the hindered sedimentation velocity. From the plot, it can be seen that at high temperature the solid sedimentation stage becomes very long and its length is comparable with the length of the hindered sedimentation.

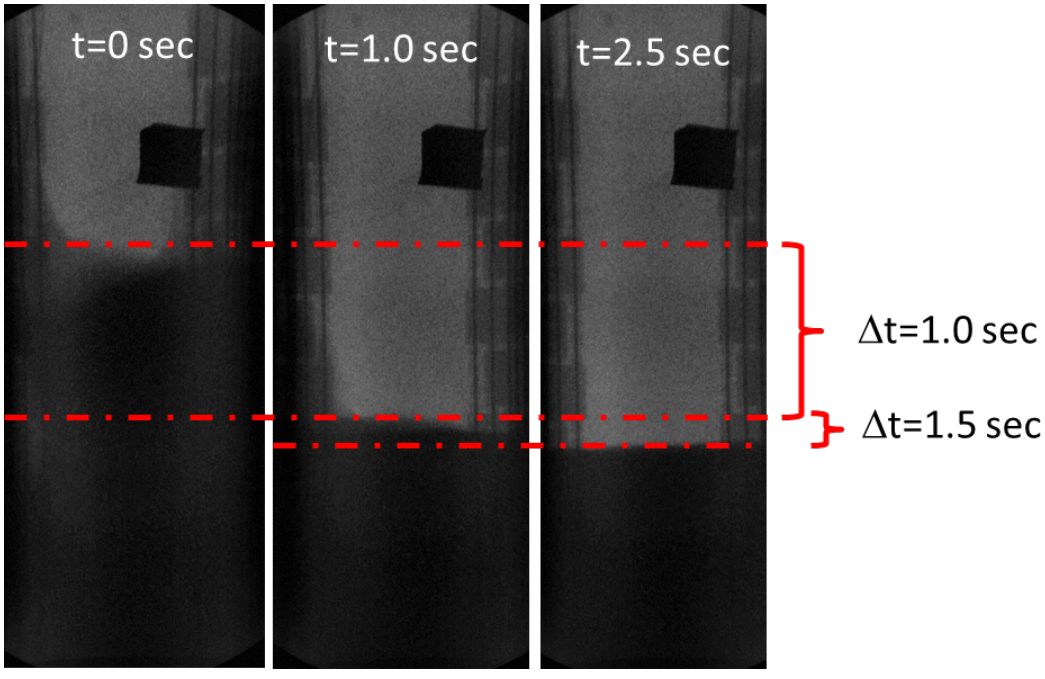

Figure 88 - X-ray images for bed collapse test of sample A5 at 0, 1 and 2.5 second.

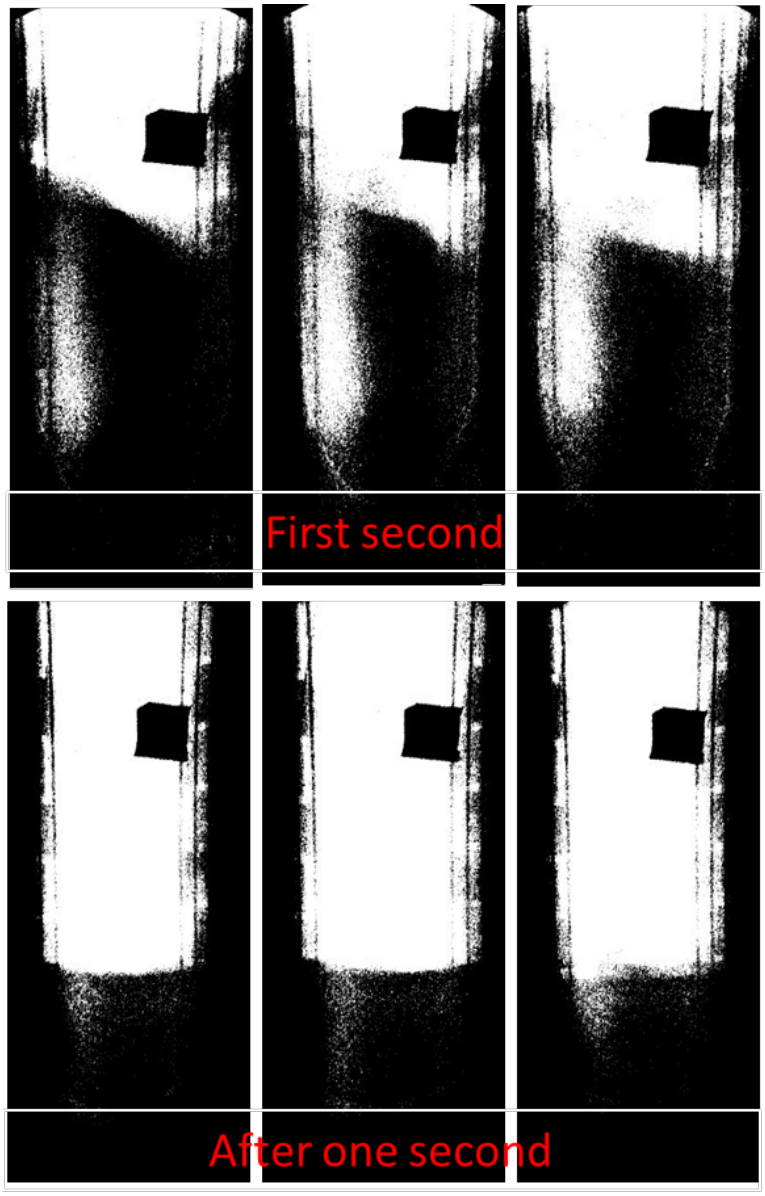

Figure 89 - Zoom on the characteristic dimension of the bubbles.

The bed collapse curves with the linear fit for sample A2 are shown in Figure 90. In this particular case, two different slopes for the hindered sedimentation can be observed, one for lower voidages and another one for higher voidages. Table 15 compares the values of the slope, the time and the height of the bed for large and small voidage of the bed. It can be seen that a relevant change in term of the time occurs around 400 °C for small ε. The latter can be attributed to an active role of the IPFs among particles. At a certain voidage of the bed, ε*, the IPFS became significant in the structure of the bed making the sedimentation process dependent on a spatial reorganization of the particles.

Table 15 - Values of the slope, the time and the height of the bed for large and small voidage of the bed for sample A2.

T °C	u_t, cm/s	ε > ε*			ε < ε*			Δt=t_1-t_2, s
		slope	t_1, s	h_{bed}, cm	slope	t_2, s	h_{bed}, cm	
25	3.5	0.26	21	27.4	0.12	31	26.1	10
100	3.0	0.23	22	27.7	0.14	32	26.4	10
200	2.5	0.24	22	28.8	0.16	33	26.9	11
300	2.2	0.27	25	29.8	0.13	35	27.3	10
400	1.9	0.3	26	30.1	0.10	48	27.6	22
500	1.7	0.3	25	30.3	0.10	49	27.6	24

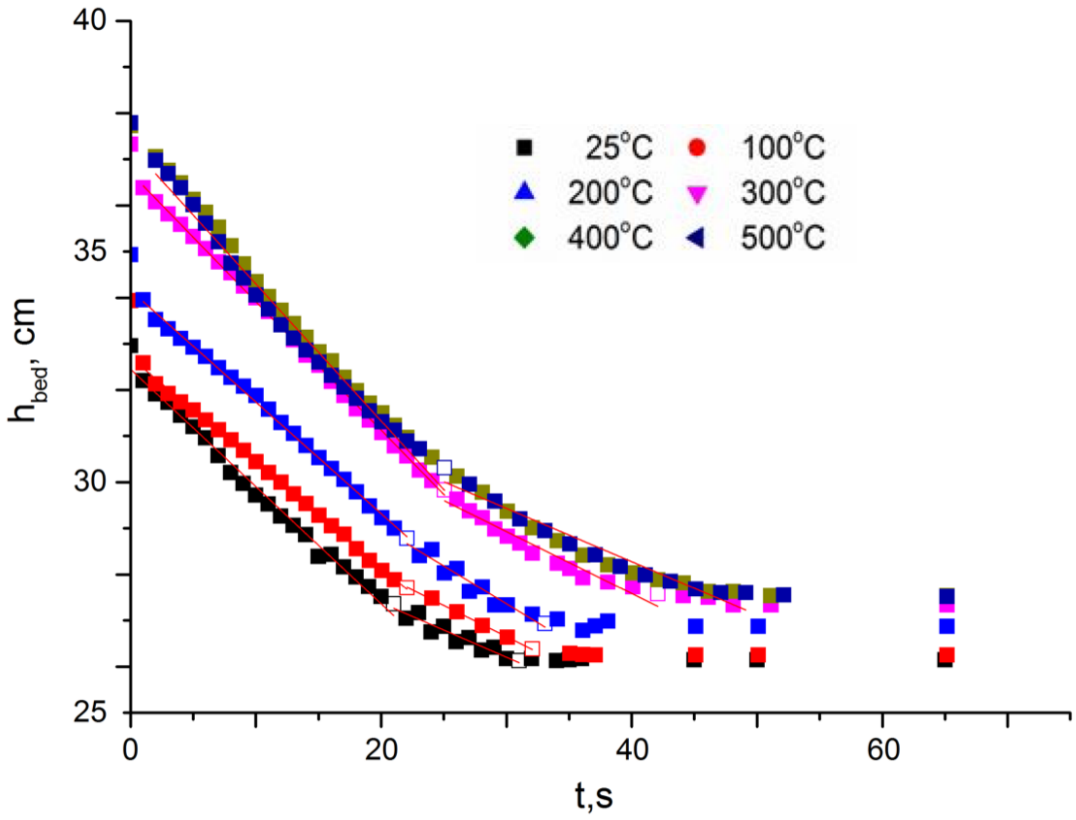

Figure 90 - Effect of temperature the bed collapse profiles sample A2 (Geldart A/C); solid lines represent the linear fit and the empty symbols where the sedimentation start and end for small voidage of the bed.

6.3.2 *Dense phase properties*

The dense phase properties, such as the dense phase voidage ε_d, the dense phase collapse rate U_{de}, the bubble escape rate U_b, the standardised collapse time SCT and the bed expansion ratio BER were determined from the collapse profiles. The effect of temperature on those parameters is reported in Figure 91 .

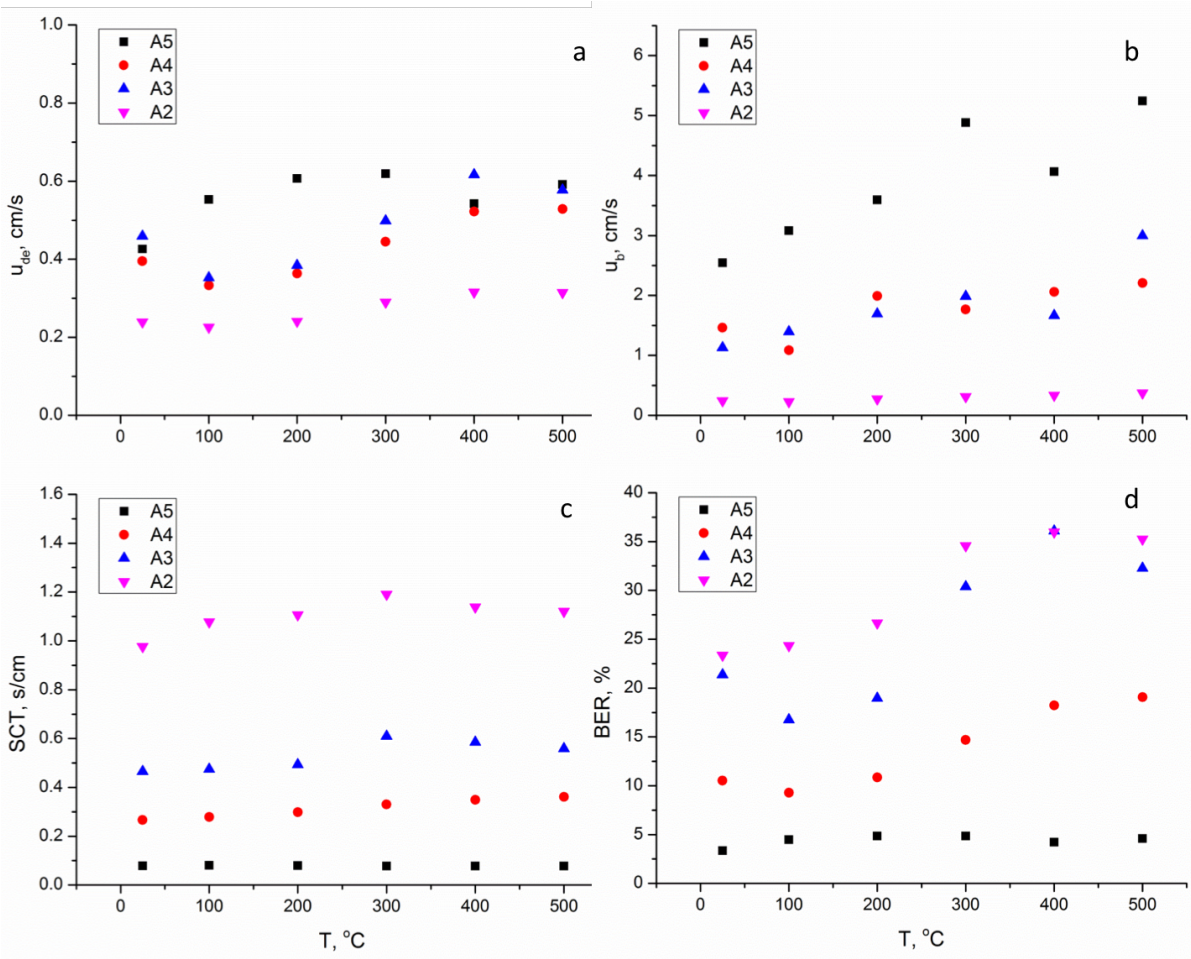

Figure 91 - Effect of temperature the bed collapse parameters; a) u_{de} vs T, b) u_b vs T, c) SCT vs T and d) BER vs T.

U_{de} measures how rapidly the interstitial aeration gas is expelled. On one side, the plot in Figure 91a shows that U_{de} decreases with the mean particle size and, on the other hand, the dense phase collapse rate slightly increases with temperature by about 25/35% for all samples. This result is not in agreement with the Abrahamsen and Geldart [107] correlation, Eq. 60, which predicts a slower collapse of the dense phase when increasing temperature [111].

$$U_{de} = \frac{0.314\rho_g^{0.023}\left(\rho_p - \rho_g\right)^{0.271} d_p^{1.282} \exp(0.508F_{45})}{\mu_f^{0.5} H_s^{0.244}} \quad \text{Eq. 60}$$

Interpretation of these experimental results suggests that these particles have a lower tolerance for withstanding rapid changes in flow in an operational unit with increasing temperature. Furthermore, the aeratability cannot be predicted by simply considering the physical characteristics of the particles and fluidizing gas, i.e. the mean particle diameter, fines content, fluid and particle density. This fact highlights an active role of the IPFs on the fluidization behaviour of these materials with increasing temperature.

The standardised collapse time, introduced by Geldart and Wong [102], is also connected to the capability of the particles to retain the air. The time required for the bed to deaerate depends on both the collapse rate and the height. For this reason, the SCT is normalised with respect to the height of the settled bed. Consequently, this parameter, which considers possible changes in the packing of the settled bed due to changes in the IPFs, represents a valid indicator for identifying changes due to the presence of interparticle forces. The SCT increases with decreasing the mean particle size and when increasing the temperature, except for the largest, which seems not to be affected. The bed expansion ratio (BER) significantly increases with PSD and temperature in agreement with the results of the expansion profiles. The bubbling escape rate (u_b) significantly decreases with particle size distribution (PSD) and slightly increases with temperature. A two stages bubbling escape was found for the largest sample A5, which depends on the size of the bubbles. Conversely, for the finest sample A2, in which the bubble size is much smaller, compared to sample A5 under the same conditions, the bubbling escape rate is very similar to the hindered sedimentation velocity.

6.4 Minimum bubbling velocity

In this work four different methodologies, described in section 3.8.2, were used to determine the minimum bubbling velocity. The methods used are:

1. Visual analyses of the images on a frame by frame basis, from the X-ray imaging technique, and noting the velocity at which the first bubble was seen breaking the bed surface, $u_{mb,v}$.
2. From the pressure drop curve, the shallow minimum of the curve identifies the $u_{mb,p}$.
3. From the "fluidization map" (u vs ε plot) as the velocity at which the bed expansion changes its trend, either a peak or an evident variation of slope occurs. In both cases, this points identify $u_{mb,e}$.
4. Again, from the "fluidization map", a second option is to consider the point where the values ε_b and ε_d became different, this point identifies $u_{mb,\,s.}$

As explained in section 3.8.2, ε_b and ε_d represent the full voidage of the bed (including bubbles) and the dense phase voidage (no bubbles), respectively.

The experimental values were also compared with the empirical correlation for the prediction of the minimum bubbling velocity proposed by Xie and Geldart [90] and Abrahamsen and Geldart [107].

$$u_{mb} = 2.07\exp(0.716F_{45})\frac{d_p\rho_g^{0.06}}{\mu^{0.347}} \qquad \text{Eq. 61}$$

$$u_{mb} = 0.3\exp(0.716F_{45})\frac{d_p\rho_g^{0.13}}{\mu^{0.5}} \qquad \text{Eq. 62}$$

6.4.1 Fluidization maps

Bed collapse experiments were repeated at different initial gas flow rates. The X-rays allowed recording the variation of the total bed height (including bubbles) as well as that of its dense phase, through a mathematical data extrapolation as described in section 2.2.4.3. This experiment provides two series of bed height data that allow the evaluation of the corresponding voidage values.

The results are reported in Figure 92-Figure 95 for all samples and temperatures investigated. It can be observed that there is no relation between mean particle size and

temperature with the type of profiles. For instance, samples A5, A4 and A3 show that, for some temperature, the split-up of the ε_f and ε_d into two different voidage curves occurs suddenly after the maximum of the ε vs u plot. In other cases, the split of the curves takes place for gas velocities larger than the one corresponding to the maximum. On the other hand, the fluidization map profiles for sample A2 show only profiles in which the maximum and split occur for the same gas velocity. In particular, from Figure 92, the overall bed voidage, ε_f, and the dense phase voidage, ε_d, increase linearly until the voidage reaches a maximum after which it splits up giving different values for the voidage at minimum bubbling velocity, namely $\varepsilon_{mb,e}$ and $\varepsilon_{mb,s}$. For temperatures higher than 200 °C, the peak and the split-up of the curves occur at the same gas velocity, defining same values for $\varepsilon_{mb,e}$ and $\varepsilon_{mb,s}$. It must be said that these two values are never far apart.

Regarding sample A4, the "fluidizing maps" reported in Figure 93, show that $\varepsilon_{mb,e}=\varepsilon_{mb,s}$, the peak and the split up of the voidage curve occur at the same gas velocity for temperature up to 300 °C. For higher temperature, $\varepsilon_{mb,e}$ slightly differs from $\varepsilon_{mb,s}$.

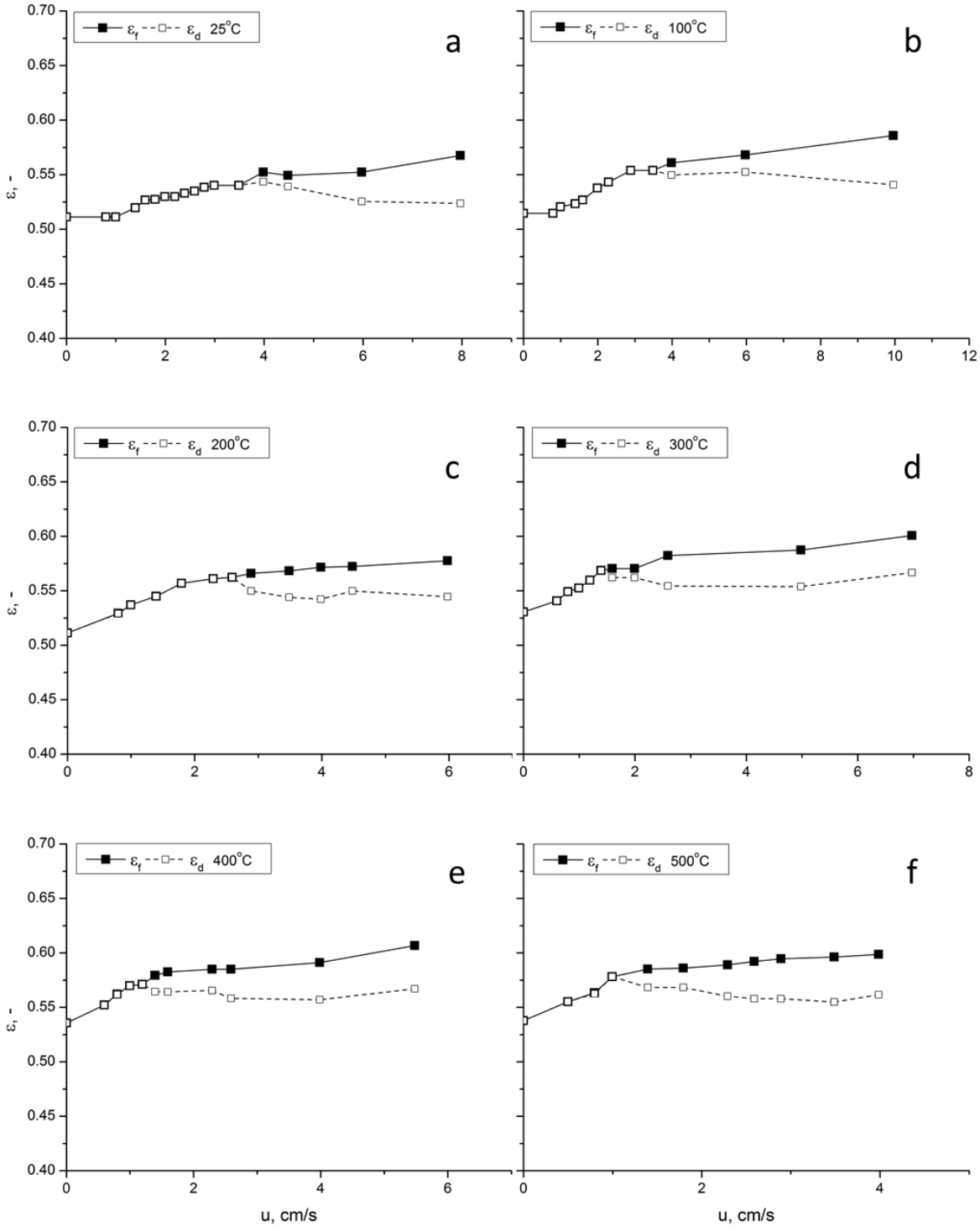

Figure 92 - Fluidization maps profiles for sample A5 (Geldart B); a) 25 °C, b) 100 °C, c) 200 °C, d) 300 °C, e) 400 °C and f) 500 °C.

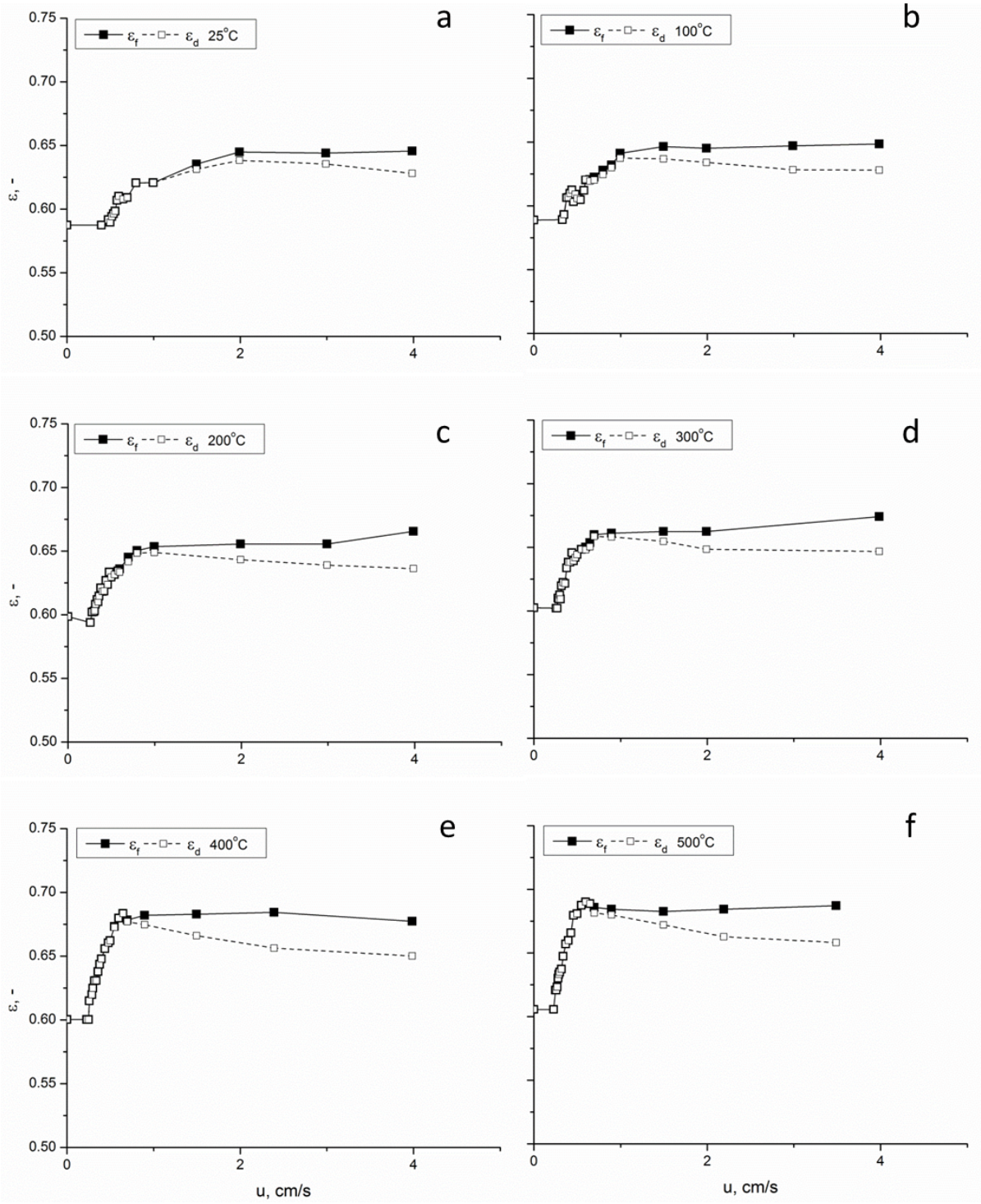

Figure 93 - Fluidization maps profiles for sample A4 (Geldart B/A); a) 25 °C, b) 100 °C, c) 200 °C, d) 300 °C, e) 400 °C and f) 500 °C.

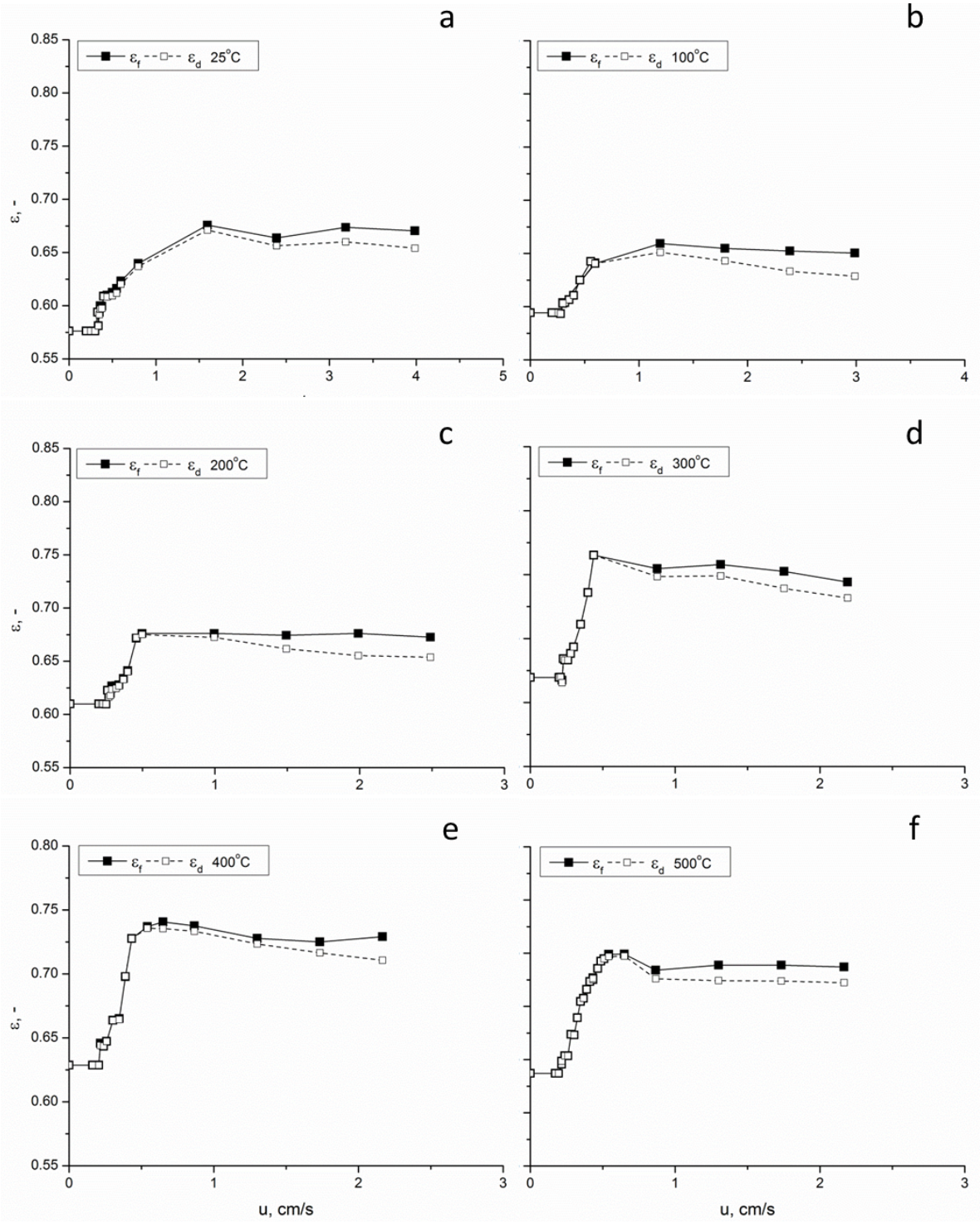

Figure 94 - Fluidization maps profiles for sample A3 (Geldart A); a) 25 °C, b) 100 °C, c) 200 °C, d) 300 °C, e) 400 °C and f) 500 °C.

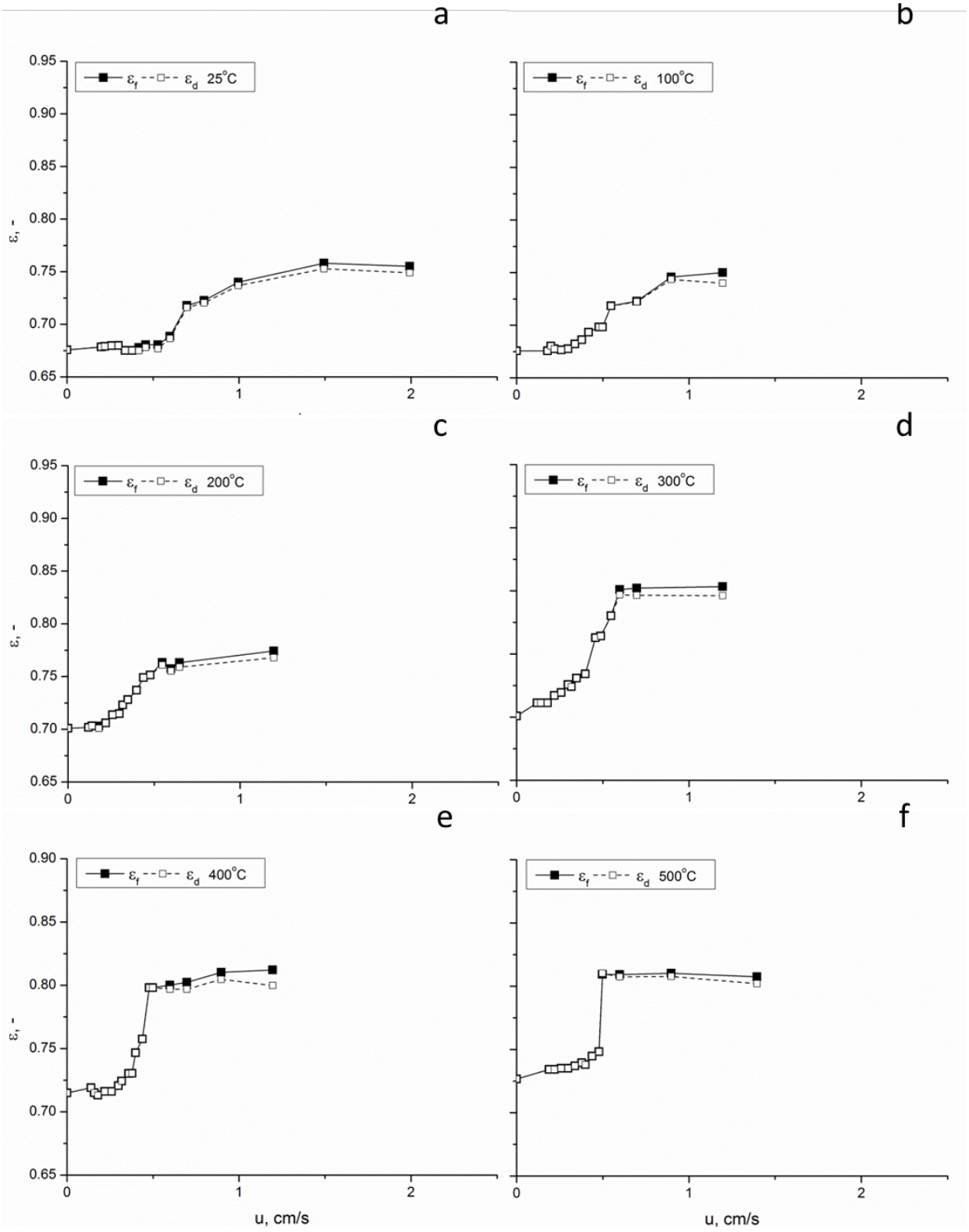

Figure 95 - Fluidization maps profiles for sample A2 (Geldart A/C); a) 25 °C, b) 100 °C, c) 200 °C, d) 300 °C, e) 400 °C and f) 500 °C.

6.4.2 *The effect of temperature on the minimum bubbling velocity*

The experimental minimum bubbling velocities, obtained for A5, are reported in Figure 96, together with the predictions given by Eq. 61 and Eq. 62. Values of $u_{mb,v}$ were found equal to the values of u_{mf} at each temperature as expected given the particle properties of this material sample. Values of $u_{mb,p}$ could not be evaluated since the pressure drop curves do not present any maximum/minimum values. From the "fluidizing maps" reported in the previous section values of $u_{mb,e}$ and $u_{mb,s}$ were found to be larger than the minimum fluidization velocity in all of the temperature range. The gap between values of u_{mf} and $u_{mb,e}$ or $u_{mb,s}$ means that the bed voidage keeps on increasing even in the presence of some bubbling. All the values of u_{mb} were found to decrease with temperature. Similar findings were also presented by Girimonte and Formisani [98].

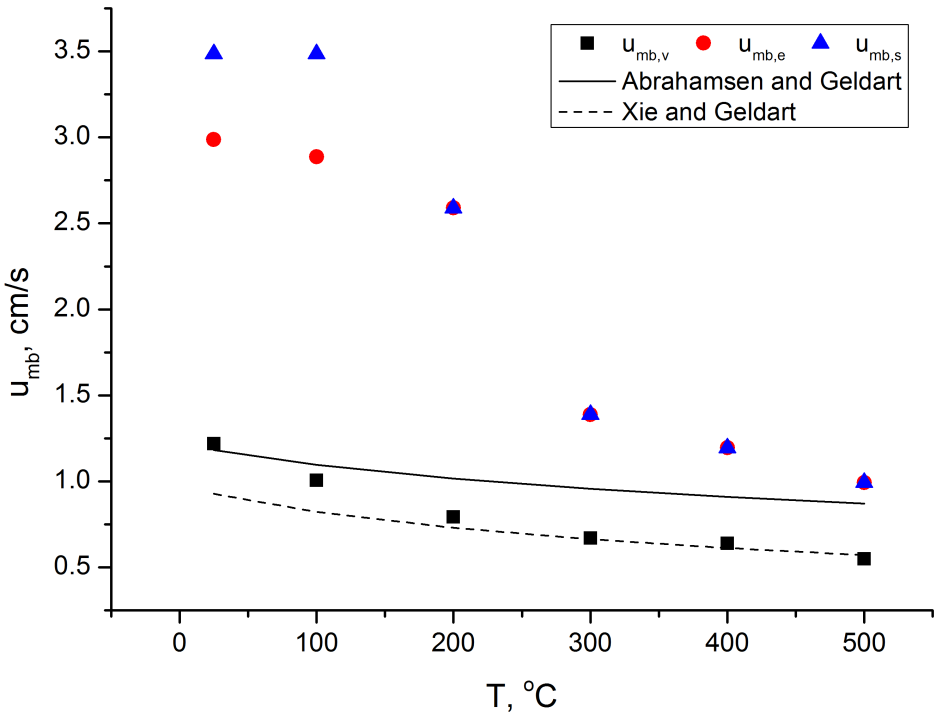

Figure 96 - Effect of temperature on the minimum bubbling velocity for sample A5 (Geldart B).

Figure 97 shows the effect of temperature on the minimum bubbling velocity for sample A4. The $u_{mb,v}$ values were found to be slightly higher than the values of the minimum fluidization velocity values for temperature between ambient and 200 °C and the same values were found for temperatures between 200-500 °C. Both $u_{mb,e}$ and $u_{mb,s}$ were found to be higher

than $u_{mb,v}$ at each temperature. Moreover, they mainly have the same trend with temperature.

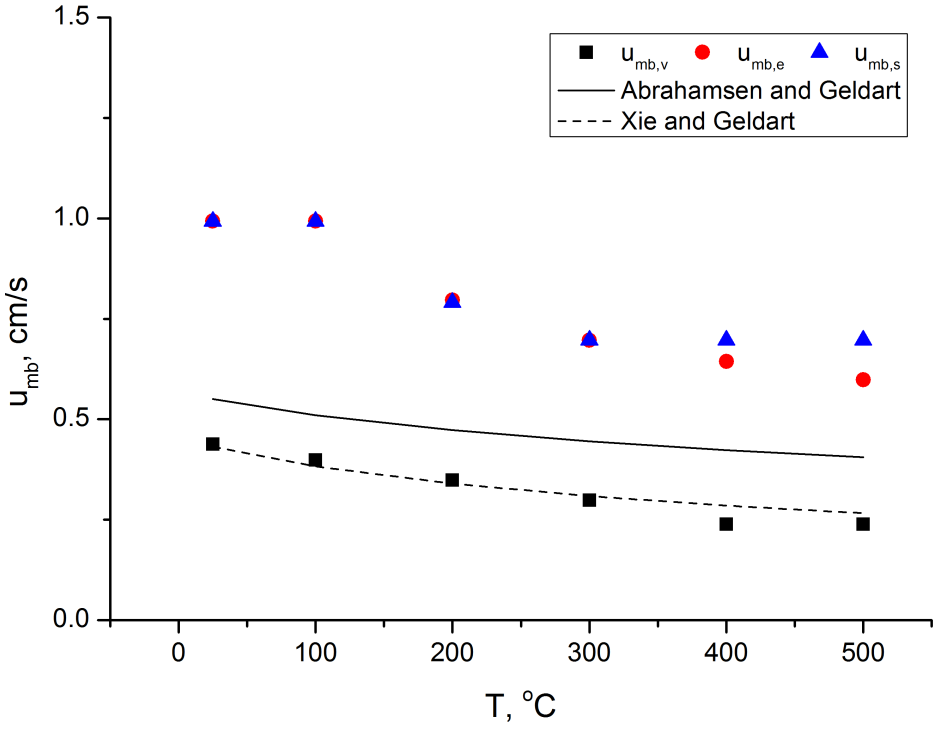

Figure 97 - Effect of temperature on the minimum bubbling velocity for sample A4 (Geldart B/A).

Samples A3 and A2 show similar features. In particular, both materials exhibit a maximum/minimum in the pressure drop profiles and the pressure drop value after the maximum is between 80 and 50%. Figure 98 displays the pressure drop profile, the bed voidage and the experimental values of u_{mb} on the same plot, (for sample A2 at 500 °C). The graph shows that when the first bubbles appears, $u_{mb,v}$, the value of the ratio ΔPm/ΔPc is around 0.5. From the pressure drop profile it is clear that the fluidization behaviour at this gas velocity is governed by instable channels. Moreover, for some temperature, as for sample A2 at 500 °C, the experimental $u_{mb,v}$ is lower than the experimental u_{mf}. This value cannot be taken as the minimum bubbling velocity; for this reason, it was also evaluated as the bubbling velocity for which the ratio ΔPm/ΔPc is around 0.95. The effect of temperature on u_{mb} is reported in Figure 99 and Figure 100. Regarding the temperature dependency of sample A3, the values of $u_{mb,v}$ and $u_{mb,p}$ follow mainly the same trend as that of u_{mf} with increasing temperature, with the values of $u_{mb,p\,95\%}$, $u_{mb,e}$ and $u_{mb,s}$ values slightly increasing for temperatures above 200 °C and 400 °C for $u_{mb,e}$ and $u_{mb,s}$. On the other hand, for

sample A2, the values of $u_{mb,v}$ and $u_{mb,p}$ also follow the same trend as u_{mf} with increasing temperature, with $u_{mb,p\,95\%}$ and $u_{mb,e}$ increasing for temperature above 300 °C.

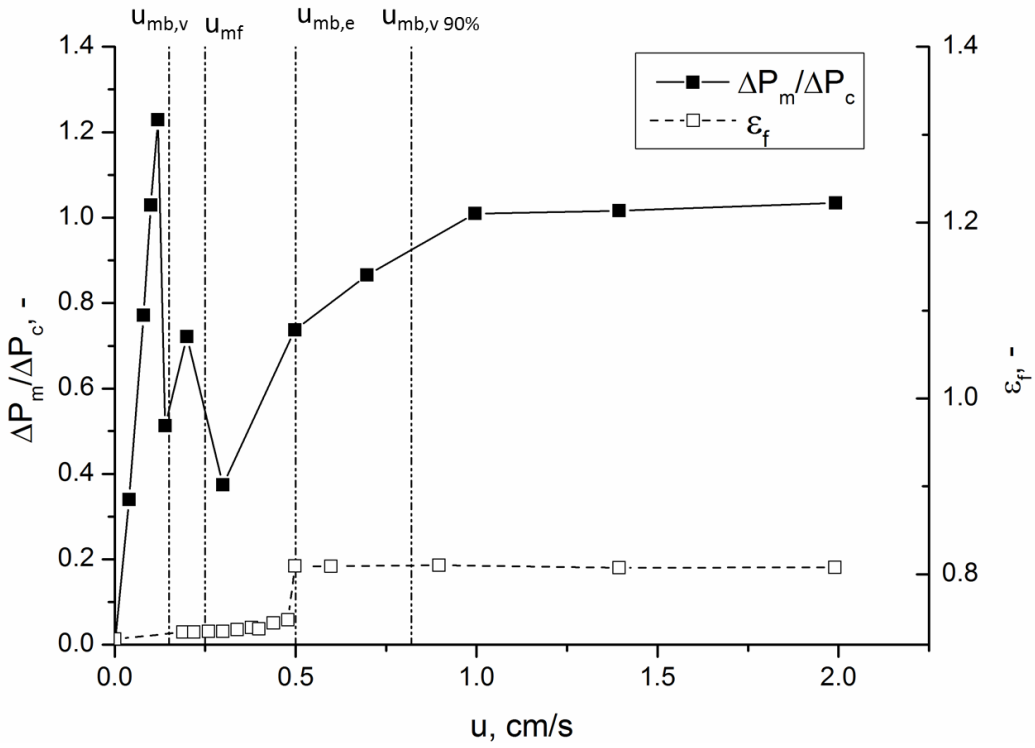

Figure 98 - Pressure drop profile and voidage of the bed for sample A2 at 500 °C.

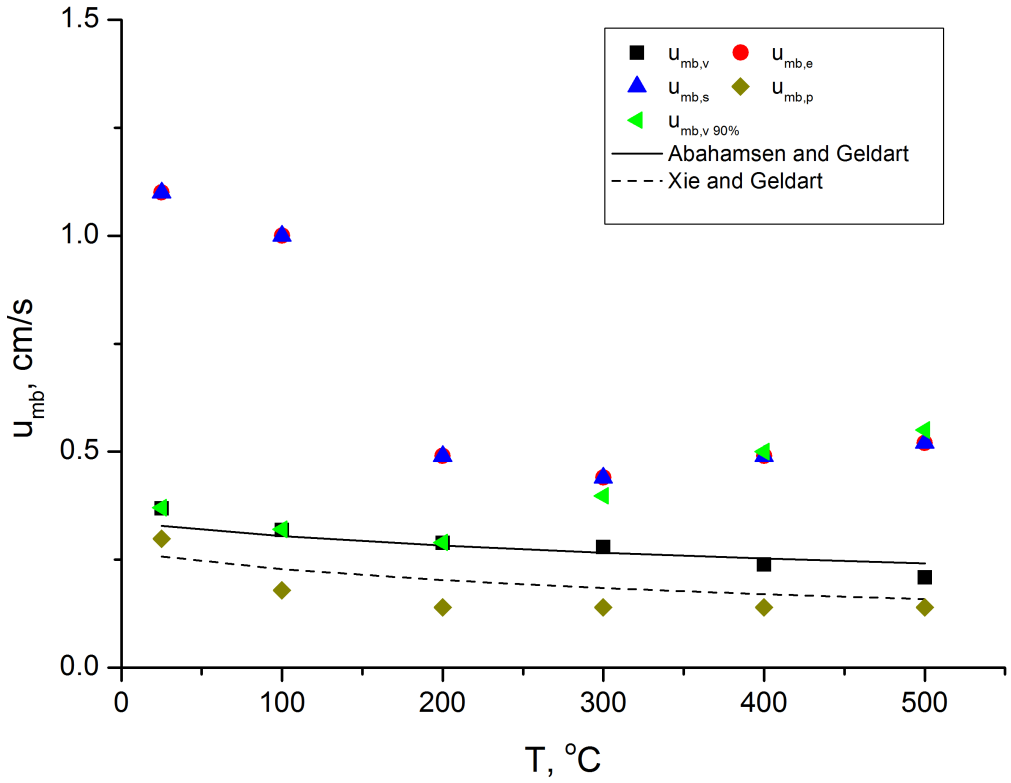

Figure 99 - Effect of temperature on the minimum bubbling velocity for sample A3 (Geldart C).

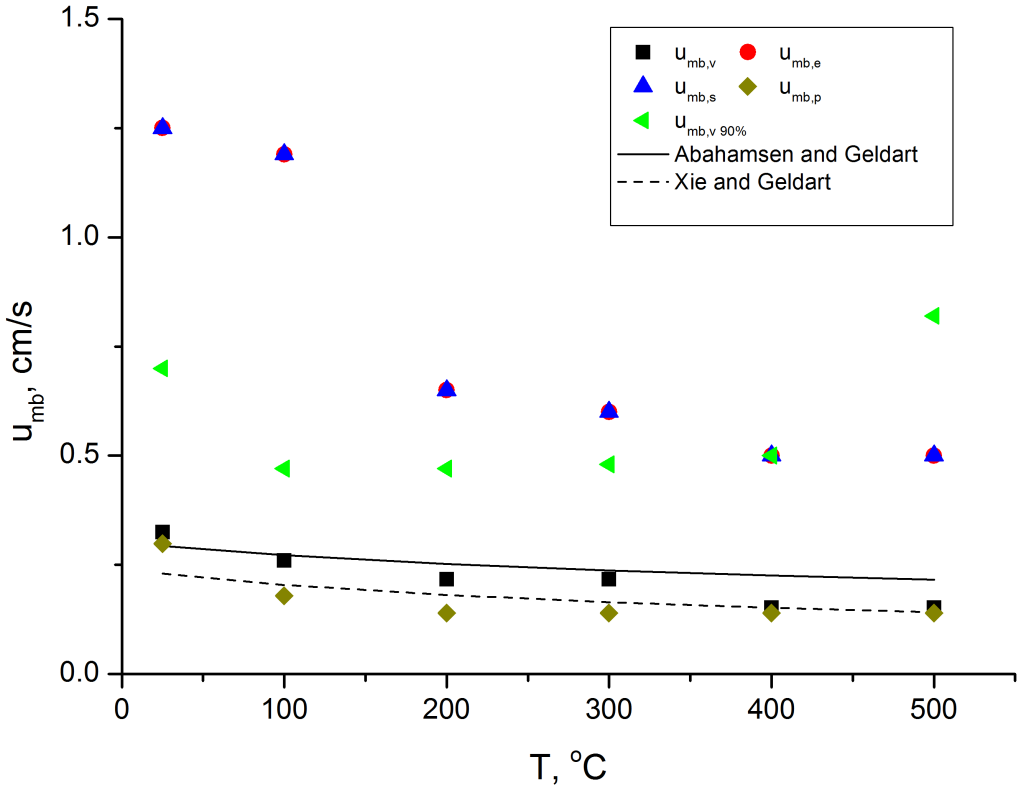

Figure 100 - Effect of temperature on the minimum bubbling velocity for sample A2 (Geldart A/C).

The minimum bubbling velocity was calculated for all the samples at each temperature with different methodologies. The results show that both $u_{mb,v}$ and $u_{mb,p}$ slightly decrease with temperature. On the other hand, when the minimum bubbling velocity is estimated through the bed voidage profiles, $u_{mb,e}$, $u_{mb,s}$ and $u_{mb,v\ 95\%}$, a non-monotonic trend with temperature can be observed.

The experimental results suggest different meanings for these parameters. For instance, $u_{mb,v}$ can describe the minimum bubbling condition in systems where the HDFs are dominant, but it could give misleading information on the final structure of the bed. In fact, the experimental data reveal that for $u>u_{mb,v}$ the voidage of the bed still changes. For systems dominated by IPFs $u_{mb,v}$ is not reliable because of the occurrence of channelling behaviour. Differently, the $u_{mb,s}$ gives information on the final structure of the bed in bubbling conditions and it can be used for describing the effect of temperature in such conditions.

6.5 Non-bubbling ratio: umb/umf

The u_{mb}/u_{mf} ratio is reported in the literature as a key parameter to characterize fluidization. It provides an indication of both how the dense phase expands or contracts and the flexibility of the fluid bed to withstand sudden changes in operating conditions. The greater the of u_{mb}/u_{mf} ratio, the smoother the fluidization quality and, thus slower the powder sample response to sudden upsets in the fluidized unit. The experimental values were also compared with the prediction proposed by Abrahamsen and Geldart [107] and Xie and Geldart [90], Eq. 63 and Eq. 64.

$$\frac{u_{mb}}{u_{mf}} = \frac{2300\rho_g^{0.126}\mu^{0.523}\exp(0.716F_{45})}{g^{0.934}\left(\rho_p-\rho_g\right)^{0.934}d_p^{0.8}} \qquad \text{Eq. 63}$$

$$\frac{u_{mb}}{u_{mf}} = \frac{333\rho_g^{0.19}\mu^{0.37}\exp(0.716F_{45})}{g^{0.934}\left(\rho_p-\rho_g\right)^{0.934}d_p^{0.8}} \qquad \text{Eq. 64}$$

The non-bubbling ratio was calculated using the experimental values of the minimum bubbling velocity, $u_{mb,s}$, and the minimum fluidization velocity. Results are reported in Figure

101. Generally, a unique trend cannot be identified for the experimental non-bubbling ratio with increasing temperature. Hence, in this work the u_{mb}/u_{mf} ration could not be used to discriminate between the powders tested with increasing temperature.

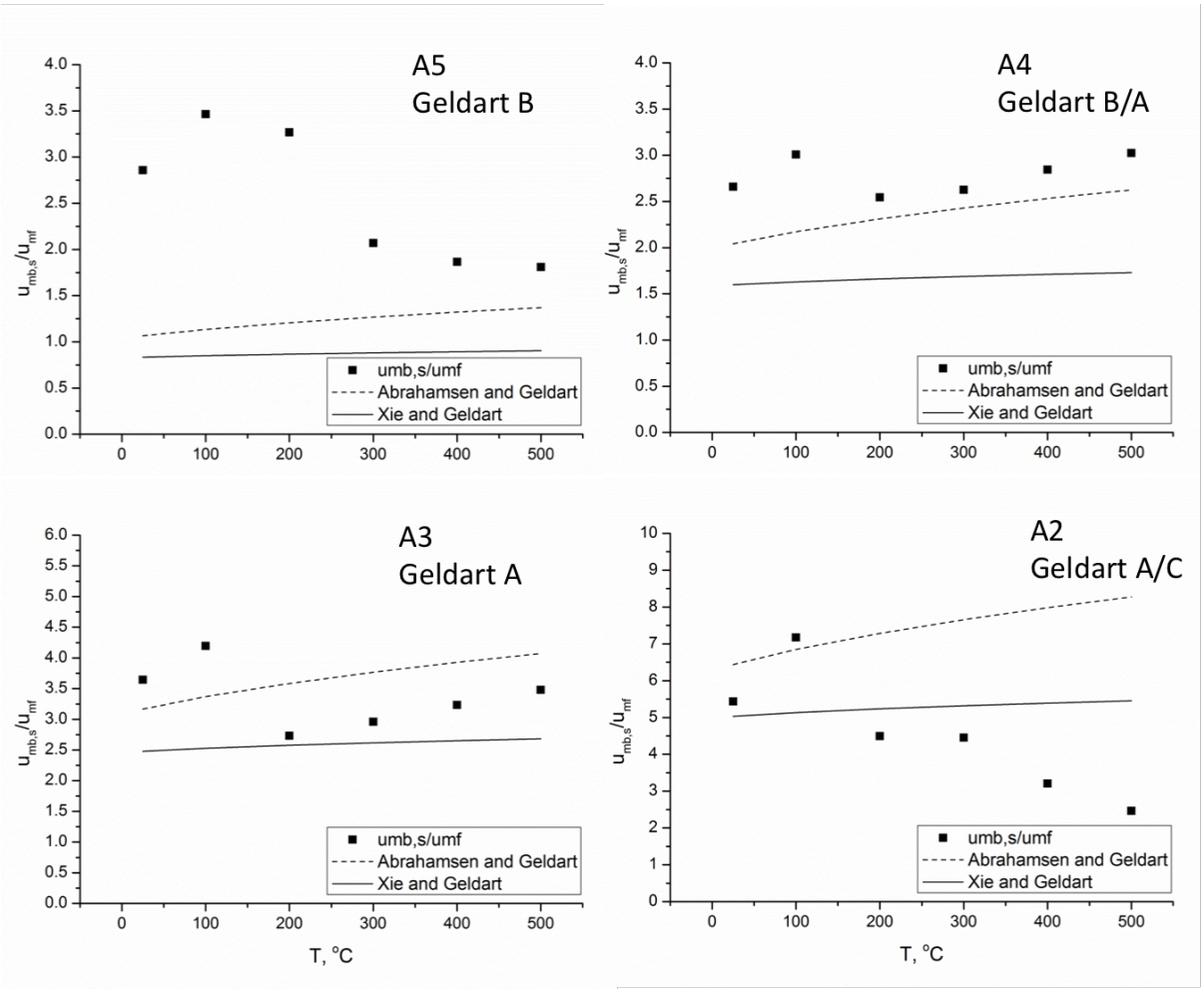

Figure 101 - Effect of temperature on the non-bubbling ratio: sample A5, sample A4, sample A3 and sample A2.

6.6 Summary of fluidization results

A complete experimental characterization of the fluidization behaviour of powder samples of different particle sizes has been performed and some key conclusions can be drawn. In particular, the slow aeration experiments show:

- Particle size distribution affects significantly the fluidization behaviour of the materials investigated;
- The ΔPm/ΔPc ratio provided a very first indication of the influence of the HDFs and IPFs on the fluidization behaviour;
- A larger overshoot in the pressure drop profiles was found for the finest particle bed, indicating higher resistance of the particles to flow;
- Hysteresis phenomena were observed in the pressure drop curves for conditions in which the IPFs play a significant role, meaning finest particles and high temperature;
- Fine particles showed a dominant role of IPFs over the HDFs when increasing temperature with a non-monotonic trend of u_{mf} with increasing temperature and consequent increase of u_{mf} for temperature higher than 300 °C;
- The X-ray images were able to identify the occurrence of channelling conditions. In this case it is possible to identify vertical or horizontal channels in the bed;
- The behaviour of powder samples at minimum fluidization conditions showed similarities with that of compacted bed. Both ε_{mf} and ε_s increase with temperature;
- Bed expansion was observed to increase with decreasing the mean particle size and the maximum expansion was found for the finest sample (A2). Furthermore, a larger bed expansion was observed when increasing temperature up to 300 °C;
- The experimental values of n* and u_t* in the Richardson-Zaki equation were found to be significantly greater than the theoretical ones, predicted using the Richardson-Zaki correlations and the Stokes law. These findings can be explained considering an active contribution of the IPFs in the particle systems;
- Two stages with two different slopes were observed in the Richardson-Zaki expansion profiles for the finest samples, A2 and A3, when increasing temperature.
- The minimum bubbling velocity obtained by the visual methodology and that based on detection of the pressure drop minimum were found to be unreliable when the

particle systems were dominated by interparticle forces, principally because of channeling and instable formation/distruption of bubbles

On the other hand, the fast deaeration experiments (BCT) show:

- The de-aeration rate U_{de} was found to decrease with the particle size and to increase with temperature;

- Larger capability of the material to retain aeration gas was observed when decreasing the particle size. The standardised collapse time (SCT) was found to slightly increase with increasing temperature up to 300 °C, whereas a further increase in temperature did not produce any relevant variation. The Abrahamsen and Geldart correlation was not capable of predicting the changes in aerability of such materials, given the active role of the IPFs on the fluidization behaviour of this sample when increasing temperature.

- The bed expansion ratio (BER) suggested a spatial reorganization of the particles due an active role of IPFs, in agreement with the results obtained in slow aeration tests;

- The analysis on the voidage of the dense phase and the overall bed expansion as function of the flow rate allowed reconstructing the sequence of phenomena through which a stable flow of bubbles across the solid mass were achieved. The equilibrium between contact and hydrodynamic forces was achieved for gas velocity $u_{mb,s}$. For $u=u_{mb,s}$ regular bubbling across a stable structured emulsion phase, $\varepsilon_{mb,s}$ was observed. Unlike other criteria, this definition identified a possible structure of the bed.

7 Link between rheology and fluidization

7.1 Bo number

The dimensionless Bond number, Bo, is frequently used for measuring the importance of gravitational forces compared to interparticle forces. Links between micro-scale (particle-level) interactions and macro-scale (fluidization) behaviour have been made previously for particles with sources of cohesion i.e van der Walls forces. For instance, to understand the effect of van der Waals forces on fluidized bed behaviour, several research groups found Bond number (ratio of maximum van der Waals force to particle weight) correlates with various fluidization velocities [13,95].

$$\mathrm{Bo_g} = \frac{\mathrm{F_t}}{\mathrm{W}} \qquad \text{Eq. 65}$$

In order to calculate the Bond number, the results from the Rumpf and Molerus model, described in section 5.4.1, were used. In particular, the van der Waals interparticle forces, F_{vdw}, estimated through the shear experiments were used as interparticle force, F_t, and the following equation was used to evaluate the gravitational force, W.

$$\mathrm{W} = \frac{1}{6}\pi\rho_p g d_p^3 \qquad \text{Eq. 66}$$

Since the shear experiments were performed only at ambient temperature and 500 °C, Equation 39, in section 5.3, was used to back calculate the values of the inteparticle forces at each temperature, using the contact radius found at ambient temperature and the literature values, depending on temperature, of the hardness [171]. In particular, since we are interested to a comparison with a fluidization, the consolidation force in Eq. 38 was considered to be zero. In principle, this is not necessarily correct, since in fluidized beds, differently from shear experiments particle are subject to dynamic situations in which hits between particles can determine finite values of relative momentum and therefore finite consolidation forces at contacts during hits. The analysis of such conditions, however, is

beyond the scope of this work and it is imagined that the particle agglomerates are the results of the expansion of a fixed bed towards fluidization. Such agglomerates are subject to external forces which can determine some internal shear and motion of the particle. Since the conditions to which the analysis is limited are close to the minimum for fluidization, fluid dynamic forces are close to the weight of the particles multiplied by the number of particles in the agglomerate, this is the reason why Eq.65 is a good estimate of the forces acting between particles in the agglomerate. These agglomerates are not necessarily static but will determine the relevant mesoscale phenomena just above the minimum for fluidization.

It should be noted that different definitions of Agglomerates and Aggregates exist [186]. In particular, following the British Standards Institution they are defined as:

- Agglomerate: collection of weakly bound particles or aggregates or mixtures of the two where the resulting external surface area is similar to the sum of the surface areas of the individual components. The forces holding an agglomerate together are weak forces, for example van der Waals forces, or simple physical entanglement. Agglomerates are also termed secondary particles and the original source particles are termed primary particles.
- Aggregate: particle comprising strongly bonded or fused particles where the resulting external surface area may be significantly smaller than the sum of calculated surface areas of the individual components. The forces holding an aggregate together are strong forces, for example covalent bonds, or those resulting from sintering or complex physical entanglement. Aggregates are also termed secondary particles and the original source particles are termed primary particles.

Figure 102 shows the results in terms of Bo number for each sample and with increasing temperature. The Bond number, for samples A5 and A4, is between 2 and 10 and does not change significantly with temperature.

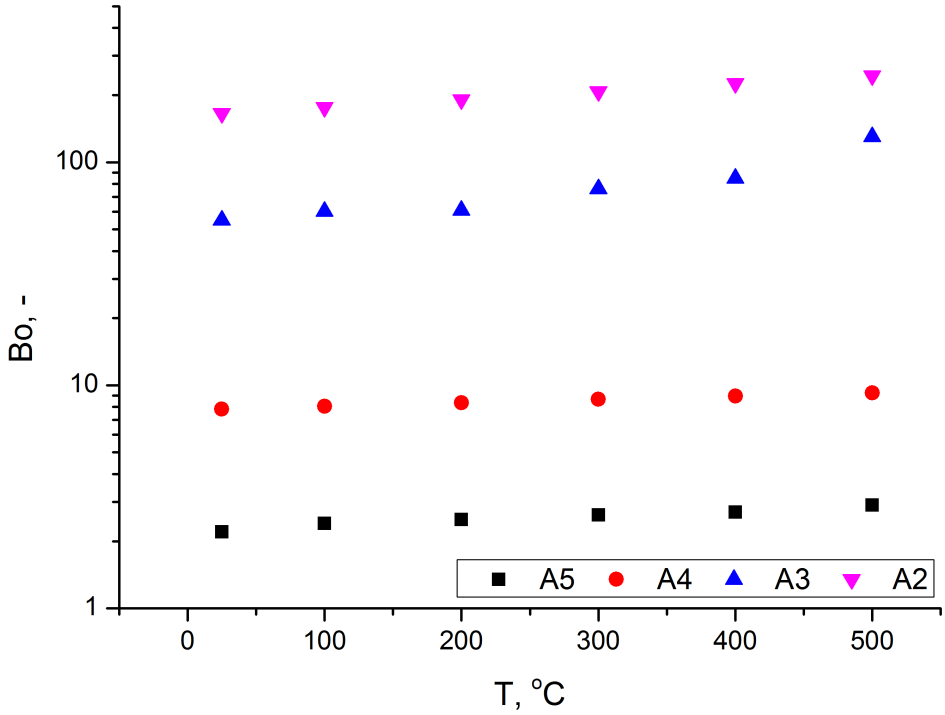

Figure 102 - Effect of temperature on the Bond number for all samples.

7.2 The relation between the voidage of the bed and the Bond number

The voidages of the bed at minimum fluidization and bubbling conditions were also analysed as function of the Bond number, calculated as explained in the previous section. Values of ε_{mf} and $\varepsilon_{mb,s}$ were plotted against the values of the Bond number for all samples and all temperatures in Figure 103. Together with the experimental data also the best fitting logarithmic curves are reported as dashed lines. For ε_{mf} and $\varepsilon_{mb,s}$ the best fitting curves are expressed by the following equations:

$$\varepsilon_{mf} = 0.026\ln(Bo) + 0.52 \qquad \text{Eq. 67}$$

$$\varepsilon_{mb,s} = 0.039\ln(Bo) + 0.53 \qquad \text{Eq. 68}$$

It can be seen that both parameters are well fitted by these functions. According to the definition of $\varepsilon_{mb,s}$, see section 6.4, it identifies the maximum bed expansion at which, in

the defluidization experiment, it is not possible to verify the presence of a stable bubbling. The comparison with fluidization experiment at increasing gas velocity has indicated that $\varepsilon_{mb,s}$ corresponds to the maximum bed expansion above the minimum fluidization. In other words, in the velocity range between u_{mf} and $u_{mb,s,}$ corresponding to voidages ε_{mf} and $\varepsilon_{mb,s}$, the bed exhibits a steady expansion. As previously observed by Valverde [95] and Jackson [83], in this range of gas velocities it is possible to identify two different regimes, a "Solid-like" regime and a "Fluid-like" regime. The fluid-like regime is characterized by a larger mobility of particles, in which it is possible to verify the presence of local non-homogeneities. Nevertheless, the fluid-like regime is still governed by the active role of interparticle cohesive forces that provide the bed with an internal structure. This structure disappears in the bubbling regime above $u_{mb,s}$ at voidages corresponding to $\varepsilon_{mb,s}$. Coherently with the above interpretation, in the region between ε_{mf} and $\varepsilon_{mb,s}$ the voidage of the dense phase was observed to increase even in the presence of small random bubbles. For $\varepsilon>\varepsilon_{mb,s}$ the bed expansion stopped and stable bubbling was observed. The similar trend of the two fitting lines for ε_{mf} and $\varepsilon_{mb,s}$ shown in Figure 103 supports the idea that interparticle forces play an active role up to the stable bubbling regime as suggested by Valverde [95] and Jackson [83]. Also the condition $\varepsilon_{mf} \approx \varepsilon_{mb,s}$ for values of the Bo number around 1, is in agreement with the findings reported by Valverde et al. [95]. The main difference between their results and those reported in this thesis is the evaluation procedure of the interparticle forces useful for the calculation of the Bond number. In fact, Valverde et al. [95] used a value of the interparticle force estimated on the basis of theoretical correlation. Instead, in this work, the interparticle forces were estimated on the basis of shear experiments.

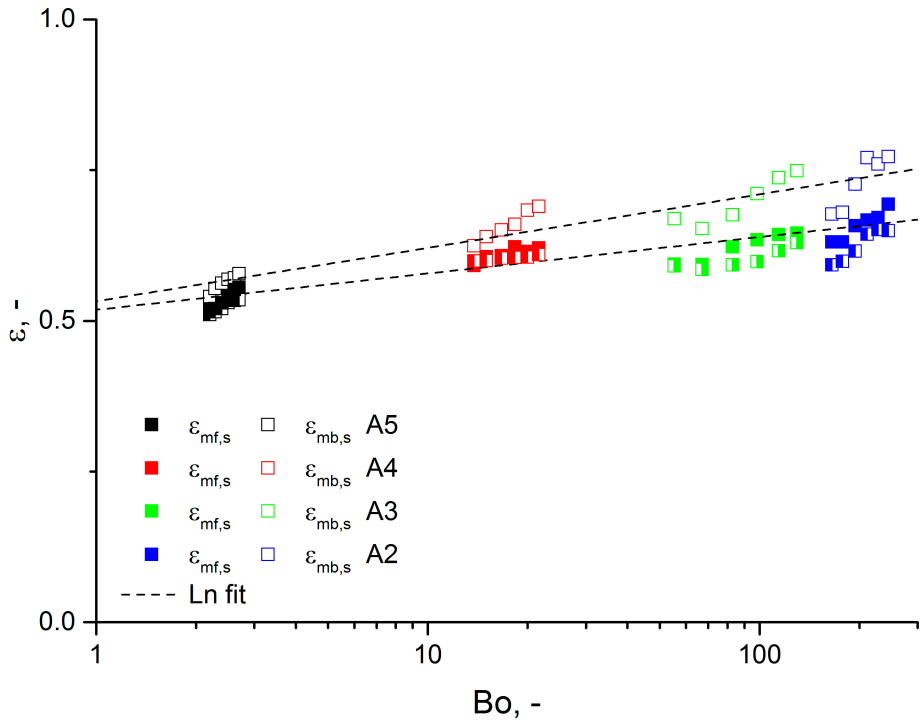

Figure 103 - Voidage of the bed at minimum velocity and bubbling condition as function of the Bond number. Lines fitting equation are reported as Eq. 67 and Eq. 68.

7.3 Gibilaro criteria of stability and Valverde analysis

Valverde et al. [187] found that the experimental results on the sedimentation rate cannot be fitted by theoretical and empirical equations available in literature mainly because these equations are derived for non-cohesive particles. They proposed a modified form of the Richardson-Zaki equation which accounts for particle aggregation. In their equation, the number of particles per agglomerate, N, and the ratio, k, of agglomerate to particle radius were included as parameters in order to account for the aggregation due to cohesive forces.

$$\frac{u_i}{u_t} = \frac{N}{k}\left[1 - \left((1-\varepsilon)\frac{k^3}{N}\right)\right]^n \qquad \text{Eq. 69}$$

Valverde et al. [187] plotted the initial settling velocities as a function of the initial bed solid fraction to estimate both N and k in Eq. 69.

In the present thesis, the same approach was used to verify if the settling velocity could be related to agglomerates whose size is estimated on the basis of the experimental bond number. In Figure 105 the experimental values of the initial settling velocity, u_i, are plotted against the corresponding bed voidages. All the reported results concern initial gas fluidization velocities below the minimum for stable bubbling, $u_{mb,s}$. The same figure reports also the plot of the Richardson-Zaki equations with the values of u_t and n values calculated on the basis of the particle size, d_p. These equations, which should describe the settling bed velocity, generally underestimate the experimental results. The greater values found for the experimental initial settling velocities, confirms the idea that the particles do not behave as individual particles in the fluidized bed but more as agglomerates. Differently from the approach followed by Valverde et al. [187], the Bo number in Eq. 70 was fixed to the value estimated on the basis of the experiments powder rheometry, as reported in section 7.1, while k remains a single fitting parameter.

$$\frac{u_i}{u_t} = \frac{Bo}{k}\left[1 - \left((1-\varepsilon)\frac{k^3}{Bo}\right)\right]^n \qquad \text{Eq. 70}$$

Table 16 reports the values of k* providing the best fitting given by Eq. 70 with the experimental data. The table also reports the average packing fraction of the particles in a single agglomerate, given by $\varphi_{agg}=Bo/k^{*3}$. These latter values were found to be larger than the average solid volume fraction of the settled powder. This finding suggests that the settled bed could keep a structure that somehow reflects the aggregative behaviour of the particles. An indirect confirmation of this comes from the plot of the settled bed voidage as a function of the bond number shown in Figure 105. Similarly to what was observed above for ε_{mf} and $\varepsilon_{mb,s}$, a clear relationship is evident between the two parameters.

Table 16 - Values of k*, φ_{agg}, φ_{int} and dp_{agg} as function of temperature.

	A3				A2			
T	k	φ_{agg}	φ_{int}	dp_{agg}	k	φ_{agg}	φ_{int}	dp_{agg}
°C	-	-	-	10^{-4} m	-	-	-	10^{-4} m
25	4.6	0.58	0.57	1.35	6.5	0.60	0.56	1.24
100	4.7	0.58	0.63	1.39	7.0	0.51	0.63	1.33
200	4.8	0.55	0.60	1.41	7.4	0.47	0.62	1.41
300	5.3	0.51	0.60	1.56	7.7	0.45	0.61	1.46
400	5.9	0.41	0.60	1.74	8.1	0.42	0.60	1.54
500	6.5	0.47	0.52	1.92	8.3	0.43	0.48	1.58

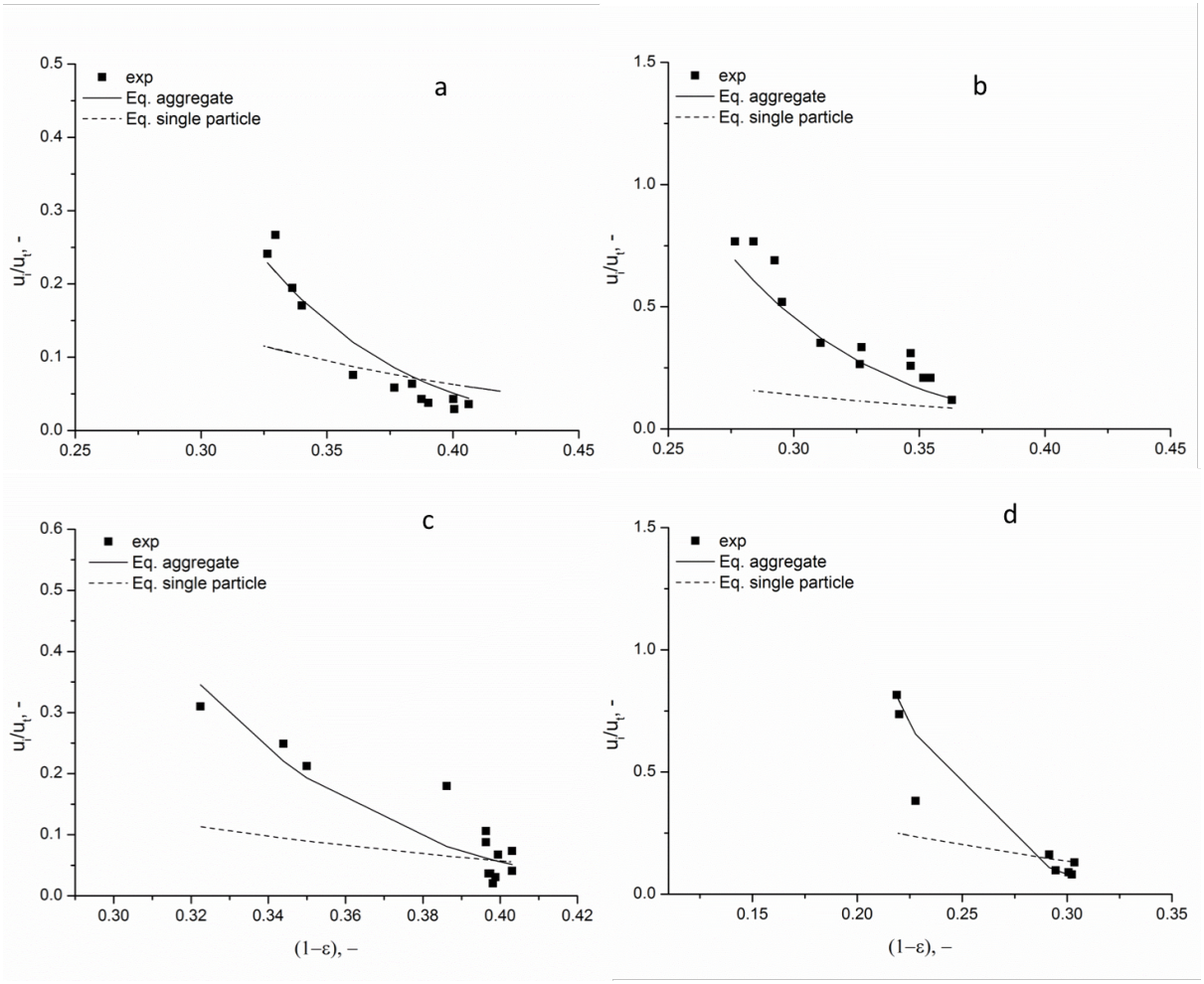

Figure 104 - Initial settling velocity as function of the solid fraction; a) sample A3 at 25 °C; b) sample A3 at 500 °C; c) sample A2 at 25 °C; d) sample A2 at 500 °C.

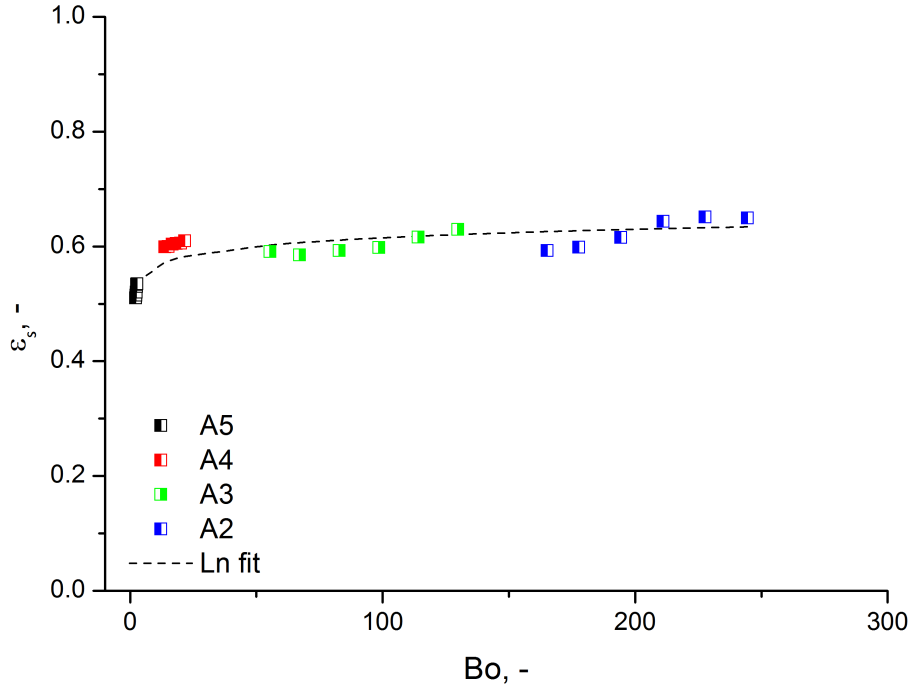

Figure 105 - Settled voidage of the bed as function of the Bond number.

The consistency of the aggregative fluidization behaviour theory was confirmed by the applicability of the stability criterion proposed by Foscolo and Gibilaro [12]. The values of φ_{int} and $d_{agg}=k*d_p$ were used in Eq. 71. This equation was used to predict the voidage of the bed at minimum bubbling condition, $\varepsilon_{mb,s}$. The experimental values of $\varepsilon_{mb,s}$ were also compared with the generalized stability criterion, Eq. 72, which account for the experimental values of the index n and u_t of the Richardson and Zaki correlation, as proposed by Lettieri [159]. Figure 106 reports the comparison between the experimental data and the predicted ones. A very good match was obtained when using the theoretical values of u_t, the values of n according to Richardson and Zaki (Table 14) and the agglomerate diameter, d_{agg}, in Eq. 71. This result suggests that the final structure of the bed, $\varepsilon_{mb,s}$ is strictly related to the formation of agglomerates due to the presence of interparticle forces.

$$\left[\frac{gd_p(\rho_p-\rho_g)}{u_t^2\rho_p}\right]^{0.5} - 0.56n(1-\varepsilon_{mb})^{0.5}\varepsilon_{mb}^{n-1} = \begin{Bmatrix}\text{positive stable}\\ \text{negative unstable}\end{Bmatrix} \qquad \text{Eq. 71}$$

$$\left[\frac{2gd_p(\rho_p-\rho_g)}{3u_t^2\rho_p}\right]^{0.5} - n^{0.5}(1-\varepsilon_{mb})^{0.5}\varepsilon_{mb}^{n-1} = \begin{Bmatrix}\text{positive stable}\\ \text{negative instable}\end{Bmatrix} \qquad \text{Eq. 72}$$

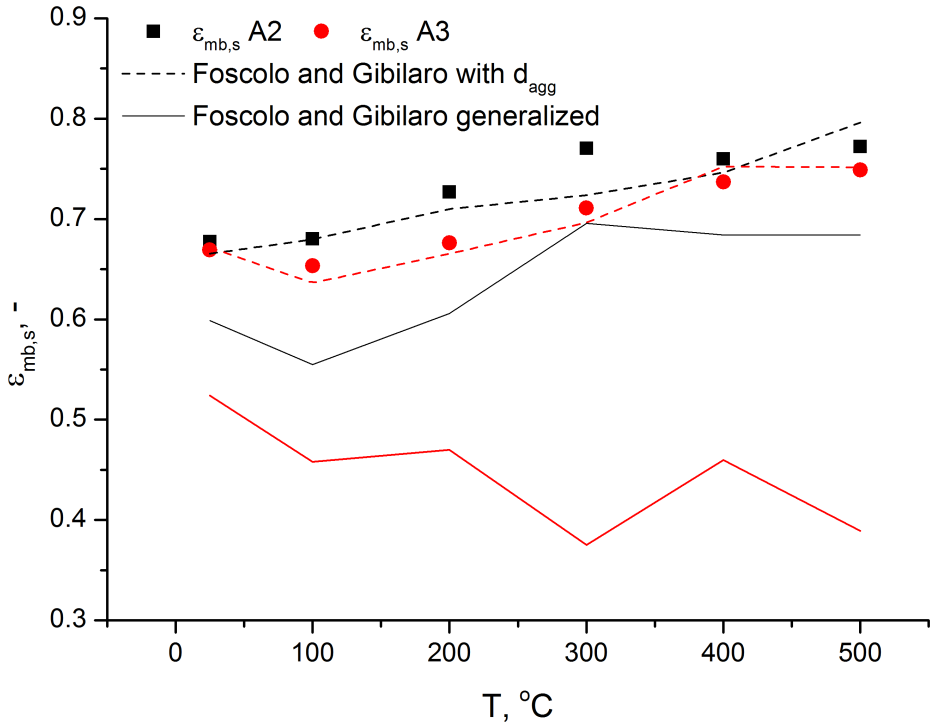

Figure 106 - The comparison of the mathematical minimum bubbling voidage of the bed calculated with the of Foscolo and Gibilaro criterion [12].

7.4 Sound assisted fluidized bed

A direct measure of the interparticle interactions (IPFs) in fluidization condition is challenging, mainly because cohesive particles cannot be fluidized under ordinary conditions. This is the reason why IPFs in this thesis were measured on the basis of the powder flow properties and the Rumpf and Molerus model, as discussed in section 5.3. In order to verify the consistency of this IPF evaluation procedure, a comparison was performed between this estimate of IPFs and a different evaluation of the IPFs acting on cohesive powders under actual fluidization conditions by using an experimental and theoretical approach. A detailed description of the approach is reported in the Appendix and was carried out with the help of the staff at Istituto di Ricerche sulla Combustione of the National Research Council (CNR) in Naples. Only a summary is reported here. The experiments consisted in sound assisted fluidization that was used to achieve a proper fluidization regime for sample A1, A2 and A3 described in section 4. Samples A4 and A5 do

not fluidize under the form of agglomerates and their fluidization behaviour is not affected by sound application according with the results shown in Appendix. The experimental apparatus, methodology and theoretical modelling can be found in the Appendix. Then, the cluster/subcluster model was applied to calculate IPFs [188] starting from the experimental results. The cluster/subcluster model previously developed in Naples, was applied in order to evaluate the frictional cohesive forces necessary to separate the subcluster from the cluster. Figure 107 shows a parity plot of the comparison between the interparticle forces estimated with the two different methodologies, F_{sound} evaluated from the cluster/subcluster model and F_{asc} calculated as described in section 7.1. The results show that even though evaluated under different conditions, the values obtained are always of the same order of magnitude. To better highlight the comparison between the two approaches, the ratio F_{ASC}/F_{sound} was evaluated and plotted in Figure 108.

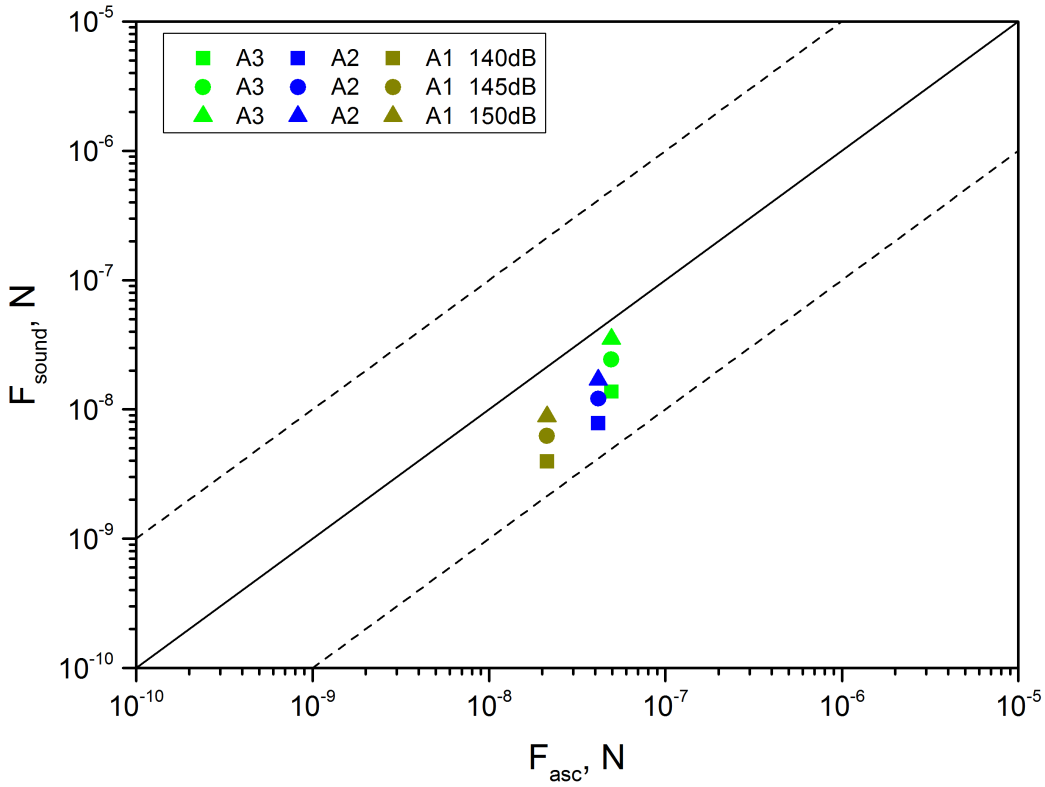

Figure 107 - Comparison between F_{ASC} and F_{sound}. (Dotted lines ± one order of magnitude) different symbols refer to different sound pressure levels as reported in the legend.

First of all, it is clear that $F_{ASC}>F_{sound}$. This evidence is due to the fact that the shear experiments in the High Temperature Shear Cell apparatus were performed in compacted conditions, which are completely different from those actually occurring inside the

fluidized bed. On the contrary, in the sound assisted fluidized bed apparatus the powders are under aeration conditions; therefore, the cohesive forces are coherently lower than those evaluated in the HT-ASC apparatus. It has to be acknowledged, however, that the particles used are characterized by a rather hard material for which interparticle forces are only slightly affected by the material consolidation. It is also clear from Figure 108 that, for each sample, the ratio F_{ASC}/F_{sound} tends to decrease with increasing Sound Pressure Levels (SPL), passing from values of 2.5-4.3 down to values of 1.4-2.1. This evidence can be explained considering that with increasing sound pressure levels the difference between the two evaluation approaches tends to decrease. This agrees with the increased cohesiveness of the samples, which means that the application of the sound is less effective, i.e. more energy is needed to disrupt the clusters into smaller subclusters.

In conclusion, these results confirm the applicability of both methodologies for the estimation of the interpaticle forces under different consolidation state.

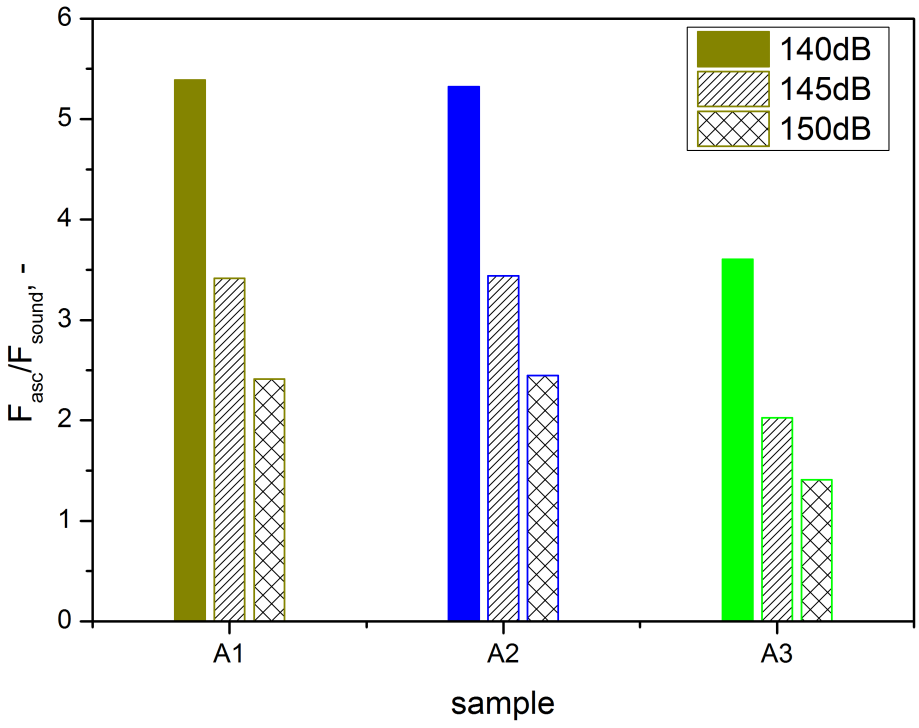

Figure 108 - Comparison between the cohesive forces evaluated in the annular shear cell (F_{ASC}) and in the sound assisted fluidized bed at different SPLs (F_{sound}).

7.5 Qualitative considerations

To date, in order to model the hydrodynamics behaviour of a fluidized bed reactor two different approaches can be followed. the first is the Euler– Euler method which is based on the classical kinetic-theory-based description in which particle interactions are binary and instantaneous in nature. In this method, each phase is considered as a continuum and specifies the particle amount in the mixture of two phases by the particle volume fraction and employs the constitutive equations of the granular theory to calculate the inter-particle forces. The second approach is the Euler–Lagrange method, which regards the fluid phase as a continuum and the solid particles as the discrete phase. Then the continuity equation for the liquid phase and the Newtonian equations for the discrete phase are solved using the force-balance method to obtain the discrete phase trajectories. Compared to the Euler–Lagrange method, the main disadvantage of Euler–Euler method is that this method does not consider the properties of the particles, such as Young's modulus, elastic modulus, particle diameter, etc., and only indirectly can include the collision between the particles and the particles-walls. Discrete Elements Methods (DEM) belongs to the deterministic model of the Euler–Lagrange method.

The interparticles forces estimated from flow properties following the procedure explained in the previous sections can, theoretically, be easily introduced in the Euler—Lagrange DEM simulations. Differently, the incorporation of complex particle physics (e.g., cohesion) is a more difficult task with Eulerian models. In particular, the averaging technique used to derive the continuum balances gives rise to terms, like the solid-phase stress tensor, which require a constitutive relation. The incorporation of cohesion into such constitutive quantities is considerably less straightforward than its incorporation into a discrete-particle model.

When considering the Euler-Euler models, also called two fluids models, two paths have been followed. The first approach is to indirectly consider the role of interparticles forces accounting for the formation of the agglomerates but not of deagglomeration phenomena and, thus of aggregative fluidization behaviour changing the volume scale from a single particle to a characteristic size of the agglomerate [189]. A similar approach was used by

McKeen and Pugsley [190] where the cohesion was accounted for by increasing the effective particle diameter used in the drag-force relation.

Gidaspow and Huilin [191] proposed a different approach of the kinetic theory. The Solids-phase granular stress tensor was modelled considering two regimes, viscous and plastic based on the packed-bed gas volume fraction, for the solids-phase granular stress tensor according with Johnson and Jackson 1987 [192]. The solids-phase granular stress tensor for the plastic regime is function of the internal angle of friction through the solid-phase viscosity, whereas in the viscous regime the solid-phase pressure is a function of the granular temperature as it is typically used in the kinetic theory.

In order to better contextualize our piece of work, the values of $\varepsilon_{mb,s}$ identify a stable dynamic condition of the bed. These results confirm the formation of agglomerates can used for describing the hydrodynamic of fluidized bed for relatively high bed voidage. It also confirms that this approach cannot be used for modelling the bed hydrodynamics for small bed voidage leading to the idea that different reference scale needs to be accounted for.

8 Conclusions

The main objective of this work was to provide a basis for understanding the factors responsible for changes in the fluidization behaviour with increasing temperature through two different methodologies: fluidization experiments and the rheological experiments on the same powders at the same temperature conditions. To this end, during this PhD work:

- a complete characterization in terms of flow properties of the powder samples was performed at ambient and high temperature by using the high temperature shear cell available at the University of Salerno;
- the Rumpf-Molerus model combining the continuum approach and the particle–particle interaction description was used to correlate the powder tensile strength with the interparticle forces;
- changes in the fluidization behaviour when changing mean particle size and the operating temperature were assessed by means of standard fluidization tests between ambient and high temperature;
- a link between the rheological and the fluidization behaviour of the powders analysed was found and its interpretation enabled to understand the conditions under which the IPFs dominate over the HDFs.

In particular, the multidisciplinary rheology/fluidization approach adopted in this work led to several conclusions.

Chapter 5 highlighted significant differences in the rheological behaviour of the ceramic powder tested. In particular, shear experiments of fresh materials highlighted a significant increase of powder cohesion at 500 °C for different cuts of the same powder, except for the finest sample A1. The powder cohesion is the parameter which appears to be mostly affected by temperature while the angle of internal friction shows a weaker dependence on temperature and consolidation level. This greater cohesiveness character resulted in a lower flowability of the particle samples with temperature. Thermal analysis on the powder samples revealed that the temperature effect on powder flow properties is only due to van der Waals forces.

A model combining the continuum approach and the particle-particle interaction description was used to correlate the powder tensile strength with the interparticle forces. For the fresh material, the model with the assumption of plastic deformation at contact points is able to predict the correct order of magnitude of the tensile strength, provided a reasonable value of the mean curvature radius at the contact points is used. Furthermore, the dependence of the tensile strength on powder consolidation and temperature is correctly described by the model.

Regarding the reacted material similar results in terms of temperature effects on the powder flow properties were found. Shear test experiments show a significant variation of the flow properties at high temperatures. Also, for these materials the most affected parameter is the cohesion. These findings together with the nature of the impurities characterized by means of EDX analysis applied to SEM imaging strongly suggest that the observed changes are due to the occurrence of capillary bridges between particles, even if DTA and TGA are not able to detect any significant phase change. However, the small amounts of liquid phase formed and confined to the particle surface are sufficient to considerably change the powder flow properties. The liquid phase produced and the estimation of the amount of liquids present in the capillary bridges based on geometrical consideration, together with a reasonable estimate of the liquid surface tension allows to correctly predicting the capillary interparticle forces and the tensile strength of the material. More in general, the results indicate that shear testing experiments at ambient and high temperatures allow to correctly estimate the intensity of interparticle forces in particulate systems

Chapter 6 showed that the mean size distribution affects significantly the fluidization behaviour of the materials investigated. In particular, significant differences were observed in the fluidization behaviour of the coarsest samples A5 and A4 and the finest sample A3 and A2. Sample A1, which exhibits the highest character cohesion, was impossible to fluidize with an ordinary fluidized bed reactor.

For all materials tested, the ΔPm/ΔPc ratio provided the very first indication of the influence of the HDFs and IPFs on the fluidization behaviour. The measured pressure drops across the bed, ΔPm, was within 1 or 2 percent of the theoretical value ΔPc for all fresh

material tested indicating that the bed material was relatively free from any dominant effect of the interparticle forces. However, an increase in the pressure deviation of the pressure drops with increasing temperature was observed to occur when the role of the IPFs was enhanced as a function of temperature. Hysteresis phenomena were observed in the pressure drop curves for the finest samples (A3 and A2) and with increasing temperature. Different structures within the bed, as detected with the X-ray images, were found. In particular, vertical channels were seen to form within the bed of the sample A3 and A2, and a maximum value with a consequently sudden decrease in the measured pressure drop was recorded in this case. Horizontal cracks were seen to form continuously within the bed of sample A1, causing the pressure drop to decrease and vary with time. This sample material was impossible to fluidize in ordinary conditions.

The effects of temperature on the minimum fluidization velocity were found to be able to indicate whether the HDFs or IPFs dominated the fluidization behaviour. Three different trends were found. u_{mf} values calculated for samples A5 and A4 decreased with increasing temperature and the values were well predicted by the viscous dominated term of the Ergun equation. Sample A3 showed a weaker decrease of u_{mf} with temperature. The Ergun equation well described the trend with temperature but it underestimated the experimental values and the shape factor back calculated were found to be larger than 1. Differently, u_{mf} values obtained for sample A2 decreased from 20 °C up to 200 °C as the fluidization behaviour is controlled by the HDFs, u_{mf} then suddenly increased between 300 °C and 500 °C when the IPFs started to become more dominant. The Ergun equation was found not to be suitable for giving the correct predictions due to the stronger role of the IPFs.

The results of the expansion profile revealed a greatest tendency to expand for beds made of the finest samples at high temperatures. Moreover, the settled and minimum fluidization voidages of the bed were found to increase with temperature. Similarly, to fluidization pressure drops, also for bed expansion of A3 and A2 systems of particles, hysteresis phenomena were observed.

The role of the IPFs on the fresh samples with increasing temperature was examined in the light of the results obtained from the bed expansion profiles plotted in the Richardson-Zaki

form. The experimental values of n* and u_t* were determined from these plots. The n* values were found to be significantly greater than the theoretical ones, predicted using the Richardson-Zaki correlations and the Stokes law. Highest values of n^* were found at ambient conditions except for the finest sample A2. Differently, the values of u_t* obtained at ambient conditions were found to be greater than the calculated ones for samples A3 and A2. High values of u_t^* can also be explained considering the presence of clusters in the homogeneous expansion. This would imply the contribution of the IPFs to the stability of these materials.

The bed collapse test was found to be a discriminating test, able to highlight changes in the powders' aeratability between low and high temperatures. It was not only used to evaluate the ability of the powders to withstand sudden changes in the fluidized unit, but also to evaluate the minimum bubbling conditions. From the collapse profiles, different behaviours were observed. Sample A5 made of the largest particle, showed only the bubble escape step. When increasing the temperature, the collapse profiles exhibited a double velocity for the bubbling escape. In the very first second, the largest bubbles rised up, then it was observed a couple of second in which the remains bubbles escaped through the bed at different velocity. On the other hand, the finest sample A2 showed two stages for the hindered sedimentation, the first one governed by the HDFs and the second one for low voidage of the bed, dominated by IPFs. The de-aeration rate U_{de} was found to increase with temperature. Only the sample A2 showed a decrease in this parameter for temperatures above 300 °C. The standardized collapse time SCT was found to slightly increase with increasing temperature up to 300 °C. While, a further increase in temperature did not produce any relevant variation. The Abrahamsen and Geldart correlation was not capable of predicting the changes in aeratability of such materials, given the active role of the IPFs on the fluidization behaviour of this sample when increasing temperature. Results for the BER ratio agreed with the results obtained with the expansion profiles. A greater BER was observed for finest sample at high temperature. These results also suggested a spatial reorganization of the particles due an active role of IPFs. This effect was enhanced when increasing temperature for the finest samples A3 and A2, as the SCT and the BER were much higher for sample A2 and A3 than for sample A4 and A5.

The detailed research of the bubbling regime transition with temperature performed with different experimental techniques has provided a better understanding of the phenomena occurring in beds of fine cohesive particles. Visual methodology and that based on detection of the pressure drop minimum were found to be unreliable when the particle systems were dominated by interparticle forces, principally because of channeling and instable formation/distruption of bubbles characterize the behavior of these particles. For such systems, these techniques could lead to incorrectly predicting the starting point of bubbling. On the other hand, the analysis of the voidage of the dense phase and the overall bed expansion as function of the flow rate allowed reconstructing the sequence of phenomena through which a stable flow of bubbles across the solid mass were achieved. Beyond dense phase expansion, stabilization or contraction of the emulsion phase was observed at higher velocity, when the role of interparticle forces due to high temperature was balanced by gas drag. The equilibrium between contact and hydrodynamic forces was achieved for gas velocity $u_{mb,s}$. For $u = u_{mb,s}$ regular bubbling across a stably structured emulsion phase, $\varepsilon_{mb,s}$ was observed. Unlike other criteria, this definition identified a final structure of the bed.

The role of HDFs and IPFs on the fluidization behavior of particle systems studied was investigated by looking at the applicability of Foscolo and Gibilaro [12] stability criterion starting from the analysis conducted by Valverde et al. [187] on the initial settling velocity of cohesive particles and the rheological results. To this end, the experimental values of the voidage at minimum bubbling, ε_{mb}, were compared with the prediction given by their model with increasing temperature. The results showed the capability of predicting the final structure of the bed with temperature when considering an aggregative fluidization behavior caused by interparticle adhesive forces.

The role of the IPFs on the fluidization of cohesive powders was also estimated by using an experimental and theoretical approach. In particular, the experimental results obtained with and without the application of sound in a lab fluidized bed were analysed with a cluster/sub-cluster model. The main output of the model results in an estimation of the interparticle forces acting in the fluidized system (F_{sound}). The latter was compared to the output evaluated by using a shear testing approach (F_{ASC}). The values obtained were always of the same order of magnitude, even though evaluated in completely different conditions.

These results confirmed the close synergy between fluidization behaviour and flow properties and, in particular, the close relationship between the particles behaviour at micro and macro scales.

8.1 Future work

The extensive experimental campaign performed during this work clearly demonstrated the relevant effect that temperature can have on both the flow properties and the fluidization behaviour of the various materials tested. In particular, the findings highlighted how temperature can enhance the role of the IPFs causing sudden changes in the fluidization behaviour. A quantification of the magnitude of the particle-particle contact forces acting in a fluidized system was proposed by applying the Rumpf and Molerus model to the rheological data.

In this work the approach proposed by Rumpf and Molerus was used to estimate properties at particle scale starting from the whole system behaviour. One of the possibilities for future work is to perform shear tests on an ideal material. This reference material should have physical and chemical properties very similar to the strong hypothesis of the model used. Furthermore, experimental evaluation of some of the properties of the powder samples can be done, such as the Hamaker constant (also as function of the temperature) and the compressive strength. Regarding the flow properties of the materials, it would also be interesting to develop an experimental procedure to measure the unconfined yield strength. This may lead to a better understanding of the IPFs role in a non-consolidate state, starting from the validation of the Mohr-Coulomb analysis.

Following the two-fold approach proposed in this thesis, future work should further explore the link between both rheological and fluidization analyses. Firstly, it would be very interesting to perform the fluidization tests also on the reacted material in order to understand the role of temperature on the IPFs, principally capillary forces, and so the effect of temperature on the fluidization behaviour. Particularly, linking the results obtained with two different approaches and conditions deserve singular attention. As a matter of fact, the model used for estimating the capillary forces from the shear experiments assumed that the static forces, dominated by surface tension, are the only

ones to be accounted for. Differently in aerated conditions, dynamic forces, which are dominated by the viscosity, can play a significant role. In such circumstance the model should include mathematical consideration, i.e. the lubrication theory, on the dynamic formation and disruption of the agglomerates, as well as, liquid bridges rupture and its related rupture energy. Although the behaviour of such particles assemblies is still hardly predictable by means of micro-mechanical models, the knowledge of simple expressions able to describe interactions at the microscopic scale is of real interest. Furthermore, tests on the effect of sound on the fluidization behaviour in presence of capillary forces would be particularly relevant for both academia and industry.

In the last decades a lot of work has been done in developing mathematical models for simulate the dynamic behaviour of granular systems under ordinary conditions. Future work should be directed to answer the question of how incorporating IPFs effects into the standard equations used for predicting the fluidization behaviour and a greater effort is needed in order to model/simulate the realistic behaviour of a cohesive fluidized bed not under ordinary operating condition. The introduction of new models accounting for interparticles forces, such as the ones estimated from shear experiments, is rather straightforward for discrete-particle DEM simulations. While the incorporation of complex interactions among particles, such as IPFs, is a more difficult task with Eulerian models. This lack of understanding now represents a barrier to further development in chemical engineering. The understanding of dynamic mesoscale structures is recognized as a common challenge for researchers. The main objective is to correlate element properties with system behavior. Because of missing links at these mesoscales, the main challenge for engineers should be in establishing correlation between elements and systems by approaches based on experimental data and assumptions. The first step should aim to define the principles that govern mesoscales in order to identify the level-specific nature of mesoscale phenomena. Otherwise, two or more mesoscales at different levels could become unclear, leading to confusion and complexity during the study of their respective governing rules.

In aerated granular systems this could be used for understanding the mesoscale phenomena in term of bubble formation, bubble size, velocity and frequency, dynamic formation of agglomerate and the dynamics of force chains. While numerical simulations

can provide some of this information in idealized systems, experimental methods are the only way to study such physics in real systems.

A further improvement of the work can be related to include the effect of changing other operating conditions, such as pressure, on both the flow properties and on the fluidization behavior of cohesive powders.

Nomenclature

DTA	Differential thermal analysis
EDX	Energy-dispersive X-ray spectroscopy
HDFs	Hydrodynamic forces
HT-ASC	High temperature annular shear cell
HTMFB	Temperature Micro-Force Balance
IPFs	Interparticle forces
SEM	Scanning Electron Microscope
PSD	Particle size distribution
TGA	Thermogravimetric analysis

d_{50}	50^{th} percentile of the volumetric distribution	m
d_{90}	90^{th} percentile of the volumetric distribution	m
d_p	Mean article diameter	m
dp_{agg}	Diameter of the agglomerate	μm
d_{sv}	Sauter mean diameter	μm
F45	fraction of fines	-
F_a	van der Walls forces	N
F_{ASC}	Interparticle forces following the Rumpf and Molerus approach	N
$F_{attractive}$	Attractive van der Waals forces	N
f_c	Unconfined yield strength	Pa
F_c	isostatic stress with the contact forces	N
F_c^*	tensile force of the bridge	Pa
F_{cap}	capillary force	N
F_e	image force	N
F_{ef}	coulombic force	N
ffc	flow factor	-
F_{mf}	Magnetic force	N
F_N	compressive normal force	N
$F_{repulsive}$	Repulsive van der Waals forces	N
F_{sound}	Disgregative force	N

F_{vdW}	Van der Waals' forces	N
g	Gravity acceleration	m/s^2
Ga	Galileo number	-
H	Materia hardness	Pa
h_a	Height of the surface asperity	m
H_d	Dense phase height	m
H_s	height of the settled bed	m
hw	Lifshitz-van der Waals constant	J
k	coordination number	-
k	Ratio of agglomerate to particle radius	-
L_p	liquid per particle	m^2
m	Particle mass	kg
M	Bed particles mass	kg
n	Index of Richardson-Zaki	-
N	number of particles per agglomerate	-
n*	Experimental index of R-Z	-
P	Pressure	atm
p_f	compressive strength	Pa
q	Particle charge	
q_m	magnitudes of magnetic poles	
R	Radius of the particles	m
R.H.	Relative humidity	%
r_{cb}	Radius of the capillary bridge	m
Re_{mf}	Reynolds number at minimum fluidization condition	-
Re_t	Reynolds number at terminal condition	-
r_{pla}	Plastic radius of the asperity	
SCT	standardized collapse time	-
St*	Viscous Stokes number	-
S_{tot}	total salt weight fraction	-
T	Temperature	°C
t_0	gas supply switched off	s
t_s	Dearation time	s
t_s	time for complete collapse	s
u	Gas velocity	cm/s

U_b	bubble escape rate	cm/s
u_{de}	Dense phase collapse rate	cm/s
u_{mb}	Minimum bubbling velocity	cm/s
$u_{mb,\ s}$	Minimum bubbling velocity from fluidization map	cm/s
$u_{mb,\ v}$	Visual minimum bubbling	cm/s
$u_{mb,p}$	Minimum bubbling velocity from pressure drop	cm/s
u_{mb}/u_{mf}	non bubbling ratio	-
u_{mf}	Minimum fluidization velocity	cm/s
u_t	Particle settling velocity	-
u_t*	Experimental values of the settling velocity from R-Z	cm/s
V*	Dimensionless bridge volume	-
V_b	bridge volume	m^3
V_b	volume of the liquid	m^3
V_l	liquid volume per unit mass of the sample	m^3
v_o	Collision velocity	m/s
W	rupture energy	J
W	gravitational force	N
W*	rupture energy	-
X_l	liquid weight fraction	-
z_o	Distance between particles	nm

Greek symbol

ε	Bed voidage	-
δ	mean curvature radius at the contacting	m
ξ	Dielectric constant	F/m
μ	permeability	H/m
α	Angle of liquid between particles	°
ϕ	Particle shape factor	-
σ	normal stress	Pa
τ	Shear stress	Pa
ξ_0	Free space dielectric constant	F/m
σ_1	Major principal stress	Pa

ε_b	overall bed voidage	-
$\sigma_c=f_c$	unconfined yield strength	Pa
ε_d	Dense phase voidage	-
ε_d	dense phase voidage	-
φ_e	Effective angle of internal friction	°
φ_i	static angle of internal friction	°
ε_{mb}	Bed voidage at minimum bubbling velocity	-
ε_{mf}	Bed voidage at minimum fluidization velocity	-
ΔP	Capillary pressure	Pa
ΔP_c	Calculated pressure drop	mmH_2O
ΔP_m	Measured pressure drop	mmH_20
ξ_r	Relative dielectric constant	F/m
ε_s	Settled Bed voidage	-
σ_s	Surface tension	N/m
σ_t	tensile strength,	Pa
σ_t	Tensile strength	Pa
μ	Viscosity	Pa*s
β	angle of the wet spherical cap of the contact	°
δ	Thickness of the liquid layer	m
δ_b	volumetric bubble fraction	-
$\varepsilon_{changing\ slope}$	Voidage at changing slope	-
$\varepsilon_{mb,e}$	Minimum bubbling bed voidage from fluidization maps	-
$\varepsilon_{mb,s}$	Minimum bubbling bed voidage from fluidization maps	-
λ_l	average liquid volume per unit surface	-
μ_l	Liquid viscosity	Pa*s
ρ_b	Bulk density	Kg/m3
ρ_f	Fluid density	Kg/m3
ρ_p	Particle density	Kg/m3
ρ_s	Solid density	Kg/m3
φ_{agg}	Particles packing fraction in a single agglomerate	-
ρ_{BDL}	loose bulk density	Kg/m^3
ρ_{BDP}	Tapped bulk density	Kg/m^3

References

1. Kunii, D., Levenspiel, O. *Fluidization Engineering*. Elsevier; 1991.

2. Grewal NS, Gupta A. Total and gas convective heat transfer from a vertical tube to a mixed particle gas-solid fluidized bed. *Powder Technol*. 1989;57:27-38.

3. Molerus O. Interpretation of Geldart's type A, B, C and D powders by taking into account interparticle cohesion forces. *Powder Technol*. 1982;33(1):81-87. doi:10.1016/0032-5910(82)85041-9.

4. Geldart D. Estimation of basic particle properties for use in fluid-particle process calculations. *Powder Technol*. 1990;60:1-13.

5. Fletcher J, Deo M, Hanson F. Re-examination of minimum fluidization velocity correlations applied to Group B sands and coked sands. Powder Technol. *Powder Technol*. 1992;69:147-155.

6. Knowlton TM. Pressure and temperature effects in fluid-particle systems. In: *Pressure and Temperature Effects in Fluid-Particle Systems*. ; 1992:27–46.

7. Yates JG. Effects of temperature and pressure on gas-solid fluidization. *Chem Eng Sci*. 2000;51:168-205.

8. Lettieri P, Yates JG, Newton D. The influence of interparticle forces on the fluidization behaviour of some industrial materials at high temperature. *Powder Technol*. 2000;110:117-127.

9. Lettieri P, Newton D, Yates JG. High temperature effects on the dense phase properties of gas fluidized beds. *Powder Technol*. 2001;120:34-40.

10. Lettieri P, Newton D, Yates JG. Homogeneous bed expansion of FCC catalysts, influence of temperature on the parameters of the Richardson–Zaki equation. *Powder Technol*. 2002;147:34-48.

11. Coltters R, Rivas AL. Minimum fluidization velocity correlations in particulate systems. *Powder Technol*. 2004;147:34-48.

12. Foscolo P, Gibilaro L. A fully predictive criterion for the transition between particulate and aggregate fluidization. *Chem Eng Sci*. 1984;39(12):1667-1675.

13. Quintanilla MAS, Castellanos A, Valverde JM. Correlation between bulk stresses and interparticle contact forces in fine powders. *Phys Rev E Stat Nonlin Soft Matter Phys*. 2001;64(3 Pt 1):31301. doi:10.1103/PhysRevE.64.031301.

14. Israelachvili JN. Intermolecular and Surface Forces 2nd edn (London: Academic). 1991.

15. Israelachvili JN. van der Waals dispersion force contribution to works of adhesion and contact angles on the basis of macroscopic theory. *J Chem Soc Faraday Trans 2 Mol Chem Phys*. 1973;69:1729-1738.

16. Tabor D. *Gases, Liquids and Solids: And Other States of Matter*. Cambridge University Press; 1991.

17. Hamaker HC. The London—van der Waals attraction between spherical particles. *physica*. 1937;4(10):1058-1072.

18. Lifshitz EM. The theory of molecular attractive forces between solids. 1956.

19. Visser J. On Hamaker constants: A comparison between Hamaker constants and Lifshitz-van der Waals constants. *Adv Colloid Interface Sci*. 1972;3(4):331-363.

20. Krupp H. Particle adhesion theory and experiment. *Adv Colloid Interface Sci*. 1967;1(2):211–239. doi:10.1016/0001-8686(67)80004-6.

21. Rietema K, Cottaar EJE, Piepers HW. The effects of interparticle forces on the stability of gas-fluidized beds—II. Theoretical derivation of bed elasticity on the basis of van der Waals forces between powder particles. *Chem Eng Sci*. 1993;48(9):1687-1697.

22. Donsì G, Massimilla L. Bubble-free expansion of gas-fluidized beds of fine particles. In: *Bubble-Free Expansion of Gas-Fluidized Beds of Fine Particles*. Vol 19. ; 1973:41-53. doi:10.1002/aic.690190604.

23. Molerus O. Theory of yield of cohesive powders. *Powder Technol*. 1975;12(3):259-275. doi:10.1016/0032-5910(75)85025-X.

24. Schubert H. Capillarity in porous solid material systems. 1982.

25. Masuda H, Higashitani K, Yoshida H. *Powder Technology Handbook*. CRC Press; 2006.

26. Fisher RA. On the capillary forces in an ideal soil; correction of formulae given by WB Haines. *J Agric Sci*. 1926;16(3):492-505.

27. Pagliai P, Simons SJR, Rhodes D. Towards a fundamental understanding of defluidisation at high temperatures: a micro-mechanistic approach. *Powder Technol*. 2004;148(2):106-112.

28. Forsyth AJ, Hutton S, Rhodes MJ. Effect of cohesive interparticle force on the flow characteristics of granular material. *Powder Technol*. 2002;126(2):150-154. doi:10.1016/S0032-5910(02)00046-3.

29. Tanaka M, Komagata M, Tsukada M, Kamiya H. Evaluation of the particle-particle interactions in a toner by colloid probe AFM. *Powder Technol*. 2008;183(2):273-281. doi:10.1016/j.powtec.2007.07.039.

30. Pagliai P, Simons SJRJR, Rhodes D. A novel experimental study of temperature enhanced cohesive interparticle forces. *Powder Technol*. 2007;174(1):71-74. doi:10.1016/j.powtec.2006.10.025.

31. Geldart D. Types of gas fluidization. *Powder Technol*. 1973;7(5):285-292. doi:10.1016/0032-5910(73)80037-3.

32. Geldart D, Harnby N, Wong ACY. Fluidization of cohesive powders. *Powder Technol*. 1984;37(1):24-37. doi:10.1016/0032-5910(84)80003-0.

33. Seville JPK, Clift R. The effect of thin liquid layers on fluidization characteristics. *Powder Technol*. 1984;37:117-129. doi:10.1016/0032-5910(84)80011-X.

34. Chirone R, Barletta D, Lettieri P, Poletto M. Bulk flow properties of sieved samples of a ceramic powder at ambient and high temperature. *Powder Technol*. 2016;288:379-387.

35. Wang J, Cao Y, Jiang X, Yang Y. Agglomeration detection by acoustic emission (AE) sensors in fluidized beds. *Ind Eng Chem Res*. 2009;48(7):3466-3473.

doi:10.1021/ie800324m.

36. Li J, Ge W, Wang W, Yang N, Huang W. Focusing on mesoscales: from the energy-minimization multiscale model to mesoscience. *Curr Opin Chem Eng*. 2016;13:10-23. doi:10.1016/j.coche.2016.07.008.

37. Li J, Kwauk M. Multiscale nature of complex fluid-particle systems. *Ind Eng Chem Res*. 2001;40(20):4227-4237. doi:10.1021/ie0011021.

38. Coppens M, Ommen JR Van. Structuring chaotic fluidized beds. 2003;96:117-124. doi:10.1016/j.cej.2003.08.007.

39. Valverde JM, Castellanos A. Effect of compaction history on the fluidization behavior of fine cohesive powders. *Phys Rev E - Stat Nonlinear, Soft Matter Phys*. 2006;73(5):1-5. doi:10.1103/PhysRevE.73.056310.

40. Li J, Tung Y, Kwauk M. Energy Transport and Regime Transition in Particle-Fluid Two-Phase Flow. *Circ Fluid Bed Technol*. January 1988:75-87. doi:10.1016/B978-0-08-036225-0.50012-5.

41. Mutsers SMP, Rietema K. The effect of interparticle forces on the expansion of a homogeneous gas-fluidized bed. *Powder Technol*. 1977;18(2):239-248. doi:10.1016/0032-5910(77)80014-4.

42. Rietema K, Piepers HW. The effect of interparticle forces on the stability of gas-fluidized beds – I. Experimental evidence. *Chem Eng Sci*. 1990;45(6):1627-1639.

43. Hou QFF, Zhou ZYY, Yu ABB. Micromechanical modeling and analysis of different flow regimes in gas fluidization. *Chem Eng Sci*. 2012;84:449-468. doi:10.1016/j.ces.2012.08.051.

44. Massimilla L, Donsì G, Zucchini C. The structure of bubble-free gas fluidized beds of fine fluid cracking catalyst particles. *Chem Eng Sci*. 1972;27(11):2005-2015. doi:10.1016/0009-2509(72)87059-3.

45. Bailey AG. Electrostatic phenomena during powder handling. *Powder Technol*. 1984;37(1):71-85.

46. Ciborowski J, Wlodarski A. On electrostatic effects in fluidized beds. *Chem Eng Sci*. 1962;17(1):23-32.

47. Boland D, Geldart D. Electrostatic charging in gas fluidised beds. *Powder Technol*. 1972;5(5):289-297.

48. Bafrnec M, Bena J. Quantitative data on the lowering of electrostatic charge in a fluidized bed. *Chem Eng Sci*. 1972;27(5):1177-1181.

49. Turner GA, Balasubramanian M. Investigations of the Contributions to the Tensile Strength of Weak Particulate Masses. *Powder Technol*. 1974;10:121-127.

50. Coelho MC, Harnby N. Moisture bonding in powders. *Powder Technol*. 1978;20(2):201-205.

51. Tyrrell JWGWG, Cleaver JASAS. The effect of atmospheric humidity on interparticle force. *ICHEME Res EVENT*. 1997:541-544.

52. LaMarche CQ, Miller AW, Liu P, Hrenya CM. Linking micro-scale predictions of capillary forces to macro-scale fluidization experiments in humid environments. *AIChE J*. 2016;62(10):3585-3597. doi:10.1002/aic.15281.

53. Landi G, Barletta D, Poletto M. Modelling and experiments on the effect of air humidity on the flow properties of glass powders. *Powder Technol*. 2011;207(1-3):437-443. doi:10.1016/j.powtec.2010.11.033.

54. Gröger T, Tüzün U, Heyes DM. Modelling and measuring of cohesion in wet granular materials. *Powder Technol*. 2003;133(1-3):203-215. doi:10.1016/S0032-5910(03)00093-7.

55. D'Amore M, Donsì G, Massimilla L. The influence of bed moisture on fluidization characteristics of fine powders. *Powder Technol*. 1979;23(2):253-259. doi:10.1016/0032-5910(79)87015-1.

56. Wormsbecker M, Pugsley T. The influence of moisture on the fluidization behaviour of porous pharmaceutical granule. *Chem Eng Sci*. 2008;63(16):4063-4069. doi:10.1016/j.ces.2008.05.023.

57. Tardos G, Mazzone D, Pfeffer R. Destabilization of fluidized beds due to agglomeration part II: experimental verification. *Can J Chem Eng*. 1985;63(3):384-389.

58. Ennis BJ, Tardos G, Pfeffer R. A microlevel-based characterization of granulation phenomena. *Powder Technol*. 1991;65(1-3):257-272.

59. Simons SJR, Seville JPK, Adams MJ. Mechanisms of agglomeration. In: *Sixth International Symposium on Agglomeration, Nagoya, Japan*. ; 1993:15-17.

60. Simons SJR, Seville JPK, Adams MJ. An analysis of the rupture energy of pendular liquid bridges. *Chem Eng Sci*. 1994;49(14):2331-2339.

61. Fairbrother RJ. A Microscopic Investigation of Particle-Particle Interactions in the Presence of Liquid Binders in Relation to the Mechanisms of" Wet" Agglomeration Processes. 1999.

62. Wright PC, Raper JA. Role of liquid bridge forces in cohesive fluidization. *Chem Eng Res Des*. 1998;76(6):753-760.

63. Formisani B, Giromonte R, Mancuso L. Analysis of the fluidization process of particle beds at high temperature. *Chem Eng Sci*. 1998;53:117-127.

64. Ergun S. Fluid flow through packed columns. *Chem Eng Prog*. 1952;48:89-94.

65. Botterill JSM, Teoman Y, Yuregir KR. THE EFFECT OF TEMPERATURE ON FLUIDIZED BED BEHAVIOUR. *Chem Eng Commun*. 1982;15:227-238.

66. Wen CY, Yu YH. A generalized method for predicting the minimum fluidization velocity. *AIChE J*. 1966;12:610-612.

67. Pattipati RR, Wen CY. Minimum fluidization velocity at high temperatures. *Ind Eng Chem Process Des Dev*. 1981;20(4):705-707. doi:10.1021/i200015a022.

68. Botterill JSM, Teoman Y, Yüregir KR. The effect of operating temperature on the velocity of minimum fluidization, bed voidage and general behaviour. *Powder Technol*. 1982;31:101-110.

69. Fletcher J, Deo M, Hanson F. Re-examination of minimum fluidization velocity correlations applied to Group B sands and coked sands. Powder Technol. *Powder Technol*. 1992;69(0):147-155.

70. Coltters R, Rivas a. L. Minimum fluidation velocity correlations in particulate systems. *Powder Technol*. 2004;147(1-3):34-48. doi:10.1016/j.powtec.2004.06.013.

71. Delebarre A. Revisiting the Wen and Yu Equations for Minimum Fluidization Velocity Prediction. *Chem Eng Res Des*. 2004;82(5):587-590. doi:10.1205/026387604323142621.

72. Lucas A, Arnaldos J, Casal J, Puigjaner L. High temperature incipient fluidization in mono and polydisperse systems. *Chem Eng Commun*. 1986;41(1-6):121-132. doi:10.1080/00986448608911715.

73. Raso G, D'Amore M, Formisani B, Lignola P. The influence of temperature on the properties of the particulate phase at incipient fluidization. *Powder Technol*. 1992;72:71-76.

74. Formisani B, Girimonte R, Pataro G. The influence of operating temperature on the dense phase properties of bubbling fluidized beds of solids. *Powder Technol*. 2002;125:28-38. doi:10.1016/S0032-5910(01)00494-6.

75. Lettieri P, Newton, D., Yates JG. High temperature effects on the dense phase properties of gas fluidized beds. *Powder Technol*. 2001;120:34-40.

76. Geldart, D., Wong ACY. Fluidization of powders showing degrees of cohesiveness—II. Experiments on rates of de-aeration. *Chem Eng Sci*. 1985;40:653-661.

77. Lin, C.L., Wey, M.Y., You SD. The effect of particle size distribution on minimum fluidization velocity at high temperature. *Powder Technol*. 2002;126:297-301.

78. Botterill JSM, Teoman Y, Yuregir KR. Comments on "Minimum fluidization velocity at high temperature" *Ind Eng Chem Process Des Dev*. 1982;21(4):784-785. doi:10.1021/i200019a042.

79. Zhou T, Li H. Estimation of agglomerate size for cohesive particles during fluidization.

Powder Technol. 1999;101:57-62.

80. Zaki WN, Richardson JF. Sedimentation and fluidisation: Part I. *Trans Inst Chem Eng*. 1954;32:35-53.

81. Agbim JA, Nienow AW, Rowe PN. Inter-particle forces that suppress bubbling in gas fluidised beds. *Chem Eng Sci*. 1971;26:1293-1294. doi:10.1016/0009-2509(71)87015-X.

82. Siegell JH. Early studies of magnetized-fluidized beds. *Powder Technol*. 1989;57(3):213-220. doi:10.1016/0032-5910(89)80077-4.

83. Jackson R. The mechanics of fluidized beds. I. The stability of the state of uniform fluidization. *Trans Inst Chem Eng*. 1963;41(13):13-21.

84. Verloop J, Heertjes P. Shock waves as a criterion for the transition from homogeneous to heterogeneous fluidization. *Chem Eng Sci*. 1970;25:825-832.

85. Wallis GB. *One-Dimensional Two-Phase Flow*. New York, NY: McGraw-Hill; 1969.

86. Brandani S, Foscolo PU. Analysis of discontinuities arising from the one-dimensional equations of change for fluidization. *Chem Eng Sci*. 1994;49(5):611-619. doi:10.1016/0009-2509(94)85007-0.

87. Piepers H, Cottaar E, Verkooijen A, Rietema K. Effects of pressure and type of gas on particle-particle interaction and the consequences for gas—solid fluidization behaviour. *Powder Technol*. 1984;37:55-70.

88. Cottaar E, Rietema K. A theoretical study on the influence of gas adsorption on interparticle forces in powders. *J Colloid Interface Sci*. 1986;109(1):249-260.

89. Rapagna S, Foscolo P, Gibilaro L. The influence of temperature on the quality of gas fluidization. *Int J Multiph Flow*. 1994;20(2):305-313.

90. Xie HY, Geldart D. Fluidization of FCC powders in the bubble-free regime: effect of types of gases and temperature. *Powder Technol*. 1995;82(3):269-277. doi:10.1016/0032-5910(94)02932-E.

91. Jean R, Fan L. On the model equations of Gibilaro and Foscolo with corrected buoyancy force. *Powder Technol*. 1992;72:201-205.

92. Lettieri P, Mazzei L. Analysis of the fluid-bed stability of FCC catalysts at high temperature in terms of bed elasticity. *Particuology*. 2008;6(1):30-37. doi:http://dx.doi.org/10.1016/j.cpart.2007.10.003.

93. Lettieri, P., Newton, D., Yates JG. Homogeneous bed expansion of FCC catalysts, influence of temperature on the parameters of the Richardson–Zaki equation. *Powder Technol*. 2002;123:221-231.

94. Mills P, Snabre P. Settling of a Suspension of Hard Spheres. *Europhys Lett*. 1994;25(9):651-656. doi:10.1209/0295-5075/25/9/003.

95. Valverde JM, Castellanos A, Mills P, Quintanilla MAS. Effect of particle size and interparticle force on the fluidization behavior of gas-fluidized beds. *Phys Rev E*. 2003;67(5):51305. doi:10.1103/PhysRevE.67.051305.

96. Castellanos A. *The Relationship between Attractive Interparticle Forces and Bulk Behaviour in Dry and Uncharged Fine Powders*. Vol 54.; 2005. doi:10.1080/17461390500402657.

97. Valverde JM, Castellanos A. Bubbling Suppression in Fluidized Beds of Fine and Ultrafine Powders. *Part Sci Technol*. 2008;26(3):197-213. doi:10.1080/02726350802026656.

98. Girimonte R, Formisani B. The minimum bubbling velocity of fluidized beds operating at high temperature. *Powder Technol*. 2009;189(1):74-81. doi:10.1016/j.powtec.2008.06.006.

99. Girimonte R, Formisani B. Effects of operating temperature on the bubble phase properties in fluidized beds of FCC particles. *Powder Technol*. 2014;262:14-21. doi:10.1016/j.powtec.2014.04.041.

100. Rietema K. Proceedings of the International Conference on fluidization. In: *Proceedings of the International Conference on Fluidization, Edited by A. A. H.*

Drinkerburg, Amsterdam. ; 1967:154.

101. Sutton HM, Richmond RA. Improving the storage conditions of fine powders by aeration. *Trans Inst Chem Eng*. 1973;51.

102. Geldart D, Wong A. Fluidization of powders showing degrees of cohesiveness—II. Experiments on rates of de-aeration. *Chem Eng Sci*. 1985;40(4):653-661.

103. Khoe G, Ip T, Grace J. Rheological and fluidization behaviour of powders of different particle size distribution. *Powder Technol*. 1991;66:127-141.

104. Lorences MJ, Patience GS, Díez F V, Coca J. Fines effects on collapsing fluidized beds. *Powder Technol*. 2003;131(2-3):234-240. doi:10.1016/S0032-5910(03)00004-4.

105. Bruni G, Lettieri P, Newton D, Yates JG. The influence of fines size distribution on the behaviour of gas fluidized beds at high temperature. *Powder Technol*. 2006;163(1-2):88-97. doi:10.1016/j.powtec.2006.01.007.

106. Brown GW. Direct measurement of FCC fluidizability helps spot problems. *Oil Gas J*. 1990;88(3).

107. Abrahamsen ARA, Geldart D. Behaviour of gas-fluidized beds of fine powders part I. Homogeneous expansion. *Powder Technol*. 1980;26(1):35-46. doi:10.1016/0032-5910(80)85005-4.

108. Barreto G, Yates J, Rowe P. The measurement of emulsion phase voidage in gas fluidized beds of fine powders. *Chem Eng Sci*. 1983;38:345.

109. Barreto G, Mazza G, Yates J. The significance of bed collapse experiments in the characterization of fluidized beds of fine powders. *Chem Eng Sci*. 1988;43(11):3037-3047.

110. Geldart D, Harnby N, Wong AC. Fluidization of cohesive powders. *Powder Technol*. 1984;37(1):25-37. doi:10.1016/0032-5910(84)80003-0.

111. Lettieri P. A study of the influence of temperature on the flow behaviour of solid materials in a gas fluidized bed. 1999.

112. Neddermann RM. Statics and kinematics of granular materials. *Cambridge Univ Press*. 1992.

113. Schulze D. Powder and Bulk Solids. *Springer-Verlag Berlin Heidelb*. 2008.

114. Janssen HA. Versuche über getreidedruck in silozellen. *Vereines Dtsch Ingenieure*. 1895;39:1045-1049.

115. Walker DM. An approximate theory for pressures and arching in hoppers. *Chem Eng Sci*. 1966;21:975-997.

116. Walters JK. A theoretical analysis of stresses in silos with vertical walls. *Chem Eng Sci*. 1973;28:13-21.

117. Fitzpatrick JJ, Barringer SA, Iqbal T. Flow property measurement of food powders and sensitivity of Jenike's hopper design methodology to the measured values. *J Food Eng*. 2004;61:399-405.

118. Chen P, Yuan Z, Shen X, Zhang Y. Flow properties of three fuel powders. *Particuology*. 2012;10:438-443.

119. Jenike AW. Storage and flow of solids. *Bull No 123, Eng Exp Station Univ Utah*. 1964.

120. Schulze D. A new ring shear tester for flowability and time consolidation measurements. In: *Proc. 1st International Particle Technology Forum*. ; 1994.

121. Schwedes J. Review on testers for measuring flow properties of bulk solid. *Granul Matter*. 2003;5:1-43.

122. Liang C, Xie X, Xu P, Chen X, Zhao C, X. W. Investigation of influence of coal properties on dense-phase pneumatic conveying at high pressure. *Particuology*. 2012;10:310-316.

123. Fu X, Huck D, Makein L, Armstrong B, Willen U, Freeman T. Effect of particle shape and size on flow properties of lactose powders. *Particuology*. 2012;10:203-208.

124. Pilpel N, Britten JR. Effects of temperature on the flow and tensile strengths of powders. *Powder Technol*. 1979;22(1):33-44. doi:10.1016/0032-5910(79)85005-6.

125. Tomas J. Assessment of Mechanical Properties of Cohesive Particulate Solids. Part 1: Particle Contact Constitutive Model. *Part Sci Technol*. 2001;19(2):95-110. doi:10.1080/02726350152772056.

126. Tomas J. Assessment of Mechanical Properties of Cohesive Particulate Solids. Part 2: Powder Flow Criteria. *Part Sci Technol*. 2001;19(2):111-129. doi:10.1080/02726350152772065.

127. Medhe M, Pitchumani B, Tomas J. Flow characterization of fine powders using material characteristic parameters. *Adv Powder Technol*. 2005;16(2):123-135. doi:10.1163/1568552053621687.

128. Carr RL. Evaluating flow properties of solids. *Chem Eng*. 1965;72(2):163-168.

129. Carr RL. Particle behaviour storage and flow. *Bri Chem Eng*. 1970;15:1541-1549.

130. Geldart D, Wong A. Fluidization of powders showing degrees of cohesiveness—I. Bed expansion. *Chem Eng Sci*. 1984;39:1481-1488.

131. Bruni G. An investigation of the influence of fines size distribution and high temperature on the fluidization behaviour of gas fluidized beds linked with rheological studies. Ph.D. Thesis. 2005;(September).

132. Santomaso A, Lazzaro P, Canu P. Powder flowability and density ratios: the impact of granules packing. *Chem Eng Sci*. 2003;58(13):2857-2874. doi:10.1016/S0009-2509(03)00137-4.

133. Bruni G, Barletta D, Poletto M, Lettieri P. A rheological model for the flowability of aerated fine powders. *Chem Eng Sci*. 2007;62:397-407.

134. Jenike AW. Gravity flow of solids. *Trans Instn Chem Engrs*. 1962;40(29):264.

135. *ASTMD6773-02 Standard Shear Test Method for Bulk Solids Using the Schulze Ring Shear Tester.*; 2008.

136. Schulze D. *Powders and Bulk Solids*. (Springer Science & Business Media, ed.). Berlin, Heidelberg: Springer Berlin Heidelberg; 2008. doi:10.1007/978-3-540-73768-1.

137. Berry RJ, Bradley MSA, McGregor RG. Brookfield powder flow tester - Results of round robin tests with CRM-116 limestone powder. *Proc Inst Mech Eng Part E J Process Mech Eng*. 2015;229(3):215-230. doi:10.1177/0954408914525387.

138. Freeman R. Measuring the flow properties of consolidated, conditioned and aerated powders - A comparative study using a powder rheometer and a rotational shear cell. *Powder Technol*. 2007;174(1-2):25-33. doi:10.1016/j.powtec.2006.10.016.

139. Leturia M, Benali M, Lagarde S, Ronga I, Saleh K. Characterization of flow properties of cohesive powders: A comparative study of traditional and new testing methods. *Powder Technol*. 2014;253:406-423. doi:10.1016/j.powtec.2013.11.045.

140. Salehi H, Barletta D, Poletto M. A comparison between powder flow property testers. *Particuology*. 2017;32:10-20. doi:10.1016/j.partic.2016.08.003.

141. Smith DH, Haddad GJ, Ferer M. Shear strengths of heated and unheated mixtures of MgSO4 and CaSO4 powders model pressurized fluidized bed combustion filter cakes. *Energy Fuels*. 1997;11:1006-1011.

142. Pilz T, Löffler F. Measurement of bulk properties at high temperature. In: *Proc. of 3rd PARTEC European Symposium Storage and Flow of Particulate Solids, Nürnberg, Germany*. ; 1995.

143. Kanaoka C, Hata M, Makino H. Measurement of adhesive force of coal flyash particles at high temperatures and different gas compositions. *Powder Technol*. 2001;118(1-2):107-112. doi:10.1016/S0032-5910(01)00300-X.

144. Ripp M, Ripperger S. Influence of temperature on the flow properties of bulk solids. *Chem Eng Sci*. 2010;65:4007-4013.

145. Kamiya H, Kimura A, Yokoyama T, Naito M, Jimbo G. Development of a splittype tensile strength and analysis of mechanism of increase of adhesion behaviour of inorganic fine powder bed at high-temperature conditions. *Powder Technol*. 2002;127:239-245.

146. Hurley PJ, Mukherjee B, Mann MD. Assessment of filter dust characteristics that cause

filter failure during hot-gas filtration. *Energy Fuels*. 2006;20:1629-1638.

147. Kamiya H, Kimura A, Yokoyama T, Naito M, Jimbo G. Development of a split-type tensile-strength tester and analysis of mechanism of increase of adhesion behavior of inorganic fine powder bed at high-temperature conditions. *Powder Technol*. 2002;127(3):239-245. doi:10.1016/S0032-5910(02)00117-1.

148. Zimmerlin B, Leibold H, Seifert H. Evaluation of the temperature-dependent adhesion characteristics of fly ashes with a HT-rheometer. *Powder Technol*. 2008;180:17-20.

149. Tomasetta I, Barletta D, Poletto M. The E ffect of T emperature on F low P roperties of F ine P owders. *Chem Eng Trans*. 2011;24:655-660.

150. Tomasetta I, Barletta D, Poletto M. The High Temperature Annular Shear Cell: A modified ring shear tester to measure the flow properties of powders at high temperature. *Adv Powder Technol*. 2013;24(3):609-617. doi:10.1016/j.apt.2012.11.007.

151. Tomasetta I, Barletta D, Lettieri P, Poletto M. The measurement of powder flow properties with a mechanically stirred aerated bed. *Chem Eng Sci*. 2012;69:373-381.

152. Johanson K, Barletta D. The influence of air counter-flow through powder materials as a means of reducing cohesive flow problems. *Part Part Syst Charact*. 2004;21:316-325.

153. Mikami T, Kamiya H, Horio M. The mechanism of defluidization of iron particles in a fluidized bed. *Powder Technol*. 1996;89(3):231-238. doi:10.1016/S0032-5910(96)03187-7.

154. Rumpf H. Zur Theorie der Zugfestigkeit von Agglomeraten bei Kraftübertragung an Kontaktpunkten. *Chemie Ing Tech*. 1970;42(8):538-540. doi:10.1002/cite.330420806.

155. Seville JPK, Silomon-Pflug H, Knight PC. Modelling of sintering in high temperature gas fluidisation. *Powder Technol*. 1998;97(2):160-169. doi:10.1016/S0032-5910(98)00008-4.

156. Lettieri P, Yates JG. New Generation X-ray Imaging for multiphase systems. *Fluid XIV*.

2013:641-648.

157. Simone S, Harriott P. Fluidization of fine powders with air in the particulate and the bubbling regions. *Powder Technol*. 1980;26(2):161-167.

158. Dry RJ, Judd MR, Shingles T. Two-phase theory and fine powders. *Powder Technol*. 1983;34(2):213-223.

159. Lettieri P. A study of the influence of temperature on the flow behaviour of solid materials in a gas fluidized bed. 1999.

160. Park JJ, Park JH, Chang IS, Atomrc K. A new bed-collapsing technique properties of gas-fluidized beds the dense phase ULJmf. 1991;66:249-257.

161. Nedderman RM. *Statics and Kinematics of Granular Materials*. Cambridge University Press; 1992.

162. Tomas J. Particle Adhesion Fundamentals and Bulk Powder Consolidation. *Kona*. 2000;18(18):157-169.

163. Tomas J. Fundamentals of cohesive powder consolidation and flow. *Granul Matter*. 2004;6(2-3):75-86. doi:10.1007/s10035-004-0167-9.

164. Tomasetta I, Barletta D, Poletto M. Correlation of powder flow properties to interparticle interactions at ambient and high temperatures. *Particuology*. 2014;12(1):90-99. doi:10.1016/j.partic.2013.02.002.

165. Antony SJ, Kuhn MR. Influence of particle shape on granular contact signatures and shear strength: New insights from simulations. *Int J Solids Struct*. 2004;41(21):5863-5870. doi:10.1016/j.ijsolstr.2004.05.067.

166. Majmudar TS, Behringer RP. Contact force measurements and stress-induced anisotropy in granular materials. *Nature*. 2005;435(7045):1079-1082. doi:10.1038/nature03805.

167. Peters JF, Muthuswamy M, Wibowo J, Tordesillas A. Characterization of force chains in granular material. *Phys Rev E - Stat Nonlinear, Soft Matter Phys*. 2005;72(4):1-8. doi:10.1103/PhysRevE.72.041307.

168. Kamrin K, Koval G. Nonlocal constitutive relation for steady granular flow. *Phys Rev Lett*. 2012;108(17):1-5. doi:10.1103/PhysRevLett.108.178301.

169. Clark AH, Kondic L, Behringer RP. Particle scale dynamics in granular impact. *Phys Rev Lett*. 2012;109(23):1-5. doi:10.1103/PhysRevLett.109.238302.

170. Israelachvili J. Intermolecular and Surface forces, 1985. *Acad London*. 2011:706. doi:10.1016/B978-0-12-375182-9.10025-9.

171. Domnich V, Aratyn Y, Kriven WM, Gogotsi Y. Temperature dependence of silicon hardness: Experimental evidence of phase transformations. *Rev Adv Mater Sci*. 2008;17(1-2):33-41.

172. Pierrat P, Agrawal DK, Caram HS. Effect of moisture on the yield locus of granular materials: Theory of shift. *Powder Technol*. 1998;99(3):220-227. doi:10.1016/S0032-5910(98)00111-9.

173. Rabinovich YI, Adler JJ, Esayanur MS, Ata A, Singh RK, Moudgil BM. Capillary forces between surfaces with nanoscale roughness. *Adv Colloid Interface Sci*. 2002;96(1-3):213-230. doi:10.1016/S0001-8686(01)00082-3.

174. Fayed M, Otten L. *Handbook of Powder Science & Technology*. 2nd ed. (Fayed ME, Otten L, eds.). Boston, MA: Springer US; 1997. doi:10.1007/978-1-4615-6373-0.

175. Pierrat P, Caram HS. Tensile strength of wet granular materials. *Powder Technol*. 1997;91(2):83-93. doi:10.1016/S0032-5910(96)03179-8.

176. Molerus O. Theory of yield of cohesive powders. *Powder Technol*. 1975;12(3):259-275. doi:10.1016/0032-5910(75)85025-X.

177. CRCT - École Polytechnique de Montréal - Génie chimique / Chemical Eng. http://www.crct.polymtl.ca/fact/phase_diagram.php?file=AlCl3-CaCl2.jpg&dir=FTsalt.

178. Janz GJ, Allen CB, Bansal NP, Murphy RM, Tomkins RPT. Physical properties data compilations relevant to energy storage. II. Molten salts: data on single and multi-component salt systems. *Natl Stand Ref DATA Syst*. 1979.

179. Janz GJ, Tomkins RPT, Allen CB, et al. Molten salts: Volume 4, part 2, chlorides and mixtures—electrical conductance, density, viscosity, and surface tension data. *J Phys Chem Ref Data*. 1975;4(871).

180. Sokolova TD, Niselson LA. Density, Viscosity and Surface Tension of Aluminum and Gallium Trichlorides. *Russ J Inorg Chem*. 1965;10(827).

181. Janz GJ, Dampier FW, Lakshminarayanan GR, Lorenz PK, Tomkins RPT. Molten Salts. Volume I. Electrical Conductance, Density, and Viscosity Data. *Natl Stand Ref DATA Syst*. 1968:149.

182. Baeyens J, Geldart D. An investigation into slugging fluidized beds. *Chem Eng Sci*. 1974;29(1):255-265. doi:10.1016/0009-2509(74)85051-7.

183. Zhu C, Yu Q, Dave RN, Pfeffer R. Gas fluidization characteristics of nanoparticle agglomerates. *AIChE J*. 2005;51(2):426-439. doi:10.1002/aic.10319.

184. Loezos PN, Costamagna P, Sundaresan S. The role of contact stresses and wall friction on uidization. 2002;57:5123-5141.

185. Bruni G, Lettieri P, Newton D, Barletta D. An investigation of the effect of the interparticle forces on the fluidization behaviour of fine powders linked with rheological studies. *Chem Eng Sci*. 2007;62(1-2):387-396. doi:10.1016/j.ces.2006.08.059.

186. Nichols G, Byard S, Bloxham MJ, et al. Nichols_A Review of the Terms Agglomerate and Aggregate with a Recommendation for Nomenclature Used in Powder and Particle Characterization_2002.pdf. 91(10):2103-2109.

187. Valverde JM, Quintanilla M a. S, Castellanos a, Mills P. The settling of fine cohesive powders. *Europhys Lett*. 2007;54:329-334. doi:10.1209/epl/i2001-00246-4.

188. Russo P, Chirone R, Massimilla L, Russo S. The influence of the frequency of acoustic waves on sound-assisted fluidization of beds of fine particles. *Powder Technol*. 1995;82(3):219-230. doi:10.1016/0032-5910(94)02931-D.

189. Kim H, Arastoopour H. Extension of kinetic theory to cohesive particle flow. *Powder*

Technol. 2002;122(1):83-94. doi:10.1016/S0032-5910(01)00395-3.

190. McKeen T, Pugsley T. Simulation and experimental validation of a freely bubbling bed of FCC catalyst. *Powder Technol*. 2003;129(1-3):139-152. doi:10.1016/S0032-5910(02)00294-2.

191. Gidaspow D, Huilin L. Equation of state and radial distribution functions of FCC particles in a CFB. *AIChE J*. 1998;44(2):279-293. doi:10.1002/aic.690440207.

192. Johnson PC, Jackson R. Frictional-Collisional constitutive relations for granular materials, with application to plane shearing. 1987:67-93.

193. Peleg M, Normand MD, Corradini MG. Interactive software for calculating the principal stresses of compacted cohesive powders with the Warren-Spring equation. *Powder Technol*. 2010;197(3):268-273. doi:10.1016/j.powtec.2009.10.003.

194. Raganati F, Ammendola P, Chirone R. Role of acoustic fields in promoting the gas-solid contact in a fluidized bed of fine particles. *KONA Powder Part J*. 2015;32(32):23-40. doi:10.14356/kona.2015006.

195. O'Neill ME. A sphere in contact with a plane wall in a slow linear shear flow. *Chem Eng Sci*. 1968;23(11):1293-1298. doi:10.1016/0009-2509(68)89039-6.

196. Ammendola P, Raganati F, Chirone R. Effect of operating conditions on the CO2 recovery from a fine activated carbon by means of TSA in a fluidized bed assisted by acoustic fields. *Fuel Process Technol*. 2015;134:494-501. http://linkinghub.elsevier.com/retrieve/pii/S0378382015001204. Accessed February 25, 2018.

197. Raganati F, Ammendola P, Chirone R. Effect of acoustic field on CO2 desorption in a fluidized bed of fine activated carbon. *Particuology*. 2015;23:8-15. https://www.sciencedirect.com/science/article/pii/S1674200115000516. Accessed February 25, 2018.

Appendices

A1 Fresh samples: Yield Loci at 500 °C

The results of the Yield Loci obtained from shear tests at 500 °C are reported in Figure A1-Figure A5 and in Table A1. In all of the plots, different colour lines identify the yield locus at specific consolidation value as reported in Table 4 in section 5.1. As for the experiments at ambient conditions, also at 500 °C the results show that the cohesion and the unconfined yield strength are inversely proportional to the particle size distribution. Moreover, a slight effect of consolidation on these flow parameters was observed for the samples A2 and A1.

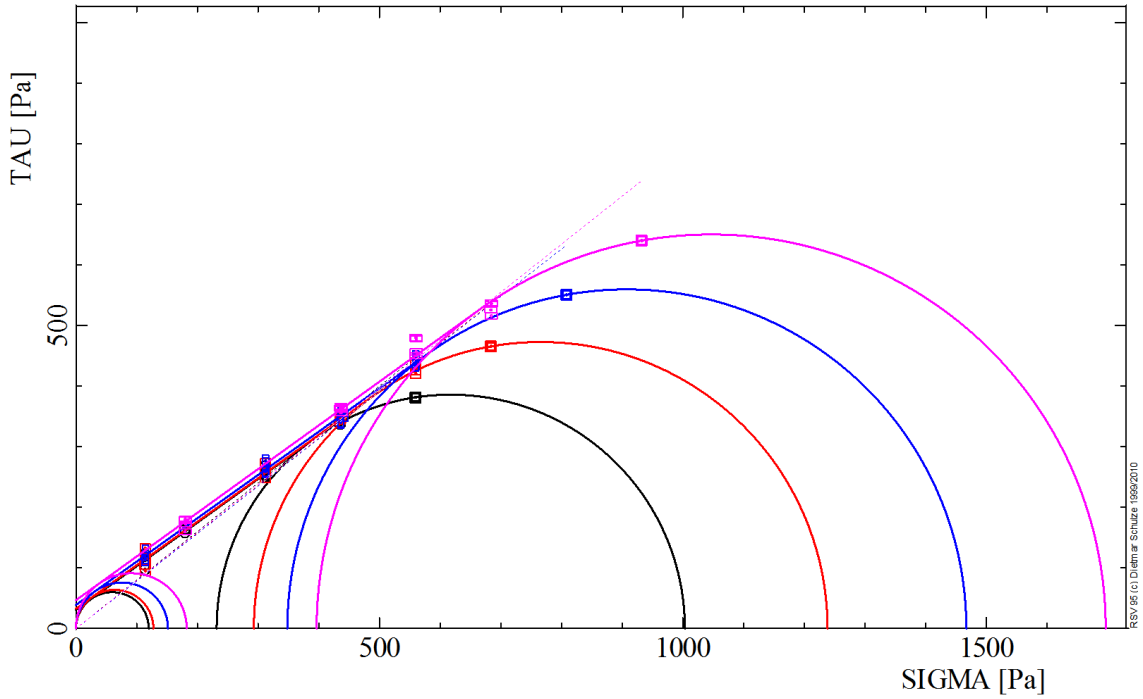

Figure A1 - Yield loci for the A5 sample measured with HT-ASC at 500 °C at all consolidation level.

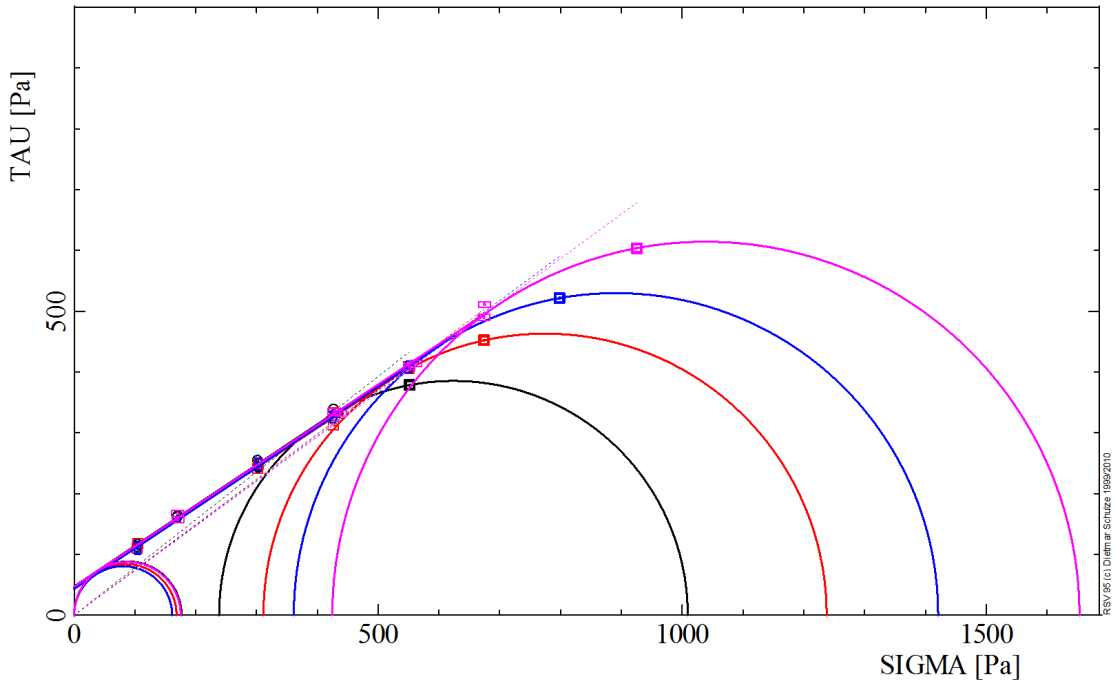

Figure A2 - Yield loci for the A4 sample measured with HT-ASC at 500 °C at all consolidation level.

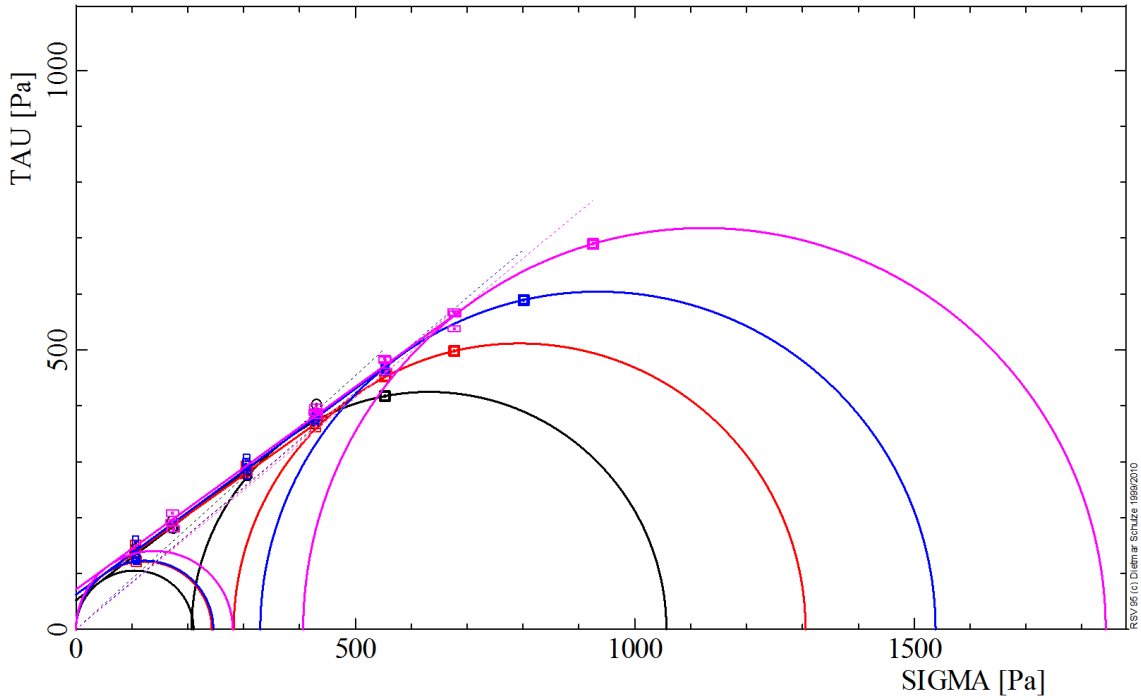

Figure A3 - Yield loci for the A3 sample measured with HT-ASC at 500 °C at all consolidation level.

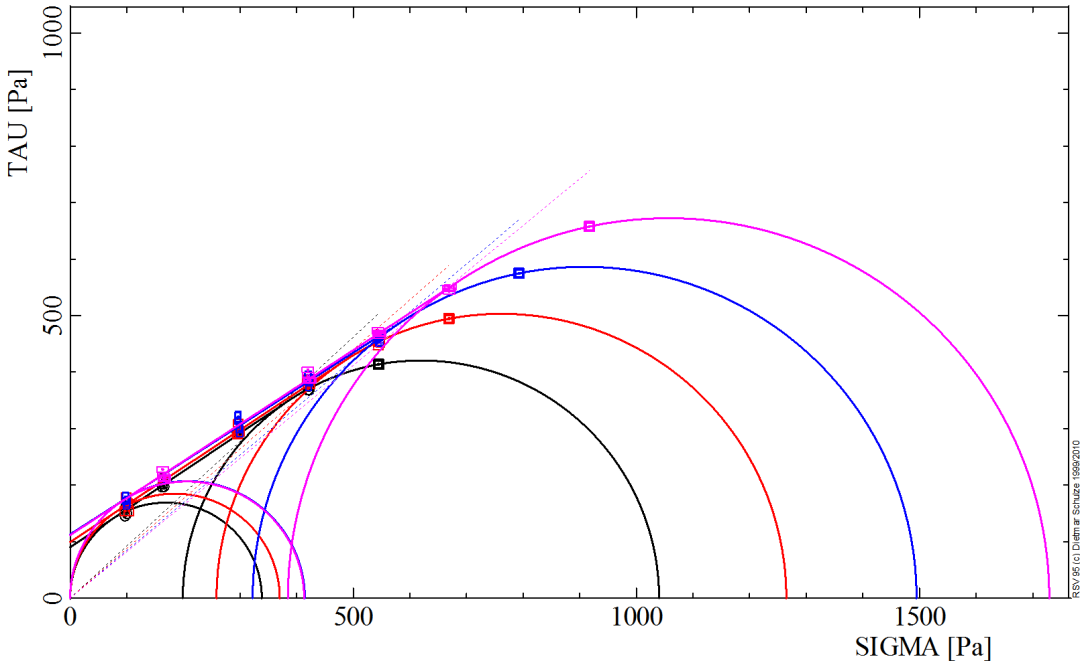

Figure A4 - Yield loci for the A2 sample measured with HT-ASC at 500 °C at all consolidation level.

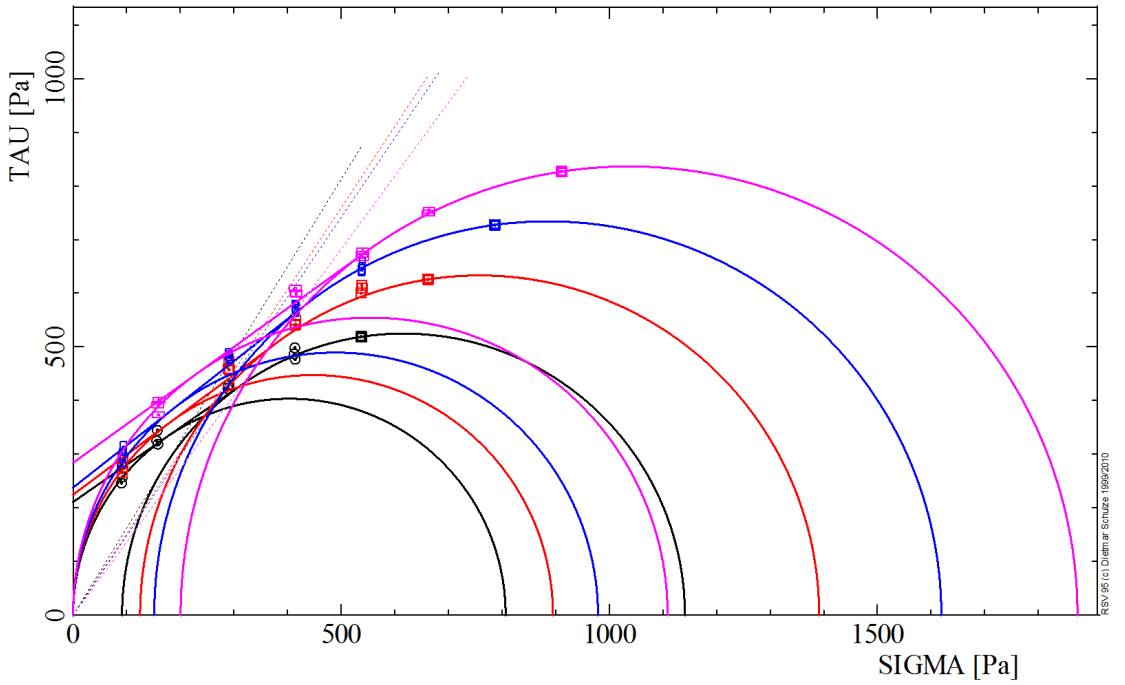

Figure A5 - Yield loci for the A1 sample measured with HT-ASC at 500 °C at all consolidation level.

Table A1 - Results of the shear tests performed on the fresh samples with HT-ASC at 500 °C.

	T, °C	σ_1, Pa	f_c, Pa	ff_c, -	C, Pa	P_b, kg/m^3	φ_i, °
A1	500	1141	807	1.41	211	608	34.8
	500	1391	895	1.55	225	629	36.7
	500	1619	979	1.65	238	646	38.1
	500	1873	1109	1.69	284	658	35.8
A2	500	1040	338	3.07	90	782	33.9
	500	1265	370	3.42	99	799	33.5
	500	1495	414	3.61	113	797	32.7
	500	1729	413	4.18	112	805	33.2
A3	500	1056	186	5.02	47	990	37.4
	500	1305	210	5.37	58	997	35.5
	500	1538	220	6.26	57	999	36.4
	500	1843	240	6.57	67	1003	35.9
A4	500	1009	177	5.71	47	965	33.7
	500	1238	168	7.35	45	924	33.3
	500	1421	161	8.82	43	930	33.7
	500	1653	175	9.43	47	1011	33.6
A5	500	1003	120	8.37	31	1159	35.7
	500	1238	128	9.71	33	1167	35.6
	500	1467	152	9.68	39	1186	35.5
	500	1697	182	9.3	47	1181	35.8

A2 *GUI matlab*

As it was widely reported in the literary review of the thesis, the powders flow behaviour is commonly described in engineering science by using a continuum mechanics methodology, which allows directly characterizing powder rheological properties and flowability, by estimating the stress distribution within powders at failure. Many testers are available both in academia and industry for powder characterization, but shear cells are currently the most used devices [119–121].

The stress distribution inside a bulk solid is usually described by combining both yield locus and Mohr circles analysis. The first one is aimed at determining the limiting shear stresses under any normal stress when failure or, more precisely, incipient flow occurs. In several applications it is assumed that the powder behaves like a solid at failure, therefore the local state of stresses can be represented in the normal-shear stresses plane (σ-τ plane) by Mohr circles tangent to the yield locus [112,113].

In order to estimate the flow properties from the shear data two different approaches can be followed. The first one is the Mohr-Coulomb analysis, in which the yield conditions are represented by a straight line in the σ-τ plane:

$$\tau = \tan\varphi_i \, \sigma + C = \left(\frac{C}{\sigma_t}\right)\sigma + C \qquad \text{Eq. A1}$$

Where the cohesion, *C*, and the tensile strength, σ_t, are the line intercepts on the τ and the σ axis, respectively. The angle of internal friction, φ_i, is the slope angle of the line.

In the second approach, the yield locus can be described by a convex curved line expressed by the Warren-Spring equation in which the curvature index is represented by a dimensionless parameter of n ($1 \le n \le 2$) [193]:

$$\tau = C\left(1 + \frac{\sigma}{\sigma_t}\right)^{\frac{1}{n}} \qquad \text{Eq. A2}$$

In this appendix the MatLab App, cYield developed for the calculation of both Coulomb and Warren-Spring approximation is presented.

The procedure was developed to programmatically estimate the best fitting parameters of the Warren Spring equation. In order to understand the effective advantage of using this equation and compare the results with the Coulomb equation, this procedure was applied to the experimental data to calculate the effective angle of internal friction and the material flow function.

The Coulomb materials are those for which the standard yield locus can be represented by a line. The slope and the intercept of this line represented by Eq. A1 are estimated by a fitting procedure using the (σ, τ) experimental yield points obtained after pre-shearing the material at a certain applied normal stress.

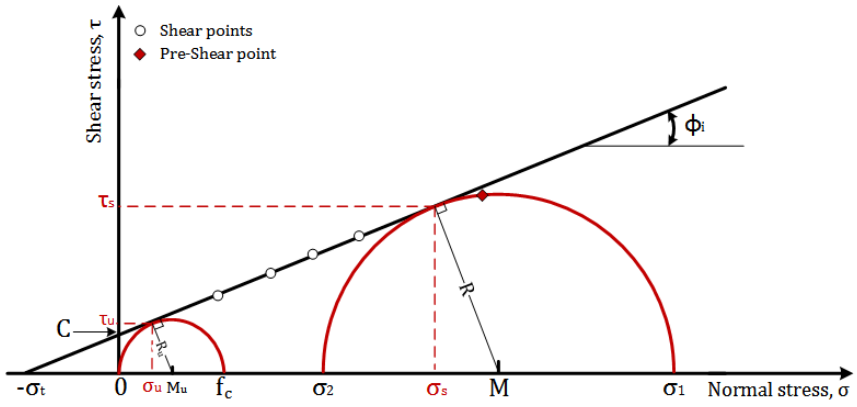

Figure A6 - General linear YL and flow properties for a Coulomb material.

In the proposed procedure, the best fitting straight line through the experimental data is estimated by using the MatLab® routine polyfit which enables to find the coefficients of a generic polynomial P(X) of specific degree N that best fits the input data in a least-squares sense. In the case when N=1 the output coefficients P(1) and P(2) are considered. All the linear yield locus parameters expressed by Eq. A1 can be calculated as function of the polynomial coefficients:

$$C = P(2) \qquad \text{Eq. A3}$$

$$\sigma_t = \frac{P(2)}{P(1)} \qquad \text{Eq. A4}$$

$$\varphi_i = \arctan\big(P(1)\big) \qquad \text{Eq. A5}$$

Regarding the curved yield locus, expressed according to Eq. A2, the best fitting line through the experimental data is estimated by minimizing the root mean square error (RMSE method). In order to perform the RMSE, the MatLab routine `fmincon` is used. This routine is based on the method of Lagrange multipliers, which enables to solve general minimization problems subjected to constraints. In this case, the problem consists in finding the values of Warren-Spring parameters which are able to provide the minimum value for RMSE. This problem is subjected to one constraint only in the space of the curve parameters, i.e. the curvature index, n, must be in the range $1 \leq n \leq 2$. Final values of the non-linear regression procedure may depend on the initial values adopted for the calculation. In all the cases these latter were set to the values found assuming a linear Yield Locus (n=1) are considered.

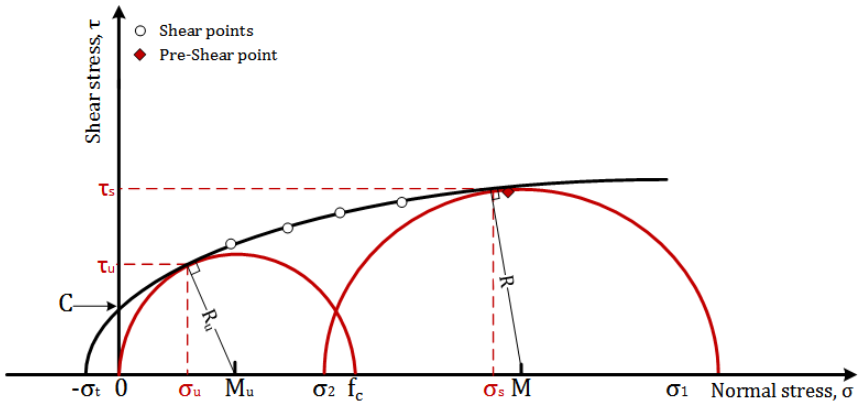

Figure A7 - General curved YL and flow properties according to Warren-Spring equation.

In order to compare results in terms of the most significant flow properties, in both the regression cases, the major principal stress during consolidation, σ_1, is calculated by the intersection of the σ-axis and the Mohr circle tangent to the yield locus and passing through the point (σ_{pre}, τ_{pre}), which is representative of the pre-shear stresses. The tangent point between the Mohr circle and the yield locus, as well as the Mohr circle radius and centre are calculated according to tangency condition between a line and a circle. In particular, the first-order Taylor series approximation of the Warren-Spring curve about the tangent point is used to obtain a linear function.

Similarly, the unconfined yield strength, f_c, representing the state of stress in the unconfined material at yield, is estimated by the intersection of the σ-axis and the Mohr circle tangent to the yield locus and passing through the origin of the axis.

The solution code was implemented on Matlab software, using the Graphical User Interface Design Environment (GUIDE) and a specific MatLab App was created. It can be freely downloaded at "https://uk.mathworks.com/matlabcentral/fileexchange/60998-cyield" to be used in the MatLab environment. Figure A8 and Figure A9 present the code structure and the view of the Graphical User Interface (GUI). There are three sub-processes within the general code process, identified by the push button bearing the corresponding name:

1. **Linear YL**, which allows to generate a linear yield locus, the related consolidation Mohr circle and the related unconfined yield Mohr circle starting from experimental data;
2. **Warren-Spring**, which allows to generate the curved yield locus, the related consolidation Mohr circle and the related unconfined yield Mohr circle starting from experimental data;
3. **Compare**, which allows comparing the results obtained by the two previous approaches.

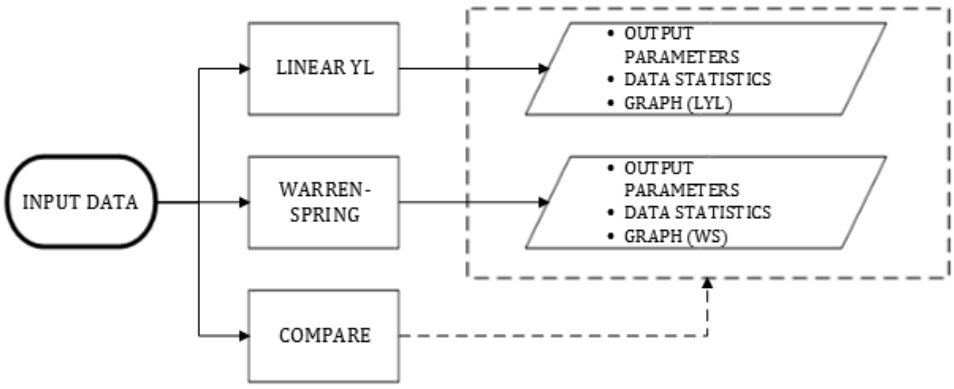

Figure A8 - Structure of the general code process.

Figure A10 and Figure A11 report the structure of the two yield loci regression sub-processes procedures. Each sub-process needs all the sets of experimental couples made by the (σ,τ) shear data points and (σ_{pre}, τ_{pre}) pre-shear data points. These values are used as input data for the sub process that returns the main bulk flow properties and the statistics data as output. In particular, the coefficient of determination (R-squared), the root-mean-square error (RMSE) and the Pearson's coefficient are reported as statistical indexes of the fitting process. The sub-processes structures are presented below. Figure

A10 and Figure A11 show the structure of the sub-process Linear YL and of the sub-process Warren-Spring respectively. As discussed in the previous section, the fitting procedure for the Warren-Spring yield locus is more complex than the linear case, and data from linear fitting are used as starting point for the analysis. A similar approach to the one presented above was proposed by Peleg et al. [193]. In particular, they realised interactive software for calculating the principal stresses of compacted cohesive powders with the Warren-Spring equation. In their application, however, the Authors forced the contact point between the yield locus with the major Mohr circle to be coincident with the pre-shear representing point (σ_{pre}, τ_{pre}). Differently, in this work, the pre-shear representing point (σ_{pre}, τ_{pre}) is considered to belong to the yield locus only in the case in which the resulting model value for the yield locus τ at σ_{pre} is larger than the experimental value τ_{pre}. Such approach is well described elsewhere [140] and it is also highlighted in Figure A10 and Figure A11 where hyphenated lines report the repeated procedure applied in case the above mentioned condition on τ_{pre} is met.

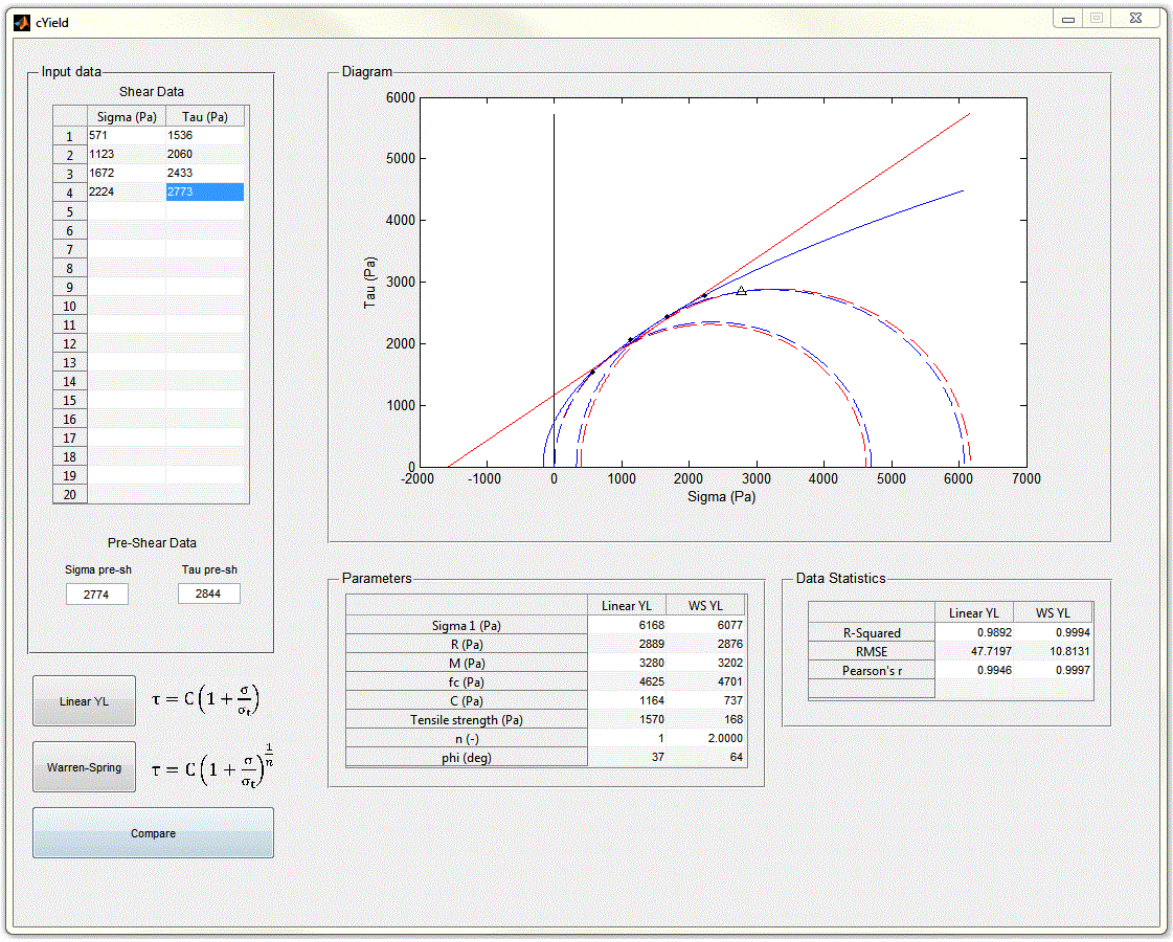

Figure A9 - GUI general view.

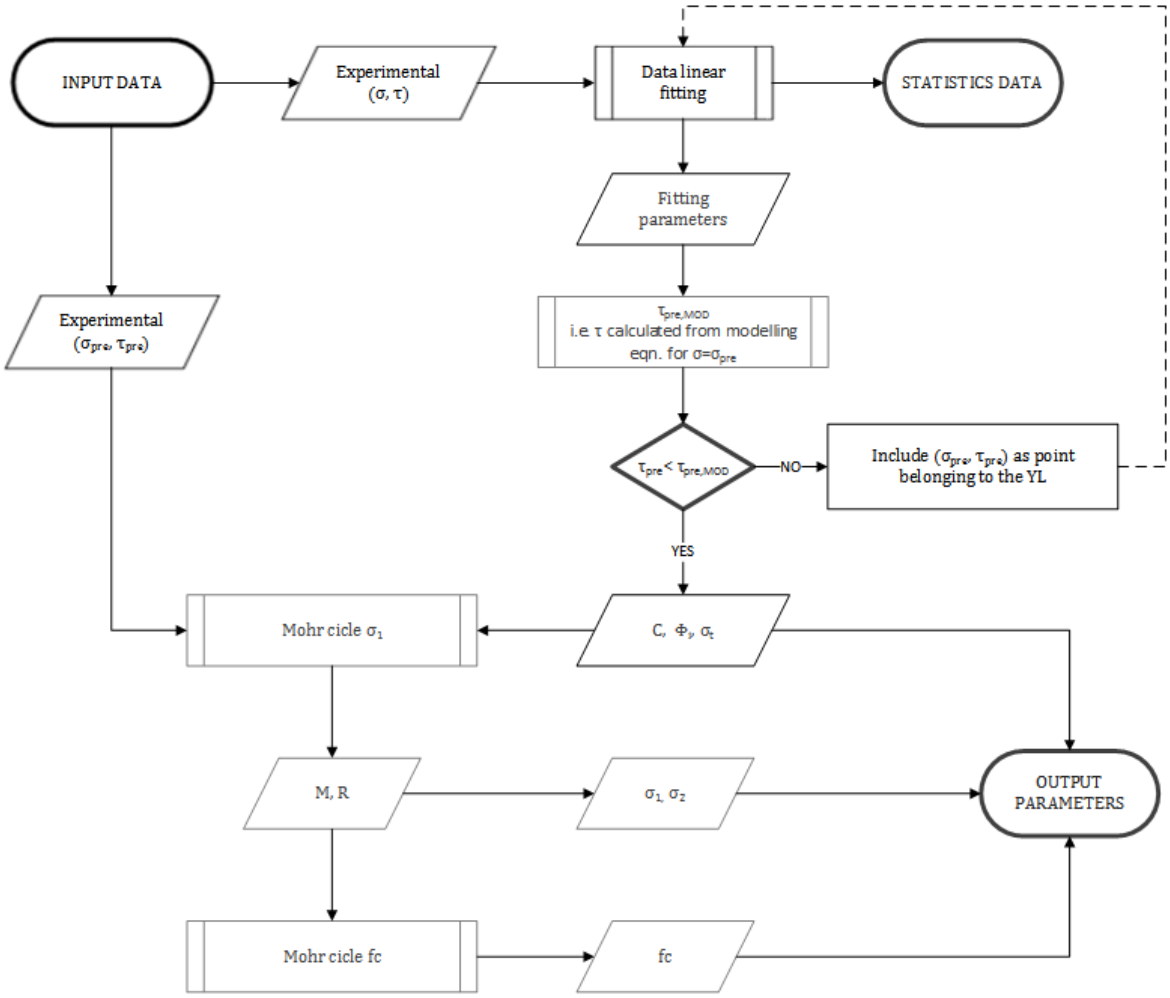

Figure A10 - Linear YL sub-process structure.

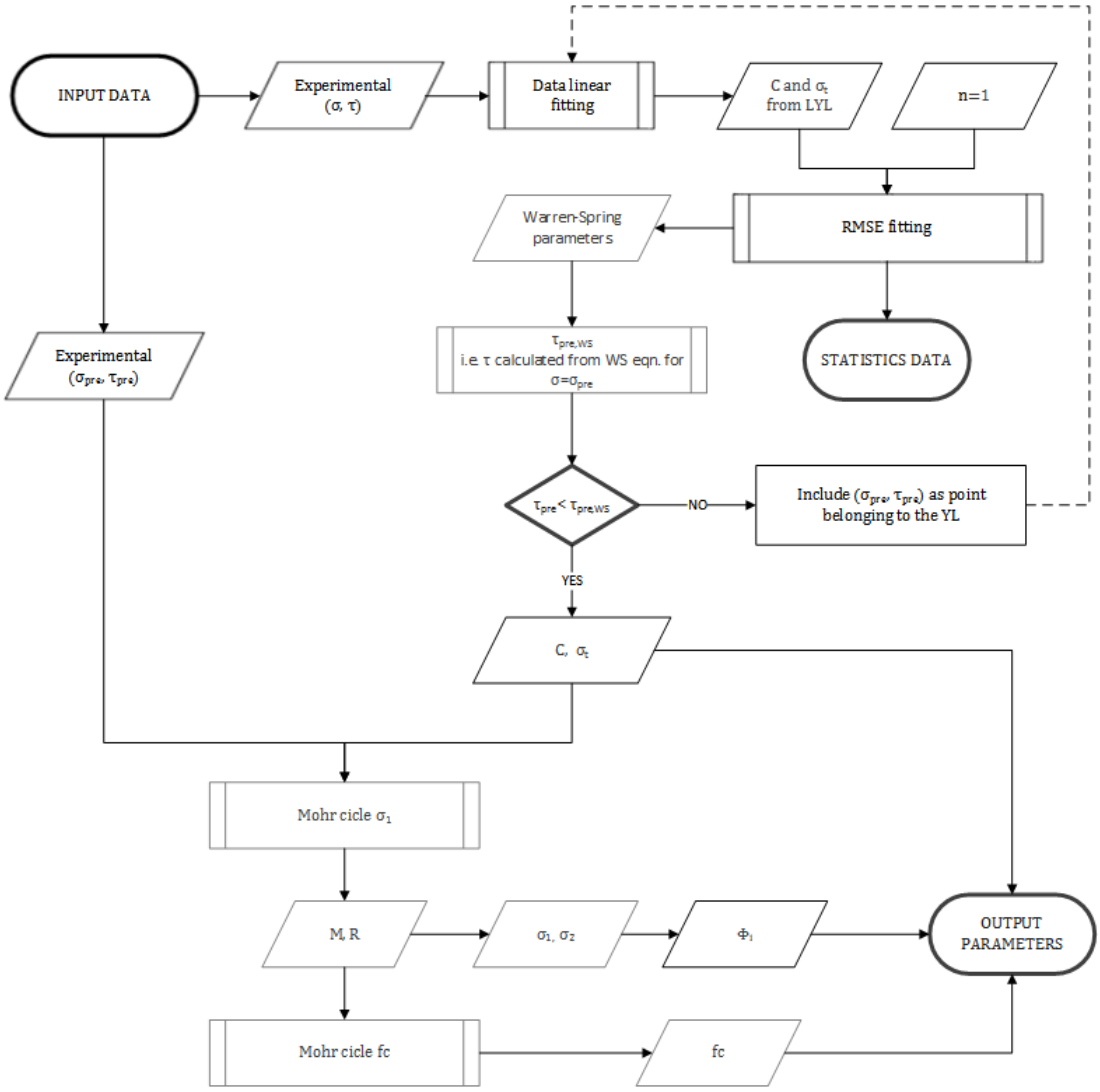

Figure A11 - Warren-Spring sub-process structure.

A3 Reacted samples: Yield Loci at all different temperature

All the measured yield loci obtained at each temperature for both the reacted samples are reported in Figure A12-Figure A19.

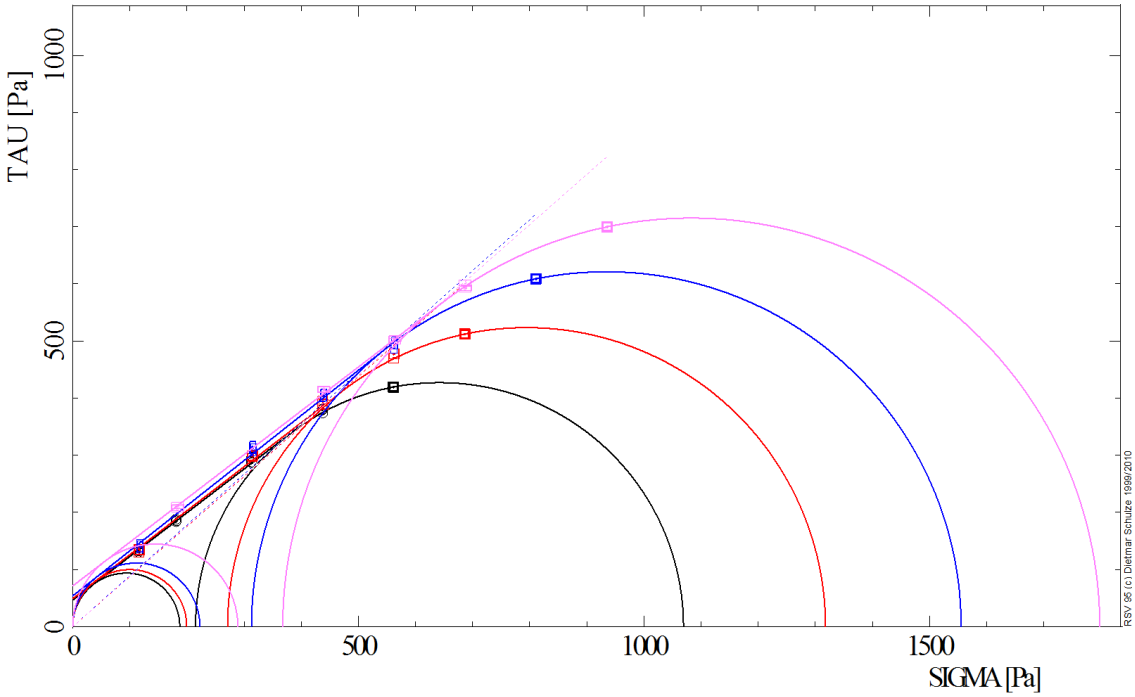

Figure A12 - Yield loci for the S1 sample measured with HT-ASC at 25 °C at all consolidation level.

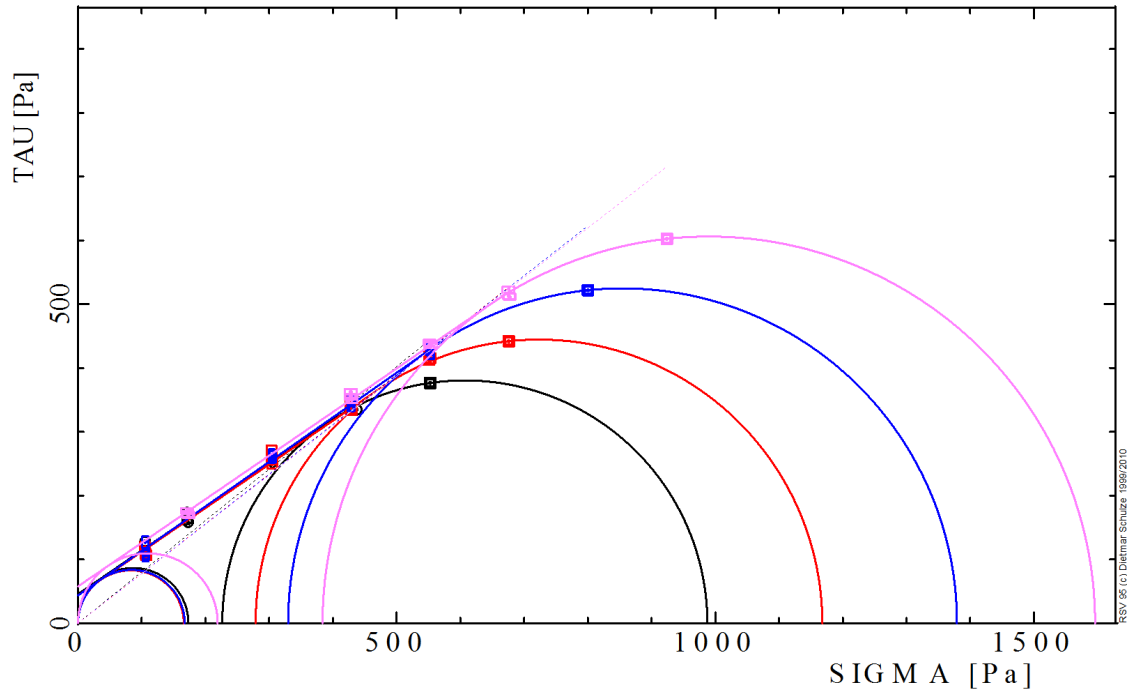

Figure A13 - Yield loci for the S1 sample measured with HT-ASC at 300 °C at all consolidation level.

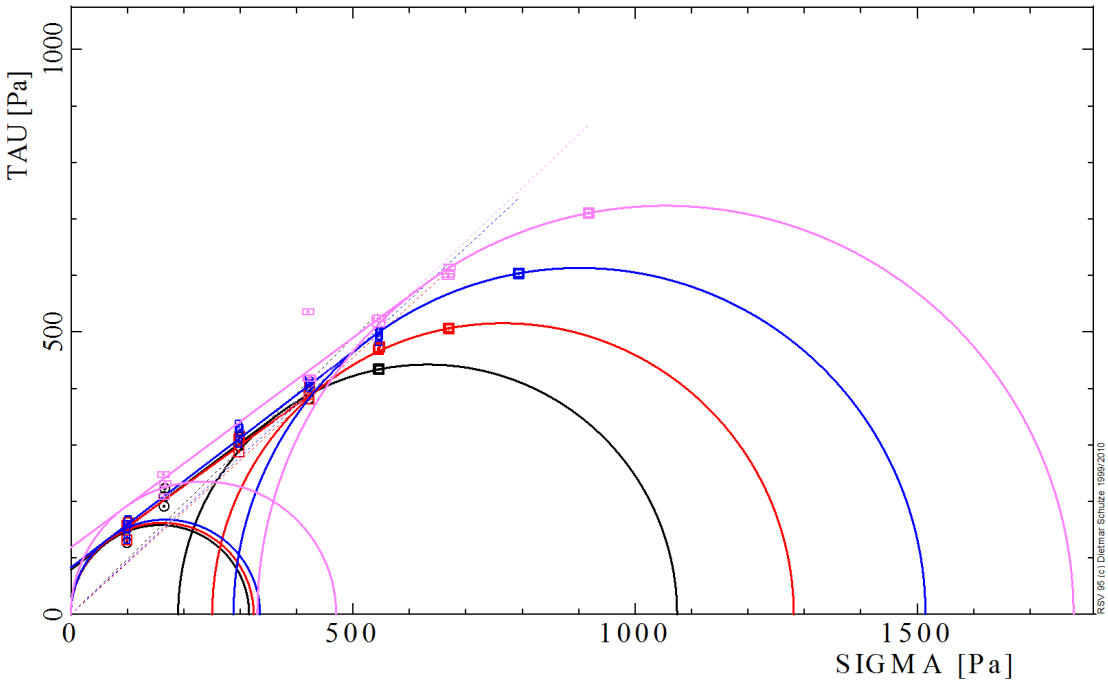

Figure A14 - Yield loci for the S1 sample measured with HT-ASC at 400 °C at all consolidation level.

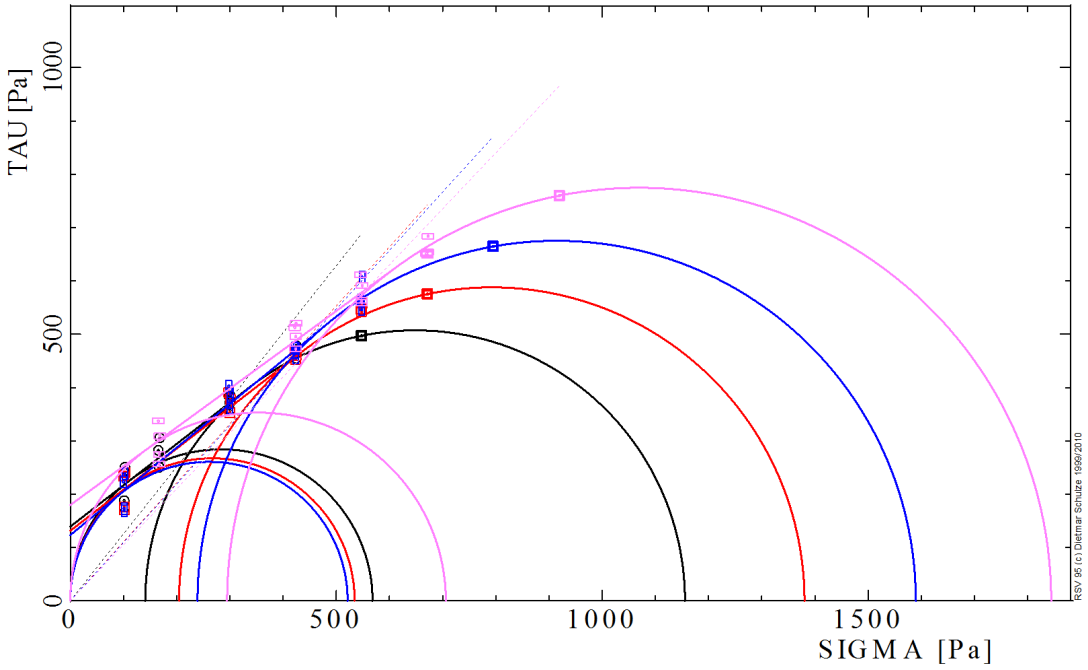

Figure A15 - Yield loci for the S1 sample measured with HT-ASC at 500 °C at all consolidation level.

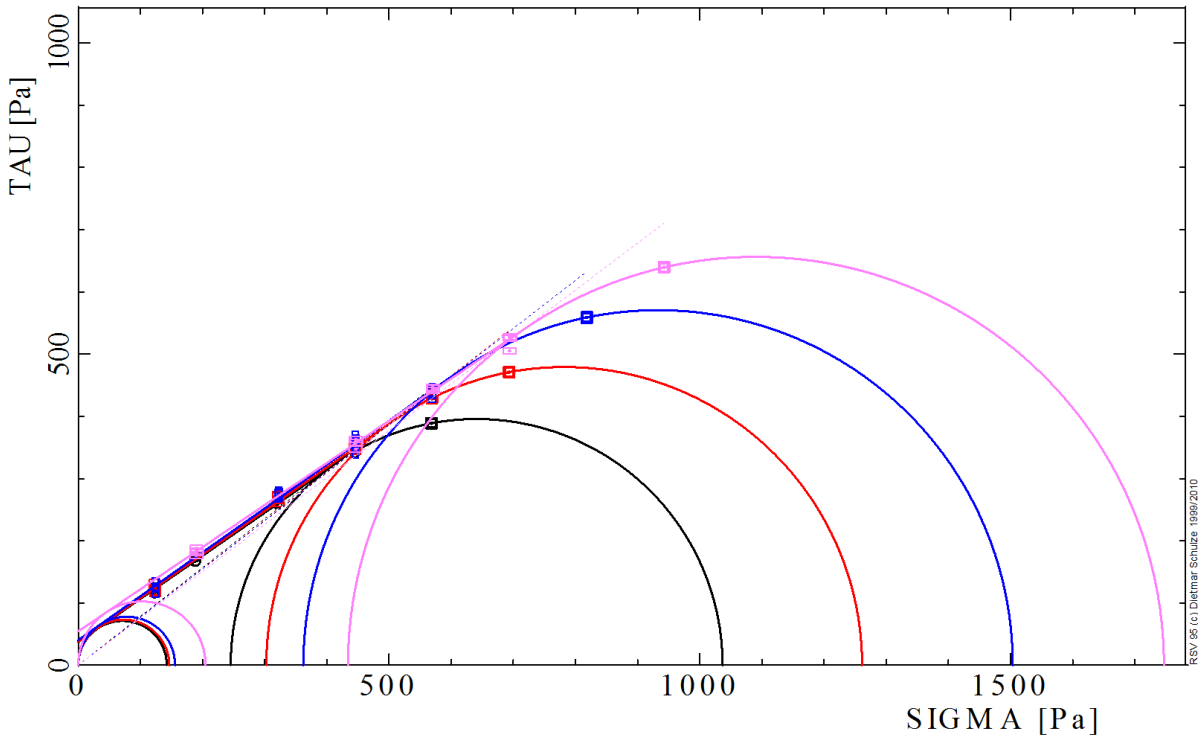

Figure A16 - Yield loci for the S2 sample measured with HT-ASC at 25 °C at all consolidation level.

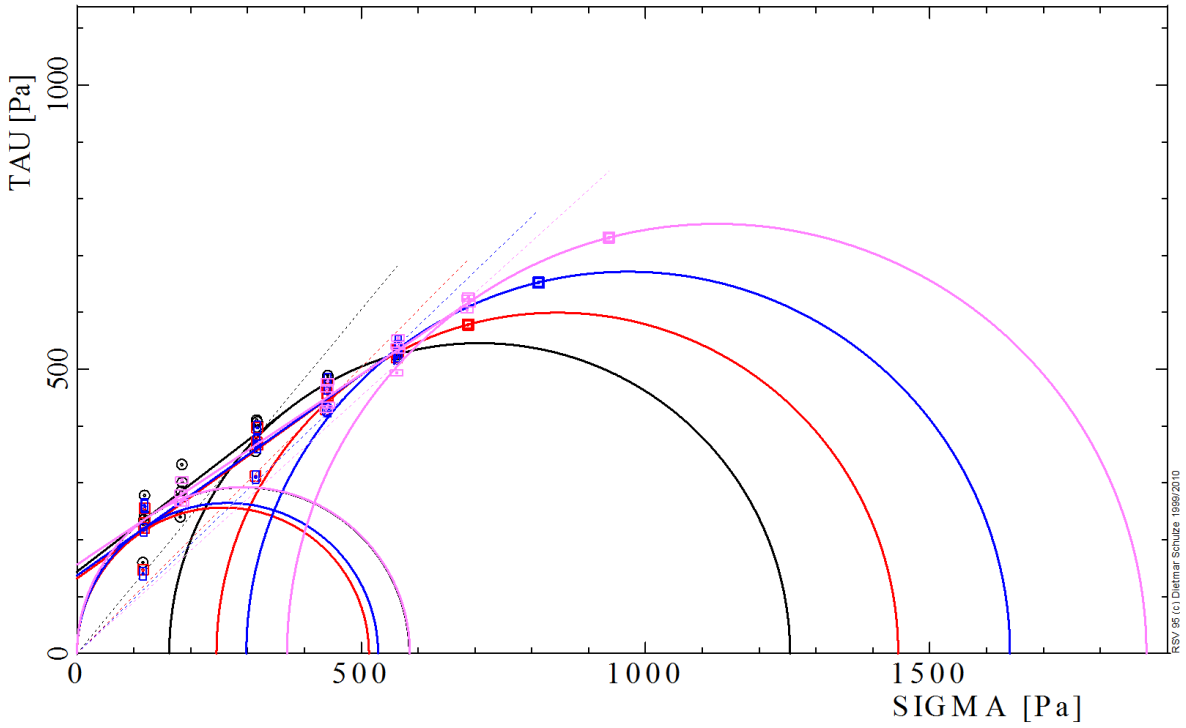

Figure A17 - Yield loci for the S2 sample measured with HT-ASC at 300 °C at all consolidation level.

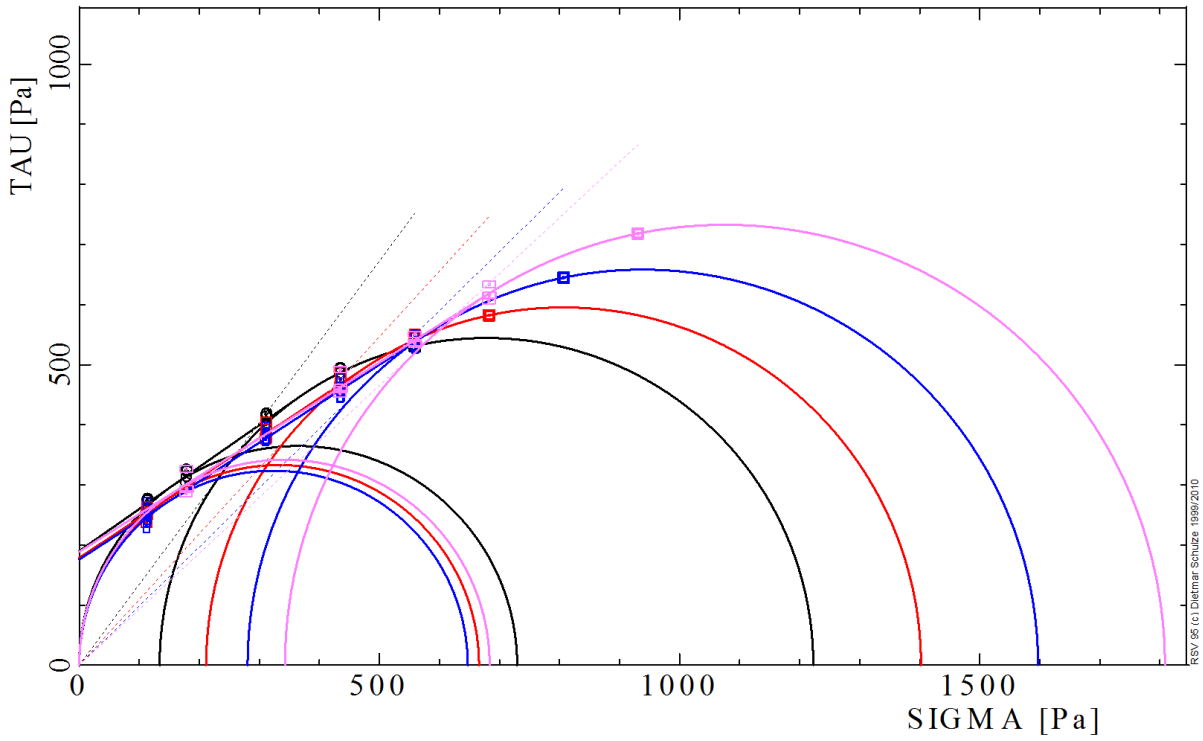

Figure A18 - Yield loci for the S2 sample measured with HT-ASC at 400 °C at all consolidation level.

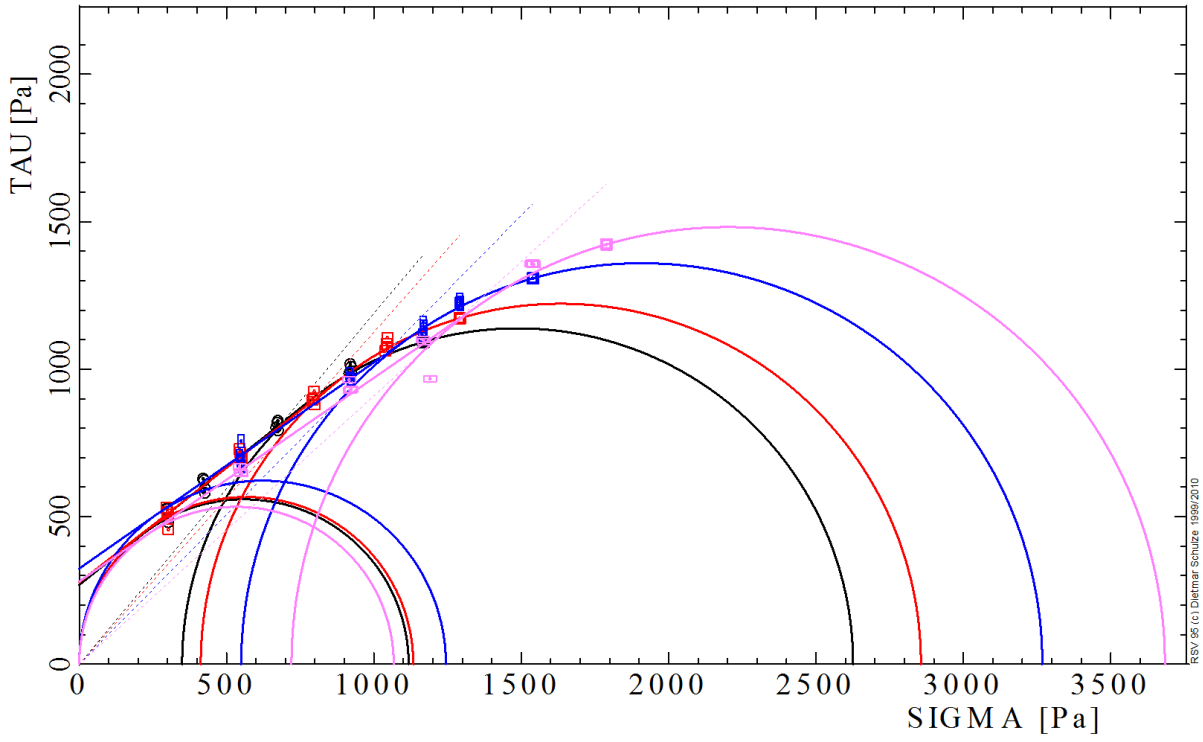

Figure A19 - Yield loci for the S2 sample measured with HT-ASC at 500 °C at all consolidation level.

A4 Tables of the fluidization experimental results

Table A2 - Experimental results for the fresh samples.

	T	u_{mf}	$u_{mb,s}$	$u_{mb,s}/u_{mf}$	$\varepsilon_{s\ slow}$	$\varepsilon_{s\ BCT}$	ε_{mf}	$\varepsilon_{mb,s}$	$(H_{max}-H_0)/H_0$
	°C	cm/s	cm/s	-	-	-	-	-	-
A5	25	1.22	3.48	2.86	0.51	0.51	0.51	0.54	0.11
	100	1.01	3.48	3.45	0.51	0.52	0.53	0.55	0.12
	200	0.79	2.59	3.28	0.51	0.52	0.53	0.56	0.15
	300	0.67	1.39	2.07	0.52	0.53	0.53	0.01	0.15
	400	0.64	1.19	1.87	0.55	0.53	0.55	0.57	0.16
	500	0.55	0.99	1.81	0.55	0.54	0.55	0.58	0.16
A4	25	0.37	0.99	2.68	0.59	0.60	0.59	0.62	0.11
	100	0.33	0.99	3.01	0.60	0.60	0.61	0.64	0.10
	200	0.31	0.79	2.55	0.60	0.60	0.61	0.65	0.12
	300	0.27	0.70	2.58	0.61	0.61	0.61	0.66	0.14
	400	0.25	0.70	2.79	0.62	0.61	0.61	0.68	0.15
	500	0.23	0.70	3.03	0.62	0.61	0.62	0.69	0.15
A3	25	0.37	1.20	3.24	0.57	0.59	0.58	0.67	0.19
	100	0.32	1.10	3.44	0.58	0.59	0.59	0.65	0.17
	200	0.29	0.65	2.24	0.59	0.59	0.60	0.68	0.19
	300	0.28	0.65	2.32	0.60	0.60	0.61	0.71	0.24
	400	0.24	0.70	2.92	0.61	0.62	0.62	0.74	0.26
	500	0.23	0.70	3.04	0.62	0.63	0.63	0.75	0.25
A2	25	0.20	1.25	6.25	0.59	0.59	0.61	0.68	0.09
	100	0.17	1.19	7.00	0.59	0.60	0.61	0.68	0.12
	200	0.14	0.65	4.64	0.60	0.62	0.61	0.73	0.21
	300	0.13	0.60	4.62	0.62	0.64	0.63	0.77	0.30
	400	0.16	0.50	3.13	0.64	0.65	0.65	0.76	0.49
	500	0.23	0.50	2.17	0.65	0.65	0.66	0.77	0.39

Table A3 - Experimental and predicted u_{mf} for fresh samples.

	T	$u_{mf, exp}$	Wen and Yu	Ergun	Baeyens and Geldart
	°C	cm/s	cm/s	cm/s	cm/s
A5	25	1.22	0.85	1.19	0.97
	100	1.01	0.72	1.01	0.85
	200	0.79	0.60	0.84	0.74
	300	0.67	0.52	0.73	0.66
	400	0.64	0.46	0.65	0.60
	500	0.55	0.42	0.58	0.56
A4	25	0.37	0.29	0.41	0.37
	100	0.33	0.25	0.35	0.33
	200	0.31	0.21	0.29	0.29
	300	0.27	0.18	0.25	0.26
	400	0.25	0.16	0.23	0.23
	500	0.23	0.14	0.20	0.21
A3	25	0.37	0.06	0.17	0.09
	100	0.32	0.05	0.15	0.08
	200	0.29	0.05	0.12	0.07
	300	0.28	0.04	0.11	0.06
	400	0.24	0.03	0.10	0.06
	500	0.23	0.03	0.09	0.05
A2	25	0.20	0.03	0.13	0.04
	100	0.17	0.02	0.11	0.04
	200	0.14	0.02	0.09	0.03
	300	0.13	0.02	0.08	0.03
	400	0.16	0.01	0.07	0.03
	500	0.23	0.01	0.06	0.03

Table A4 - Experimental and predicted u_{mb} for fresh samples.

	T	$u_{mb,v}$	$u_{mb,p}$	$u_{mb,e}$	$u_{mb,s}$	u_{mb} Eq. 62	u_{mb} Eq. 63
	°C	cm/s	cm/s	cm/s	cm/s	cm/s	cm/s
A5	25	1.22	-	2.99	3.48	1.18	0.93
	100	1.01	-	2.89	3.48	1.10	0.82
	200	0.79	-	2.59	2.59	1.02	0.73
	300	0.67	-	1.39	1.39	0.96	0.66
	400	0.64	-	1.19	1.19	0.91	0.61
	500	0.55	-	0.99	0.99	0.87	0.57
A4	25	0.44	-	0.99	0.99	0.55	0.43
	100	0.40	-	0.99	0.99	0.51	0.38
	200	0.35	-	0.80	0.79	0.47	0.34
	300	0.30	-	0.70	0.70	0.45	0.31
	400	0.24	-	0.64	0.70	0.42	0.29
	500	0.24	-	0.60	0.70	0.41	0.27
A3	25	0.37	0.34	1.20	1.20	0.33	0.26
	100	0.32	0.28	1.10	1.10	0.30	0.23
	200	0.29	0.24	0.49	0.65	0.28	0.20
	300	0.28	0.22	0.44	0.65	0.27	0.18
	400	0.24	0.20	0.49	0.70	0.25	0.17
	500	0.21	0.20	0.52	0.70	0.24	0.16
A2	25	0.32	0.30	1.25	1.25	0.29	0.23
	100	0.26	0.18	1.19	1.19	0.27	0.20
	200	0.22	0.14	0.65	0.65	0.25	0.18
	300	0.22	0.14	0.60	0.60	0.24	0.16
	400	0.15	0.14	0.50	0.50	0.23	0.15
	500	0.15	0.14	0.50	0.50	0.22	0.14

Table A5 - Experimental results from the Bed Collapse Test for fresh samples.

	T	H_f	H_b	H_d	H_s	$\varepsilon_{s,\,BCT}$	t_b	t_c	U_b	U_{de}	BER	SCT
	°C	cm	cm	cm	cm	-	s	s	cm/s	cm/s	-	s/cm
A5	25	39.0	36.3	36.8	35.6	0.51	1.0	2.8	2.5	0.4	3.4	0.08
	100	40.4	37.2	37.5	35.9	0.52	1.0	2.9	3.0	0.6	4.5	0.08
	200	40.9	37.2	38.1	36.3	0.52	1.0	2.9	3.5	0.6	4.8	0.08
	300	42.3	37.2	38.9	37.1	0.53	1.0	2.9	4.8	0.6	4.8	0.08
	400	42.9	37.2	38.9	37.4	0.53	1.4	2.9	4.0	0.5	4.2	0.08
	500	43.2	37.2	39.2	37.5	0.54	1.0	2.9	5.7	0.6	4.6	0.08
A4	25	56.3	54.7	55.1	49.9	0.60	1.1	13.3	1.4	0.4	10.5	0.27
	100	56.4	53.8	54.6	49.9	0.60	2.3	13.9	1.1	0.3	9.3	0.28
	200	58.1	55.5	56.0	50.5	0.60	1.3	15.0	1.9	0.4	10.8	0.30
	300	59.2	57.7	58.1	50.6	0.61	0.9	16.7	1.8	0.5	14.6	0.33
	400	63.0	58.9	60.0	50.7	0.61	2.0	17.7	2.1	0.5	18.2	0.35
	500	63.0	60.3	61.0	51.2	0.61	1.2	18.6	2.2	0.5	19.0	0.36
A3	25	45.2	44.0	44.5	36.6	0.59	1.0	17.0	1.1	0.5	21.3	0.47
	100	43.5	41.8	42.2	36.1	0.59	1.1	17.1	1.4	0.4	16.7	0.48
	200	45.4	43.3	43.8	36.8	0.59	1.2	18.1	1.7	0.4	18.9	0.49
	300	50.4	48.0	48.6	37.3	0.60	1.2	22.7	1.9	0.5	30.4	0.61
	400	54.1	52.7	53.2	39.1	0.62	0.8	22.8	1.6	0.6	36.1	0.58
	500	56.4	52.8	53.5	40.5	0.63	1.2	22.6	3.0	0.6	32.3	0.56
A2	25	33.6	31.9	32.2	26.1	0.59	1.2	25.5	0.2	0.2	23.3	0.98
	100	33.9	32.4	32.7	26.3	0.60	1.3	28.3	0.2	0.2	24.3	1.08
	200	34.9	33.9	34.1	26.9	0.62	0.1	29.8	0.3	0.2	26.6	1.11
	300	37.3	36.5	36.8	27.4	0.64	1.2	32.6	0.3	0.3	34.5	1.19
	400	37.7	38.0	37.6	27.7	0.65	1.1	31.5	0.3	0.3	35.9	1.14
	500	37.7	36.0	37.4	27.6	0.65	4.4	31.0	0.4	0.3	35.3	1.12

Table A6 - Experimental values of the bed voidage as a function of the dimensionless Bond number for fresh samples.

	T	Bo	ε_{mf}	$\varepsilon_{mb,s}$
	°C	-	-	-
A5	25	2.2	0.51	0.54
	100	2.3	0.53	0.55
	200	2.4	0.53	0.56
	300	2.5	0.53	0.01
	400	2.6	0.55	0.57
	500	2.7	0.55	0.58
A4	25	13.8	0.59	0.62
	100	15.0	0.61	0.64
	200	16.7	0.61	0.65
	300	18.3	0.61	0.66
	400	19.9	0.61	0.68
	500	21.6	0.62	0.69
A3	25	55.3	0.58	0.67
	100	67.1	0.59	0.65
	200	82.8	0.60	0.68
	300	98.5	0.61	0.71
	400	114.1	0.62	0.74
	500	129.8	0.63	0.75
A2	25	165.2	0.61	0.68
	100	177.7	0.61	0.68
	200	194.4	0.61	0.73
	300	211.1	0.63	0.77
	400	227.7	0.65	0.76
	500	244.4	0.66	0.77

A5 Sound assisted fluidized bed experiments

A5.1.1 Experimental apparatus

A laboratory scale sound-assisted fluidized bed was used for the experimental campaign. The reactor column is made of a Plexiglas (40 mm ID X 1500 mm high) equipped with a porous gas distributor plate located at 300 mm from the bottom of the column. The section of the column below the gas distributor acts as wind-box. It is filled with Pyrex rings in order to maximize the uniformity of the gas flow entering the fluidized bed. The column is provided with a pressure probe located at the wall, 5 mm above the gas distributor, to measure the pressure drops across the bed of particles. The sound-generation system consists of a digital signal generator, a power audio amplifier rated up to 40 W and a 8 W woofer loudspeaker. More detailed information about the sound generation and insulation system can be found elsewhere [194]. The acoustic field is introduced inside the column through an ad-hoc designed sound wave guide located at the top of the freeboard. The sound wave guide was properly designed to prevent the elutriated powders from dirtying the loudspeaker and the set-up was also designed according to the Helmholtz resonator, i.e. one of the most used engineering noise control methods, in order to reduce the sound insulation even for high intensity acoustic fields. Gas feed is prepared using N2 cylinders (99.995%). The flowrates were set and controlled by two mass flow controllers (Brooks 8550S).

A5.1.2 Methodology

The fluidization behaviour of all the samples was assessed under both ordinary and sound assisted conditions (sound intensity, SPL = 140–150 dB and frequency, f = 50–120 Hz) in the experimental apparatus described in the previous section. All the tests were performed at ambient temperature and pressure, using N2 as the fluidizing gas in order to avoid the effect of the air moisture. For all the tests 100 g of powder were loaded in the fluidization column. For each test, pressure drop curves were obtained, i.e. the pressure drop of the gas was measured and plotted as a function of the superficial gas velocity. The experimental pressure drop data were elaborated, by means of a graphic procedure, in order calculate the minimum fluidization velocity, u_{mf}. Then, from the experimental u_{mf} the size of the fluidizing agglomerates was evaluated using the correlation proposed by

Wen and Yu, Eq. 55. In particular, we considered an internal voidage of 0.25 for the cohesive samples (S1, S2 and S3) to account for the apparent density.

A5.1.3 Cluster/subcluster model

In this work the cluster/subcluster model was used to calculate the magnitude of the cohesive forces between fluidizing agglomerates. The model was proposed originally by Russo et al. [188] to describe the fluidization behaviour of cohesive powders (i.e. belonging to the C group of Geldart's classification). They interpreted the break-up of agglomerated solids in sound-assisted fluidization on the basis of two distinct physical phenomena:

- the hydrodynamic stresses due to gas flowing
- the grade of cohesiveness of the agglomerates, which in turn depends both on the packing of primary particles within the agglomerate and on the strength of the elementary interparticle interaction.

The main assumptions of the model are here summarized:

- The presence of elastic forces between clusters and subclusters, active at the contact points, was assumed. In other words, according to this model, an elastic behaviour of the whole cluster-subcluster structure arises as a result of the elasticity of the interparticle contacts. The form of the elastic force is “kx”, where k is the elastic constant relative to the force acting at each contact point between a cluster and a subcluster and x the vertical displacement of the subcluster relative to the cluster. Moreover, a subcluster is in contact with the cluster at n points, so that the overall elastic constant is defined as [nk]. The number of contact points is is a function of to the external surface area of the subcluster.
- The cohesive frictional force between a cluster and a subcluster is described by the following equation:

$$F_c = n\mu F_{cw} \qquad \text{Eq. A6}$$

μ = 0.1 is a static friction coefficient and Fcw is the van der Waals force along straight lines through centers of a cluster and a subcluster. Even though electrostatic, capillary and

van der Waals forces may develop at contact points between solids, in our case only van der Waals forces are considered. Electrostatic forces are omitted because of the low fluidization velocity and capillary forces are neglected considering the low humidity of the fluidizing gas. The cohesive frictional force, Fc, tends to keep the subcluster in place.

- A subcluster detaches from the cluster when the elastic force [nk]x (i.e., the force that, would be necessary to keep together cluster and subcluster) is larger than the cohesive frictional force Fc. In the sound assisted fluidized bed the disaggregating force is due to the application of the acoustic field, F_{sound}. In this case the a subcluster separates from a cluster when F_{sound} is larger than the cohesive force Fc:

$$F_{sound} \geq F_c \rightarrow [nk][x] \geq n\mu F_{cw} \qquad \text{Eq. A7}$$

Equation A8 is the force balance acting on the subcluster which takes into account of inertial, elastic and drag forces:

$$m\frac{d^2x}{dt^2} + [nk][x] - c_{ds}\left(U\sin(\pi ft2) - \frac{dx}{dt}\right) = 0 \qquad \text{Eq. A8}$$

where m is the mass of the subcluster, U is the amplitude of the air particle velocity, f the sound frequency and c_{ds} the drag force per unit gas velocity. In particular, the overall velocity of gas impacting on clusters and subclusters is the sum of two components, the upward velocity u_0 due to the gas flux for fluidization and the velocity Usin(2πft) due to sound. c_{ds} is given by:

$$c_{d_s} = 3\pi\beta\nu\rho_g d \qquad \text{Eq. A9}$$

Where ν, ρ_g and ds are the kinematic viscosity, the density of the gas and the subcluster diameter, respectively, and β=1.7 is a correction factor accounting for the influence of neighbouring clusters [195]. For c_{ds}=0 Eq. A8 becomes:

$$\frac{d^2x}{dt^2} + [nk][x] = 0 \qquad \text{Eq. A10}$$

By solving Eq. A10, the natural frequency of the undamped oscillator, f_n, can be evaluated:

$$f_n = \frac{1}{2\pi}\sqrt{\frac{[nk]}{m}} = \sqrt{\frac{[nk]}{(\pi/6)\rho_s d_s^3}}\frac{1}{2\pi} \quad \text{Eq. A11}$$

Then, the overall elastic constant [nk] can be expressed as:

$$[nk] = (2\pi f_n)^2 m \quad \text{Eq. A12}$$

Substituting Eq. A12 in Eq. A8, the integration lead to:

$$x(t) = \frac{U}{2\pi\sqrt{f^2 + \left(\frac{2\pi m}{c_{d_s}}\right)^2 (f_n^2 - f^2)^2}} \sin(2\pi ft + \varphi) = A(f)\sin(2\pi ft + \phi) \quad \text{Eq. A13}$$

where, A is the amplitude of the displacement of the subcluster relative to the cluster, and ϕ is the phase lag between the velocity of the gas and the displacement of the subcluster:

$$\phi = \tan^{-1}\left(\frac{c_{ds} f}{2\pi m(f^2 - f_n^2)}\right) \quad \text{Eq. A14}$$

Then, the peak of the A(f) curve occurs at the frequency f_0 which is the resonance frequency of the damped oscillator given by:

$$f_0 = f_n\left(1 - \left(\frac{c_{d_s}}{4\pi f_n m}\right)^2\right)^{0.5} \quad \text{Eq. A15}$$

Combining Eq. A12 and Eq. A15, the overall elastic constant [nk] can be expressed as a function of f_0:

$$[nk] = (2\pi)^2\left[f_0^2 + 2\left(\frac{c_{d_s}}{4\pi m}\right)^2\right]m \quad \text{Eq. A16}$$

The value of the disaggregating force, Fsound, (i.e. the force generated by sound application) was evaluated by applying the failure conditions, Table given by Eq. 65. Therefore, F_{sound} is the disaggregating force that is necessary for subclusters of size $ds*$ to detach from clusters. d_s^* was evaluated from experimental data as the size of subclusters obtainable at the maximum response frequency, f_0^*, i.e. the frequency at which, for given

SPL, subclusters of minimum size $ds*$ detach from clusters. The maximum response frequency is the counterpart of f_0, i.e. the resonance frequency of the subcluster behaving like a damped forced oscillator, namely $f_0 = f_0^*$. The occurrence of the failure condition implies a tangency condition

$$[nk]A(f) = n^*\mu F_{cw} \qquad \text{Eq. A17}$$

Being n* the number of active contact points between the subcluster of size $ds*$ and the cluster it detaches from. Namely, F_{sound} can be evaluated using a graphical procedure as the maximum of the curve of the elastic force. In particular, the curve of the elastic force, [n*k] A(f), can be plotted as a function of sound frequency. Then, the failure condition implies that the horizontal line corresponding to the cohesive forces ($n*\mu F_{cw}$), which is independent of the sound frequency, is tangent to the maximum of the curve of elastic force. This procedure can be used to obtain the disaggregating force directly, overcoming the lack of knowledge of the number of active contact points n*.

A5.1.4 Experimental results

Figure A20 reports the dimensionless pressure drops (ΔPm/ΔPc vs u) curves obtained for all the samples under ordinary and sound-assisted conditions (140 dB–80 Hz), respectively. For uniform fluidization, the pressure drops are equal to the material weight per unit area (i.e. ΔPm/ΔPc = 1), meaning that the whole bed is fluidized. As expected, samples A3, A2 and A1 are characterized by a poor fluidization quality under ordinary conditions, as confirmed by the quite irregular pressure drops curves, as typical of cohesive powders due to channelling and plugging phenomena occurring inside the bed. On the contrary, pressure drops curves obtained with the assistance of sound are far more regular, both qualitatively and quantitatively. Therefore, the application of the sound is required to achieve a proper fluidization regime. In particular, the role of the sound assistance in a fluidized bed of fine powders is to induce a continuous break-up mechanism of the large agglomerates present inside the bed into smaller fluidizable ones due to the action of external (drag and inertial) forces, which counteract the internal (cohesive) forces [194]. The

coarser samples, A5 and A4, in contrast, are characterized by a good fluidization under ordinary conditions and they are insensible to the application of the acoustic field.

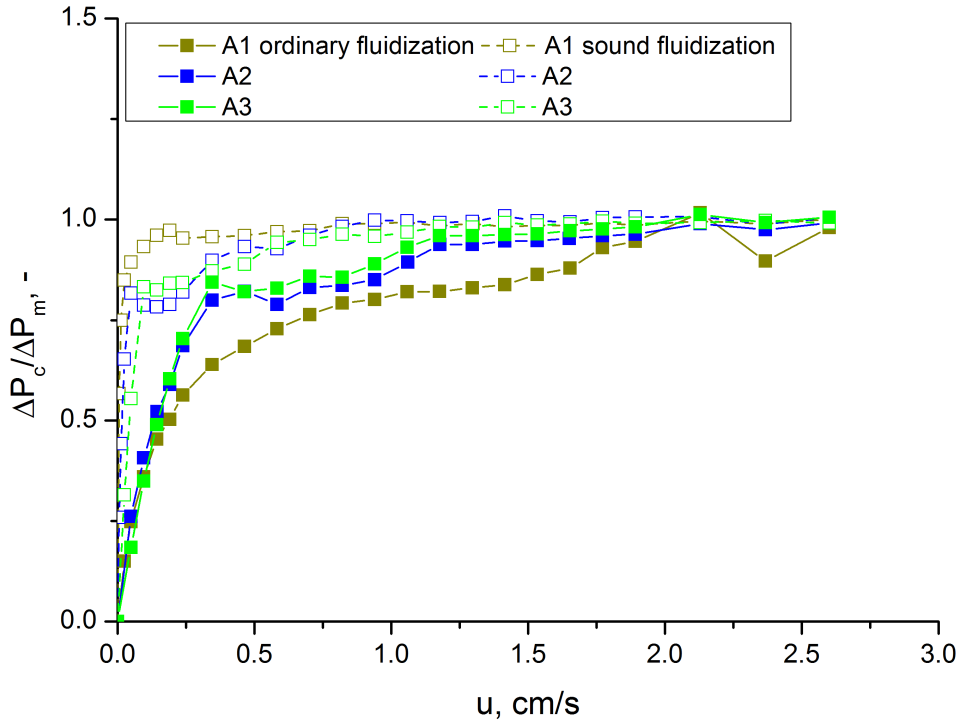

Figure A20 - Dimensionless pressure drops curves under ordinary (full marker) and sound assisted conditions (140 dB – 80 Hz).

Figure A21a and b report the experimental values of u_{mf} and the values of the fluidizing agglomerate size of all the sample obtained under ordinary and sound assisted conditions. First of all, in contrast to their nominal size, the dimension of the fluidizing structures (and u_{mf} as a consequence) follows the order A1>A2>A3, in agreement with the increasing cohesive character with the powders becoming finer. Obviously, samples A4 and A5 show a more straightforward behaviour, in agreement with their nominal size.

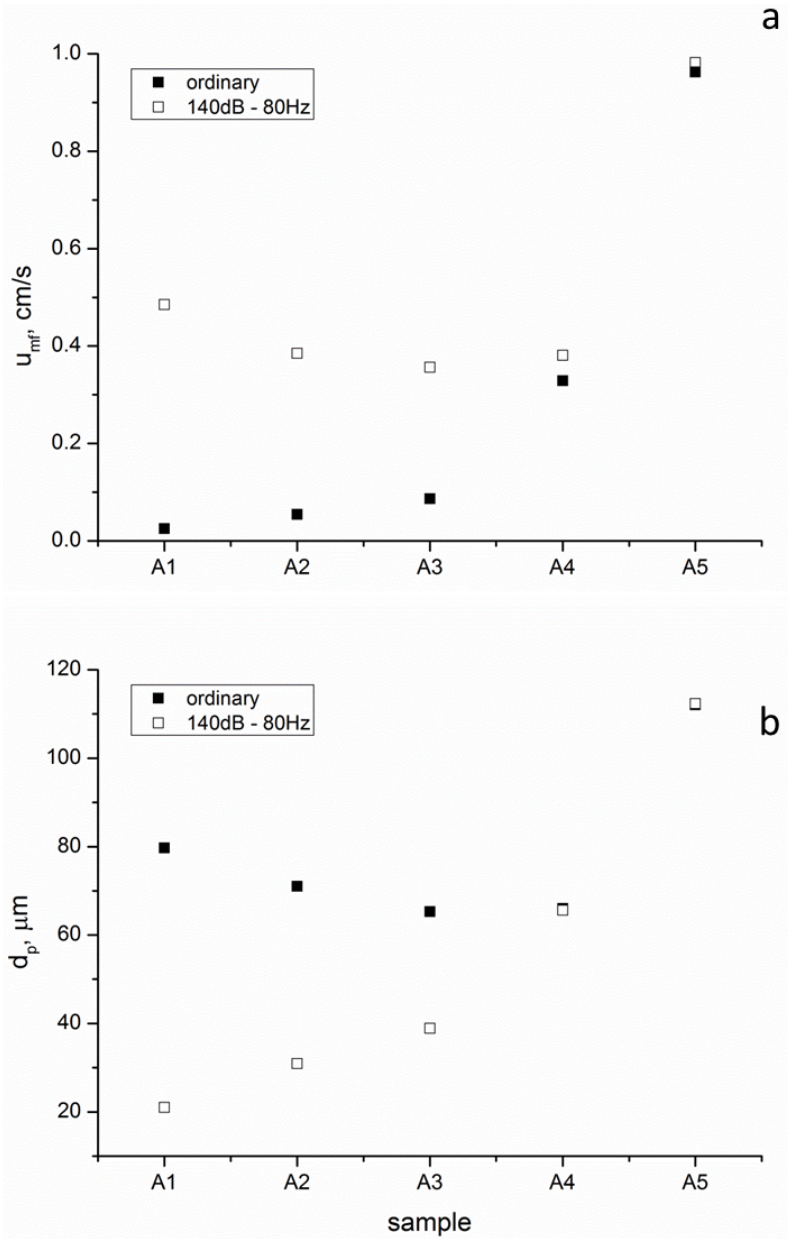

Figure A21 - (a) Experimental values of the minimum fluidization velocity and (b) fluidizing agglomerate diameter for the different samples under ordinary and sound assisted fluidization conditions.

Then, under sound assisted conditions (140 dB–80 Hz) all the cohesive samples, i.e. A1, A2 and A3, are characterized by values of u_{mf} lower than those obtained under ordinary conditions, according to the fluidization quality being enhanced by the application of the sound. This means that under ordinary conditions the fluidizing agglomerates are remarkably larger than those fluidizing under sound assisted conditions, as confirmed by Figure A21b, i.e. it can be inferred from reduction of u_{mf} that the acoustic perturbation disrupts the original clusters into smaller subclusters. Clearly, the difference observed

between ordinary and sound assisted conditions tends to decrease passing from sample A1 to A2 to A3, in agreement with the reduced cohesiveness with the samples becoming coarser. However, the application of an acoustic perturbation of such SPL and frequency is not enough to break up the clusters down to the Sauter diameter. Finally, as expected, samples A4 and A5 are completely unaffected by the application of the acoustic field. Figure A22 reports the values of the subcluster diameter as a function of SPL.

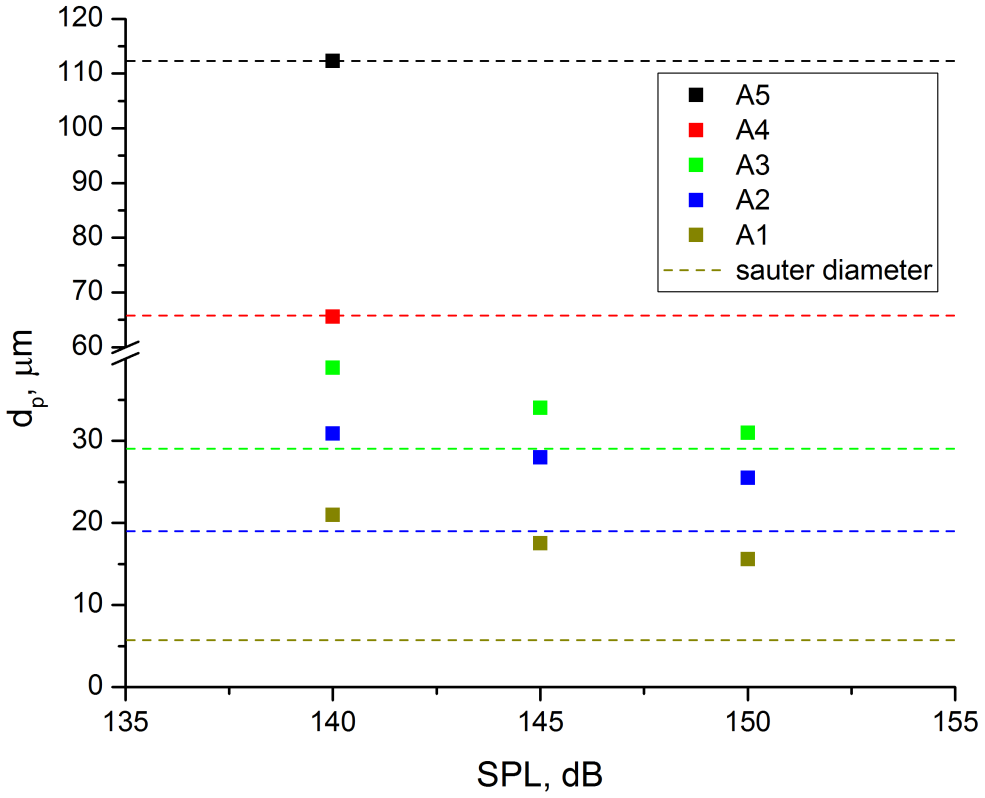

Figure A22 - Subcluster diameter as a function of the SPL for the different samples. Sauter diameters (dashed lines) of each sample are also reported.

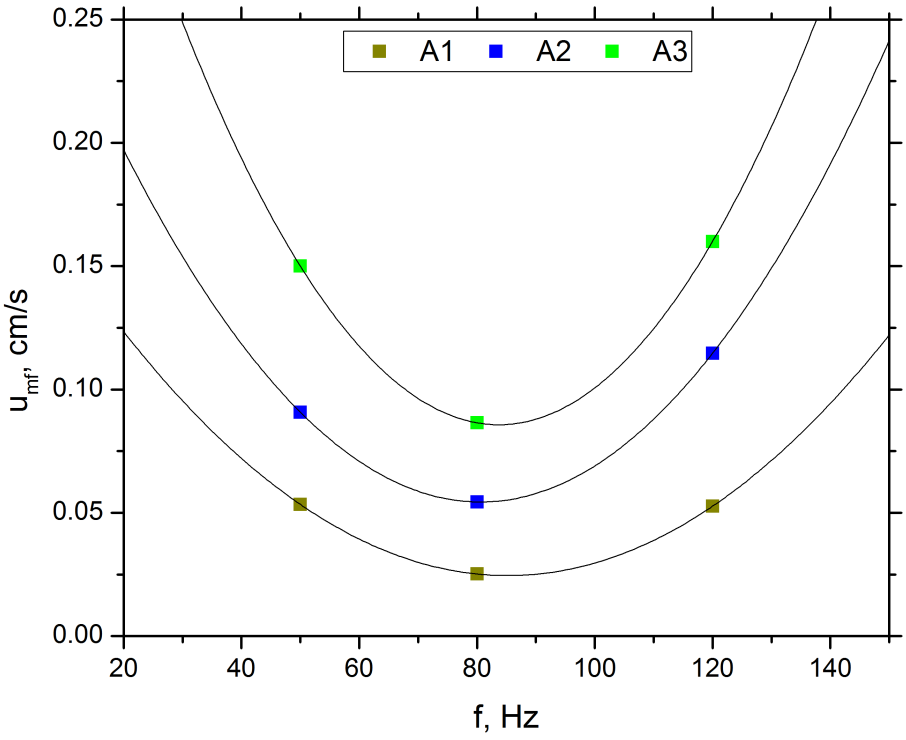

Figure A23 - Effect of sound frequency, at fixed SPL (140 dB), on u_{mf} for the cohesive samples.

As reported in literature [194], SPL has a beneficial effect on the fluidization quality of cohesive powders, indeed, ds (and u_{mf} as a consequence) is always decreased passing from 140 to 150 dB. This evidence is due to the fact that with increasing SPLs more energy is introduced inside the bed, thus making the break-up of larger clusters more and more efficient. However, even though the increase of SPL is effective in enhancing the break-up mechanism, it is also clear that for the cohesive samples, A1, A2 and A3, not even SPLs as high as 150 dB are capable to disrupt the clusters down to the size obtained from the granulometric distribution. In addition, the gap between the size of the granulometric distribution and the actual size of the fluidizing agglomerates decrease passing from the finer, A1, to the coarser cohesive sample, A3. With reference to samples A4 and A5, they fluidize in the form of particles with actual size corresponding to their Sauter diameter, regardless of the application of the sound (i.e. their fluidization behaviour is not affected by the acoustic perturbation since they are not cohesive). With reference to the effect of sound frequency, in agreement to several works reported in literature, it has a not monotonic effect on the fluidization quality of the cohesive samples, as confirmed by the fact that the curve of u_{mf} is characterized by a minimum value at 80 Hz (f_0*), i.e. the maximum response frequency (Figure A23). This behaviour is due to the fact that the

frequency directly affects the relative motion between clusters and subclusters, which, in turn, promotes the essential break-up and re-aggregation mechanism. In particular, for too high frequencies the acoustic field cannot properly propagate inside the bed; the sound absorption coefficient is proportional to the square of sound frequency as sound propagates through the bed of particles [188]. Consequently, for too high sound frequencies, most of the acoustic energy is absorbed by the upper part of the bed (since the sound source is located at the top of the column), whereas, only an attenuated sound energy reaches the bed bottom, thus failing to efficiently disrupt large agglomerates at the bottom of the bed and, hence, fluidization quality decreases (i.e. umf increases) [196,197]. On the contrary, for too low frequencies the relative motion between larger and smaller sub-agglomerates is practically absent. In particular, the period of the acoustic excitation is long with respect to the time needed for the flow of fluidizing gas to set up local channelling in the bed, which, after the initial perturbation, has recovered its adhesion [194]. Clearly, the fluidization quality of samples A3 and A4 is not affected by sound frequency.

A5.1.5 Model application

The cluster/subcluster model was applied for the cohesive samples, A1, A2 and A3, in order to evaluate the frictional cohesive forces F_{sound}. The model was not applicable for the coarser samples, A4 and A5; since they are not cohesive, they do not fluidize under the form of agglomerates and their fluidization behaviour is not affected by sound application.

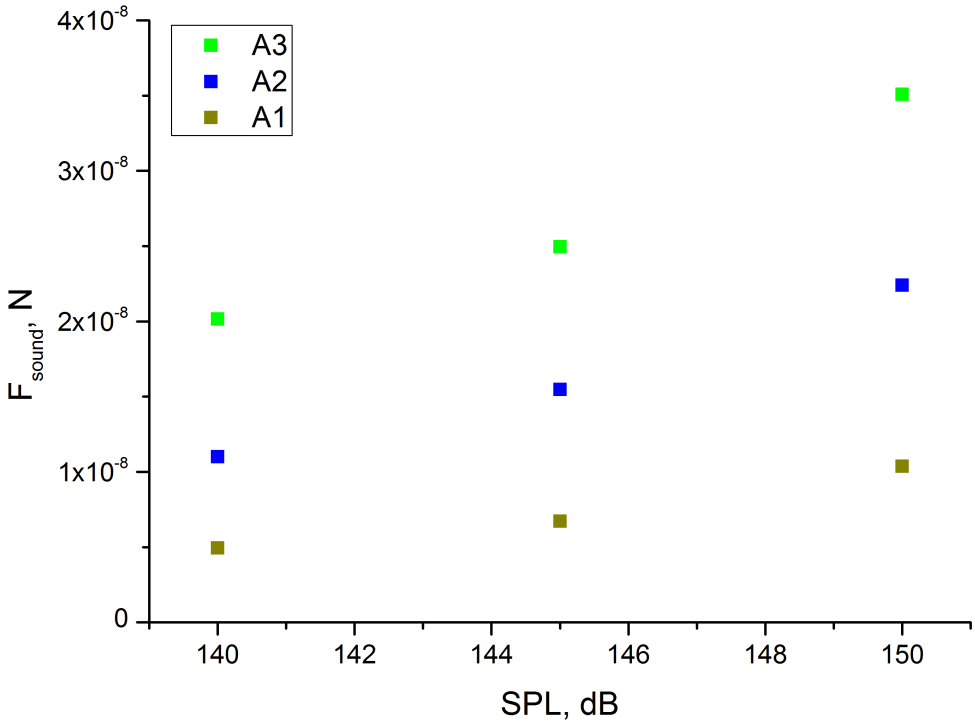

Figure A24 - Disaggregating force due to the application of the acoustic field as a function of SPL for the different samples.

The values of F_{sound} evaluated from the model are reported in Figure A24 as a function of the SPL. It is clear that the disaggregating force due to the application of the acoustic field (i.e. the cohesive frictional force at contact points between subclusters and clusters) is enhanced with increasing values of SPL, in agreement with the experimental results obtained from the fluidization tests. Indeed, as shown in Figure A22, increasing SPL from 140 to 150 dB results in a decrease of the fluidizing subcluster size, i.e. more energy is introduced inside the bed, thus making the break-up mechanism more efficient.

List of Publications

Chirone R, Barletta D, Lettieri P, Poletto M. Bulk flow properties of sieved samples of a ceramic powder at ambient and high temperature. *Powder Technol*. 2016;288:379-387. doi:10.1016/j.powtec.2015.11.040.

Chirone R, Raganati F, Ammendola P, Barletta D, Lettieri P, Poletto M. A comparison between interparticle forces estimated with direct powder shear testing and with sound assisted fluidization. Powder Technol. 2018;323:1-7. doi:10.1016/j.powtec.2017.09.038.

Chirone R, Barletta D, Poletto M, Lettieri P. Detection and estimation of capillary interparticle forces in the material of a fluidized bed reactor at high temperature by powder flow characterization. Powder Technol. February 2018. doi:10.1016/J.POWTEC.2018.02.024.

Sofia D, **Chirone R**, Lettieri P, Barletta D, Poletto M. Methods of preparation of materials for the Selective Laser Sintering of ceramic powders with bimodal particle size distribution. *MethodsX*. 2018;Submitted:536-547. doi:10.1016/j.cherd.2018.06.008

Chirone R, Barletta D, Poletto M, Lettieri P. The effect of temperature on the minimum fluidization conditions and on the bed expansion of industrial cohesive powdes. Powder Technol. (under review)

Chirone R, Barletta D, Poletto M, Lettieri P. The effect of temperature on the minimum bubbling conditions of industrial cohesive powdes: link with rheological studies. (to be submitted in Powder Technol.)

Macri, D., **Chirone, R.**, Barletta, D., Lettieri, P., Poletto, M. A new Matlab App for the analysis of bulk flow properties of compacted powders from shear tests. (to be submitted in Powder Technol.).

Chirone, R., Barletta, D., Lettieri, P., Poletto, M. Flow properties of ceramic powder at room and high temperature, in (proceeding) AIChE Annual Meeting, Atlanta, November 2014.

Chirone, R., Barletta, D., Lettieri, P., Poletto, M. Measurement of high temperature powder flow properties to estimate interparticle forces in high temperature fluidization, proceeding in The 8th International Conference for Conveying and Handling of Particulate Solids Tel—Aviv, Israel, May 2015.

Chirone, R., Lettieri, P., Poletto, M., Barletta, D. The relevance of surface impurities on the effect of temperature on powder flow behaviour, Fluidization XV, Canada, May 2016.